CONSTITUTIVE BEHAVIOR OF A TWARON® FABRIC/NATURAL RUBBER COMPOSITE: EXPERIMENTS AND MODELING

A Dissertation

by

VALLIYAPPAN DAVID NATARAJAN

Submitted to the Office of Graduate Studies of
Texas A&M University
in partial fulfillment of the requirements for the degree of

DOCTOR OF PHILOSOPHY

December 2009

Major Subject: Materials Science and Engineering

CONSTITUTIVE BEHAVIOR OF A TWARON® FABRIC/NATURAL RUBBER COMPOSITE: EXPERIMENTS AND MODELING

A Dissertation

by

VALLIYAPPAN DAVID NATARAJAN

Submitted to the Office of Graduate Studies of
Texas A&M University
in partial fulfillment of the requirements for the degree of

DOCTOR OF PHILOSOPHY

Approved by:

Co-Chairs of Committee,	Xin-Lin Gao
	Stefan Hurlebaus
Committee Members,	Anastasia Hanifah Muliana
	Xinghang Zhang
Intercollegiate Faculty Chair,	Tahir Cagin

December 2009

Major Subject: Materials Science and Engineering

ABSTRACT

Constitutive Behavior of a Twaron® Fabric/Natural Rubber Composite:

Experiments and Modeling. (December 2009)

Valliyappan David Natarajan, B.Eng.; M.Sc.,

Universiti Kebangsaan Malaysia, Bangi, Malaysia

Co-Chairs of Advisory Committee: Dr. Xin-Lin Gao
Dr. Stefan Hurlebaus

Ballistic fabrics made from high performance polymeric fibers such as Kevlar® and Twaron® fibers and composites utilizing these fabrics are among the leading materials for modern body armor systems. Polymeric fibers used to produce ballistic fabrics often behave viscoelastically and exhibit time- and rate-dependent stress-strain relations. This necessitates the study of the constitutive behavior of composites filled by ballistic fabrics using viscoelasticity models.

In the present work, the constitutive behavior of Twaron CT709® fabric/natural rubber (Twaron®/NR) composite is studied using three viscoelasticity models (i.e., a three-parameter generalized Maxwell ($GM^{n=1}$) model, a four-parameter Burgers model, a five-parameter generalized Maxwell ($GM^{n=2}$) model) and a newly developed para-rheological model. The new model utilizes a three-parameter element to represent the Twaron® fabric and the affine network based molecular theory of rubber elasticity to account for the deformation mechanisms of the NR constituent. The uniaxial stress-strain relation of the Twaron®/NR composite at two constant strain rates is experimentally determined. The values of the parameters involved in all the models are

extracted from the experimental data obtained in this study. The stress-relaxation response (under a uniaxial constant strain) and the creep deformation (under a uniaxial constant stress) of the composite are also experimentally measured.

The stress-strain relation at each strain rate predicted by the newly developed para-rheological model is seen to be in good agreement with the measured stress-strain curve over the entire strain range studied. It is shown that the new model also predicts the elastic moduli and ultimate stress of the Twaron®/NR composite well. An implicit solution provided by the para-rheological model is shown to predict the creep response of the composite more accurately than all the other models at both the primary and secondary stages. The mathematical complexity that arises from including an additional Maxwell element to the $GM^{n=1}$ model to obtain the $GM^{n=2}$ model with enhanced predictability is traded with the use of simple characteristic time functions in the para-rheological model. The relaxation and creep trends predicted by the para-rheological model indicate that the long time viscoelastic response of the composite lies between that of a crosslinked polymer and a semi-crystalline thermoplastic.

DEDICATION

Dedicated to my family and teachers

ACKNOWLEDGEMENTS

First and foremost, I would like to express my gratitude to the co-chair of my dissertation committee, Dr. Xin-Lin Gao for his patience, encouragement and direction throughout the duration of my study. Dr. Gao has been a persistent motivator who has guided me along the challenging path to a doctoral degree. His academic wisdom and firm belief in quality have been inspirational to the timely completion of my doctoral program. I would like to thank the co-chair of my dissertation committee, Dr. Stefan Hurlebaus for his scholastic and technical supports. I truly appreciate his understanding and continuous encouragement during the hard times in the Ph.D. pursuit. I am thankful to the members of my dissertation committee, Dr. Anastasia Muliana and Dr. Xinghang Zhang for their insightful questions and valuable ideas which have contributed to the scientific discourse presented in this dissertation.

I am grateful to my employer, Universiti Teknologi MARA in Malaysia for the financial support all through the extent of my doctoral study. I would like to convey my sincere appreciation to the United States Department of State for conferring me the Fulbright Fellowship and enriching my Fulbright experience during my stay here in the United States of America. I am thankful to the US Army – Soldier Equipment Program that partly supported the work presented in this dissertation. My heartfelt gratitude also goes to the offices of the Sponsored Student Programs, the Department of Mechanical Engineering, and the Materials Science and Engineering Program at Texas A&M University for facilitating matters related to my academic program and sponsorship.

All of the experimental tests reported in this dissertation were conducted at the Materials and Testing Laboratory, Department of Aerospace Engineering, Texas A&M University under the supervision of Mr. Rodney Inmon. I thank Mr. Inmon for his physical support and the arrangements that he made to perform the tests at different points in time during the project.

The time that I spent at Texas A&M University was made enjoyable, memorable and meaningful by fellow US and international Fulbrighters, laboratory mates, and friends from all over the world. Their hospitality, moral support and encouragement have been instrumental in one way or the other in completing the project and in writing-up this dissertation.

I would like to thank my family members and friends for their constant encouragement, love and prayers. For my beloved dad, thank you for raising me with a consciousness for truth and a passion for math. For my dear mom, thank you for teaching me how to write and count. And especially for my dearest wife Veni and beloved son Keshava Robert, thank you for your unconditional support. I am most lucky to have a life partner who remained faithful in my abilities and who together endured the hardship of earning a doctorate in a foreign land with me. Thank you!

Valliyappan David Natarajan
Texas A&M University
October 2009

TABLE OF CONTENTS

CHAPTER Page

CHAPTER Page

Page

LIST OF FIGURES

Page

Page

Page

LIST OF TABLES

Page

CHAPTER I

INTRODUCTION

Ballistic fabrics are made from polymeric fibers that possess high tensile strength and high elastic modulus (e.g., Tabiei and Nilakantan, 2008; Rao et al., 2009). Such polymeric fibers often exhibit viscoelastic stress-strain behavior. That is, they demonstrate both elastic and viscous responses during deformation. The mechanisms responsible for these two types of material responses can be related to the molecular features of the fibers (Termonia and Smith, 1986; Sperling, 2006).

At the molecular scale, the elastic behavior of a material arises primarily from distortions of chemical bonds, including elongation and scission. Strain energy is stored in the material when the bond lengths deviate from the equilibrium separation distance (in the minimum energy configuration). In polymeric materials, the molecular mechanisms for viscoelastic behavior include molecular entanglement (Doi and Takimoto, 2003), chain motion, viscous flow, bond interchange (Sperling, 2006), chain scission (Bjork and Stenberg 1990), and conformational changes (Ortiz et al., 1998a).

The stress-strain (constitutive) relations of viscoelastic fibers at different strain rates can be mathematically modeled using rheological elements called springs and dashpots, which can be assembled in various quantities and configurations (e.g., Akyildiz et al., 1990; Brinson and Brinson, 2008). The stiffness and viscosity constants

---

This dissertation follows the style of International Journal of Solids and Structures.

for these springs and dashpots are parameters that could be related to the deformation mechanisms and the molecular structures of the polymeric fibers (e.g., Khan and Zhang, 2001). The mechanical responses of the ballistic fabrics can then be predicted using viscoelasticity models that incorporate the morphological features of the fabrics and fibers, with the phenomenological parameters involved in these models determined from experimental data (e.g. Termonia and Smith, 1986). This approach is generally known as phenomenological modeling. The utility of this approach, together with its constraints for linear viscoelastic analysis, is further discussed below.

High-performance polymers (e.g., Twaron® fibers and natural rubber) exhibit time-dependent, non-linear mechanical responses to tensile loading. Higher order models, utilizing non-constant rheological elements, are necessary to predict the non-linear stress-strain relations (e.g., Corr et al., 2001). Fortunately, for small deformations, the material response is usually linear, and linear viscoelasticity can therefore be applied (e.g., Briscoe and Motamedi, 1992; Chen et al., 1995; Shim et al., 2001; Sebastian et al., 2008). A widely used approach to modeling linear viscoelastic polymers is the linear differential operator method that involves simple mathematical derivations (e.g., Findley et al., 1976; Lim et al., 2003; Tan and Ching, 2006). The result of this method can be summarized as

$$P\sigma = Q\varepsilon \quad . \tag{1.1}$$

Eq. (1.1) could be used to express the stress-strain relation of a linearly viscoelastic polymer under different uniaxial loading or deformation conditions. In Eq. (1.1), P and Q represent a series of linear time-derivative operators and are defined as follows:

$$P = \sum_{m=0}^{M} p_m \frac{d^m}{dt^m}, \quad Q = \sum_{n=0}^{N} q_n \frac{d^n}{dt^n}. \tag{1.2a,b}$$

Representation of the viscoelastic behavior (e.g., the stress relaxation) of a polymeric material can be modeled by a proper selection of the number of terms of the linear time-derivative operators series in Eqs. (1.2a,b). The resulting differential equation can alternatively be derived from rheological models consisting of the rheological elements mentioned earlier (e.g., Park, 2001).

By limiting the rheological elements to behave linearly, the deformation of a polymeric material induced by an applied load (or stress) can be divided into elastic, delayed elastic and viscous flow responses in the context of linear viscoelasticity. The elastic response is time-independent and reversible, while the viscous flow is time-dependent and irreversible. The former can be represented by a spring element, while the latter can be characterized by a dashpot. The delayed elastic response is time-dependent and reversible, which can be described by combining a spring and a dashpot that are either in series or in parallel. In the event of the stress level exceeding the material yield stress, plastic deformation will occur, whose description requires the use of partly reversible (elastic) and partly irreversible (plastic) elements (e.g., Baltussen and Northholt, 2003).

Other approaches to modeling the constitutive relations of ballistic fabrics include micromechanical models (e.g., Tan, et al., 1999; Xue et al., 2005; Barbero, et al., 2005), multiscale modeling (e.g., Nadler, et al., 2006), and variational principles (e.g., Roy and Sihn, 2001). These modeling techniques, which take into account the

geometrical structure and weaving architecture of the fabrics in the formulation, lead to governing differential equations that can either be solved analytically or numerically using the finite element method. The fractional derivative approach has also been employed to model the constitutive relation of some frequency-dependent viscoelastic solids (e.g., Torvik and Bagley, 1984; Pritz, 1996). The models obtained from these approaches are able to predict the stress values (for given strain values) with different degrees of accuracy. Moreover, the time-dependent deformation mechanisms of the fibers that compose the fabrics are not clearly accounted for in these models. Besides these modeling techniques, purely empirical equations developed just to fit the experimental data have also been utilized (e.g., Vleeshouwers et al., 1989; Huang and Gibson, 1991; Kromm et al., 2003; Kolarik and Pegoretti, 2006; Fallatah et al., 2007).

In this dissertation, the viscoelastic behaviors of a ballistic-grade Twaron® fabric and a composite based on the Twaron® fabric under different loading conditions are investigated. The ballistic fabrics selected in this study are made from two-dimensional plain-weave Twaron CT716® and Twaron CT709® fibers. The constitutive relations, i.e., the stress-strain relation and its dependence on the strain rate, of a Twaron CT716® fabric and a Twaron CT709® fabric/natural rubber composite are experimentally determined. The constitutive relations are then modeled using the linear differential operator method in tandem with the rheological modeling method in viscoelasticity. Three viscoelasticity models, (i.e., a four-parameter Burgers model, a three-parameter generalized Maxwell ($GM^{n=1}$) model, a five-parameter generalized Maxwell ($GM^{n=2}$) model) and a newly developed para-rheological model are utilized throughout this study.

The pertinence of the model parameters in characterizing the deformation mechanisms of the composite is explored.

A complete understanding of viscoelastic behavior of a composite entails a general appreciation of all the manifestations of the viscoelastic response and the corresponding analytical representation. In this work, the viscoelastic response of the Twaron®/NR composite has also been conceptualized in terms of the stress relaxation function and the creep function that are both determined through experiments. Each of these functions emphasizes a different aspect of the viscoelastic behavior of the composite. The creep and stress relaxation of the composite are characterized using the three viscoelasticity models mentioned above and the para-rheological model developed in this study.

CHAPTER II

BALLISTIC FABRICS: CONTEMPORARY AND PROSPECTIVE MATERIALS AND RELATED PROTECTION MECHANISMS

2.1 Introduction

Body armor has been used in military and combat actions for centuries since the Roman era (c. 145 BC). During the medieval times (AD 400 to c. 1500), full steel plate harness was used to protect the torso which was the most vulnerable part in the medieval knight style of combat (Starley, 1999). To date, the primary functions of body armor remain the same: to impede weapon and projectile penetration into the human body and to diffuse the impact energy. However, modern military operations, technology-driven war tactics and current on-street weapons and ammunition demand a flexible (wearability and mobility of the wearer), damage-resistant, and lightweight ballistic protection garment with superior energy absorbing capacity (Scales, 2006). Body armor intended for law enforcement and corrections personnel also requires similar traits (NIJ Guide 100–01, 2001). As a result, demand is on the increase for more reliable and enhanced anti-ballistic body armor fabrics.

Ballistic fabrics based on high performance polymeric fibers such as Kevlar®, Twaron® and Spectra® fibers and composites made from these ballistic fabrics are among the leading materials used in modern body armor designs. These fabrics are typically made from woven yarns, which consist of interlocked natural or synthetic fibers. A number of studies related to novel concepts and designs of ballistic fabrics and

composites based on ballistic fabrics have been conducted in the past two decades to meet the new demands mentioned above. Material properties and ballistic resistance mechanisms of such materials have been extensively investigated via experiments and analytical methods (e.g., Barauskas and Abraitiene, 2007; Colakoglu et al., 2007). Based on a comprehensive and critical review of the advances and findings resulting from these investigations, a comparative study on design, protection mechanisms and performance evaluation of various types ballistic fabrics of body armor made from is presented in this chapter. Body armor systems made from different fabrics and exhibiting distinct ballistic energy absorption mechanisms are discussed, and key factors that influence the ballistic performance and energy absorbing mechanisms of the ballistic fabric systems are identified.

2.2 Mechanism of ballistic energy absorption

Most ballistic fabrics exhibit a two-dimensional (2-D) plain weave pattern that is formed by interlacing warp and fill (or weft) yarns in two orthogonal directions (e.g., Gao and Mall, 2000). Stress waves, which are generated at the point of impact, travel along the yarns toward the fabric edges where they are reflected. These waves are also partially transmitted and partly reflected at the warp-fill yarn cross-over points. The speed at which the stress waves travel along the yarns depends on the density and stiffness of the yarns (and thus of the fibers).

When a projectile strikes a body armor fabric at a certain speed, it is caught in a web of the fibers to which its kinetic energy is transferred. This kinetic energy, carried by the stress waves as described above, is dissipated through fiber deformations and

inter-fiber friction when they slip or slide against each other. It has been found that the structure and frictional characteristics of these fibers significantly affect the overall performance of the fabric (Barauskas, 2005). The undissipated energy is absorbed by each successive layer (if present) of the material until the bullet has been stopped. Otherwise, the remaining energy may cause material damage such as fabric tear or slit. In the case of multilayer fabrics, the presence of physical interaction between layers makes the stress waves travel in both the planar and transverse directions, thereby further increasing energy dissipation. The bonding/connecting condition of fabric layers influences the wave propagation in the transverse direction and thus the energy absorption mechanism of the fabric armor.

2.3 Fabric characteristics related to ballistic performance

The factors affecting the performance of a ballistic fabric include the fabric weave types and fiber properties (e.g., Tan et al., 2005a), far-field boundary conditions (e.g., Zeng et al., 2005), inter-yarn friction (e.g., Nadler et al., 2003; Duan et al., 2005; Duan et al., 2006; Zeng et al., 2006), fabric-projectile friction (e.g., Duan et al., 2005), interaction between layers (upon impact) (e.g., Barauskas and Abraitiene, 2007), and projectile geometry (albeit an external factor) (e.g., Cheeseman and Bogetti, 2003; Ulven et al., 2003).

Among these factors, the inter-yarn friction plays a critical role. It was shown in Briscoe and Motamedi (1992) that the interfacial frictional work dissipated at yarn-yarn junctions affects the stiffnesses of the yarn (tensile) and the fabric (transverse), which in turn influences the ballistic performance of the fabric. A mesoscopic discrete model for

fabric deformations was developed by Boubaker et al. (2007), which accounts for the yarn-yarn interaction occurring at yarn crossing-over points. Their results indicated that fabrics with high yarn-yarn friction dissipate more energy than fabrics with low inter-yarn friction.

The inter-yarn sliding friction can be characterized using the static coefficient of friction (FSs). This parameter is usually determined experimentally (e.g., using a quasi-static yarn pull-out test; see Tan et al., 2005a) and is assumed to be independent of the sliding velocity for the sake of simplicity. The yarn-projectile friction can be described by using the kinetic coefficient of friction (FSk). The FSk was determined by a simple experiment involving the pulling of a block made from the projectile material across a flat sheet of the fabric (target) being tested (Lim et al., 2003). A study on the ranges of FSs and FSk that would break four yarns to perforate a fabric was performed in (Barauskas and Abraitiene, 2007), which provided the following results: $0.1 < FSs, FSk < 0.2$, with $0.1 < FSs + FSk < 0.3$.

Also, some ballistic fabrics exhibit stress-strain relations that are strongly strain-rate dependent. For instance, it was experimentally determined that Twaron® fabric is a strain-rate dependent, viscoelastic material (Shim et al., 2001). It was found that the failure strain of the fabric material decreases with increasing strain-rate. This characteristic of the fabric limits its deformation at high strain rates and causes the fabric to fail in a brittle mode, both of which lead to a reduction of impact energy absorption by the fabric. Besides the failure strain, two other measures that are usually used in the

textile industry to characterize ballistic fabrics in terms of their physical density and strength are the denier and tenacity, respectively. These measures are described next.

Denier is a measure of linear density (mass per unit length) of a yarn. The Industrial Fabrics Association International defines this measurement based on grams per 9000 meters of fiber or yarn. Another measure of linear density of fabric fibers is known as Tex and is measured in g/km. Tenacity is the amount of force (in grams) required to break a yarn, normalized with respect to the denier, and hence the 'gram/denier' quantity. Tenacity thus reflects the strength of a fabric.

In order to obtain enhanced anti-ballistic performance, high tenacity yarns may have to be used on the anterior and/or posterior of the fabric faces. As described in Gehring, Jr. (2000), this would depend on the degree of hazard and the type of ammunition. If the tenacity of a fabric yarn is greater than 15 gram/denier with a yarn modulus of 44 to 176.5 GPa, the fabric is designated as a high performance fabric suitable for ballistic protection (Magat, 1980). Dimensional and thermal stability also counts toward this designation. Some additional information about the material properties that influence the performance of ballistic fabrics can be found in (Cheeseman and Bogetti, 2003).

2.4 Performance measures of ballistic fabrics

Ballistic performance of a fabric is often characterized by its ballistic limit and its specific ballistic energy, which represents the mass efficiency of the fabric (Tan et al., 2005b). The ballistic limit, V_{bl} (in m/s), is a measure of velocity at which the projectile

(with mass m, in kg) has just started to penetrate the armor with areal density A_ρ (in kg/m^2). The specific ballistic energy, E_s (in J·m^2/kg), defined by

$$E_s = \frac{mV_{bl}^2}{2A_\rho}, \tag{2.1}$$

refers to the kinetic energy of the projectile at the ballistic limit per unit areal density (e.g., Tan et al., 2005b). The areal density of an armor material comprising n fabric layers is defined as

$$A_\rho = \sum_{i=1}^{n} t_i \rho_i , \tag{2.2}$$

where t_i and ρ_i are, respectively, the thickness and density of the ith layer.

The dissipated projectile kinetic energy may be written as (e.g., Lee et al., 2003)

$$E = \frac{1}{2} m(V_i^2 - V_r^2), \tag{2.3}$$

where E is the dissipated energy (in J), V_i is the initial projectile velocity (in m/s) (which can be V_{bl}), and V_r is the residual velocity of the projectile after penetration (in m/s). This quantity E is usually normalized with respect to the initial kinetic energy of the projectile. In the event that only partial or no penetration could be achieved, $V_r = 0$ and Eq. (2.3) would reduce to

$$E = \frac{1}{2} m V_i^2 . \tag{2.4}$$

The baseline ballistic limit, which refers to the impact velocity at which a projectile completely penetrates an armor component 50% of the time (or in other words, 50% probability for full penetration, denoted as V50), needs to be experimentally

determined and statistically obtained (NIJ Standard 0101.06, 2008; MIL-STD-662F Standard, 1997). Note that V50 defined in (NIJ Standard 0101.06, 2008) differs from the ballistic limit (V_{bl}) mentioned above.

It should be mentioned that most publications cited in subsequent sections are related to Twaron® and Kevlar® fabrics, which appear to have been more extensively studied and utilized.

2.5 Enhancement of ballistic performance

As indicated above, the inter-yarn friction of a woven fabric has an important effect on its ballistic performance. This leads to the novel concept of modifying commercially available anti-ballistic fabrics with shear-thickening fluids to increase the inter-yarn friction of the fabrics during impact. Another innovative way to improve the ballistic performance of the fabrics is to enhance their bending stiffness via rubber or resin coating. These approaches are discussed next.

The concept of shear thickening fluid (STF) was studied by Bender and Wagner (1996), and Lee et al. (2003). STF is a liquid filled with high concentrations of rigid colloidal particles, whose viscosity increases with the shear stress rate (Lee et al., 2003). When impacted by a penetrating projectile, the high shear stress rate enables hydrodynamic forces to overcome repulsive inter-particle forces. This affects the formation of hydroclusters of particles. Clusters of particles are formed via aggregation of particle groups. The short range lubrication effect by the projectile increases the viscosity of the STF. Clusters will then face more resistance to move against each other. This affects the frictional interaction between the yarns and thereby improves the

ballistic properties. Collisions of the hydroclusters transform the flexible fabric into a macroscopically rigid armor.

The ballistic impact characteristics of Kevlar KM-2® (600 denier with an areal density of 180 g/m^2) woven fabrics impregnated with a colloidal STF consisting of silica particles (with an averaged diameter of 450 nm) in ethylene glycol was reported by Lee et al. (2003). The Kevlar® fabric layers were impregnated with 2, 4 and 8 ml of the STF per layer, respectively. Their results indicated that the energy absorption of four layers of the Kevlar® fabric is proportional to the amount of the STF. For example, four layers of the Kevlar® fabric impregnated with 8 ml of the STF dissipated about 93% of impact energy, which is comparable to that (~90%) of 14 layers of the neat Kevlar® fabric albeit the sample weight of the former is more than twice of the latter. This observation signifies the trade-off between the improved performance and the fabric weight. The performance enhancement provided by the STF was thought to be due to the increased frictional interaction between the yarns, which is yet to be further investigated.

The ballistic performance of a Twaron CT615® plain-weave fabric (500 denier with areal density of 150 g/m^2) impregnated with a silica-water suspension (SWS) consisting of silica colloids with concentrations of 0, 20 wt%, 40 wt% and 50 wt%, respectively, was studied in Tan et al. (2005b). SWS is a class of STF, but silica colloids in water were used by Tan et al. (2005b) as opposed to a suspension of silica colloids in ethylene glycol employed by Lee et al. (2003). Their results showed that a 40 wt% SWS particle concentration yields the highest ballistic limit for single, double and quadruple ply fabric systems, with the double ply system showing the greatest improvement. The

ballistic limit and the specific ballistic energy of the double ply system with the 40 wt% SWS particle concentration were, respectively, 65% and 90% higher than those of the neat double ply system. The improvement in the ballistic resistance was attributed to the increase in the projectile-fabric friction and inter-yarn friction arising from the addition of the silica particles (with a nominal size of 100 nm in diameter) and the formation of silica clusters. This is similar to what was observed by Lee et al. (2003), as indicated earlier.

Very recently, another innovative approach to modifying the Twaron CT709® microfilament fabric (840 denier with an areal density of 202 g/m^2) was undertaken by coating the fabric with different grades (in terms of tensile modulus) of natural rubber (NR), namely high modulus, medium modulus and low modulus (Ahmad et al., 2007). The 4-layer fabric systems consisting of alternating neat and coated fabric layers resulted in a higher ballistic limit than the all-neat 4-layer fabric system, with the fabric systems containing layers coated by natural rubber with a higher modulus dissipating more energy. A 21 – 26% increase in the ballistic limit for the three different combinations of the neat and coated fabrics (4 layers) in comparison to the all-neat system was observed. The energy absorbed at the ballistic limit by the 4-layer fabric systems is 45 – 59% higher than that by the all-neat system. Observations of the yarn pull-out of damaged samples revealed that the natural rubber coated fabric layer suffers less yarn damage with smaller slit size. The natural rubber layer acted as a stiff membrane to deflect and absorb more impact energy, and hence the improvement. In addition, their study also indicated that the enhancement of ballistic performance was related to the higher inter-

yarn friction and restricted yarn movement due to the coating material that penetrated and held the yarns tightly. This agrees with the earlier findings by the other two groups mentioned above.

Table 2.1 provides the ballistic limits of four different enhanced body armor materials and the improvements achieved. The ballistic limit for the Kevlar® system was determined at a fixed penetration velocity (244 m/s), and, as a result, no comparison could be made with the neat system. Fig. 2.1 shows the performance enhancement of the ballistic energy absorption and damping mechanism of these systems.

Table 2.1
Ballistic limits of different body armor material systems and designs.

System and configuration	Ballistic limit, V50 (m/s)	Ballistic Limit of neat system (m/s)	Improvement
Kevlar® + silica colloidal (in ethylene glycol); 4 layers + 8ml STF	253	-	-
Twaron CT615® + silica colloidal (in water); Double ply + 40wt% SWS	223	135	65%
Twaron CT709® + NR; 2 neat + 2 high modulus (alternating layers)	252	200	26%
Woven (Sentinel®) + Nonwoven layers; Inventive (needle punched woven/non-woven layers)	385	302	28%

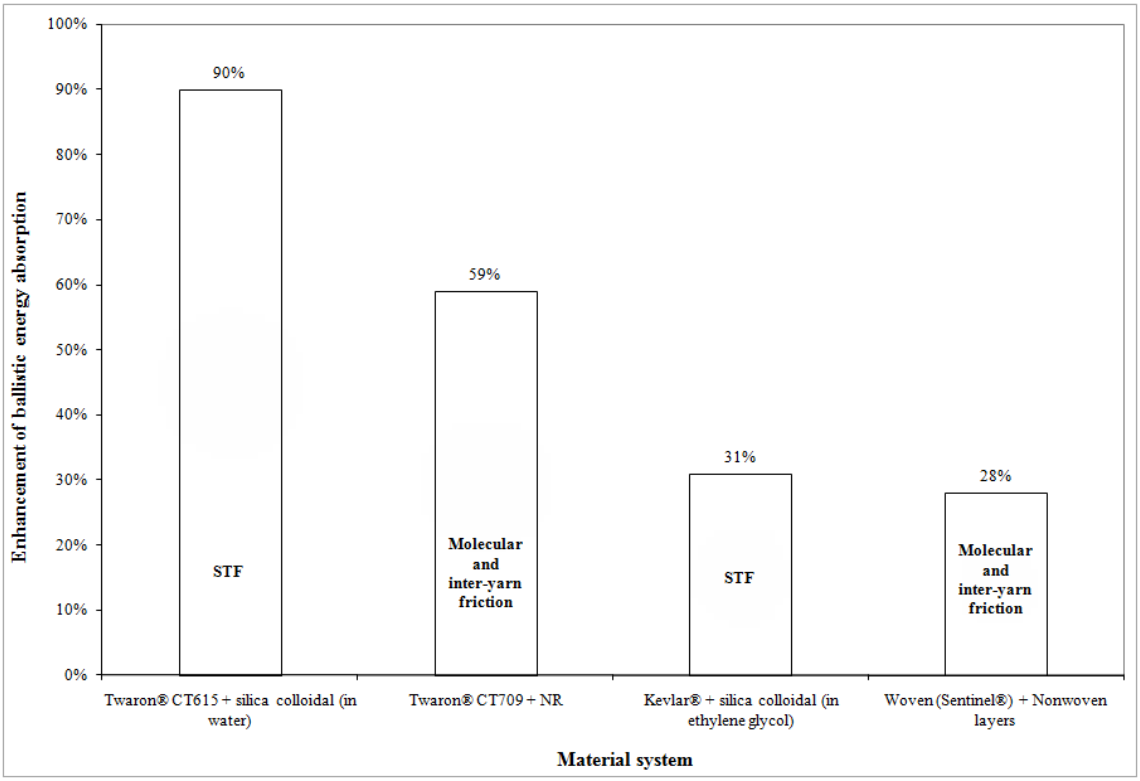

Fig. 2.1 Comparison of the energy absorption of four different material systems.

However, thermal analysis was not performed on the as-received and post-impact fabric materials to determine their thermal stability in the investigations reviewed here. Therefore, the effects of different types of suspension fluids on the thermal stability of the modified fabrics remain to be explored.

Alteration of the bending properties of fabric materials by resin coating has also been investigated. The effect of a resin (undisclosed) coating on Kevlar 29® fabric sheets was analytically studied by Walker (2001). The ballistic performance, V50, of a number of sheets coated with the resin was compared with that of the uncoated Kevlar 29® sheets for the same relative areal density. It was found by Walker (2001) that the fabric sheets

without resin coating outperform the resin coated fabrics with an equivalent relative areal density up to a certain point, after which the converse was observed. Similar results were experimentally demonstrated by Cunniff (1999).

The effect of resin coating is mainly on the bending strength of the fabric. The "dry fabric" can only support tensile membrane stresses. In the presence of resin, the resin/fabric system turns into a hard and stiff panel (e.g., Egres et al., 2004; Roylance et al., 1995). This increases the bending resistance of the fabric and enhances the resin/fabric panel's resistance to inward deformation, thereby improving the ballistic performance. Similar findings were reported by other groups (Lee et al., 2001; Silva et al., 2003).

As mentioned in Section 2.5, in spite of their high strength, most ballistic fibers are susceptible to UV light induced degradation after a sufficient long exposure time. Four methods of enhancing the UV resistance of some ballistic fibers are outlined by Said et al. (2006). In addition, an approach to combating the UV degradation of a Kevlar® fabric was studied by Katangur et al. (2006), where it was reported that using nanostructured polymer coatings helps the Kevlar® fabric to retain 95% of its tensile strength after 7 days of UV exposure.

2.6 Effects of woven architecture of fabrics on ballistic performance

As mentioned in Section 2.1, most ballistic fabrics have 2-D plain weave patterns. A three-dimensional (3-D) woven architecture is an integrated structure comprising the conventional 2-D weaves and transverse yarns that connect the in-plane yarns along the thickness direction. The transverse yarns thus provide through-thickness

reinforcement (*z*-reinforcement). The 3-D woven architecture contributes to the structural integrity of a fabric or a composite made from the 3-D fabric (Miravete, 1999). The relevant anti-ballistic benefits of the intermingled 3-D architecture include improved stiffness and strength in the transverse direction and increased resistance to the disentanglement of in-plane weaves. The impact load on a 3-D woven fabric gets resolved in three orthogonal directions rather than only in two in-plane directions, thereby enhancing the energy absorption capability of the fabric.

Various weaving techniques have resulted in a wide range of structural configurations for woven fabrics. The architectural features of a woven fabric, such as warp-weft crossing over, influence the stress wave propagation in the fabric, which in turn affects the energy absorption of the fabric. Weave patterns thus have a significant effect on the ballistic performance of woven fabrics.

The ballistic resistance of 3-D woven fabric composites was studied by Grogan et al. (2007), where the benefit of using 3-D fabrics in controlling and localizing the delamination upon impact was noted. It was observed that the 3-D woven structures give fewer complete penetrations than 2-D woven fabric composites due to the *z*-reinforcement, which was pivotal in arresting inter-lamina cracks. It was also found that absorption of kinetic energy is mainly achieved through intra-lamina delamination. The sizes of the delamination in the 3-D woven composites were found to be smaller than those in the 2-D woven composites. A comprehensive discussion of various energy absorbing mechanisms of woven fabric composites was provided in (Naik et al., 2006), where energy absorption by the primary yarns (i.e., yarns directly below the projectile),

deformation of the secondary yarns (i.e., yarns within the conical impact zone), delamination and matrix cracking, and projectile-fabric friction were studied.

The effect of fiber arrangements on low-velocity impact behavior of 3-D woven composites using the basalt and the para-aramid (Kevlar®) fibers was investigated by Wang et al. (2008). Two types of fiber arrangements, i.e., alternating layers each consisting of plain weaves of one yarn type (i.e., inter-ply hybrid) and sequential layers each comprising plain weaves of different yarn types (i.e., intra-ply hybrid), were examined. The Kevlar® yarn was used as the *z*-reinforcement to vertically weave six warp yarn layers and seven weft yarn layers. The fabrics were woven using a 3-D weaving machine. The impact energy absorption was found to depend on the failure mode, which in turn was a function of the fiber arrangements. It was also observed that the inter-ply hybrid failed in a layer-by-layer mode giving larger energy absorption, while intra-ply hybrid failed in a brittle mode absorbing very little energy.

2.7 Flexible composite armor

Flexible composite armor or soft armor is mainly used for body protection and for the sake of wearer's mobility. The armor materials are primarily woven fabrics composed of high-stiffness, densely stacked organic fibers. Ability to absorb impact energy without extensive deformation so as to protect the wearer from being struck by the ammunition is the main design consideration of flexible composite armor (Hogg, 2006). By and large, flexible composite armor materials are closely associated with ballistic fabrics.

2.7.1 Fabric systems

A host of commercial fabric material systems such as those made from Kevlar®, Twaron® and Spectra® fibers has been used in the design of vests and helmets for the United States military troops involved in the on-going battle in Iraq and Afghanistan. Discussions on the design of new material systems based on these commercial fabrics have been provided in Sections 2.6 and 2.8. Besides the para-aramid fibers used to produce the Kevlar® and Twaron® fabrics, other high performance fibers being utilized to manufacture ballistic fabrics include the UHMWPE, PBO and S-2 glass fibers. The degradation aspects of the PBO and UHMWPE fibers and fabrics have been discussed in Section 2.4. An overview of the chemistry and ballistic properties and a juxtaposition of the advantages and disadvantages of these fibers were provided in (Lane, 2005).

The polypyridobisimidazole organic fiber, also known as the M5® fiber, is worth mentioning here. This fiber was developed by Magellan Systems, LLC (a subsidiary of DuPont Advanced Fiber Systems) and has been tested for the Future Force Warrior project by the United States Army Soldier Systems Center. The M5® fiber is said to be stronger and lighter than the para-aramid fibers and the UHMWPE fiber. For instance, the M5® fiber provides at least 35% weight saving for the same level of protection offered by the Kevlar® fiber (SSC-Natick Press Release, 2003). The M5® fiber has been described as a rigid rod polymer featuring bi-directional hydrogen bonding that creates a 3-dimensional honeycomb network (McConnell, 2006). Even though the M5® fiber possesses strength and weight advantages, some issues related to its manufacturability and its stability at higher temperatures still need to be addressed (Cervenka et al., 2005).

2.7.2 Polymer composites

Polymer matrix composites have been utilized for protection against ballistic impact. Epoxy and polyester are two types of polymers that have been widely studied for body armor applications. Carbon and glass fibers, usually in fabric preforms (mats), are commonly employed to enhance the strength and toughness of the epoxy and polyester matrices. Other high strength polymeric fibers (such as the para-aramid and UHMWPE fibers) have also been investigated (e.g., Faur-Csukat, 2006). Polymer matrix composite plates can be used as protective inserts in modular body armor vests, e.g., the Interceptor Body Armor (Mil-Tech Editorial Review, 2006).

The ballistic performance of plates made from polyester reinforced by E-glass mats and filled with coarse sand was studied by Sabet et al. (2008). The areal density of the three-phase, lightweight composite panels varies between 0.61 g/cm^2 and 1.65 g/cm^2, depending on the thickness of the laminated plates and the volume fraction of the filler. It was found that the V50 ballistic limit and the corresponding specific ballistic energy (see Eq. (2.1)) of the composite plates increase with the volume fraction of the micro-sized (600 – 700 μm) sand filler. High velocity impact tests with the impact velocity ranging between 70 m/s and 200 m/s were conducted on the plates. For unfilled composite specimens, it was found that the specific ballistic energy tends to increase with the thickness (i.e., number of layers) of the plates. A similar finding was reported in (Faur-Csukat, 2006). The V50 ballistic limit generally increases with the thickness of the composite plates and the filler volume fraction. Adding sand into the composite improves the stiffness of the composite. For thin plates (i.e., 4 layers at about 4 mm

thick), it was observed that the sand-filled composite plates perform better than the unfilled composite plates in terms of V50 due to the stiffening effect of the filler. The thick specimens (i.e., 12 plies at about 10 mm thick) absorbed 400% more energy per unit areal density than the thin ones mainly by delamination. Thus, the overall protection mechanism against penetration involves the E-glass fiber straining and the delamination of the plies, even though the later may dominate in energy absorption under high-velocity impact loading, as elaborated in (Thaumaturgo and Da Costa Jr., 1997).

The ballistic properties of Kevlar 29®/Polivnyl Butyral™ (KPB) woven fabric composites and UHMWPE laminated plates for lightweight armor design were investigated by Colakoglu et al. (2007). The thickness of the KPB and UHMWPE specimens was 4 mm and 2.9 mm, respectively. The plates were made from 20 layers of individual composite laminas. The areal density of the KPB specimen was 9.28 kg/m^2 and that of the UHMWPE was 5.04 kg/m^2. The ballistic performance of the composites was tested against a 9 mm full metal jacket bullet. It was determined that the V50 of the KPB specimen is 680 m/s, whereas the UHMWPE plate has a V50 equaling 480 m/s. The ballistic performance of the composites was quantified in terms of V50 and the back face deformation. For the same areal density, the UHMWPE plate yielded a V50 that is 30% higher and a back face deformation that is 100% smaller than those of the KPB composite. It was found that the higher elastic modulus and strength of the UHMWPE composite enhance its ballistic performance. Also, a higher projectile mass was observed to reduce the V50.

2.8 Summary

The design, protection mechanisms and performance evaluation of ballistic fabrics normally used for body armor systems are discussed. The ballistic performance of these materials is evaluated on different but corresponding bases. In general, factors that directly influence the ballistic limits of body armor systems are areal density (and thickness), type and velocity of projectile, and material configuration. In addition, elastic modulus, strength and toughness are important properties that affect the projectile defeat mechanisms and enhance the impact energy absorption of body armor. Several innovative modifications of existing ballistic fabric materials to cater for the needs of improved safety and reduced weight were outlined. The development of high performance fabrics for the next generation body armor will depend heavily on high tenacity yarns made from fibers with high modulus, high strength, and excellent anti-degradation traits.

CHAPTER III

VISCOELASTIC MODELING OF BALLISTIC FABRICS AT DIFFERENT STRAIN RATES

3.1 Introduction

As was mentioned in Chapter II, ballistic fabrics are made from high performance polymeric fibers, which often exhibit viscoelastic behavior. The stress-strain relations of such viscoelastic fibers at different strain rates can be modeled using rheological elements called springs and dashpots, which can be assembled in various quantities and configurations (e.g., Brinson and Brinson, 2008). The stiffness and viscosity constants for these springs and dashpots are phenomenological parameters that could be related to the molecular structures of the polymeric fibers. The mechanical responses of the ballistic fabrics can then be predicted using viscoelasticity models that incorporate the morphological features of the fabrics and fibers, with the parameters involved in these models determined from experimental data.

A number of viscoelasticity-based models have been proposed to characterize ballistics fabrics. For example, a network of nodal masses connected by one-dimensional viscoelastic elements was used by Tan et al. (2005a) to model responses of the Twaron CT716® fabric to impact loading. In (Cheng and Chen, 2006), a continuum model was developed using a pseudo-elasticity theory to describe the stress-strain behavior of Kevlar KM2® fibers. Most existing studies on constitutive modeling of ballistic fabrics utilize a single model to analyze the fabric behavior at both low and high strain rates

(e.g., Tan and Ching, 2006). There is a lack of studies that employ different rheological models or parameter values to correlate with distinct microstructural mechanisms at various stages of fiber deformation and failure. This motivated the work presented in this chapter.

In this chapter, a one-term generalized Maxwell ($GM^{n=1}$) model and a generalized Kelvin-Voigt (GKV) model, which are both three-parameter viscoelasticity models, are proposed to describe the viscoelastic behavior of a ballistic fabric, Twaron CT716®, at the strain rates of 1 s^{-1} and 495 s^{-1}. These models differ in how the discrete rheological elements are configured. The $GM^{n=1}$ model, also known as the Wiechert model (Koh et al., 2008), consists of a Maxwell element (including a viscous dashpot and a spring in series) and a second spring in parallel to the Maxwell element, while the GKV model is an assembly of a Kelvin-Voigt (KV) element (containing a viscous dashpot and a spring in parallel) and a second spring in series with the KV element.

The values of the parameters involved in the $GM^{n=1}$ model and the GKV model are extracted from the experimental data via curve-fitting. A parametric study is conducted to relate the values of the parameters of these two models to the deformation mechanisms of the Twaron® fibers at the molecular scale. It is shown that the constitutive law for both the models can be transformed into each other and therefore both the models are equivalent by using optimized parameter values. A simple and efficient model that could represent the viscoelastic behavior of the Twaron® fabric constituent will be chosen from the two models tested here for utilization in the next chapter.

3.2 Viscoelastic modeling of para-aramid fibers

As defined by the US Federal Trade Commission, aramid fiber is a generic term for a manufactured fiber whose forming substance is a long-chain synthetic polyamide, with at least 85% of the amide linkages attached directly to two aromatic rings (e.g., Yang, 2000). Twaron® fiber is a *para*-aramid fiber with para-oriented phenylene segments (IUPAC, 1997). The molecular structure of a *para*-aramid fiber is schematically shown in Fig. 3.1.

The repetitive monomer unit shown in Fig. 3.1 is connected by intramolecular covalent bonds to form a polymer chain. These covalent bonds are the primary chemical interaction between molecules in a single chain. Adjacent polymer chains are linked by the secondary bonds including van der Waals forces and hydrogen bonds, which are two types of intermolecular forces, with the latter being the stronger one (e.g., Kalantar and Drzal, 1990). The secondary bonds between polymer chains (with the dissociation energy ranging from 0.5 to 7 $kJ \cdot mol^{-1}$) are weaker than the intramolecular covalent bonds having the dissociation energy in the range of 50 – 200 $kJ \cdot mol^{-1}$ (e.g., Brinson and Brinson, 2008).

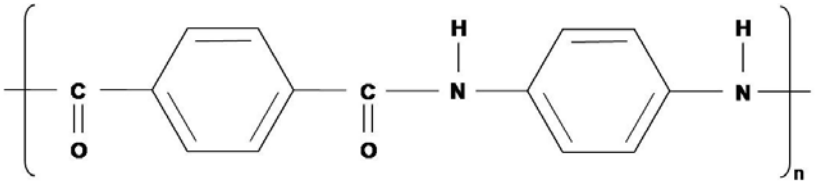

Fig. 3.1 Monomer unit of a *para*-aramid fiber.

3.3 Mechanical analogue of polymer chains

The reaction of the polymer chains to a mechanical strain (due to impact and subsequent wave propagation) depends on how the chain bonding is affected by the straining. The more the chains are stretched, the greater the fiber extension will be.

The mechanical analogue of the polymer chains, as shown in Fig. 3.2, consists of springs (to represent the solid-like response of the fiber) and dashpots (to describe the viscous (fluid-like) behavior) (e.g., Shim et al., 2001). The concept of such a representation is based on what was elaborated by Termonia and Smith (1986) for the poly(*p*-phenylene terephthalamide) molecules that make up the Kevlar® fiber.

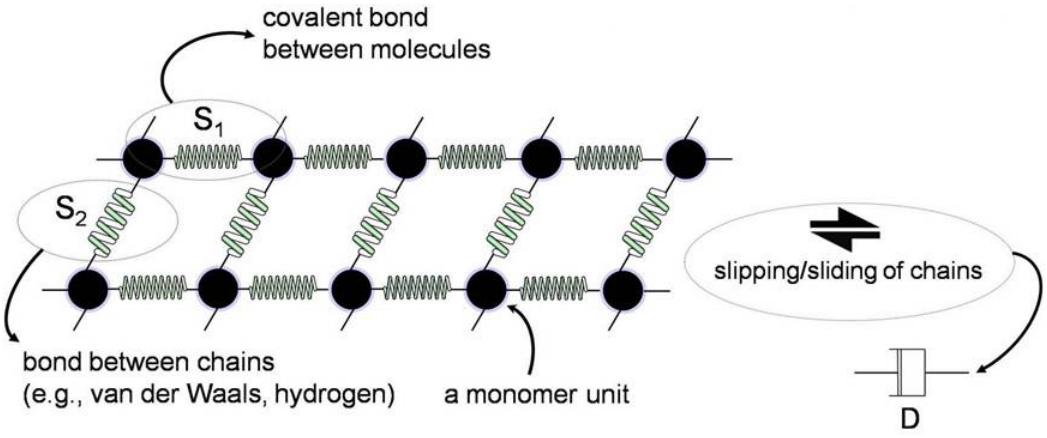

Fig. 3.2 Mechanical analogue of highly ordered polymer chains.

Aramid fibers such as Twaron® fibers have highly ordered molecular structures featured with macromolecular long chains (e.g., Shim et al., 1995). This permits the primary (strong) and secondary (weak) bonds within and between the polymer chains to be modeled by Hookean springs S_1 and S_2 (with $S_1 > S_2$), respectively. The slipping and

sliding of polymer chains relative to each other is a viscous process, and this feature can be captured by the Newtonian dashpot element D. The stiffness of the fiber is governed by both the primary and secondary bonds (e.g., Shim et al., 1995). The fiber deformation mechanisms and the effect of strain rate on the fiber failure process are discussed next.

3.4 Deformation mechanisms of aramid-based fabrics

The structure-property relationships for para-aramid fibers (including Kevlar® and Twaron® fibers) of different grades were examined in (Yeh and Young, 1999) where it was observed that the deformation mechanisms in all of the fibers tested are similar in spite of their different molecular structures and morphology.

On the macroscopic level, the material in the impact zone is displaced out of the fabric surface by an impinging projectile. The yarns that are directly impacted by the projectile are called the primary yarns. The immediate consequence of the impact is the transverse deflections of the primary yarns, which result in strains (and stresses) in the fabric yarns and the propagation of longitudinal waves along the primary yarns (e.g., Smith et al., 1962). The transverse deflections of the primary yarns continue until the maximum strain due to impact exceeds the breaking strain of the yarn, after which the projectile perforates the fabric. The tensile failure of the primary yarns, the deformations of other yarns, and the energy dissipated during the wave propagation are the major energy absorbing mechanisms of ballistic fabrics (e.g., Morye et al., 2000; Naik and Shrirao, 2004).

At the molecular scale, stress in an aramid fiber is related to the intermolecular resistance to deformation and the resistance associated with the molecular (re)orientation during the deformation of the fiber (Boyce et al., 2000). Such resistances would influence the extension of the polymer chains and the relative motion between the chains that could lead to entanglement of the chains and increased rigidity of the fiber, as the applied strain increases. These deformation mechanisms on the molecular level are captured by the rheological (viscoelasticity) model shown in Fig. 3.2. The $GM^{n=1}$ (or GKV) model mentioned in Section 3.1 would then be sufficient to cater for different deformation mechanisms, depending on the strain rate.

Polymers fail in different modes including brittle fracture, shear yielding, and crazing (e.g., Koh et al., 2008). Brittle failure occurs when a polymeric material possesses a low failure strain and absorbs a very small amount of energy. Brittle fracture is caused by scission of both the primary and secondary bonds in a short duration of time (in the range of micro-seconds). In this mode of failure, the breakage of the primary intramolecular bond (represented by S_1 in Fig. 3.2) is more prominent, and plastic flow is insignificant. Shear yielding, which is caused by intermolecular slipping, is represented by the dashpot element (D in Fig. 3.2) in the viscoelasticity model. The shear failure mode requires adequate relative mobility between polymer chains that permits intermolecular sliding, which can be logically achieved by overcoming the secondary bonds.

3.5 Effect of strain rate on fiber deformation

At low strain rates (e.g., 0.1 s^{-1}), plastic deformations (of the chains) and/or intermolecular slippage are possible causes of fiber failure. This necessitates the breakage of the secondary bonds (i.e., van der Waals forces and hydrogen bonds). The slow deformation rate allows more time for greater energy absorption and larger failure strain. However, at high strain rates (e.g., 100 s^{-1}), the stress level increases rapidly, which gives very little time for plastic deformations to occur. The fiber fails in a brittle mode at high strain rates via the breakage of the primary bonds. It was observed in (Shim et al., 1995; Koh et al., 2008) that when the strain rate increased from 0.002 s^{-1} to 400 s^{-1}, the failure mode went from ductile to brittle, with the failure stress and stiffness increased while the failure strain decreased. These and other studies also indicate that the failure strain is closely related to the failure mode. The failure mode is in turn dictated by the strain rate and the stress magnitude. The configuration of the rheological elements can be modified to improve the sensitivity of the viscoelasticity model to strain rate (Karim and Hoo Fatt, 2006). However, as was noted by Roylance (1977), a straightforward $GM^{n=1}$ (or GKV) model should be sufficient to study the viscoelastic stress-strain behavior of ballistic fibers.

3.6 Constitutive equations of the $GM^{n=1}$ and GKV models

The effect of a sudden stress on a Maxwell element (consisting of a viscous dashpot and a spring in series) is the rapid deformation of the Hookean spring element (instantaneous elasticity). Upon release of the stress, the spring tends to return to its

original configuration, while the dashpot behaves viscously. As a result, an irreversible stress accumulates after the release of the applied stress, enabling the Maxwell element to exhibit a liquid-like response. In contrast, in a Kelvin-Voigt (KV) element (consisting of a viscous dashpot and a spring in parallel), deformations are reversible, as controlled by the elastically deformed spring. The response of the KV element therefore represents a solid-like behavior.

The Kelvin-Voigt and Maxwell rheological (viscoelasticity) models have been used to characterize stress-strain relations of such fabrics at different strain rates. However, these two-parameter models have been found to be inadequate and inaccurate in some applications. The attachment of a third component, a spring, to a Maxwell element and a KV element will, respectively, lead to the $GM^{n=1}$ and GKV models, which can better depict the mechanical behavior of viscoelastic polymers, as discussed above.

It is proposed here that the constitutive relations of the Twaron CT716® fabric be described using two three-parameter viscoelasticity models, namely the $GM^{n=1}$ and GKV models. The primary bonding (described by S_1), secondary bonding (modeled by S_2) and intermolecular slipping (simulated by D) shown in Fig. 3.2 are, respectively, represented by K_1, K_2 and η in the $GM^{n=1}$ and GKV models to be discussed in detail next.

3.6.1 A one-term generalized Maxwell ($GM^{n=1}$) model

The $GM^{n=1}$model consists of a Maxwell element (hence the denotation one-term) and a second spring in parallel to the Maxwell element, as shown in Fig. 3.3. The two-parameter Maxwell element is not adequate in representing the viscoelastic behavior of

an aramid fiber because it caters for the secondary bonds but does not accommodate the primary bonds (see Fig. 3.2). However, the $GM^{n=1}$ model, which contains a second spring, is capable of predicting the viscoelastic response of the fiber at different strain rates.

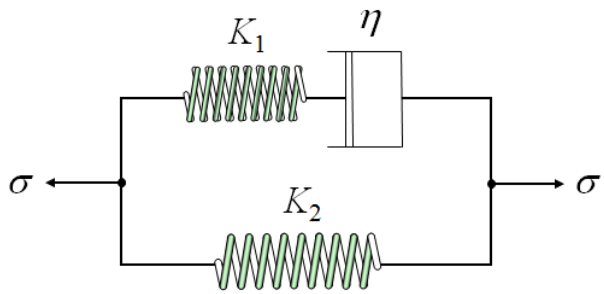

Fig. 3.3 A one-term generalized Maxwell ($GM^{n=1}$) model.

It can be shown that the stress-strain relation described by the $GM^{n=1}$ model illustrated in Fig. 3.3 has the following form (see *Appendix A.1*):

$$\sigma(t) = K_2\varepsilon(t) + \eta\dot{\varepsilon} + c_1 e^{-\frac{K_1}{\eta}t}, \tag{3.1}$$

where K_1 and K_2 are the spring constants, η is the dashpot viscous constant, and c_1 is an integration constant to be determined from an initial condition. In reaching Eq. (3.1), use has been made of the assumption that the strain rate is constant (i.e., $\dot{\varepsilon}$ = constant).

Consider the initial conditions:

$$\sigma(0) = 0, \quad \varepsilon(0) = 0, \tag{3.2a,b}$$

which give, upon using Eq. (3.1),

$$c_1 = -\eta\dot{\varepsilon}\,. \tag{3.3}$$

Note that $\frac{d\varepsilon}{dt} = \dot{\varepsilon}$ = constant, together with Eq. (3.2b), results in $\varepsilon = \dot{\varepsilon} t$. Using this relation and Eq. (3.3) in Eq. (3.1) then yields

$$\sigma(t) = K_2 \varepsilon(t) - \eta \left(e^{-\frac{K_1}{\eta}\frac{\varepsilon}{\dot{\varepsilon}}} - 1 \right) \dot{\varepsilon} \tag{3.4}$$

as the constitutive relation given by the $GM^{n=1}$ model shown in Fig. 3.3.

According to Eq. (3.4), the stress experienced by the fabric (at a given time) is a function of the applied strain (at that time) and strain rate. The first term in the square brackets on the right hand side (RHS) of Eq. (3.4) decays to zero as t $(= \varepsilon/\dot{\varepsilon}) \rightarrow \infty$, implying that this term corresponds to the initial transient response. The first and second terms on the RHS of Eq. (3.4) represent the instantaneous and delayed elastic responses of the fabric, respectively.

3.6.2 Generalized Kelvin-Voigt (GKV) model

The GKV model consists of a KV element and a second spring in series with the KV element, as shown in Fig. 3.4. Similar to that for the Maxwell element, the two-parameter KV element is not adequate to represent the viscoelastic behavior of an aramid fiber because it caters for the secondary bonds but does not account for the primary bonds in the absence of a second spring (see Fig. 3.2).

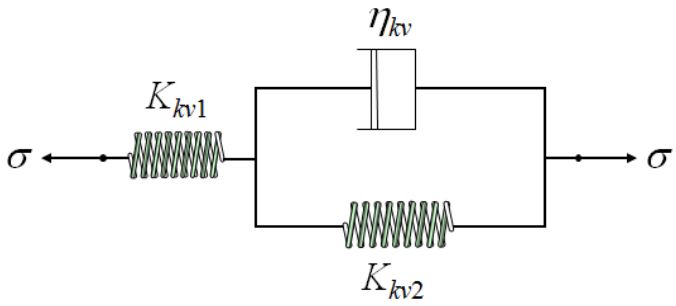

Fig. 3.4 Generalized Kelvin-Voigt (GKV) model.

It can be shown that the stress-strain relation described by the GKV model illustrated in Fig. 3.4 is (see Appendix B)

$$\sigma(t) = \frac{K_{kv1}K_{kv2}}{K_{kv1}+K_{kv2}}\varepsilon(t) - \frac{K_{kv1}{}^2\eta_{kv}}{(K_{kv1}+K_{kv2})^2}\left(e^{-\frac{K_{kv1}+K_{kv2}}{\eta_{kv}}\frac{\varepsilon}{\dot{\varepsilon}}} - 1\right)\dot{\varepsilon}, \qquad (3.5)$$

where use has been made of the initial conditions and the constant strain rate assumption that are the same as those used in deriving Eq. (3.4).

According to Eq. (3.5), the stress experienced by the fabric (at a given time) is a function of the applied strain (at that time) and strain rate. The first term in the square brackets on the RHS of Eq. (3.5) decays to zero as t (= ε/ε̇) → ∞, implying that this term stands for the initial transient response. Similar to those in Eq. (3.4), the first and second terms on the RHS of Eq. (3.5) represent, respectively, the instantaneous and delayed elastic responses of the fabric.

3.7 Results and discussion

3.7.1 Parametric analysis

The following sections are intended to illustrate the capability of the GM$^{n=1}$ model and the GKV model for characterizing the Twaron CT716® ballistic fabric. In this regard, Eqs. (3.4) and (3.5) are used for a parametric study of the GM$^{n=1}$ and GKV models, respectively. The three parameters, K_1, K_2 and η, involved in these equations are identified to fit and compare with the experimental data for the Twaron® fabric reported in (Shim et al., 2001), which are reproduced and shown in Fig. 3.5 here for convenience.

Based on the testing results reported in (Shim et al., 2001) and shown in Fig. 3.5, the strain ranges to be used here and in the sequel are $0 < \varepsilon < 0.18$ and $0 < \varepsilon < 0.02$ for the low strain rate (1 s^{-1}) and high strain rate (495 s^{-1}), respectively.

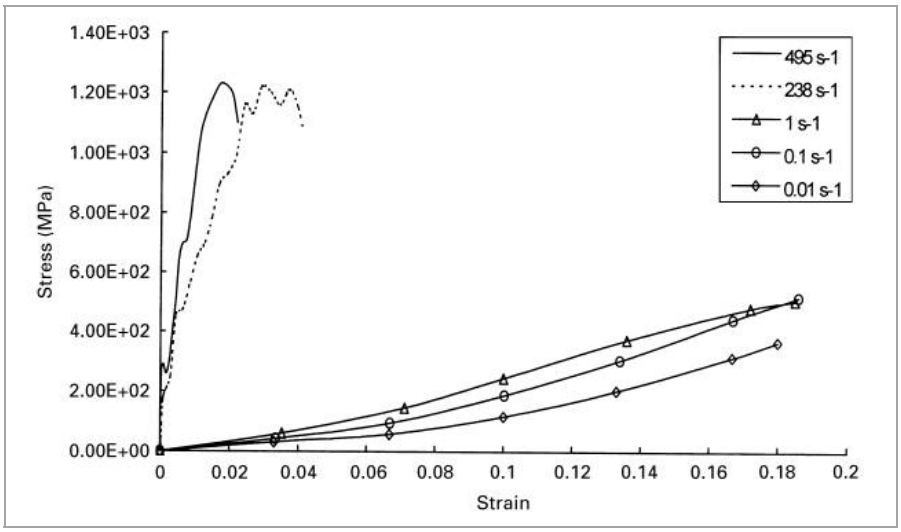

Fig. 3.5 Experimental stress-strain curves of the Twaron CT716® fabric at various strain rates. (*Source*: Shim et al. (2001).)

The parameter values are first taken to be $K_1 = K_{kv2} = 2.80\times10^9$ Pa, $K_2 = K_{kv1} = 1.60\times10^{11}$ Pa and $\eta = \eta_{kv} = 3.00\times10^6$ Pa·s, which were used in (Lim et al., 2003) for various strain rates and are called the *initial* parameter values here. These values are then *adjusted* to match the experimental data of Shim et al. (2001). The adjusted parameter values are further *modified* as needed for strains over certain values (see Table 3.1) to improve the correlation between the predicted results and the experimental data.

3.7.1.1 Predictions of the GM$^{n=1}$ model at low and high strain rates

Table 3.1 shows the *initial*, *adjusted,* and *modified* values of the parameters of the GM$^{n=1}$ model. The values in the parentheses are *modified* parameter values for strains greater than 0.13 mm/mm at the low strain rate. The value in the square brackets is a *modified* parameter value for strains greater than 0.0076 mm/mm at the high strain rate. The other values are *adjusted* parameter values for strains less than 0.13 mm/mm and 0.0076 mm/mm for the low and high strain rates, respectively.

Table 3.1
Values of the parameters used in the GM$^{n=1}$ model.

Model	Strain rate	K_1 (Pa)	K_2 (Pa)	η (Pa·s)
GM$^{n=1}$	1 s^{-1}	2.80E+09	2.40E+09 (2.80E+09)	9.50E+06 (1.00E+07)
	495 s^{-1}	2.80E+09	1.20E+11 [9.00E+10]	3.00E+05

Figs. 3.6 and 3.7 show the experimental stress-strain curves of the Twaron® fabric together with the predictions by the GM$^{n=1}$ model at a low strain rate ($\dot{\varepsilon}$ = 1 s^{-1}) using the parameter values given in Table 3.1.

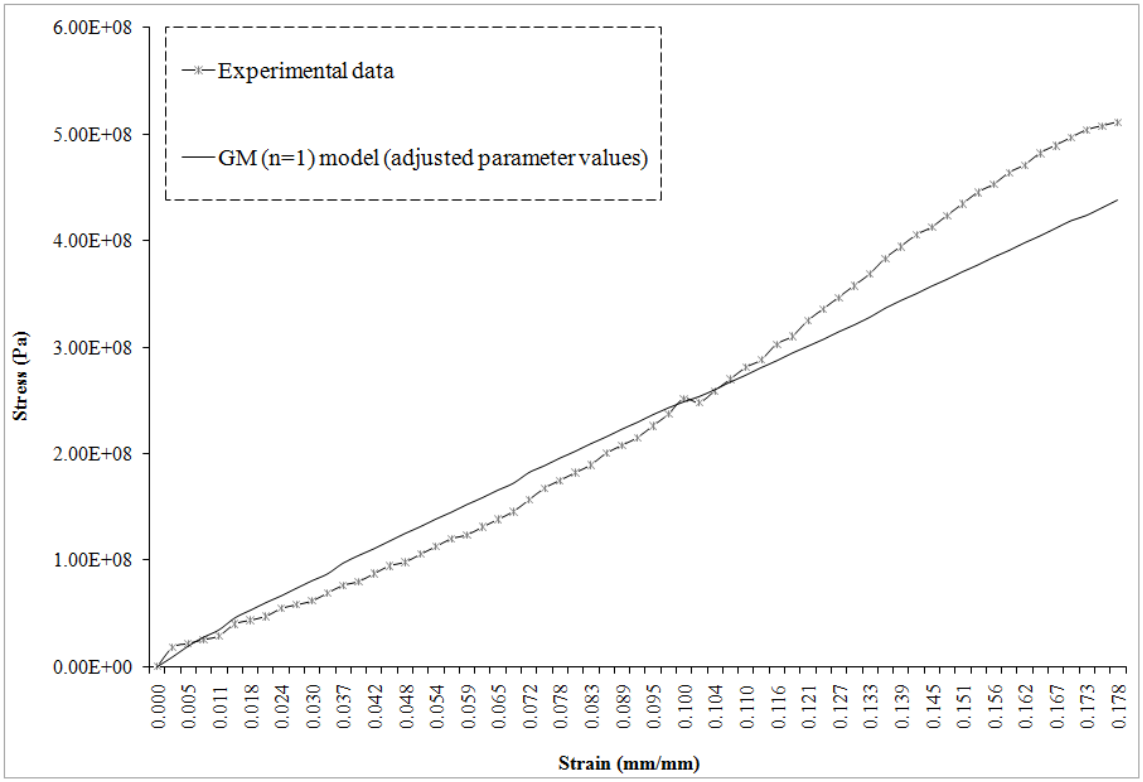

Fig. 3.6 Stress-strain curves of the Twaron® fabric at a low strain rate ($\dot{\varepsilon}$ = 1 s^{-1}): Experimental data and predictions by the GM$^{n=1}$ model with the *adjusted* parameter values.

It is seen from Fig. 3.6 that the use of the *adjusted* parameter values identified above (see Table 3.1) leads to a poor correlation to the experimental data. However, Fig. 3.7 shows that using the *adjusted and modified* values of K_1, K_2 and η listed in Table 3.1

gives a good fit with the testing results, indicating that the GM$^{n=1}$ model is capable of describing the stress-strain relation of the Twaron CT716® fabric at $\dot{\varepsilon} = 1\ \mathrm{s}^{-1}$.

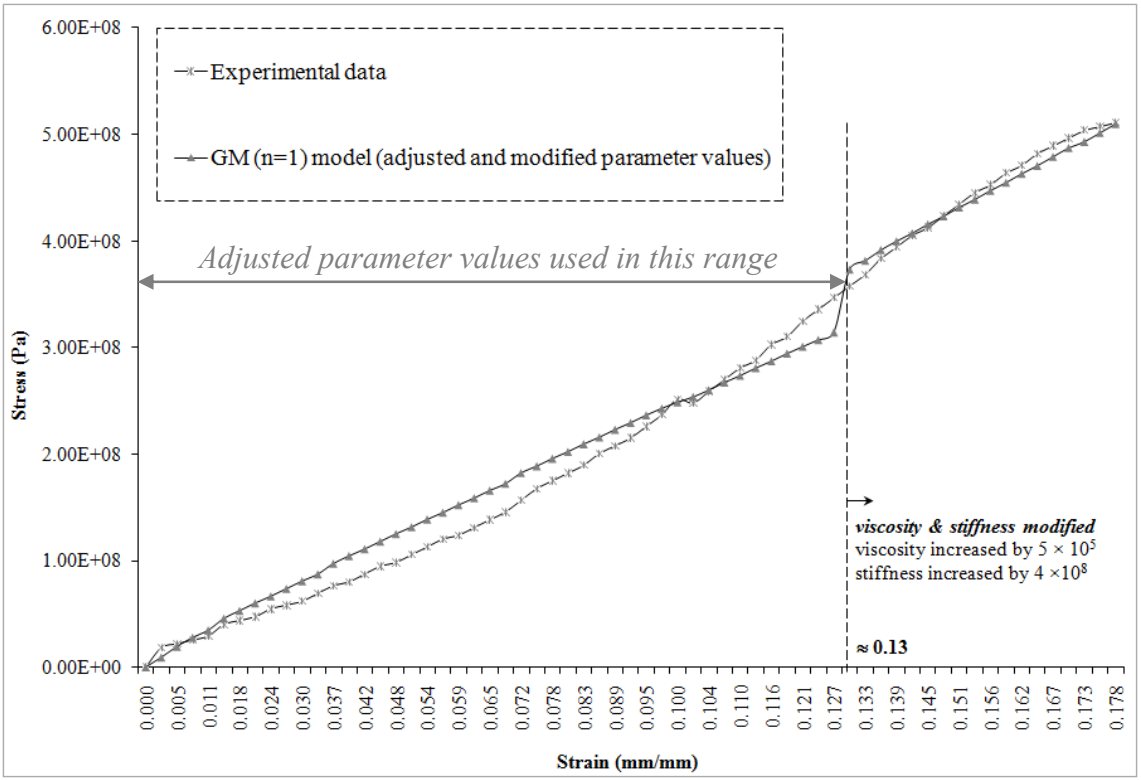

Fig. 3.7 Stress-strain curves of the Twaron® fabric at a low strain rate ($\dot{\varepsilon} = 1\ \mathrm{s}^{-1}$): Experimental data and predictions by the GM$^{n=1}$ model with the *adjusted* and *modified* parameter values.

The results predicted by the GM$^{n=1}$ model at a high strain rate ($\dot{\varepsilon}$ = 495 s^{-1}) are shown in Fig. 3.8. As in the case of the low strain rate deformation discussed above, it is seen from Fig. 3.8 that the use of the *initial* parameter values in the GM$^{n=1}$ model gives a poor correlation with the experimental data, with the predicted stress values being always less than the experimental values. On the other hand, Fig. 3.8 shows that the

$GM^{n=1}$ model with the *adjusted and modified* parameter values listed in Table 3.1 provides a good fit with the experimental data for the strain range from 0.3% to 1.2%. This observation conforms to a general result in viscoelasticity, which states that a single functional constitutive relation is not sufficient to completely characterize a material undergoing large deformations and/or at high strain rates (Christensen, 2003).

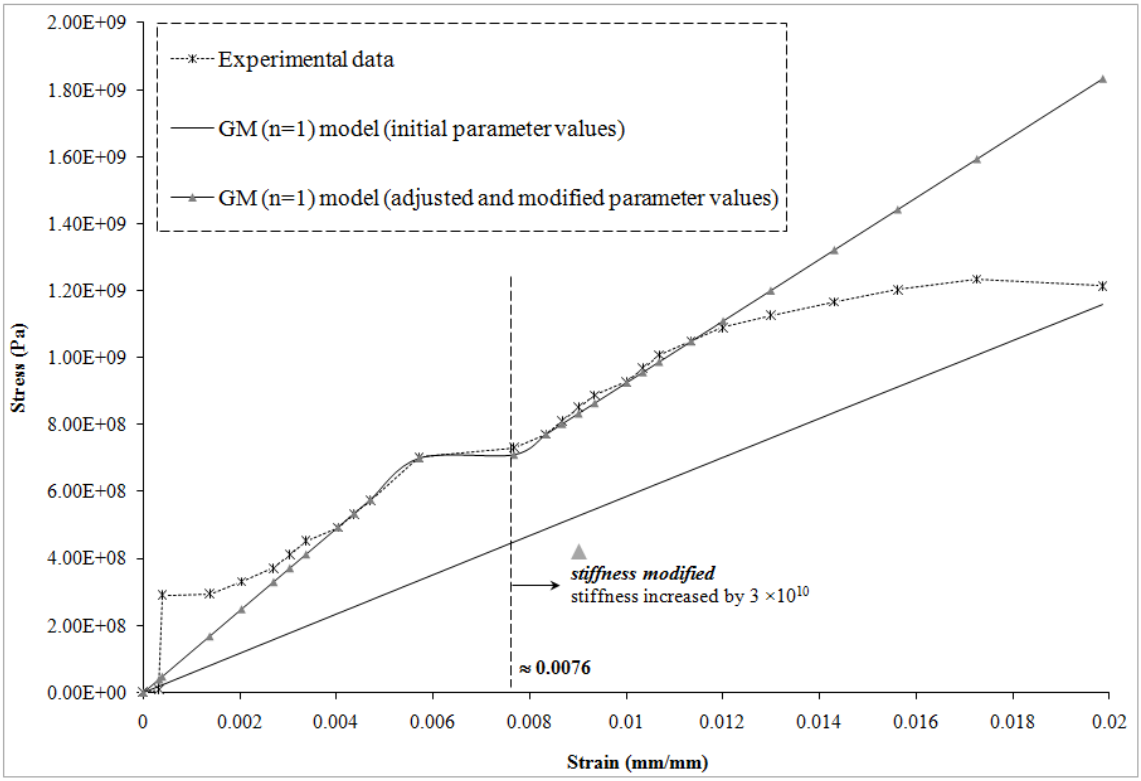

Fig. 3.8 Stress-strain curves of the Twaron® fabric at a high strain rate ($\dot{\varepsilon} = 495\ s^{-1}$): Experimental data and predictions by the $GM^{n=1}$ model with the *initial*, *adjusted* and *modified* parameter values.

It can be seen from Table 3.1 that the value of the dashpot viscous constant, η, is reduced and the primary bond parameter, K_2, is increased to match the experimental data for the high strain rate application of the GM$^{n=1}$ model.

The reduction of the viscous constant could be attributed to the destruction of the original molecular structure of the polymer at high strain rates, whereby the polymer chains attain greater mobility (Averyanov et al., 1980). At the high strain rate, the failure strain is significantly reduced, as can be seen from Fig. 3.5. This large reduction indicates that the fiber may have failed in a brittle mode at the high strain rate. As mentioned in Section 3.2, brittle fracture is caused by scission of both the primary and secondary bonds in a short period of time in which the breakage of the primary intramolecular bonds (denoted by S_1 in Fig. 3.2) is more prominent and the intermolecular slip (represented by D in Fig. 3.2) is insignificant (e.g., Ellyin et al., 2007). The predictability of the GM$^{n=1}$ model with the increased K_2 value at the high strain rate signifies the role of the primary bonds in the fiber failure process.

3.7.1.2 Predictions of the GKV model at low and high strain rates

Table 3.2 shows the *initial*, *modified* and *adjusted* values of the parameters of the GKV model.

Table 3.2
Values of the parameters used in the GKV model*.

Model	Strain rate	K_{kv1} (Pa)	K_{kv2} (Pa)	η_{kv} (Pa·s)
GKV	1 s^{-1}	1.60E+11	♣2.50E+09	♣3.30E+06
			2.80E+09	3.00E+06
			§2.90E+09	
	495 s^{-1}	8.00E+05	2.80E+05	3.00E+06

*The values indicated are the *modified* parameter values for strains less than ♣0.12 mm/mm, and larger than §0.136 mm/mm at the strain rate of 1 s^{-1}. The other values are *adjusted* parameter values.

The experimental data are slightly non-linear at the low strain rate, as shown in Fig. 3.5. The results predicted by the GKV model using the *initial* parameter values are good around ε = 0.13 mm/mm. A better fit of the experimental data for other values of strain was achieved by using the *adjusted and modified* parameter values listed in Table 3.2. The GKV model using the *initial* parameter values over-predicts the stress by 22.5% at the strain value of 0.083 mm/mm, as shown in Fig. 3.9.

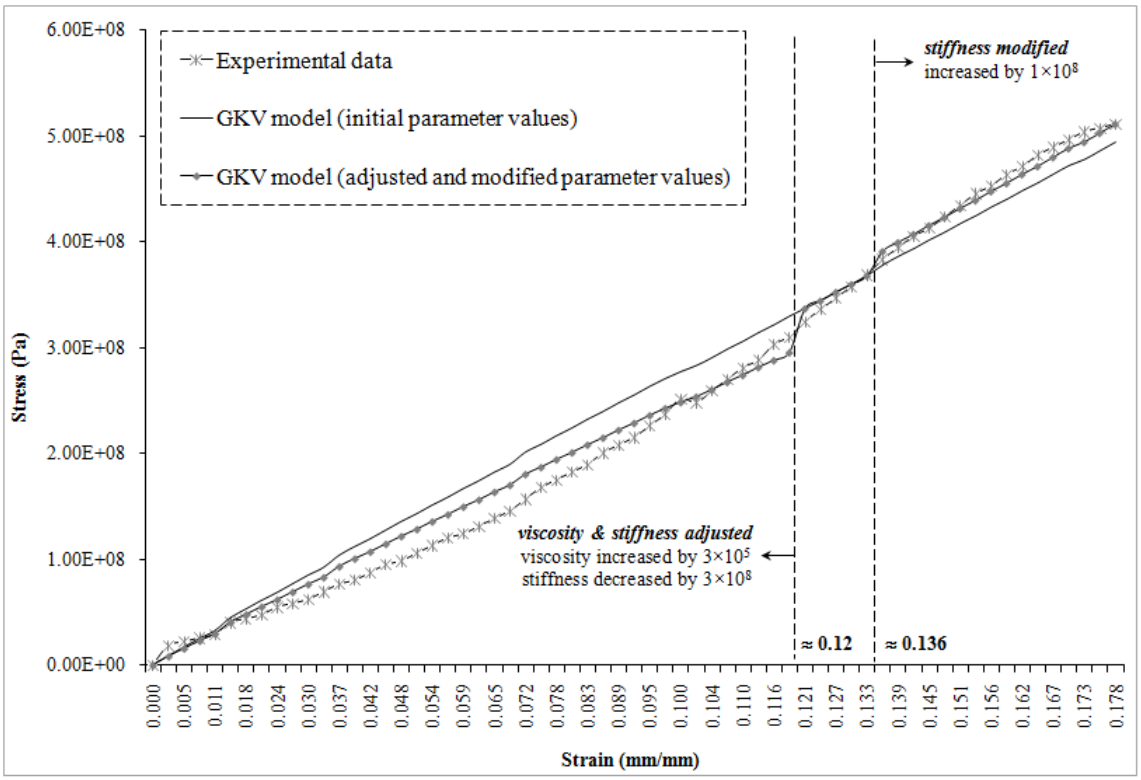

Fig. 3.9 Stress-strain curves of the Twaron® fabric at a low strain rate ($\dot{\varepsilon} = 1\ \mathrm{s}^{-1}$): Experimental data and results predicted by the GKV model with the *initial*, *adjusted* and *modified* parameter values.

In order to optimize the curve fitting over the entire strain range considered, parametric changes are implemented into the model. The parametric adjustments accorded to the model reflect the material evolution at the molecular scale as the strain increases. The resulting predictions may be divided into two response regimes. As shown in Fig. 3.9, the strain range is divided into the stiffness (K_{kv2}) dependent regime at strains greater than 0.13 mm/mm and the other regime below 0.13 mm/mm where both the stiffness (K_{kv2}) and viscosity (η_{kv}) of the secondary bonds control the best fit of the experimental curve. An increase of η_{kv} by 3×10^5 Pa·s coupled with a reduction of K_{kv2} by

3×10^8 Pa provided a better fit in the first regime. On the other hand, in the second regime, i.e., the stiffness controlled regime, a better fit is obtained through increasing K_{kv2} by 1×10^8 Pa. This may be explained as follows.

Both springs in the GKV model elongate when a load is applied at a low strain rate. The value of K_{kv2} is, however, smaller than that of K_{kv1} (see Table 3.2), indicating a higher magnitude of the applied stress required for the K_{kv1} spring than for the K_{kv2} spring to achieve the same amount of strain in both springs. Then, it follows that the weaker bond represented by the K_{kv2} spring will be overcome first provided that the duration of the deformation is sufficiently long. Thus, the breakage of the secondary bonds and the intermolecular slip dominate the fiber failure at the low strain rate. The slow deformation rate also implies that the deformation process consumes more time in breaking the primary bonds (represented by K_{kv1}). A direct result of this is a larger value of failure strain (0.18 mm/mm, as shown in Fig. 3.5) and a greater amount of energy absorption.

Fig. 3.10 shows the results predicted by the GKV model for the high strain rate deformation and their comparison with the experimental data reported in (Shim et al., 2001). It is seen that the predictions using both the *initial* and *adjusted* parameter values are not in good agreement with the testing data, although both sets of the predictions show a similar trend, i.e., a slight increase of stress for increasing strain up to failure.

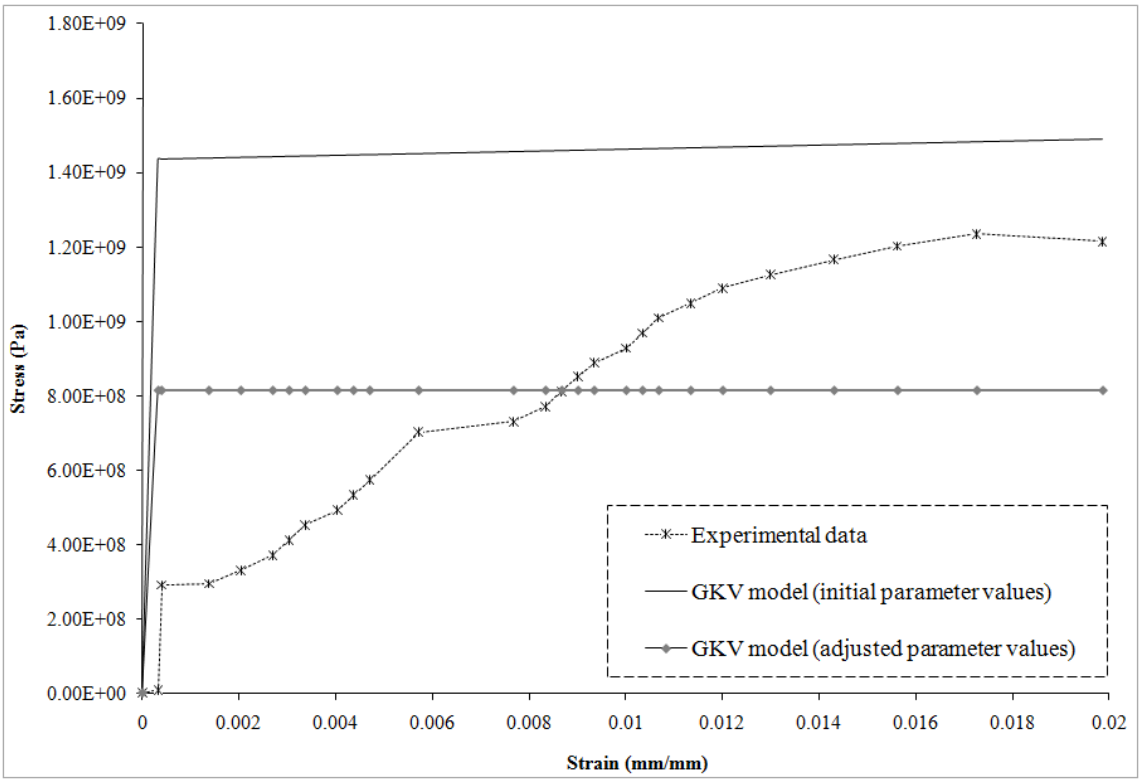

Fig. 3.10 Stress-strain curves of the Twaron® fabric at a high strain rate ($\dot{\varepsilon} = 495\ \mathrm{s}^{-1}$): Experimental data and results predicted by the GKV model with the *initial* and *adjusted* parameter values.

Referring to the GKV model shown in Fig. 3.4, at a higher strain rate, the strain in the K_{kv2} spring would be smaller due to the higher stress level in the dashpot, and, as a result, the K_{kv1} spring would be subjected to a larger strain. This indicates that the primary bonds represented by K_{kv1} spring would be severed before the secondary bonds, leading to brittle failure of the fabric at high strain rates. Further discussions on the predictability of the GKV model are presented next.

3.7.2 Effect of strain rate and predictability of the GM$^{n=1}$ and GKV models

The predictability of the GM$^{n=1}$ and GKV models at a low strain rate is illustrated and compared in Fig. 3.11. It is seen that both of the models provide fairly good predictions at the low strain rate.

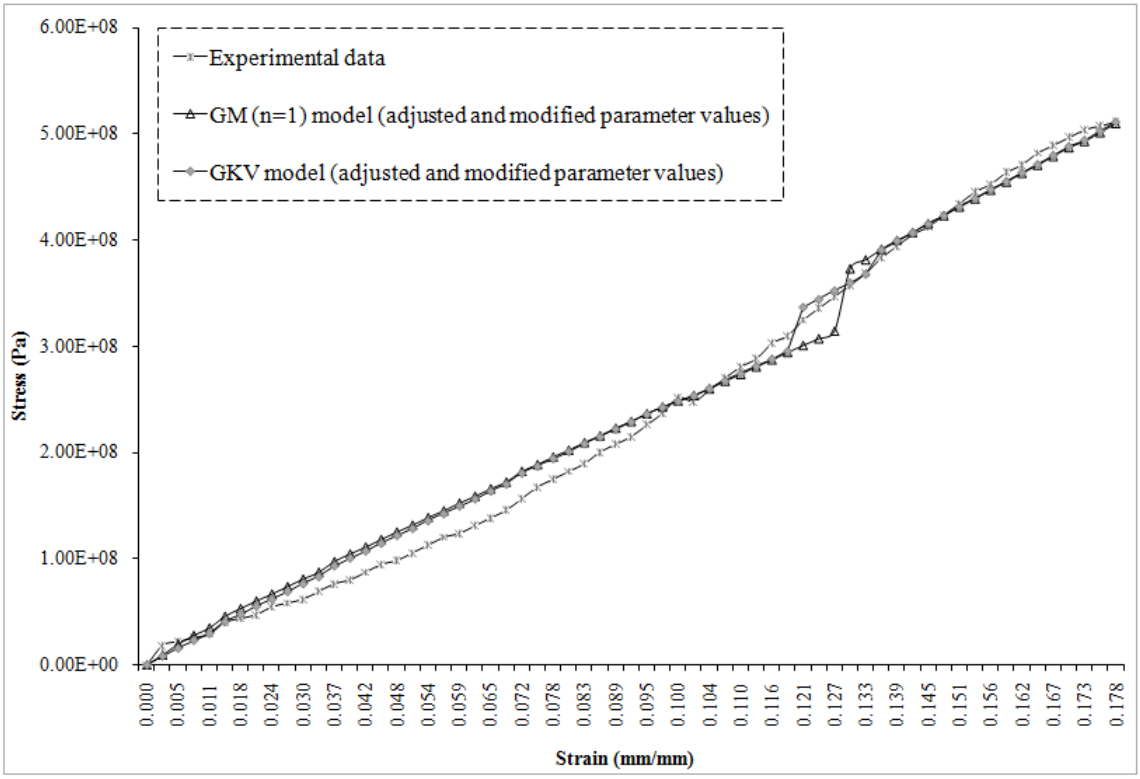

Fig. 3.11 Stress-strain curves of the Twaron® fabric at a low strain rate ($\dot{\varepsilon} = 1\ s^{-1}$): Experimental data and results predicted by the GM$^{n=1}$ and GKV models.

At high strain rates, the GM$^{n=1}$ model is found to do better than the GKV model. A least-square regression analysis is performed for each set of the following results: the experimental data, the predictions by the GM$^{n=1}$ model using the *initial* parameter values, and the predictions by the GM$^{n=1}$ model using the *adjusted and modified*

parameter values, as shown in Fig. 3.12. The elastic modulus (stiffness) of the Twaron CT716® fabric given by the current least square regression analysis of the experimental data reported in (Shim et al., 2001) is 80 GPa.

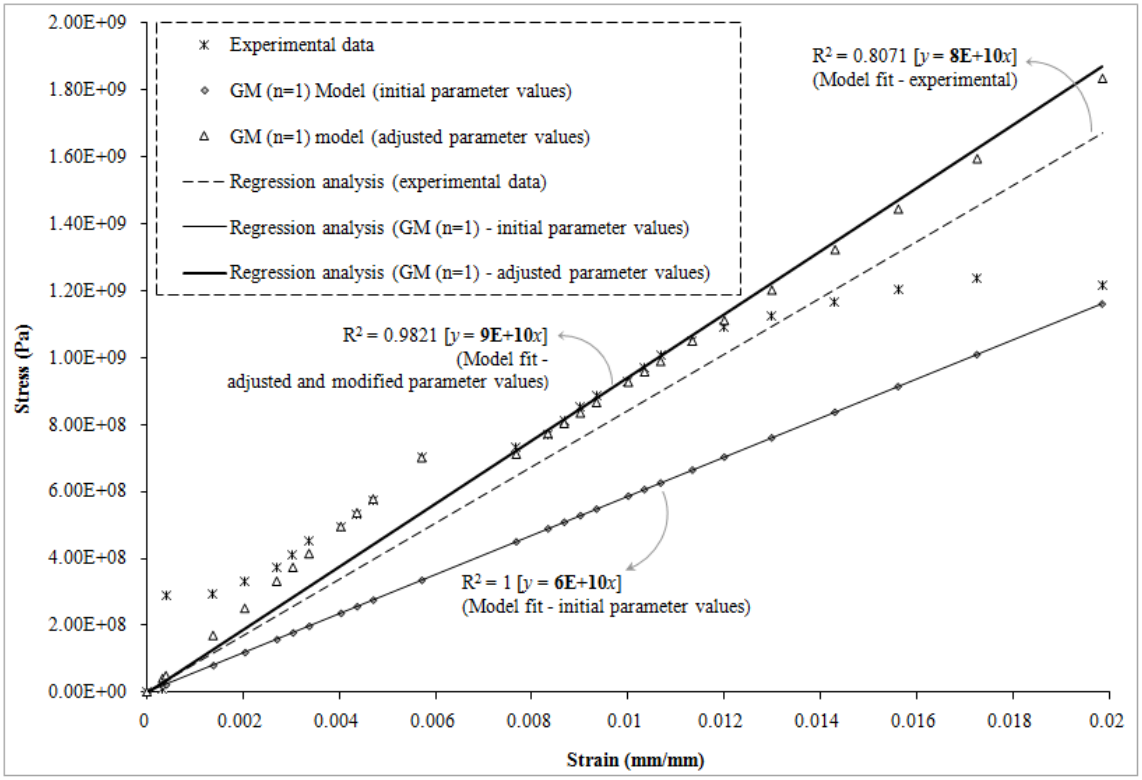

Fig. 3.12 Linear regression analysis and comparison of the experimental data for the Twaron® fabric and the predictions by the GM$^{n=1}$model at a high strain rate ($\dot{\varepsilon} = 495\ \mathrm{s}^{-1}$).

The GM$^{n=1}$ model with the *initial* parameter values predicts a stiffness of 60 GPa, while the GM$^{n=1}$ model with the *adjusted and modified* parameter values yields 90 GPa, which is closer to the experimental result of 80 GPa. The GKV model does not have a similar predictability at the high strain rate, as shown in Fig. 3.13.

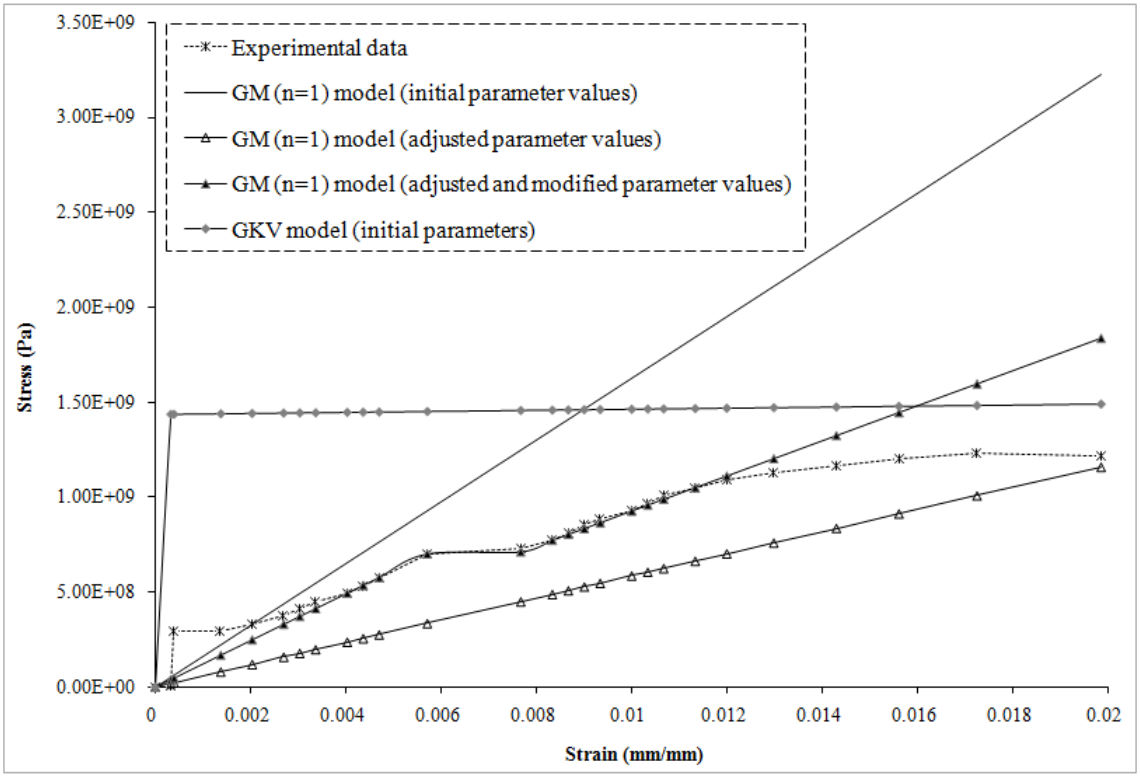

Fig. 3.13 Stress-strain behavior of the Twaron® fabric at a high strain rate ($\dot{\varepsilon} = 495\ s^{-1}$): Comparison of the results predicted by the GM$^{n=1}$ and GKV models using the *initial*, *adjusted* and *modified* parameter values.

It is clear from Fig. 3.13 that the GM$^{n=1}$ model predicts a trend matching with the experimental observations at the high strain rate. However, the increase of stress with strain predicted by the GM$^{n=1}$ model is not obtained from the GKV model. Also, the GKV model predicts higher stress values than the experimental values. In addition, the elastic modulus cannot be accurately predicted using the GKV model. Hence, the predictability of the GM$^{n=1}$ model is better than the GKV model at high strain rates.

3.7.3 Equivalency of the GM$^{n=1}$ and GKV models

The parametric analysis discussed in the preceding section showed how the parameter values and the configuration of the rheological elements in both of the three-parameter models can be utilized to study the deformation characteristics of the Twaron® fabric. A closer inspection of Eqs. (3.4) and (3.5) shows that Eq. (3.5) can be obtained from Eq. (3.4) if the following substitutions are made to the coefficients of ε, $\dot{\varepsilon}$, and the exponential terms on the RHS of Eq. (3.4), respectively:

$$K_1 = \frac{{K_{kv1}}^2}{K_{kv1} + K_{kv2}}, \quad K_2 = \frac{K_{kv1}K_{kv2}}{K_{kv1} + K_{kv2}}, \quad \eta = \frac{{K_{kv1}}^2\eta_{kv}}{(K_{kv1} + K_{kv2})^2} \tag{3.6}$$

Thus, the constitutive laws for both the GM$^{n=1}$ and GKV models are mathematically equivalent and can be transformed into each other by using the relations given in Eq. (3.6). Clearly, the coefficients that appear in the constitutive equation of the GM$^{n=1}$ model are straightforward, i.e., just the values of the K_1, K_2, and η parameters. Hence the advantage of the GM$^{n=1}$ model over the GKV model, which requires greater computational effort to determine the coefficients using the values of the K_{kv1}, K_{kv2}, and η_{kv} parameters. The simplicity of the GM$^{n=1}$ model compared to the GKV model observed here was also analytically verified using the fractional rheological constitutive equation for these two models by Schiessel et al. (1995).

Furthermore, the GKV model is equivalent to the GM$^{n=1}$ model insofar as the depiction of solid-like behavior of a viscoelastic material is concerned (e.g., Arridge, 1975). Both the models are collectively called the standard linear solid model and

reaches an equilibrium stress level under a constant applied strain at long times (see Chapters V and VI).

An optimization routine called 'fminunc' that can be found in the Matlab® Optimization Toolbox™ 4.3 is used here to determine the optimum value of the parameters of the GM$^{n=1}$ model and the GKV model at both the strain rates used in Section 3.7.1. Predictions of the stress at every instant t_i (e.g., 63 instances in total for the low strain of 1 s^{-1}) by the GM$^{n=1}$ and GKV models are compared to the experimental data at that time instant and the values of the model parameters (e.g., K_1, K_2, and η for the GM$^{n=1}$ model) are optimized by minimizing the least squares error of an objective function, g:

$$\min_{K_1,K_2,\eta} g = \sum_{t_i=0}^{63} \left[\sigma_i^{model}(t_i) - \sigma_i^{exp}(t_i) \right]^2 . \tag{3.7}$$

where, from Eq. (3.4),

$$\sigma_i^{model}(t_i) = K_1 \varepsilon(t) - \eta \left(e^{-\frac{K_2}{\eta}\frac{\varepsilon}{\dot{\varepsilon}}} - 1 \right) \dot{\varepsilon} . \tag{3.8}$$

An illustration of the fitting procedure using the 'fminunc' optimization algorithm to determine the optimal values of the parameters for both the models is provided in Appendix C. The optimized parameter values are tabulated in Table 3.3.

Table 3.3
Optimized values of the parameters used in the $GM^{n=1}$ and GKV models.

Model	K_1 (Pa)	K_2 (Pa)	η (Pa·s)
$GM^{n=1}$	2.8E+09	3.0E+09	3.0E+06
Model	K_{kv1} (Pa)	K_{kv2} (Pa)	η_{kv} (Pa·s)
GKV	6.2E+09	5.8E+09	1.0E+07

Fig. 3.14 shows the results of the $GM^{n=1}$ model and the GKV model at the low strain rate of 1 s^{-1}. This result confirms the equivalency of both the models.

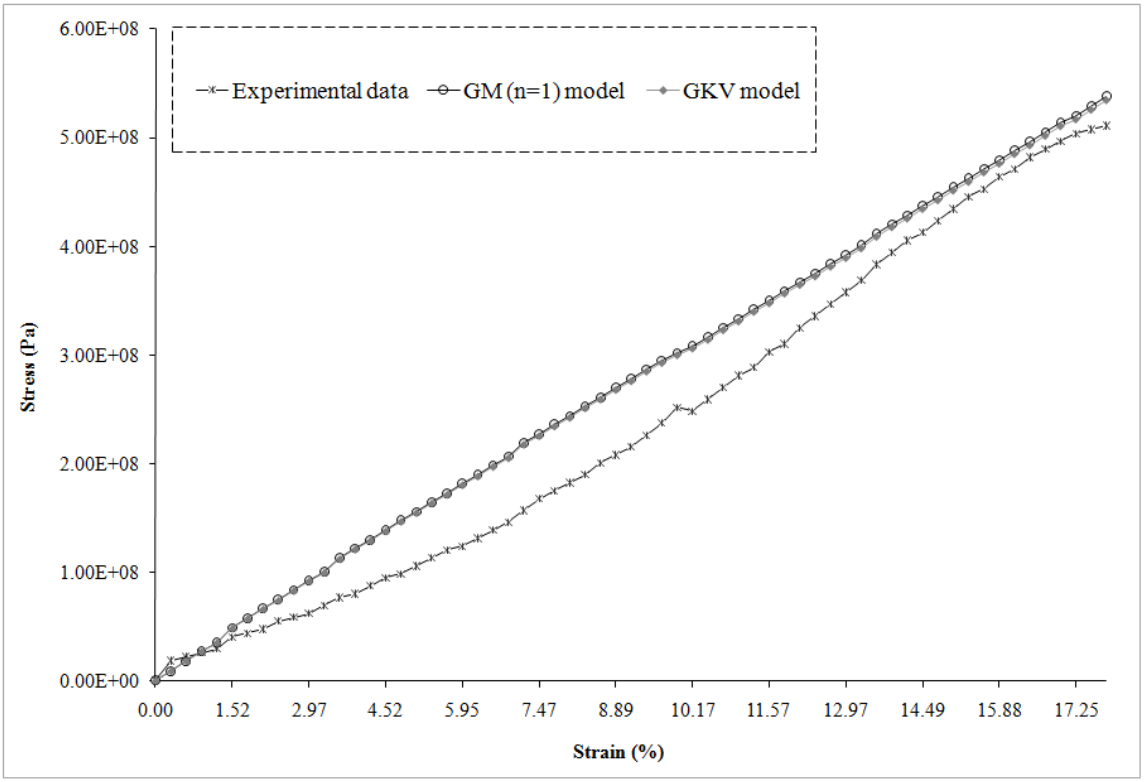

Fig. 3.14 Stress-strain behavior of the Twaron® fabric at a low strain rate ($\dot{\varepsilon} = 1\ s^{-1}$): Equivalency of the $GM^{n=1}$ and GKV models using the optimized parameter values.

3.8 Summary

A one-term generalized Maxwell ($GM^{n=1}$) model and a generalized Kelvin-Voigt (GKV) model, which are both three-parameter viscoelasticity models, are proposed to describe the constitutive relations of a ballistic fabric, Twaron CT716®, at low (1 s^{-1}) and high (495 s^{-1}) strain rates. These two models can capture the molecular level deformation mechanisms of aramid fibers. Both the primary and secondary bond scissions are involved in the deformation process of such fibers, but the primary bond breakage predominates at the high strain rate, leading to brittle failure of the fibers at a lower strain value. For the low strain rate deformation, the predictions by both models are in good agreement with the experimental data, with the GKV model being more accurate. The $GM^{n=1}$ model performs better at the high strain rate, while still providing accurate predictions for the low strain rate responses. In addition, the $GM^{n=1}$ model is able to provide good predictions of the fabric stiffness.

The constitutive equations for both the $GM^{n=1}$ and GKV models are mathematically equivalent and can be converted from one to the other by transforming the coefficients involved. The stress-strain equation of the $GM^{n=1}$ model can be obtained in a relatively straightforward manner compared to that of the GKV model. Furthermore, the $GM^{n=1}$ model requires lesser computational effort to determine the coefficients that appear in its constitutive equation. The $GM^{n=1}$ model is thus found to be a simple and efficient model that is able to simulate the viscoelastic behavior of the Twaron® fabric.

CHAPTER IV

STRESS-STRAIN BEHAVIOR OF A TWARON®/NATURAL RUBBER COMPOSITE AT CONSTANT STRAIN RATES

4.1 Introduction

In this chapter, the uniaxial stress-strain relation of a Twaron CT709®/natural rubber (Twaron®/NR) composite is studied experimentally at two constant strain rates of 0.00001 s^{-1} and 0.01 s^{-1}. The constitutive behavior of the composite is then simulated using two fully rheological viscoelasticity models and a newly developed para-rheological model. The $GM^{n=1}$ model, which was found to emulate well the constitutive relation of the Twaron® fabric in the preceding chapter, is used here to characterize the fabric constituent in the Twaron®/NR composite. In the present study, the $GM^{n=1}$ model that consists of a Maxwell element (including a viscous dashpot and a spring in series) and a second spring in parallel to the Maxwell element is denoted as 'GM element'.

The two viscoelasticity models used to study the constitutive behavior of the Twaron®/NR composite are a four-parameter Burgers model (composed of a Maxwell element and a Kelvin-Voigt element in series) and a proposed two-term generalized Maxwell ($GM^{n=2}$) model (consisting of a Maxwell element and the one-term generalized Maxwell ($GM^{n=1}$) element in parallel). The values of rheological parameters involved in each model are extracted from the experimental data via a curve-fitting optimization procedure. As a result, morphological changes on the molecular level that link to the

macroscopic deformation of the composite are vigilantly incorporated in each viscoelasticity model in a phenomenological manner.

Besides this, the predictions of stresses by a five-parameter model (consisting of a Maxwell element with a free dashpot and a $GM^{n=1}$ element in an iso-stress configuration) and those estimated by the $GM^{n=2}$ model (comprising a Maxwell element and a $GM^{n=1}$ element in iso-strain condition) are compared with the measured values in order to corroborate the assumption of iso-strain loading condition of the Twaron®/NR composite. Based on the results of these three viscoelasticity models and in an attempt to enhance the physical correspondence of a model to the deformation mechanisms of either the Twaron® fabric or the NR constituent on the molecular level, a new para-rheological model comprising a $GM^{n=1}$ element and a stress network element in parallel is developed and presented in this chapter. The stress network element in the new model makes use of the affine network based molecular theory of rubber elasticity. The value of the parameter associated with the stress network element is directly acquired from the tensile modulus of the NR constituent at room temperature.

4.2 Constitutive modeling of polymer matrix composites

Constitutive modeling of polymers and polymer matrix composites has attracted a lot of attention (e.g., Chen et al., 1995; Corr et al., 2001; Ju and Liu, 2002; Sebastian et al., 2008; Fritsch et al., 2009). A constitutive model for a polymeric material can be developed using discrete rheological components including springs and dashpots. The characteristic constants for these springs and dashpots are phenomenological parameters

that could be related to the deformation mechanisms and molecular structure of the material (e.g., Khan and Zhang, 2001).

The mechanical response of a linearly behaving polymeric material to an applied stress (or force) can be categorized as elastic, delayed elastic, or viscous flow. The elastic response is time-independent and reversible, while the viscous flow is time-dependent and irreversible. The former can be represented by a spring, whereas the latter can be characterized by a dashpot. On the other hand, the delayed elastic response is time-dependent and reversible, which can be described by combining a spring and a dashpot that are either in series or in parallel. When the stress level in a material exceeds the yield stress of the material, plastic deformations will occur, whose description requires the use of partly reversible (elastic) and partly irreversible (plastic) rheological components (e.g., Baltussen and Northholt, 2003).

The elastic behavior of a polymeric material is linked to distortions of chemical bonds, including elongation and scission, at the molecular scale. Strain energy is stored in the material when the bond length deviates from the equilibrium separation distance (in the minimum energy configuration). High-performance polymers (such as Twaron® fibers and natural rubber) exhibit time-dependent, non-linear mechanical responses to tensile loading. Higher-order models, utilizing rheological elements with time-varying constants, are necessary to predict the non-linear stress-strain relations (e.g., Corr et al., 2001). However, for small deformations, the viscoelastic response of such a polymer is usually linear, and linear viscoelasticity (e.g., Reddy, 2008) can therefore be applied (e.g., Chen et al., 1995; Sebastian et al., 2008).

4.3 Modeling of para-aramid fibers

Twaron® fiber is a semi-crystalline aramid fiber with para-oriented phenylene segments, as shown in Fig. 3.1. The primary chemical link between the repetitive monomer units in a polymer chain of the fiber is intra-molecular covalent bonds. Adjacent polymer chains are coupled by secondary bonds including van der Waals forces and hydrogen bonds.

In developing phenomenological models, these bonds and the corresponding deformation mechanisms at the molecular scale can be represented by using suitable combinations of rheological elements as discussed for the $GM^{n=1}$ and GKV models in the previous chapter. In those models, which are intended to describe the constitutive behavior of a Twaron® fabric made from para-aramid fibers, it was assumed there that both the primary and secondary bond scissions are involved in the deformation process of the para-aramid fibers, leading to a linear mechanical response up to failure. At low strain rates, the duration of the deformation is sufficiently long, which allows the weaker secondary bonds to be overcome first. The secondary bonds are represented by a spring whose constant is smaller than that of another spring representing the primary bonds. The breakage of the secondary bonds and the inter-molecular slip (described using a dashpot) dominate the fiber failure at low strain rates. The combination of the spring and dashpot rheological elements as in the $GM^{n=1}$ model will be employed in the present study to represent the para-aramid fibers in the Twaron® fabric in the composite.

4.4 Mechanical response of natural rubber

Natural rubber (NR) is an incompressible elastomeric material composed of long macromolecular polymer chains of randomly oriented molecules, which are connected by covalent bonds. Fig. 4.1 shows the chemical structure of NR.

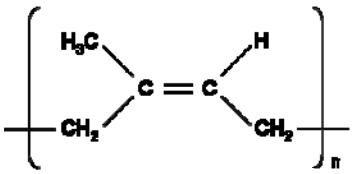

Fig. 4.1 Monomer unit of NR or poly(cis-1,4 isoprene), $(C_5H_8)_n$.

These long chains are susceptible to physical entanglements and chemical cross-linking, which are two key features that pose restrictions on the mobility of the macromolecular chains, thereby affecting the tensile deformation and mechanical properties of NR. The network of crosslinks is typically formed during the curing (vulcanization) of NR through the creation of disulfide bonds between the chains. Crosslinks are permanent chemical junctions where load transfer between molecular chains takes place. Entanglements are considered impermanent (transient) physical crosslinks that facilitate chain slippage, which occurs as the material attempts to balance the uneven distribution of chain segments caused by the deformation (Hiemenz, 1984). The crosslinks (chemical junctions) and entanglements (physical links) in NR also have a considerable impact on its viscoelastic properties such as creep and stress relaxation. The mechanical response of an amorphous NR continuum to a tensile load is usually

hyper-elastic. The overall response of NR (as an elastomeric polymer) to an applied load can be energy storage (elastic), energy dissipation (viscous), or a combination of the two.

The application of a stress provides energy to a polymeric material and causes the polymer chains to rotate and/or elongate. Changes of internal energy (by bond distortions) in NR are usually negligible (e.g., Ward and Sweeney, 2004). The chain re-arrangements in NR are primarily induced by the entropic effect of conformational changes (e.g., Mark, 1992). NR molecular chains are mostly coiled, which renders NR to be in a high entropic state at its thermal equilibrium with a stable conformation. Statistically, the coiled shape can be obtained by twirling the chains in many possible ways, while the fully stretched shape (with zero entropy) can be acquired only in one possible conformation of chains. In thermodynamic terms, the entropy of NR chains in the coiled conformation is always high. Stretched NR chains (with low entropy) would seek to increase the entropy by shrinking back to coiled shapes (having higher entropy) due to this entropic effect.

The affine network based molecular (or statistical or kinetic) theory of rubber elasticity is built upon thermodynamics and statistical mechanics (e.g., Flory, 1961, 1985; Erman and Mark, 1989; Mark, 1992; Ward and Sweeney, 2004). It can be used to establish a simple relation between the elastic modulus of NR and the volume density of crosslinks (i.e., the number of elastically effective crosslinks per unit volume). For uniaxial elongation, this theory gives (e.g., Treloar, 1976, 2005; Mark, 1981; Flory, 1985; Ward and Sweeney, 2004)

$$\sigma_\lambda = NkT\left(\lambda - \frac{1}{\lambda^2}\right), \tag{4.1}$$

where σ_λ is the nominal stress (i.e., force per unit undeformed area), k is the Boltzmann constant, N is the volume density of elastically effective crosslinks, T is absolute temperature (in Kelvin), and λ is the extension ratio of the NR macromolecular chain in the elongated direction. Eq. (4.1) can be rewritten as

$$\sigma_\lambda = E_{NR}\hat{e}, \quad E_{NR} = NkT, \quad \hat{e} = \lambda - \frac{1}{\lambda^2}, \tag{4.2}$$

where E_{NR} is the elastic modulus of NR, and $\hat{e}$ is a strain measure that reduces to 3 times of the engineering normal strain in small deformations (see Appendix D).

The macroscopic behavior of the Twaron®/NR composite is related to two distinct mechanisms at the molecular scale. Firstly, for the NR constituent, elastic stretching is preceded by the uncoiling of molecules chains, and the macroscopic stress-strain response is governed by Eq. (4.2). The second mechanism is attributed to the deformation process of the Twaron® fibers involving bond scissions and chain slippage. The present study aims to model the molecular deformation mechanisms and link them to the macroscopic constitutive behavior of the composite.

4.5 Experimental results

The specimens used here are made from a Twaron/NR composite, which is a NR coated Twaron CT709® plain-weave fabric. The Twaron CT709® fabric was coated with

pre-vulcanized NR via a dipping process. No other additive or reactive stabilizer was used in the sample fabrication. The Twaron®/NR composite is considered to be isotropic. The quasi-static uniaxial tensile tests were performed at the ambient temperature and humidity (i.e., 25 °C and 50%, respectively). The strip method, where the entire width of the specimen is gripped in the clamps, was employed according to the ASTM D5035 – 95 (2003) standard (see Fig. 4.2). The tests were conducted at two constant strain rates, i.e., 0.00001 s^{-1} and 0.01 s^{-1}, using an MTS Insight30™ tensile testing machine. Polyethylene tabs were attached to the specimen ends to avoid slippage and improve gripping of the ends. A tare pre-load of 1 ~ 2 N was applied to straighten the coated fabric specimen and to ensure that the test commenced from the zero load position.

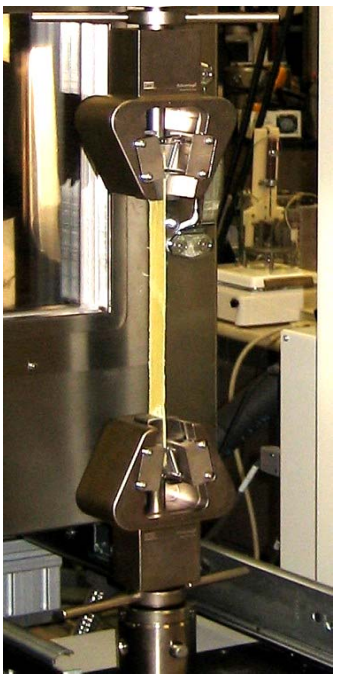

Fig. 4.2 Tensile test set-up (strip method).

Three specimens were tested for each of the strain rate mentioned above and the average values were used for the current study. Figs. 4.3 and 4.4 show the experimental stress-strain curves of all the specimens tested at the 0.00001 s^{-1} and 0.01 s^{-1} strain rates, respectively. The noticeable variation of the stress-strain curves shown in Fig. 4.3 may be attributed to a small non-uniformity of the cross-sectional length of the specimens, or humidity change of the specimens. The mechanical properties determined from the tensile tests namely, the maximum load, ultimate stress, maximum elongation and failure strain for all the specimens tested at the 0.00001 s^{-1} and 0.01 s^{-1} strain rates are listed in Tables 4.1 and 4.2, respectively.

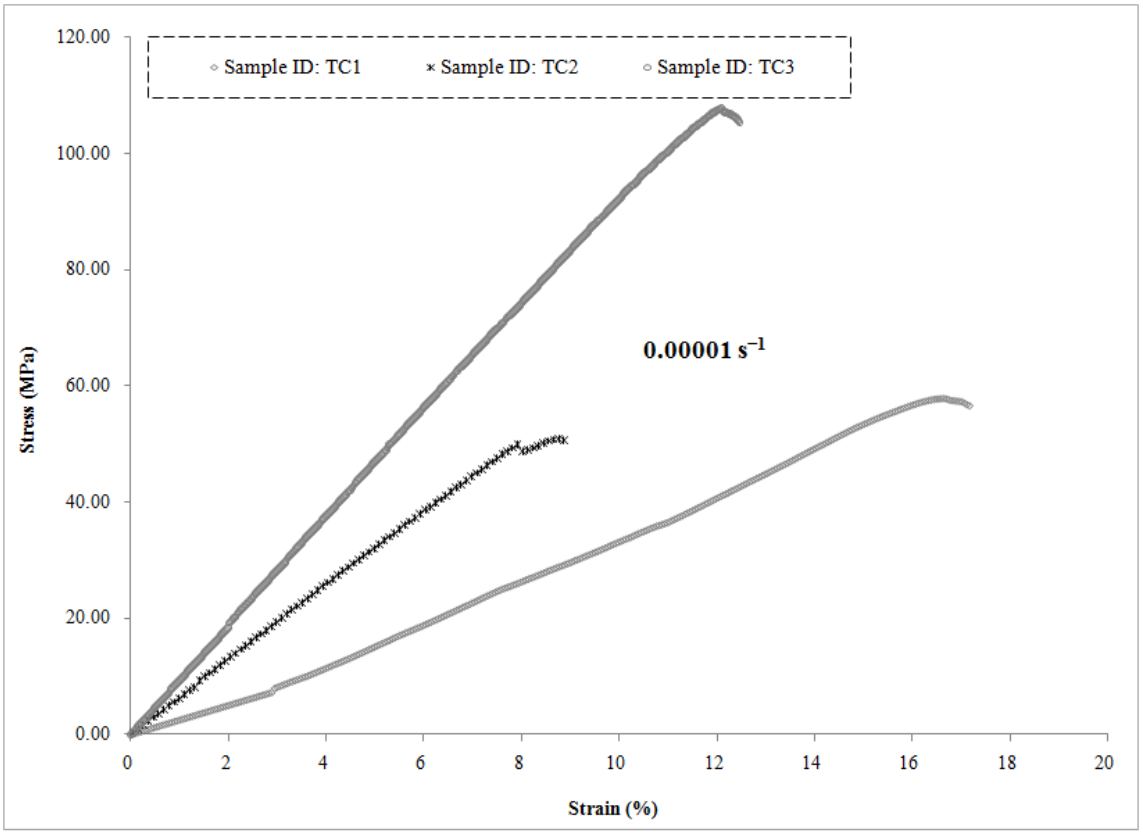

Fig. 4.3 Stress and strain curves of three Twaron®/NR composite specimens measured at the 0.00001 s^{-1} strain rate.

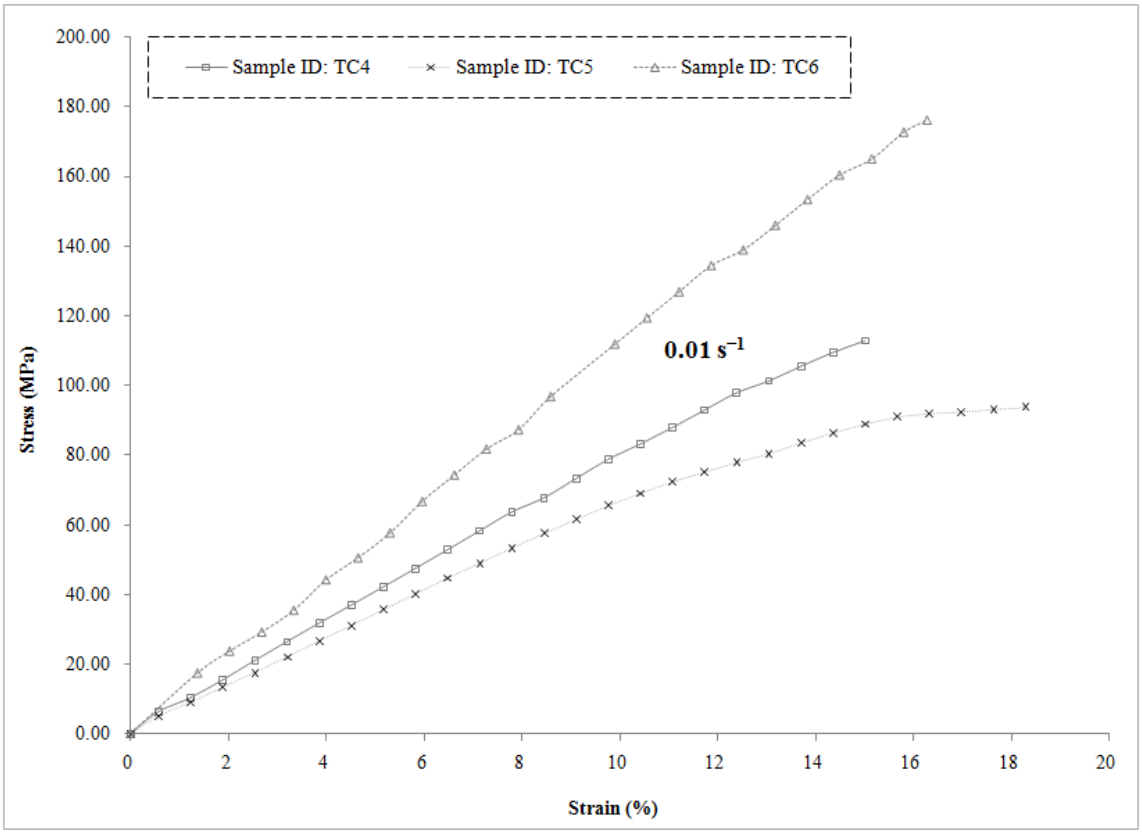

Fig. 4.4 Stress and strain curves of three Twaron®/NR composite specimens measured at the 0.01 s^{-1} strain rate.

Table 4.1
Mechanical properties of specimens TC1, TC2 and TC3 measured at the 0.00001 s^{-1} strain rate.

Measurand	**Value**		
	TC1	**TC2**	**TC3**
Maximum load	1460.0 N	1289.9 N	2735.2 N
Ultimate (peak) stress	57.70 MPa	49.9 MPa	107.68 MPa
Maximum elongation	7.16 mm (0.00716m)	4.57 mm (0.00457m)	6.09 mm (0.00609m)
Failure strain (strain at break)	14.1%	8.8%	12.1%
Elastic modulus (machine)	428.6 MPa	647.1 MPa	938.4 MPa

Table 4.2
Mechanical properties of specimens TC4, TC5 and TC6 measured at the 0.01 s^{-1} strain rate.

Measurand	Value		
	TC4	**TC5**	**TC6**
Maximum load	2866.8 N	1905.4 N	4472.4 N
Ultimate (peak) stress	112.9 MPa	93.8 MPa	176.1 MPa
Maximum elongation	7.84 mm (0.00784 m)	9.39 mm (0.009398m)	8.38 mm (0.008382m)
Failure strain (strain at break)	15.1%	18.3%	16.3%
Elastic modulus (machine)	816.0 MPa	689.8 MPa	1075.9 MPa

Tables 4.3 and 4.4 show the statistical analysis of the experimentally determined tensile modulus and tensile strength of the Twaron®/NR composite, respectively. Figure 4.5 and Figure 4.6 are the graphical representation of the statistical mean and error of, in order, the elastic modulus and the ultimate stress (i.e., tensile strength) of the composite at the two strain rates.

Table 4.3
Statistical analysis of measured elastic modulus of the Twaron®/NR composite.

Strain rate	Specimen ID	Elastic modulus (MPa)	Mean (MPa)	Standard deviation (MPa)
0.00001 s^{-1}	TC1	340.9	626.00	285.60 (+286.1/–285.1)
	TC2	625.0		
	TC3	912.1		
0.01 s^{-1}	TC4	818.8	892.47	188.24 (+213.9/–140.3)
	TC5	752.2		
	TC6	1106.4		

Table 4.4
Statistical analysis of measured tensile strength of the Twaron®/NR composite.

Strain rate	Specimen ID	Ultimate stress (MPa)	Mean (MPa)	Standard deviation (MPa)
0.00001 s^{-1}	TC1	57.7	71.77	31.36 (+35.9/–14.1)
	TC2	49.9		
	TC3	107.7		
0.01 s^{-1}	TC4	112.9	127.60	43.07 (+48.5/–33.8)
	TC5	93.8		
	TC6	176.1		

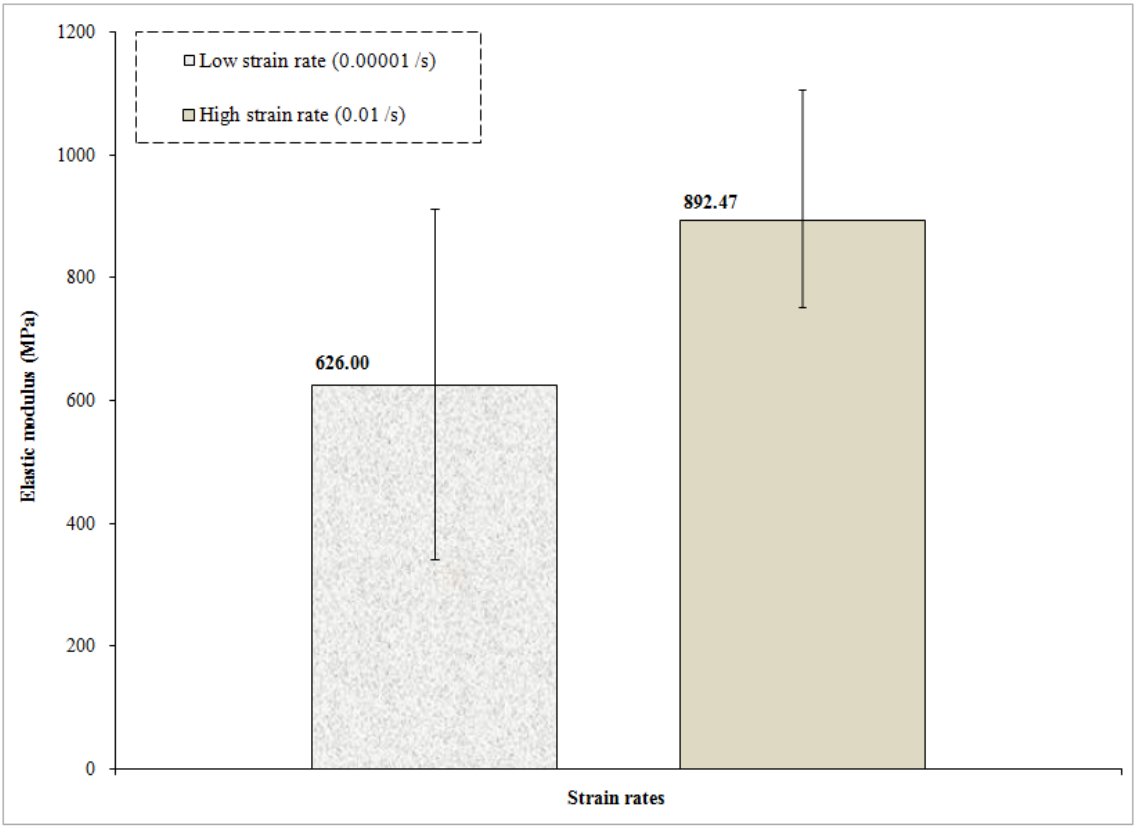

Fig. 4.5 The statistical mean and error of the measured elastic modulus of the Twaron CT709®/NR composite at the two strain rates.

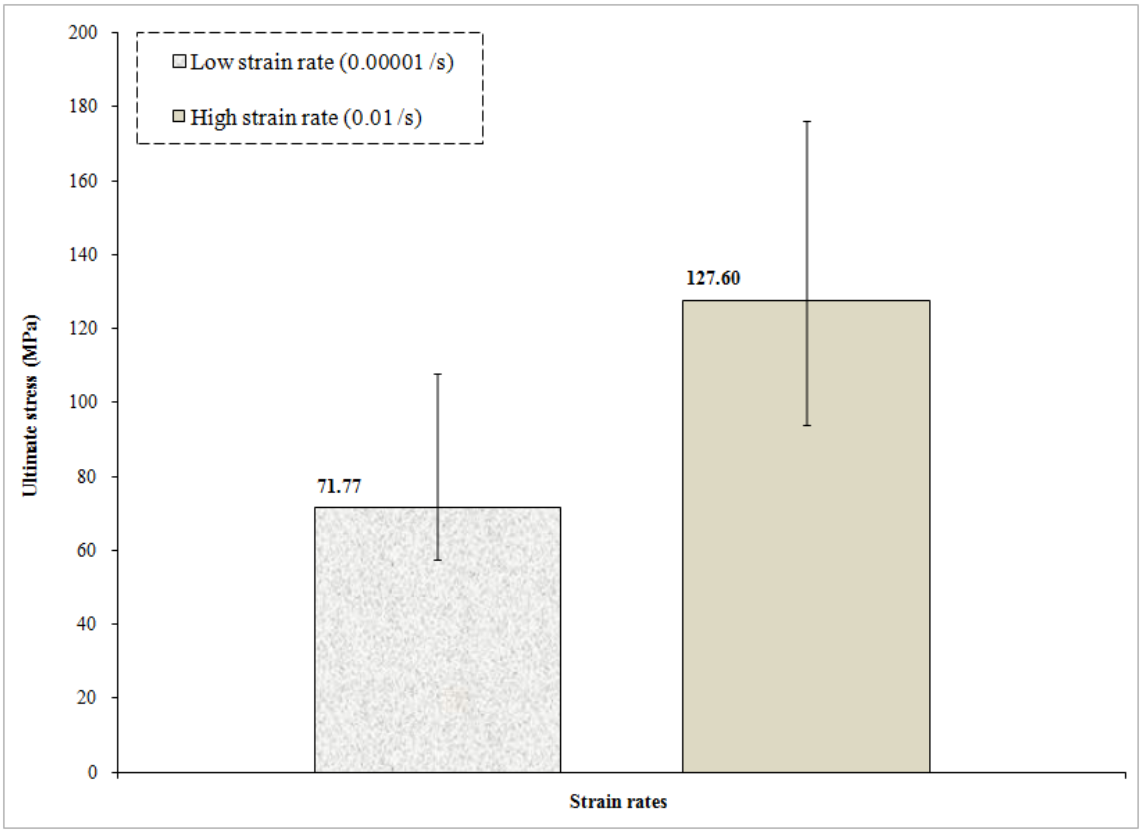

Fig. 4.6 The statistical mean and error of the measured ultimate stress (tensile strength) of the Twaron CT709®/NR composite at the two strain rates.

Fig. 4.7 shows average values (arithmetic mean) of the experimental stress-strain curves at the two strain rates. The arithmetic averages of the mechanical properties determined from the tensile tests are listed in Table 4.5.

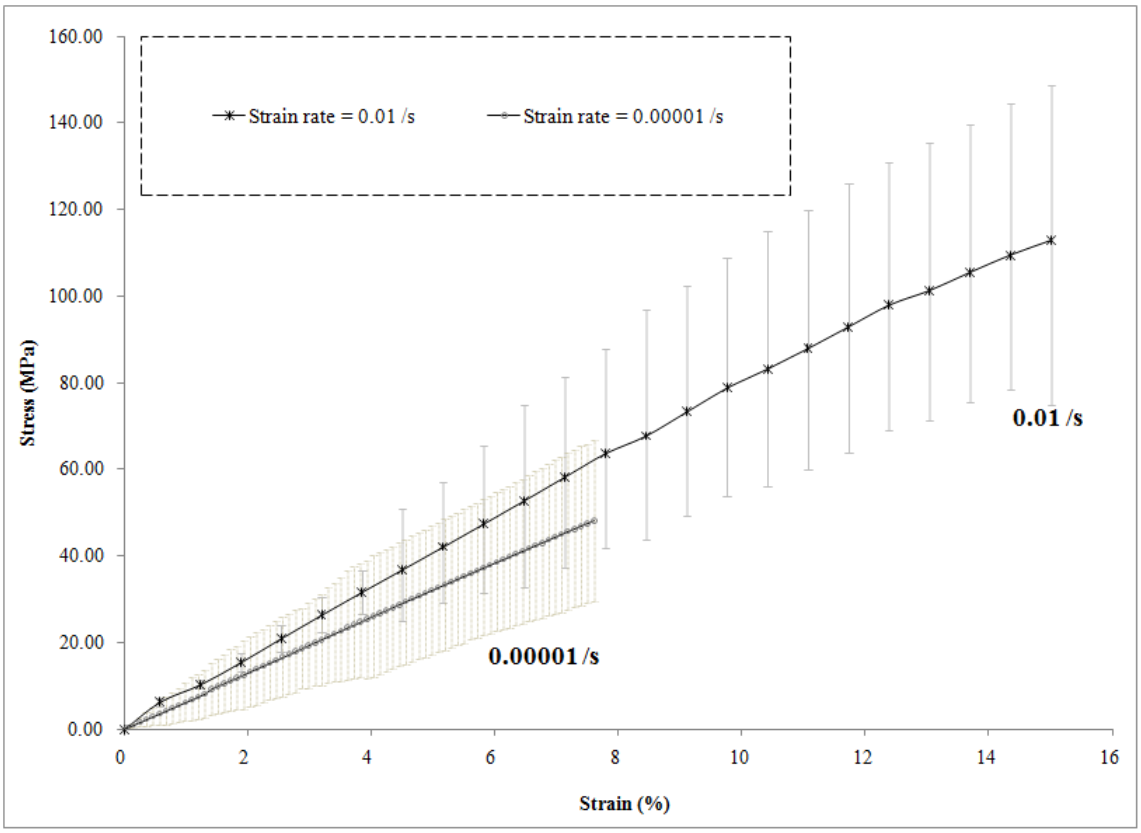

Fig. 4.7 Stress and strain curves (average values) measured at the two strain rates.

Table 4.5
Average values and standard deviations of the mechanical properties of the Twaron®/NR composite.

Property	Strain rate	
	0.00001 s^{-1}	**0.01 s^{-1}**
Maximum load	1828.4 ± 789.9 N	3081.7 ± 1297.1 N
Ultimate stress	71.8 ± 31.4 MPa	127.6 ± 43.1 MPa
Maximum elongation	5.9 ± 1.3 mm	8.5 ± 0.8 mm
Failure strain	11.6 ± 2.7%	16.7 ± 0.8%
Elastic modulus	626.0 ± 285.6 MPa	892.5 ± 188.2 MPa

It is seen from Fig. 4.7 and Table 4.5 that the values of all mechanical properties increase as the strain rate is increased from 0.00001 s^{-1} to 0.01 s^{-1}. Specifically, the ultimate stress and elastic modulus are increased by 77.8% and 42.6%, respectively. Similar observations were made by Lim et al. (2003) for an un-coated Twaron® fabric. However, unlike those results obtained in (Lim et al., 2003), the maximum elongation and the failure strain of the current NR-coated Twaron® fabric increase with the strain rate. This may be attributed to the reinforcing effect of NR, whose failure strain can reach about 450% at 25 °C (Findik et al., 2004). The testing temperature of 298.15 K (or 25 °C) is far above the glass transition temperature of NR (i.e., 200.5 ± 0.5 K (Loadman, 1985)). This enables greater chain mobility, thereby giving NR its rubbery nature and permitting it to elongate significantly without breaking via uncoiling and straightening of the macromolecule chains. On the other hand, the high modulus of the un-coated Twaron® fabric (e.g., 4 GPa at strain rates below 0.1 s^{-1} (Lim et al., 2003)) is largely reduced after coating it with NR whose elastic modulus is three orders of magnitude lower than that of the fabric (e.g., Treloar, 1944; Hamza et al., 2008; Ramorino et al., 2009).

4.6 Constitutive modeling

The physical configuration of the Twaron®/NR composite is schematically shown in Fig. 4.8. The Twaron®/NR composite is considered to be isotropic. The viscoelasticity models developed here evolve from the $GM^{n=1}$ model (see Chapter III), which was found to be suitable for characterizing the viscoelastic response of Twaron®

fabrics. In the current study, the Burgers four-parameter viscoelasticity model (e.g., Dietrich et al., 1998) is used, and a two-term generalized Maxwell ($GM^{n=2}$) model and a para-rheological model are developed for predicting the stress-strain response of the NR coated fabric and for achieving a better parametric correspondence of the rheological elements to the molecular deformation mechanisms.

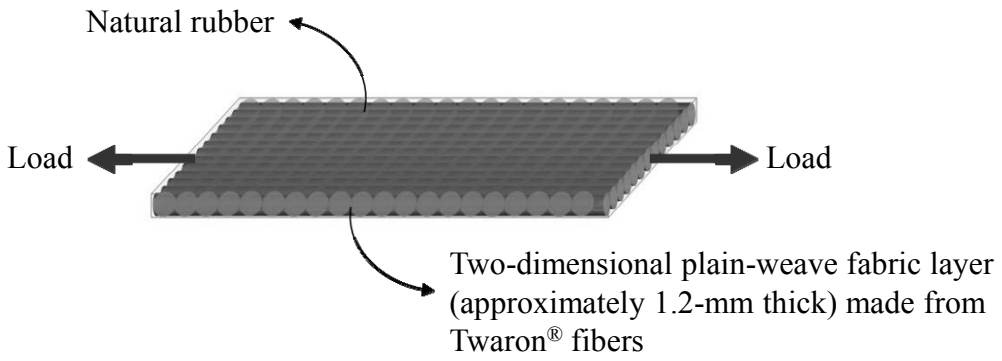

Fig. 4.8 NR-coated Twaron® fabric.

4.6.1 Burgers model

The four-parameter Burgers model consists of a Maxwell element and a Kelvin-Voigt (KV) element in series (e.g., Reddy, 2008), as shown in Fig. 4.9. In using this configuration, it is believed that the Maxwell element captures the instantaneous elasticity and irreversible viscous response of the NR constituent (e.g., Schallamach et al., 1965), while the KV element characterizes the delayed elasticity of the Twaron® fabric (e.g., Bernard et al., 2007). In Fig. 4.9, K_{B1} and K_{B2} are the spring constants, and η_{B1} and η_{B2} are the viscosity constants of the dashpots.

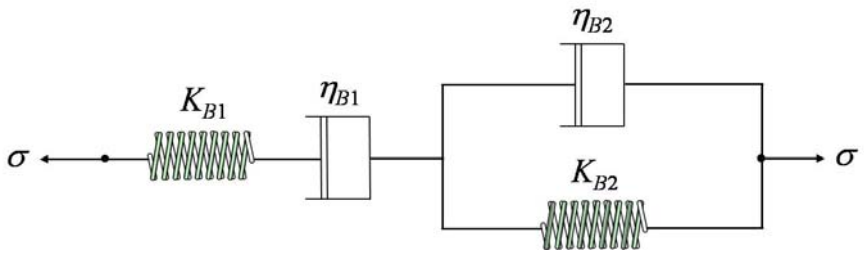

Fig. 4.9 Four-parameter Burgers model.

The viscoelastic response of NR is represented by the Maxwell element consisting of the K_{B1} spring and η_{B1} dashpot in series, as shown in Fig. 4.9. In this Maxwell element, the K_{B1} spring represents the intra-molecular covalent bonds and crosslinks in the chemical structure of NR (see Fig. 4.1), while the η_{B1} dashpot describes the chain slippage through entanglements at low strain rates. As mentioned in Section 4.4, the chain entanglements function as effective crosslinks over brief time intervals. During the deformation, the entanglements gradually get unfolded to permit possible slip of the macromolecule polymer chains over each other. The K_{B2} spring and η_{B2} dashpot in the KV element represent the primary and secondary bonds (as described in Section 4.4), and the chain slippage, respectively, of the para-aramid fibers in the Twaron® fabric.

It can be shown that the stress-strain relation described by the Burgers model illustrated in Fig. 4.9 has the following form (see *Appendix E.1* for derivations):

$$\sigma = \left[\left(1 + \frac{\lambda_1 e^{\frac{\varepsilon}{\dot{\varepsilon}}\lambda_2} - \lambda_2 e^{\frac{\varepsilon}{\dot{\varepsilon}}\lambda_1}}{\lambda_2 - \lambda_1} \right) \eta_{B1} + \frac{e^{\frac{\varepsilon}{\dot{\varepsilon}}\lambda_2} - e^{\frac{\varepsilon}{\dot{\varepsilon}}\lambda_1}}{\lambda_2 - \lambda_1} K_{eff}^{B} \right] \dot{\varepsilon} \,, \tag{4.3}$$

where λ_1, λ_2 and K_{eff} are, respectively, given in Eqs. (E1.5a), (E1.5b) and (E1.9) in *Appendix E.1* as

$$\lambda_1 = -\frac{1}{2\eta_{B1}\eta_{B2}} \left[\begin{array}{l} \eta_{B1}\left(K_{B1} + K_{B2}\right) + \eta_{B2} K_{B1} - \\ \sqrt{(\eta_{B1} + \eta_{B2})^2 K_{B1}^2 + \eta_{B1}^2 K_{B2}^2 + 2\eta_{B1}^2 K_{B1} K_{B2} - 2\eta_{B1}\eta_{B2} K_{B1} K_{B2}} \end{array} \right], \tag{4.4a}$$

$$\lambda_2 = -\frac{1}{2\eta_{B1}\eta_{B2}} \left[\begin{array}{l} \eta_{B1}\left(K_{B1} + K_{B2}\right) + \eta_{B2} K_{B1} + \\ \sqrt{(\eta_{B1} + \eta_{B2})^2 K_{B1}^2 + \eta_{B1}^2 K_{B2}^2 + 2\eta_{B1}^2 K_{B1} K_{B2} - 2\eta_{B1}\eta_{B2} K_{B1} K_{B2}} \end{array} \right], \tag{4.4b}$$

$$K_{eff}^{B} = \frac{K_{B1} K_{B2}}{K_{B1} + K_{B2}}. \tag{4.4c}$$

From Eq. (4.3), the elastic modulus of the NR coated fabric can be analytically determined as

$$E = \lim_{\varepsilon \to 0} \frac{d\sigma}{d\varepsilon} = K_{eff}^{B}, \tag{4.5}$$

where K_{eff}^{B} is given in Eq. (4.4c).

In deriving Eq. (4.3), use has been made of the following initial conditions that reflect the conditions of the actual tests:

$$\sigma(0) = 0,\ \varepsilon(0) = 0. \tag{4.6a,b}$$

Note that the original parameters (except for η_{B1}) of the Burgers model do not appear directly in the constitutive equation listed in Eq. (4.3). Instead, the stress is expressed in terms of another set of four parameters, namely λ_1, λ_2, K_{eff}^{B} and η_{B1}, the first three of which contain all of the four original parameters (i.e., K_{B1}, K_{B2}, η_{B1} and η_{B2}), as seen from Eqs. (4.4a,b,c).

4.6.2 A two-term generalized Maxwell GM$^{n=2}$ model

The GM$^{n=2}$ model proposed here consists of a Maxwell element and a GM element in parallel, as shown in Fig. 4.10. In this configuration, it is assumed that the Maxwell element (consisting of the K_1 spring and the η_1 dashpot) represents the NR constituent, and the GM element (composed of the K_2, K_3 springs and the η_2 dashpot) characterizes the Twaron® fabric. The GM$^{n=2}$ model thus comprise five parameters. The reason for using the Maxwell element here is the same as that provided in Section 4.6.1. The adoption of the GM element in this model is based on the finding in Chapter III that it can describe the stress-strain response of the Twaron® fabric well.

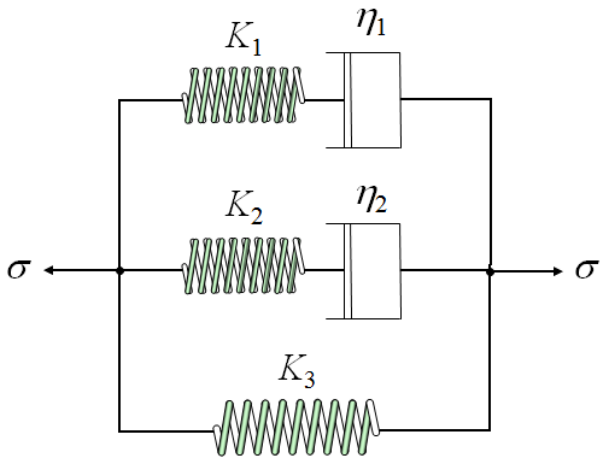

Fig. 4.10 GM$^{n=2}$ model.

It can be shown that the stress-strain relation described by the GM$^{n=2}$ model illustrated in Fig. 4.10 has the following form (see *Appendix F.1*):

$$\sigma = \eta_1 \left(1 - e^{-\frac{t}{\tau_1}} \right) \dot{\varepsilon} + \eta_2 \left(1 - e^{-\frac{t}{\tau_2}} \right) \dot{\varepsilon} + K_3 \varepsilon \,, \tag{4.7}$$

where η_1 and η_2 are the dashpot viscous constants and K_3 is the spring constant. τ_1 and τ_2 in Eq. (4.7) are the characteristic time constants of the GM$^{n=2}$ model given in Eq. (F1.9) in *Appendix F.1* as

$$\tau_1 = \frac{\eta_1}{K_1}$$

$$\tau_2 = \frac{\eta_2}{K_2} \tag{4.8a,b}$$

In reaching Eq. (4.7), use has been made of the assumption that the strain rate is constant (i.e., $\dot{\varepsilon}$ = constant).

Using the initial conditions specified in Eq. (4.6a,b) together with the constant strain rate assumption, i.e., $\frac{d\varepsilon}{dt}$ = constant, gives

$$t = \frac{\varepsilon}{\dot{\varepsilon}}. \tag{4.9}$$

Eq. (4.7) together with Eq. (4.9) shows that the stress experienced by the composite (at a given time) is a function of the applied strain (at that time) and strain rate. The first two terms in the parentheses on the right hand side (RHS) of Eq. (4.7) vanishes at t = 0, implying that the initial response of the model is entirely contributed by the instantaneous elastic response of the K_3 spring. The first two terms on the right hand side (RHS) of Eq. (4.7) represent the delayed elastic response of the fabric.

From Eq. (4.7), the elastic modulus of the NR coated fabric can be analytically determined as

$$E = \lim_{\varepsilon \to 0} \frac{d\sigma}{d\varepsilon} = K_1 + K_2 + K_3 \tag{4.10}$$

4.6.3 An iso-stress state five-parameter model

The GM and Maxwell elements in the GM$^{n=2}$ model presented above are in an iso-strain state, i.e., they undergo the same strain (see Fig. 4.10). The prediction of stresses by the GM$^{n=2}$ model, which assumes an iso-strain state, may be compared with the predictability of a counterpart model with the elements configured in an iso-stress

state. A five-parameter model consisting of a Maxwell element and a GM element in series is proposed in this section. Fig. 4.11 shows the iso-stress state five-parameter model proposed here. For sake of brevity, this model will just be referred to as the five-parameter model throughout the present study.

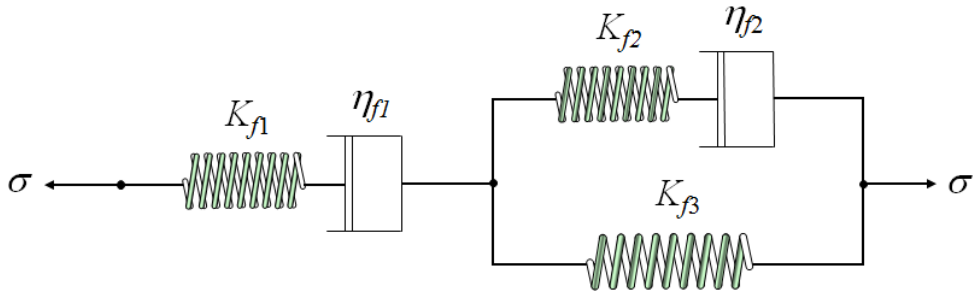

Fig. 4.11 Iso-stress state five-parameter model.

In this configuration, it is assumed that the Maxwell element (consisting of the K_{f1} spring and the η_{f1} dashpot) represents the NR constituent, and the GM element (composed of the K_{f2}, K_{f3} springs and the η_{f2} dashpot) characterizes the Twaron® fabric. The five-parameter model thus also (obviously) involves five parameters as the GM$^{n=2}$ model but unlike in the GM$^{n=2}$ model, the Maxwell and GM elements here experience the same stress. The reason for using the Maxwell element here is the same as that provided in Section 4.6.1. Again, the espousal of the GM element in this model is made based on its ability to portray the constitutive response of the Twaron® fabric well.

It can be shown that the stress-strain relation furnished by the five-parameter model illustrated in Fig. 4.11 has the following form (see Appendix G for derivations):

$$\sigma = \left[\left(1 + \frac{\omega_1 e^{\frac{\varepsilon}{\dot{\varepsilon}}\omega_2} - \omega_2 e^{\frac{\varepsilon}{\dot{\varepsilon}}\omega_1}}{\omega_2 - \omega_1} \right) \eta_{f1} + \frac{e^{\frac{\varepsilon}{\dot{\varepsilon}}\omega_2} - e^{\frac{\varepsilon}{\dot{\varepsilon}}\omega_1}}{\omega_2 - \omega_1} K_{eff}^{f} \right] \dot{\varepsilon}, \tag{4.11}$$

where ω_1, ω_2 and K_{eff} are, respectively, given in Eqs. (G14a), (G14b) and (G18) in Appendix G as

$$\omega_1 = -\frac{1}{2\eta_{f1}\eta_{f2}\left(K_{f1}+K_{f2}+K_{f3}\right)} \left[\begin{array}{l} \eta_{f1}\left(K_{f1}K_{f2}+K_{f2}K_{f3}\right)+\eta_{f2}\left(K_{f1}K_{f2}+K_{f1}K_{f3}\right)- \\ \sqrt{\begin{array}{l} \eta_{f1}^2\left(K_{f1}^2K_{f2}^2+K_{f2}^2K_{f3}^2+2K_{f1}K_{f2}^2K_{f3}\right)+ \\ \eta_{f2}^2\left(K_{f1}^2K_{f2}^2+K_{f1}^2K_{f3}^2+2K_{f1}^2K_{f2}K_{f3}\right)- \\ \eta_{f1}\eta_{f2}\left(2K_{f1}^2K_{f2}K_{f3}+2K_{f1}K_{f2}^2K_{f3}+2K_{f1}K_{f2}K_{f3}^2-2K_{f1}^2K_{f2}^2\right) \end{array}} \end{array} \right], \tag{4.12a}$$

$$\omega_2 = -\frac{1}{2\eta_{f1}\eta_{f2}\left(K_{f1}+K_{f2}+K_{f3}\right)} \left[\begin{array}{l} \eta_{f1}\left(K_{f1}K_{f2}+K_{f2}K_{f3}\right)+\eta_{f2}\left(K_{f1}K_{f2}+K_{f1}K_{f3}\right)+ \\ \sqrt{\begin{array}{l} \eta_{f1}^2\left(K_{f1}^2K_{f2}^2+K_{f2}^2K_{f3}^2+2K_{f1}K_{f2}^2K_{f3}\right)+ \\ \eta_{f2}^2\left(K_{f1}^2K_{f2}^2+K_{f1}^2K_{f3}^2+2K_{f1}^2K_{f2}K_{f3}\right)- \\ \eta_{f1}\eta_{f2}\left(2K_{f1}^2K_{f2}K_{f3}+2K_{f1}K_{f2}^2K_{f3}+2K_{f1}K_{f2}K_{f3}^2-2K_{f1}^2K_{f2}^2\right) \end{array}} \end{array} \right], \tag{4.12b}$$

$$K_{eff}^{f} = \frac{K_{f1}\left(K_{f2}+K_{f3}\right)}{K_{f1}+K_{f2}+K_{f3}}. \tag{4.12c}$$

From Eq. (4.11) it follows that the elastic modulus of the NR coated fabric has the form:

$$E = \lim_{\varepsilon \to 0} \frac{d\sigma}{d\varepsilon} = \frac{K_1\left(K_2+K_3\right)}{K_1+K_2+K_3}, \tag{4.13}$$

which is the same as K_{eff}^{f} (see Eq. (4.12c)).

In deriving Eq. (4.12), use has been made of the initial conditions specified in Eq. (4.6a,b). Note that the original parameters (except for η_1) involved in the five-parameter model do not appear explicitly in Eq. (4.11). Instead, the stress is expressed in terms of ω_1, ω_2, K_{eff}^{f} and η_{f1}, where the first three parameters are defined in Eqs. (4.12a,b,c) as functions of the original parameters (i.e., K_{f1}, K_{f2}, K_{f3}, η_{f1} and η_{f2}). This means that the number of parameters involved in the final constitutive equation of the five-parameter model has been reduced from five to four.

The effect of the Maxwell element (as characterized by the K_{f1} and η_{f1} parameters) on the stress-strain relation of the Twaron®/NR composite material can be clearly seen from Eqs. (4.11)–(4.13), where K_{f1} and η_{f1} are explicitly involved. This direct influence will be quantitatively shown in the next section, where the five-parameter model given in Eqs. (4.11)–(4.13) and different values of K_{f1} and η_{f1} will be used to represent different material responses.

4.6.4 Para-rheological model

The two viscoelasticity models presented above are fully rheological in the sense that they contain only springs and dashpots, which are the two basic types of rheological elements. A different type of model, known as a para-rheological model, is developed here, which involves a stress network element in addition to springs and dashpots. The configuration of this model is shown in Fig. 7.

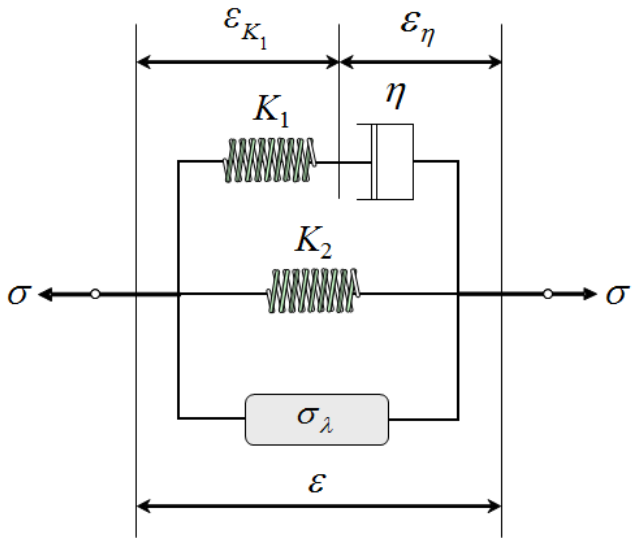

Fig. 4.12 Para-rheological model for the Twaron®/NR composite.

The GM element, which can well describe the viscoelastic response of the Twaron® fabric, is included in this model to represent the fabric, as done in the five-parameter model. It consists of the K_1, K_2 springs and the η dashpot, as shown in Fig. 4.12.

In order to represent the deformation mechanisms of the NR constituent, a stress network element is used. This network element, which encapsulates the constitutive equation of NR based on the molecular theory of rubber elasticity (see Eqs. (4.1) and (4.2)), is denoted by 'σ_λ' and added to the GM element that characterizes the Twaron® fabric, as shown in Fig. 4.12. The resulting 'para-rheological' model comprises the GM element and the stress network element σ_λ in parallel. The Twaron®/NR interfacial adhesion is taken to be perfect, and, as a result, the GM element and the σ_λ-network

element experience the same strain, i.e., ε (see Fig. 4.12), thereby enabling the elements to be in an iso-strain state.

It can be shown that the stress-strain relation provided by the para-rheological model illustrated in Fig. 4.12 has the following form (see *Appendix H.1* for derivations):

$$\sigma = K_{eff}\varepsilon + K_{ve}\left(1 - e^{-\frac{1}{\tau}\frac{\varepsilon}{\dot{\varepsilon}}}\right)\dot{\varepsilon}\,, \tag{4.14}$$

where K_{eff} (the effective stiffness), K_{ve} (the viscous stiffness) and τ (the characteristic time constant) are defined in Eq. (H1.5a,b,c) in *Appendix H.1* as

$$K_{eff} = K_2 + 3E_{NR}\left(1 - \frac{2\eta}{K_1}\dot{\varepsilon}\right), \tag{4.15a}$$

$$K_{ve} = \eta\left(1 + \frac{6E_{NR}\eta}{K_1^2}\dot{\varepsilon}\right) = \tau\left(\frac{K_1^2 + 6E_{NR}\eta\dot{\varepsilon}}{K_1}\right), \tag{4.15b}$$

$$\tau = \frac{\eta}{K_1}\ . \tag{4.15c}$$

By using Eq. (4.14), the elastic modulus of the NR coated fabric can be readily found to be

$$E = \lim_{\varepsilon \to 0}\frac{d\sigma}{d\varepsilon} = K_1 + K_2 + 3E_{NR}\ . \tag{4.16}$$

This is consistent with the iso-strain condition satisfied by the elements of the para-rheological model.

In deriving Eq. (4.14), use has been made of the initial conditions specified in Eqs. (4.6a,b). Note that the original parameters of the para-rheological model (i.e., K_1, K_2, σ_λ and η_1) do not appear explicitly in Eq. (4.14). Instead, the constitutive equation contains a new set of three parameters, K_{eff}, K_{ve} and τ, each of which is a combination of two or more original parameters. This leads to the reduction of the number of model parameters to three from the original four. These new parameters represent the effective elastic (K_{eff}) and the time-dependent viscoelastic (K_{ve} and τ) responses of the Twaron®/NR composite, with the latter contributed mainly by the Twaron® fabric.

The influence of the stress network element through the parameter E_{NR} on the material response of the Twaron®/NR composite is mathematically shown in Eqs. (4.14) –(4.16), where E_{NR} is explicitly involved. This effect will be graphically illustrated in the next section, where the para-rheological model given in Eqs. (4.14)–(4.16) will be used alone with two other models to predict the stress-strain relation of the composite at different strain rates.

Note that the affine network based molecular theory invoked in developing the current para-rheological model (see Eqs. (4.1) and (4.2) and *Appendix H.1*) accounts for the entropic effect of conformational changes of macromolecular chains through the minimization of the Helmholtz free energy of the NR. According to this theory, the mechanical work done to the NR material by an applied tensile force is directly related to the temperature and entropic change of the NR. As a result, the para-rheological model containing the stress network element that represents the NR via the molecular

theory of rubber elasticity can capture the effect of energy change in the composite system on the constitutive behavior of the Twaron®/NR composite.

A comparison of the stress-strain relations predicted by the three models provided here and those determined from experiments described in Section 4.5 is given in the next section.

4.7 Results and discussion

The results obtained using the rheological and para-rheological models elaborated in Section 4.6 are presented here together with a comparison with the experimental results provided in Section 4.5.

Figs. 4.13 and 4.14 show the predicted and measured stress-strain curves at the two constant strain rates of 0.00001 s^{-1} and 0.01 s^{-1}, respectively. These curves are plotted by using Eqs. (4.3) and (4.4a,b,c), Eqs. (4.7) and (4.8a,b,c), Eqs. (4.11) and (4.12a,b,c), and Eqs. (4.14) and (4.15a,b,c) for the Burgers model, the GM$^{n=2}$ model, the five-parameter model, and the para-rheological model, respectively. Table 4.6 provides the values of the model parameters used. These parameters are obtained from the experimental data by curve fitting, which is optimized based on minimizing the discrepancy between the two sets of the values of the elastic modulus obtained from the experiments and the models. The 'fminunc' routine in the Matlab® Optimization Toolbox™ 4.3 as illustrated in Appendix C is used for the optimization. The value of E_{NR} listed in Table 2 is in the range of experimentally determined values of the elastic modulus of NR (e.g., Treloar, 1944; Hamza et al., 2008; Ramorino et al., 2009).

Table 4.6
Values of the optimized model parameters at the two strain rates.

Strain rate (s^{-1})	Model	K_1 (Pa)	K_2 (Pa)	K_3 (Pa)	η or η_1 (Pa·s)	η_2 (Pa·s)	E_{NR} (Pa)
0.00001	Burgers	8.4E+10	2.9E+09	–	9.0E+12	4.5E+10	–
	Five-parameter	8.5E+08	7.6E+08	2.0E+09	1.5E+13	4.0E+10	–
	GM$^{n=2}$	7.0E+06	3.0E+07	6.0E+08	1.0E+10	1.0E+11	–
	Para-rheological	2.8E+06	6.3E+08	–	4.3E+06	–	1.0E+06
0.01	Burgers	1.1E+09	2.9E+09	–	1.0E+11	4.0E+10	–
	Five-parameter	1.2E+09	9.0E+07	2.5E+09	1.1E+10	3.5E+10	–
	GM$^{n=2}$	4.2E+07	2.4E+09	6.0E+08	6.0E+10	8.0E+11	–
	Para-rheological	2.8E+06	7.7E+08	–	4.0E+06	–	1.0E+06

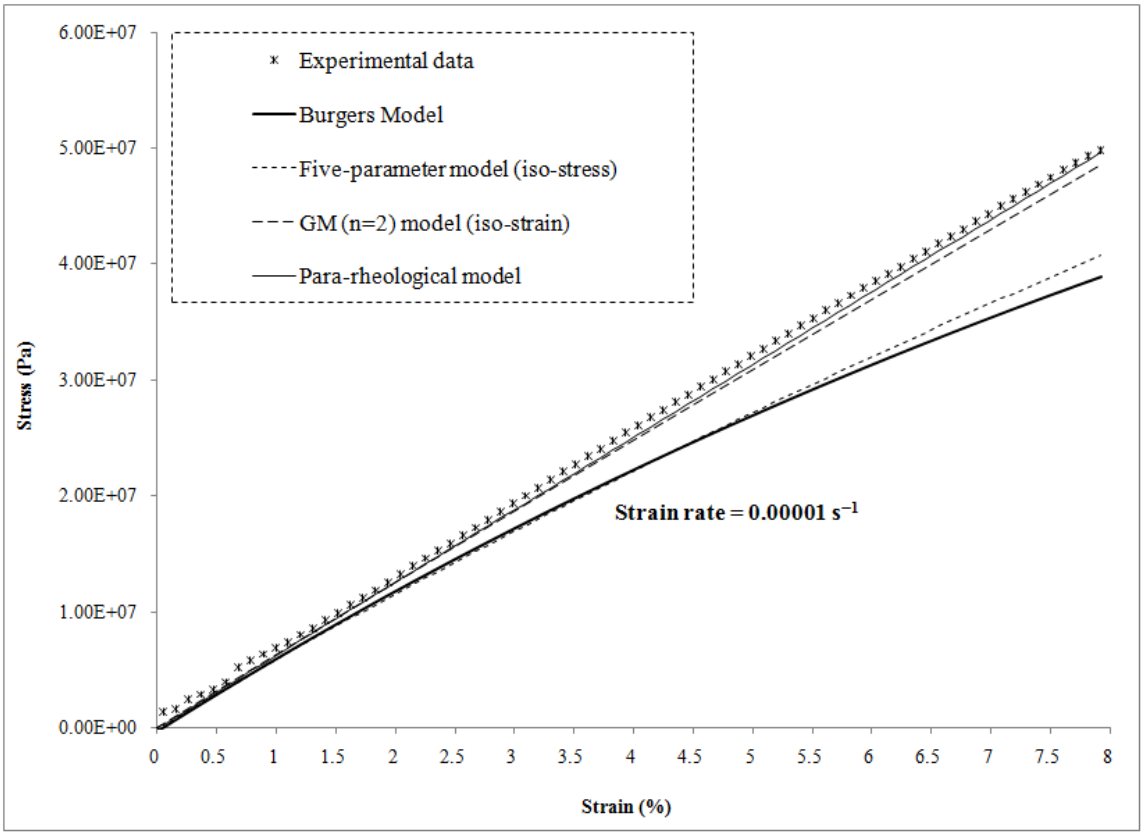

Fig. 4.13 Stress-strain curves for the Twaron®/NR composite at $\dot{\varepsilon} = 0.00001\ s^{-1}$.

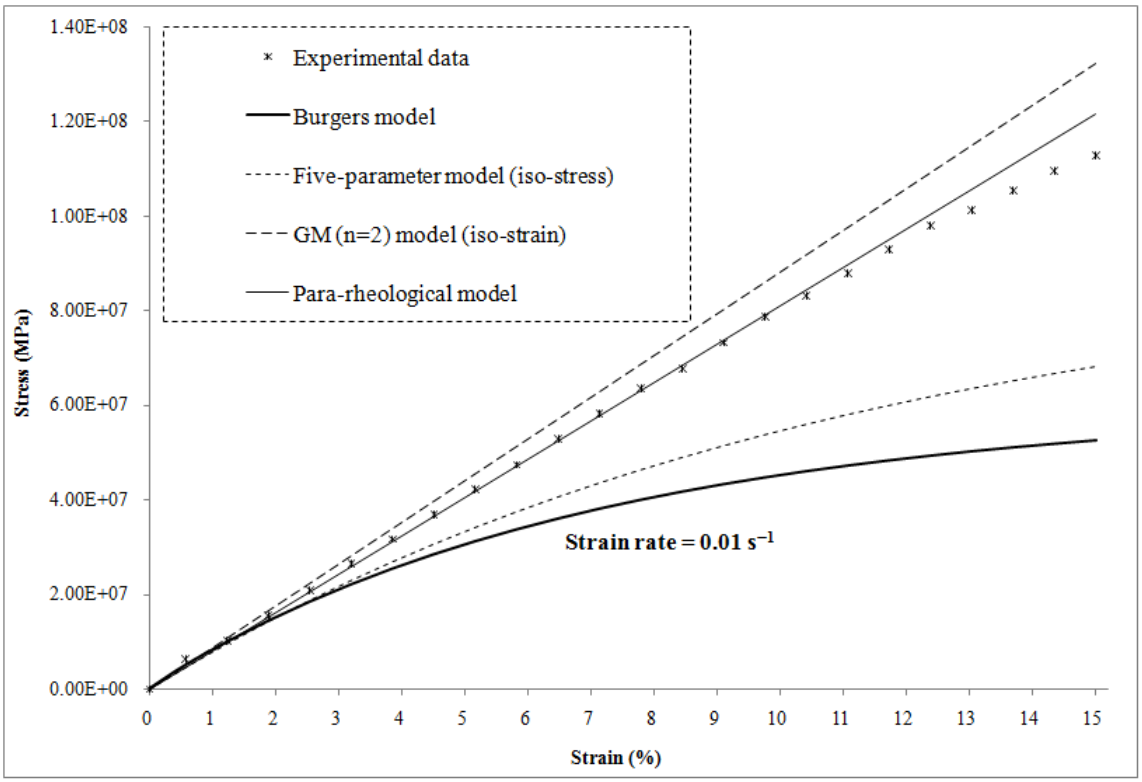

Fig. 4.14 Stress-strain curves for the Twaron®/NR composite at $\dot{\varepsilon} = 0.01\ s^{-1}$.

4.7.1 Parametric analysis

A regression analysis of the linear fitting of the experimental data (see Fig. 4.7) gives a squared coefficient of correlation of 0.9991 and 0.9981 for the strain rates of 0.00001 s^{-1} and 0.01 s^{-1}, respectively. This reveals that the stress-strain relation can be taken to be linear up to the failure of the Twaron®/NR composite at both the strain rates.

A combination of constant parameter values that would provide an accurate prediction of the stress-strain response over the entire strain range could not be established for the Burgers model and the five-parameter model, as indicated in Figs. 4.13 and 4.14. In contrast, the $GM^{n=2}$ and para-rheological models, which are based on

the iso-strain assumption, are found to provide a better estimation of the stresses with the para-rheological model being more accurate for both the strain rates. The values of the elastic modulus and the ultimate stress predicted by the viscoelasticity models and those obtained from the experimental stress-strain curves at the two strain rates are tabulated in Table 4.7. Note that the values of the elastic modulus of the composite listed here, as the slopes of the stress-strain curves at $\varepsilon = 0$, are determined directly by using Eqs. (4.5), (4.10), (4.13), and (4.16). Also, the values of the ultimate stress given in Table 4.7 correspond to the failure strains of 11.6% and 16.7% for $\dot{\varepsilon} = 0.00001\ s^{-1}$ and $\dot{\varepsilon} = 0.01\ s^{-1}$, respectively.

Table 4.7
Values of the ultimate stress and elastic modulus of the Twaron®/NR composite at the strain rates of 0.00001 s^{-1} and 0.01 s^{-1}.

Model	Ultimate stress (MPa)		Elastic modulus (MPa)	
	0.00001 s^{-1}	**0.01 s^{-1}**	**0.00001 s^{-1}**	**0.01 s^{-1}**
Experimental	71.8	127.6	626.0	892.5
Burgers	38.9	52.5	646.9	873.8
Five-parameter	40.7	68.2	627.6	805.6
$GM^{n=2}$	48.5	136.0	636.9	881.9
Para-rheological	49.6	121.6	626.5	808.8

As mentioned in Section 4.5, the current experimental data reveal that the elastic modulus and ultimate stress increase with the strain rate (see Table 4.5), which agrees with the general trend observed by others (e.g., Lim et al., 2003; Sun et al., 2005; Koh et al., 2008). All of the three models are capable of predicting this trend albeit at varying degree of accuracy, as indicated in Table 4.7. For example, for the strain rate of 0.00001 s^{-1}, the ultimate stress predicted by the Burgers model is 45.8% smaller than that

obtained from the experiment, while the elastic modulus estimated by the Burgers model is 3.33% greater than that measured. The five-parameter model underestimates the ultimate stress and overestimates the elastic modulus by 43.3% and 0.26%, respectively. The $GM^{n=2}$ model also provided a mixed level of accuracy with underestimation of the ultimate stress by 32.5% and overestimation of the elastic modulus by 1.74%. In comparison, for the same strain rate of 0.00001 s^{-1}, the para-rheological model gives a much better prediction of the ultimate stress with only a –30.9% error, while its estimation error for the elastic modulus, at 0.08%, remains quite small.

In addition, it can be observed from Figs. 4.13 and 4.14 that the stresses predicted at both the strain rates by the Burgers model and the five-parameter model are significantly lower than the experimental values and those predicted by the para-rheological models for strain values over 2% and 3% at $\dot{\varepsilon}$ = 0.00001 s^{-1} and $\dot{\varepsilon}$ = 0.01 s^{-1}, respectively. This under-prediction of stresses by the Burgers model and the five-parameter model, together with the large discrepancies in the ultimate stress just discussed above, indicate that these two fully rheological models inadequately represent the deformation mechanisms of the Twaron®/NR composite, which will be discussed further next.

4.7.2 Deformation mechanisms

As mentioned in Section 4.3, the primary and secondary bonds are involved in the deformation of the Twaron® fabric, and the magnitude of the dissociation energy of the former is much greater than that of the latter. The values of the spring constants

representing these bonds reflect the magnitudes of the dissociation energy of the corresponding bonds, as shown in Table 4.6.

The Burgers model accounts for the inter-molecular slippage through the η_{B2} parameter in the KV element and neglects the secondary bonds in the Twaron® fibers. As a result, this model is inaccurate for deformations at low strain rates (see Figs. 4.13 and 4.14), where sufficient time is available for the applied loading to act on the weaker secondary bonds, as mentioned near the end of Section 4.3. In the absence of another spring to represent the secondary bonds, the value of K_{B2} in the Burgers model needs to be greater than that in the other two models (each of which has another spring to account for the secondary bonds). Table 4.6 shows that the value of K_{B2} in the Burgers model is indeed higher than that of the counterpart spring in the other two models for each loading case, which enables the Burgers model to compensate for its inability to account for the contribution from the secondary bonds. Even with this compensation, the results obtained from the Burgers model are still in large disagreement with the experimental data for large strain values at both the strain rates of 0.00001 s^{-1} and 0.01 s^{-1}. No complete physical correspondence to the deformation mechanisms of the para-aramid fibers in the Twaron® fabric could be established by this model except for the continuous scission of the primary bonds and chain slippage represented by K_{B2} and η_{B2}, respectively.

In comparison, the GM element in the five-parameter and $GM^{n=2}$ models is more inclusive and represents the primary and secondary bonds, and the chain slippage involved in the deformation of the para-aramid fibers. The presence of this GM element

improves the predictability of both the five-parameter and GM$^{n=2}$ models, as indicated by the numerical results. The predictions of stress by the GM$^{n=2}$ model, which are better than those by the five-parameter model, could be related to the iso-strain state of the Maxwell and GM elements (or analogously, constituent-representatives) in the GM$^{n=2}$ model. Further discussion on the predictability of the GM$^{n=2}$ and five-parameter models in relation to the configuration states of the elements of these models is provided in the following section. An account of the deformation mechanisms of the composite with regard to the parameters of the five-parameter model is given next.

In the five-parameter model, the value of K_{f3}, which accounts for the primary bonds, is smaller at the lower strain rate of 0.00001 s^{-1} than that at the higher strain rate of 0.01 s^{-1}. However, the value of K_{f2}, which represents the secondary bonds, is smaller at the higher strain rate (see Table 2). At the higher strain rate, the scission of the primary bonds becomes more significant as less time is available to fully break the secondary bonds for the same amount of strain experienced by both the K_{f2}-η_{f2} spring-dashpot unit and the K_{f3} spring. As the strain increases, more primary bonds are overcome, which is accounted for by the five-parameter model. This advantage of the five-parameter model can also be seen from Figs. 4.13 and 4.14, where the margin of error in the stresses predicted by the five-parameter model is lower than that by the Burgers model. Nevertheless, the stresses predicted by these two models are significantly distanced from the experimental data. The foregoing discussion indicates that the deficiency of the fully rheological Burgers model in predicting the stresses may

be due to the inability of the Maxwell element to accurately characterize the NR constituent, as will be discussed further next.

The deformation of NR is represented by a linear spring and a dashpot in series, i.e., a Maxwell element, in the Burgers model and the five-parameter model. The element is able to account for continuous stretching induced by an applied stress in a time-dependent fashion until failure. However, the results obtained from these two models indicate that this representation is not a very good one and the effectiveness of the $GM^{n=2}$ model can still be improved. This motivated the development of the current para-rheological model by using the molecular theory of rubber elasticity (see Eqs. (4.1) and (4.2)) to account for the deformation mechanisms of NR. The entropic basis of rubber elasticity is accounted for in this molecular theory (e.g., Mark, 1992) and is included in the σ_λ-network element that represents the NR constituent (see Fig. 4.12).

Figs. 4.13 and 4.14 clearly show that the para-rheological model provides a better prediction of the stresses at both the strain rates. Based on the parameter values given in Table 4.6, the numerical values of the new parameters involved in this model (see Eqs. (4.15a,b,c)) are calculated and listed in Table 4.8.

Table 4.8
Values of the para-rheological model parameters at different strain rates.

Parameter	**Strain rate (s^{-1})**	
	0.00001	**0.01**
K_{eff} (MPa)	632.9	773.0
K_{ve} (MPa·s)	4.30	4.12
τ (s)	1.54	1.43

The effective stiffness, K_{eff}, which reflects the collective effect of instantaneously elastic responses (at a constant strain rate) of all time-independent model elements on the stiffness of the composite, is greater at the higher strain rate of 0.01 s^{-1} because of the larger value of K_2 (see Eq. (4.15a)), which represents the increased contribution of the primary bonds. This is consistent with the experimental data that confirm the increasing stiffness of the composite at the macroscopic scale, which goes from 626.0 MPa to 892.5 MPa when the strain rate is increased from 0.00001 s^{-1} to 0.01 s^{-1} (see Table 4.5).

The elastic modulus of the composite predicted by the para-rheological model deviates only by 0.08% and –9.38%, respectively, from the experimental values at the strain rates of 0.00001 s^{-1} and 0.01 s^{-1}, as seen from comparing the relevant values given in Table 4.7. Also, as observed earlier from examining Figs. 4.13 and 4.14, the margin of errors in the stresses predicted using the para-rheological model is smaller than that using the other two models.

The 'viscous stiffness' of the composite, K_{ve}, can be regarded as a measure of the contribution of the viscous responses of both the NR and fabric constituents to the total stress. Table 4 shows that the values of K_{ve} did not vary considerably as the strain rate increases. This indicates that the physical entanglements and molecular mobility, which affect the viscous response of polymer chains (e.g., Sperling, 2006) in both the NR and fabric constituents of the composite, are not significantly altered as the strain rate increases from 0.00001 s^{-1} to 0.01 s^{-1}.

The retardation time, τ, as defined in Eq. (4.15c), provides a measure of the viscous response of the Twaron® fabric, which results from slipping of the polymer

chains (represented by η_1) and breakage of the secondary bonds (denoted by K_1) of the para-aramid fibers during a tensile deformation (Tomita & Uchida, 2005). It is seen from Table 4.8 that there is only a small change in the values of τ as the strain rates increases from 0.00001 s^{-1} to 0.01 s^{-1}. This reaffirms the conclusion drawn above based on examining the change in the values of K_{ve} listed in Table 4.8.

Clearly, these observations show that the newly developed para-rheological model has a better predictability than the Burgers model and the five-parameter model, which is attributed to the inclusiveness of the model in accommodating all relevant deformation mechanisms of the Twaron®/NR composite on the molecular level. The $GM^{n=2}$ model is found to be competitive to the para-rheological model in terms of numerical accuracy. However, the para-rheological model has the desired predictive power with regard to both the numerical and the description of deformation mechanisms of the constituents of the composite. A quantitative analysis of the accuracy of the stresses predicted by the para-rheological and $GM^{n=2}$ models is given in the following section.

4.7.3 Model configurations and predictability

As shown in Figs. 4.13 and 4.14, the stress-strain curves of the Burgers and five-parameter models both predicted an exponential increase of the stresses to a finite value as strain increases. However, as discussed in Section 4.7.1, this trend does not match the measured one. Conversely, the $GM^{n=2}$ and para-rheological models both exhibit a linear trend of the stress-strain plot that is comparable to the experimentally behavior of the

composite. Two inferences can be made from these observations based on the types and configuration of the model elements. The first inference is given next.

The exponential decrease of the slope of the stress-strain curve of the five-parameter model is mainly caused by the deformation of the free spring and the free dashpot, i.e., K_{f1} and η_{f1}, respectively, in the Maxwell element of the five-parameter model. The free spring provides the instantaneously elasticity, i.e., a linear stress versus strain curve, to the element. The free dashpot continuously relaxes some of the stresses as time increases. In a constant strain rate loading, the time can be interpreted as only strain (Brinson and Brinson, 2008). This gives rise to the fluid-like (viscous flow) response of the element as strain increases. The combination of the two responses mentioned above is thus responsible to the convex bending of the stress-strain curve to a limiting stress value. Similar observation can be made regarding the Burgers model, which also has a free dashpot and a free spring (i.e., K_{B1} and η_{B1}). In fact, the constitutive laws of both the Burgers and five-parameter models are identical in form (see Eq. (4.3) and Eq. (4.11)). These remarks thus elucidate the inaptness of having a free dashpot in a model to represent the experimentally observed behavior of the Twaron®/NR composite, which tend to be a solid-like response.

The second inference is related to the iso-strain assumption of the $GM^{n=2}$ and para-rheological models, and its applicability for the actual composite. Figs. 4.13 and 4.14 show that the stresses predicted by the $GM^{n=2}$ model are closer to the measured values than those estimated by the five-parameter model. This may again be possibly related to the configuration of the constituent-representative elements in both models

namely, the Maxwell element (represents the NR constituent) and the GM element (characterizes the fabric constituent). In the $GM^{n=2}$ model, these elements are combined in parallel to each other and thereby are in an iso-strain condition. In the five-parameter model, these elements are in an iso-stress state. The better prediction of stresses by the $GM^{n=2}$ model compared to those by the five-parameter model casts the idea that the Twaron® and NR constituents underwent a comparable amount of strain at every time instant during the test.

Both of the inferences presented above collectively imply that the representation of the NR constituent by a Maxwell element is inadequate and that an iso-strain assumption is more suitable to simulate the actual loading condition. The shortfall of the five-parameter model, in which the Maxwell element is linked in an iso-stress state with the GM element, is directly caused by the viscous damper effect of the free dashpot in the Maxwell element as strain increases. Connecting the Maxwell element in parallel to the GM element improves the prediction of stresses of the resulting $GM^{n=2}$ model. However, as the strain rate increases from 0.00001 s^{-1} to 0.01 s^{-1}, this model does not provide a good estimation of the stresses. These observations motivated the use of the stress network element in an iso-strain state with the GM element in the para-rheological model (see Fig. 4.12). The stress network element directly invokes the rubbery response of NR (see Section 4.4) in the model and undergoes an equal amount of strain as the GM element. The accuracy of the para-rheological model vis-à-vis that of the $GM^{n=2}$ model is discussed next.

The coefficient of determination (*COD*), as defined in Eq. (4.17), represents the percentage of the experimental data that is the closest to the model curves. This measure is used here to quantitatively compare the prediction of stresses by the GM$^{n=2}$ model and the para-rheological model developed in the present study with the measured values.

$$COD = 1 - \frac{1}{n}\left[\frac{\Sigma\left(\sigma_{exp} - \sigma_{mod\,el}\right)^2}{\Sigma\left(\sigma_{exp} - \bar{\sigma}\right)^2}\right] \times 100\% \tag{4.17}$$

In Eq. (4.17), n is the total number of stress values measured at each time instant during the experiment, $\bar{\sigma}$ is the mean strain computed from $\left(\sum_{i=1}^{n}\sigma_{exp}\right)/n$, and σ_{exp} and σ_{model} denote the strain values measured during the experiment and predicted by the models at every time instant, respectively. Table 4.9 lists the values of n, $\bar{\sigma}$ and the *COD* for these two models at both the constant strain rates. Clearly, the numerical accuracy of the para-rheological model is superior to that of the model at both strain rates.

Table 4.9
Coefficient of determination (*COD*) of the GM$^{n=2}$ and para-rheological models at different strain rates.

Model	**Strain rate**					
	0.00001 s^{-1}			0.01 s^{-1}		
	n	$\bar{\sigma}$ (MPa)	*COD*	n	$\bar{\sigma}$ (MPa)	*COD*
GM$^{n=2}$	76	25.8	0.954	24	59.3	0.899
Para-rheological			0.956			0.998

4.8 Summary

The stress-strain curves of a Twaron CT709®/natural rubber (NR) composite are determined experimentally at two constant strain rates of 0.00001 s^{-1} and 0.01 s^{-1}. The constitutive behavior of the composite is then simulated using three viscoelasticity models, with the model parameters extracted from experimental data.

It is found that the four-parameter Burgers model and the iso-stress state five-parameter model, which are both fully rheological, could not establish complete physical correspondence to the deformation mechanisms of either the Twaron® fabric or the NR constituent on the molecular level. The Burgers model and the five-parameter model are seen to underestimate the stresses for large strain values at both the strain rates. These two models are therefore not very accurate in describing the viscoelastic response of the composite.

The $GM^{n=1}$ model, developed for the Twaron® fabric in the preceding chapter, is denoted as 'GM element' in the present chapter and used in the five-parameter model and in a $GM^{n=2}$ model to characterize the fabric constituent in the study presented in this chapter. Comparison of the results obtained from the $GM^{n=2}$ and five-parameter models with the experimental data imply that the representation of the NR constituent by a Maxwell element is inadequate and that an iso-strain assumption enables the simulation of the actual loading condition.

In order to improve the accuracy of the predictions, a new para-rheological model is developed in the current study. This model utilizes a GM element to represent the Twaron® fabric and the affine network based molecular theory of rubber elasticity to

account for the deformation mechanisms of the NR constituent. The numerical results revealed that the stresses predicted by the newly developed para-rheological model agree very well with the experimental data. The new model also predicts the elastic moduli and the ultimate stresses well at both the strain rates. The ability of the para-rheological model in simulating the constitutive behavior of the Twaron CT709®/natural rubber composite and the fidelity of this newly developed model in accounting for the deformation mechanisms of the constituents of the composite is demonstrated in this chapter.

CHAPTER V

STRESS RELAXATION OF A TWARON®/NATURAL RUBBER COMPOSITE

5.1 Introduction

Ballistic fabrics made from high performance polymeric fibers including Kevlar®, Twaron® and Spectra® fibers have been extensively studied (e.g., Matveev and Budnitskii, 1996; Lim et al., 2003; Tan et al., 2008; Rao et al., 2009). These fibers often behave viscoelastically and exhibit time-dependent responses (such as creep and stress relaxation) under various stress, strain or strain rate conditions and at different temperatures (e.g. Gauthier et al., 2000). As an example, in a polymeric fiber often the stress induced by an applied constant strain decays over time. This phenomenon, known as stress relaxation, occurs as the deformed fiber continuously attempts to mitigate the induced stress to an equilibrium level (Brinson and Brinson, 2008).

In this chapter, the stress relaxation behavior of a Twaron CT709® fabric/natural rubber (Twaron®/NR) composite under a uniaxial constant strain is studied using three viscoelasticity models and the newly developed para-rheological model. The three models employed are a one-term generalized Maxwell ($GM^{n=1}$) model (comprising one Maxwell element with an additional spring in parallel), a two-term generalized Maxwell ($GM^{n=2}$) model (including two Maxwell elements with an additional spring in parallel) and a four-parameter Burgers model. These three models are of different levels of complexity, and have been developed and used in Chapter III and Chapter IV.

The stress relaxation of the Twaron®/NR composite under a uniaxial constant applied strain of 5% for 1 hour is experimentally determined. The three viscoelasticity models and the newly developed para-rheological model are then used to characterize the stress relaxation behavior and to predict the longer time response of the composite. The parameter values needed in each model are extracted from the experimental data and optimized using the least square method. The mechanisms for the relaxation behavior are described phenomenologically by analyzing the responses predicted by the viscoelasticity models and the values assigned to the model parameters. The accuracy of each model in describing the stress relaxation behavior of the composite is quantitatively compared.

5.2 Molecular bases of stress relaxation in polymers

There are different molecular bases for stress relaxation in polymers. These include chain scission (Andrews et al., 1946; Bjork, 1990), bond interchange and molecular re-configuration (Ortiz et al., 1998b), molecular entanglement (Doi and Takimoto, 2003), viscous flow, and chain motion of the reptation type (Sperling, 2006). As mentioned in (Sperling, 2006), chain scission and bond interchange are examples of chemical relaxation, while the other molecular bases stated above are tied to the physical relaxation of polymer chains. More than one of these causes can act in concomitant as a function time and contribute to stress relaxation in a polymer during a physical stress relaxation experiment. Some of these causes are elaborated next.

The chemical bonds, e.g., ionic and covalent bonds, in a polymer may be severed by the application of a stress. The breakage of macromolecule chains, or chain scission, causes the reduction in the elastic modulus of the polymer, because the remaining chains that are still intact would withstand a lower stress for the same amount of strain. Initial chain scission occurs at random locations within the polymer chains and triggers a rapid reduction in the molecular weight of the chains (Ebewele, 2000). Stress relaxation by chain scission of covalent bonds is eminent when the load is applied for a long time and/or at a high temperature (Ortiz et al., 1998b). Application of stress would just stress the chemical bonds but not necessarily severe them. The molecules in the chains or the atoms in the molecule may then attempt to rearrange their position in order to reduce the stress level.

Chemical bonds that tie the atoms and/or molecules in the polymer chains will be stressed when the polymer is subjected to a uniaxial tensile force. Bond interchange involves swapping of a number of atoms and/or molecules under tension with those still in equilibrium. Chain scission or bond swapping are examples of localized stress relaxation. At a larger scale, the motion of the polymer chains as a mean to ease the stress is also possible.

Stress relaxation can also occur owing to ‘viscous flow’ of molecular chains. In the context of polymer chain motion, the random motion of the chains is of the Brownian type. A polymer chain or a segment of a long chain is situated amongst other chains and segments. The environment where the chains are located can be regarded as viscous because of the friction that the chains may possibly exert on the Brownian

motion of a chain or segment (e.g., Grassia and Hinch, 1996). The chain or segment can then be imagined as being immersed in a 'viscous medium'. It is hypothesized that when the polymer is deformed to a certain strain level, the molecular chains will start to slip past each other under the presence of drag force. The drag force reduces the speed of the chain motion, which is a function of time and the viscosity of the medium. The chain motion thus contributes to the relaxation process of the polymer chains if the material is held long enough in the deformed state (Illers et al., 1961). The viscous motion of the chains is an irreversible process.

The stress relaxation mechanisms elaborated here is generally applicable to most polymers including elastomers. Other molecular bases associated with the stress relaxation in elastomers encompass the conformational changes of the polymer chains in the elastomer due to deformation and the entailing entropic elasticity, which are discussed in the next section.

5.3 Types of stress relaxation in polymers

Stress relaxation in a polymer can be categorized as primary relaxation or secondary relaxation, depending on the mechanisms that cause the stress decay (e.g. Ginic-Markovic et al., 2000). The primary relaxation, also known as structural relaxation, is due to the large scale co-operative segmental motion at temperatures close to the glass transition temperature (T_g) of the polymer. The secondary relaxation can be caused by different manifestations of localized polymer chain motion such as side group rotation. The secondary relaxation usually has a short time-scale (Ngai, 1998). The

primary and secondary relaxations can be of chemical or physical nature, which is briefly mentioned below.

The stress relaxation effect in a deformed polymer arises from a combination of physical and chemical processes. The physical process involves the motion of chain entanglements and the relaxation of chain ends towards new configurations in equilibrium in the strained state (Patel et al., 2005; Le at al., 2009). The chemical stress relaxation originates from the stress decay by chain scission and formation of new covalent bonds. The rate of chemical stress relaxation and its temperature dependence are influenced by the physical state of the polymer such as its crosslink density and molecular weight (Ito, 1982). These processes will be elaborated in the next section.

5.4 Stress relaxation mechanisms in natural rubber

As mentioned in Section 4.4, natural rubber (NR) is an incompressible elastomeric material composed of long macromolecular polymer chains of randomly oriented molecules, which are connected by covalent bonds. The chemical structure of NR is schematically shown in Fig. 4.1. These long chains are subject to physical entanglement and chemical cross-linking, which are the two features that pose restrictions on the mobility and the conformational changes of the macromolecular chains thereby affecting the viscoelastic behavior of NR.

Stress relaxation in a cross-linked (vulcanized) NR comprises the chemical relaxation at longer times and the shorter-term physical relaxation (Bhowmick and Stephens, 2001). Chemical stress relaxation, as mentioned in Section 5.3, involves chain

scission and bond restoration. The decrease of stress via chemical relaxation is usually a linear function of time. Physical stress relaxation is related to the conformational (shape) changes and is also typically a linear function of time. The latter process is further explained as follows.

Stress relaxation through conformational changes in elastomers such as NR is influenced by the shape and mobility of the segmental units of the polymer chains that make up the elastomeric network. These factors, discussed in the same sequence below, have a bearing on the minimization of internal energy of the chains in order to stabilize the entropy of NR after deformation.

Long chains are necessary in order to generate a wide range of molecular conformations of macromolecular polymer chains (Fisher, 1948). The length of the chains is essential but not sufficient to afford the high entropic state of an elastomer at room temperature. The macromolecular chain segments should have adequate conformational mobility, a property that increases as the temperature is increased above T_g of the elastomer (–70°C for the case of NR). Sufficient mobility is required so that long polymer chains of an elastomer will be able to rearrange to a new conformation of increased entropy after the applied strain is removed or held at a constant value above its T_g (Munch et al., 2006). Segmental mobility assists the physical stress relaxation process (Ginic-Markovic et al., 2000).

The cause of stress relaxation in elastomers (such as NR) or elastomer-based composites (e.g., carbon black filled NR) is largely related to the conformational

changes of the polymer chains (e.g. Tobolsky, 1960; Ortiz et al., 1998b; Patel et al., 2005; Le et al., 2009).

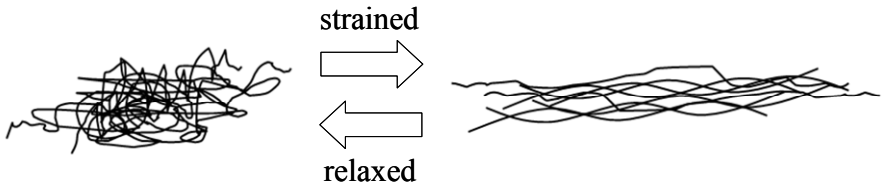

(a) (b)

Fig. 5.1 Typical NR molecular chain conformation: (a) the 'squirmed' – disordered and coiled conformation at equilibrium (high entropy), and (b) conformation when strained.

In an undeformed elastomer, the preferred conformation (i.e., geometrical arrangement) of the macromolecular polymer chains resembles a random coil (see Fig. 5.1(a)). The random coil conformation confers the elastomer a high entropic state at thermal equilibrium and thus its conformational stability. In statistical terms, random coiling of a macromolecular chain can be done in many different ways as opposed to completely stretching the long chain to a fully uncoiled shape, which is possible in one particular way only. In thermodynamic terms, the entropy of the elastomer in the coiled conformation is always high (Treloar, 1976; see Appendix D).

A stretched elastomer (shown in Fig. 5.1(b)) in a low entropy state would seek to increase its entropy by shrinking back to the coiled shape (a higher state of entropy). When an elastomer is stretched and held constant for a period of time, as in the case of a relaxation test, the equilibrium is perturbed and the entropy of the extended conformation is altered. The macromolecule chains would then shrivel to a higher

entropic state to be in thermo-kinetic equilibrium. The recoiling of the polymer chains reduces the free energy. The recoiling process of the polymer chains involves cooperative motions between neighboring segments, the dipole-dipole and the van der Waals interactions between polymer chains as well as the rotation of carbon-carbon covalent bonds (Ortiz et al., 1998b).

Stress relaxation due to the conformational changes of an elastomer elaborated above is also affected by molecular entanglements (e.g., Andrews et al., 1946; Doi and Takimoto, 2003; Konyali et al., 2008), molecular weight between entanglements (e.g., Fuller and Fulton, 1990; Chenal et al., 2007), cross-link density of the network (e.g., Ngai and Plazek, 2005), and network defects due to dangling chains (Curro and Pincus, 1983; Urayama et al., 2009).

5.5 Approaches to modeling stress relaxation in polymers

Stress relaxation of a polymer or a polymer based composite has been modeled in a variety of ways to characterize the mechanisms responsible for the stress decay. For example, the tensile relaxation modulus based on the bead-spring model proposed in Rouse (1953) is studied in Tobolsky and Aklonis (1964). It was shown in their work that the stress contribution per chain (calculated using Kramer's stress formula) in the bead-spring model reduces with time if the deformed state is held constant. Similar methods have been employed by others to study stress relaxation in polymers (e.g., Grassia and Hinch, 1996; Doi and Takimoto, 2003; Ramirez et al., 2007; Konyali et al., 2008). A micro-mechanical method to determine stress relaxation of polymer composites

consisting of linearly viscoelastic matrices and transversely isotropic elastic fibers was recently presented in (Abadi, 2009). Another approach to simulating stress relaxation in polymers is based on phenomenological models utilizing rheological elements i.e., springs and dashpots. The use of multiple Maxwell elements (a spring and a dashpot in series) arranged in parallel has been found to be capable of representing stress relaxation arising from physical, temperature and chemical effects, and coupled effects between them (Biot, 1954; Bartenev et al., 1981; D'Amore et al., 2006; Machiraju et al., 2006; Meera et al., 2009). Multiple units of the three-element Eyring model (a spring in parallel to a pair of spring and dashpot in series) with the model parameters evolving with strain or stress has been employed to represent the nonlinear viscoelastic response of polymers (Joseph, 2005).

5.6 Experimental results

The specimens used here are made from a NR coated Twaron CT709® plain-weave fabric. The Twaron®/NR composite is considered to be isotropic. The failure strain of the composite is determined to be 16.7% at a strain rate of 0.01 s^{-1} (see Table 4.5). The uniaxial tensile relaxation tests were performed at the room temperature and humidity (i.e., 25 °C and 50%, respectively) according to the ASTM E328 – 02 (2008) standard (see Fig. 5.2(a)). The tests were conducted using an MTS Insight30™ tensile testing machine. A tare pre-load of 1 ~ 2 N was applied to straighten each coated fabric specimen. The specimens were loaded at a constant strain rate of 0.01 s^{-1} up to 5% (i.e.,

the initial strain, ε_0 = 5%), after which the strain was held constant for 1 hour while the stress is measured as a function of time (see Fig. 5.2(b)).

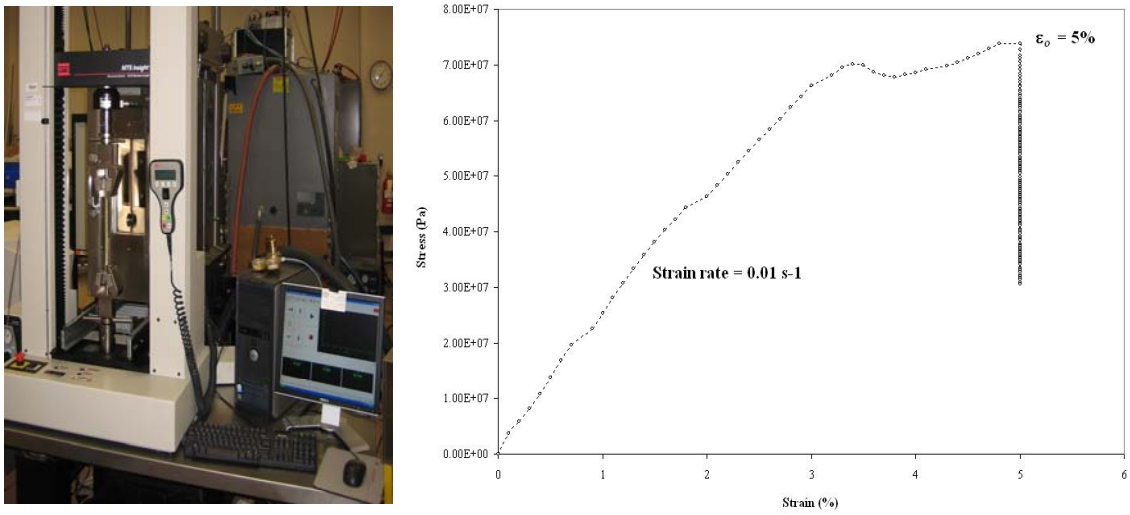

(a) (b)

Fig. 5.2 (a) Test set-up, and (b) stress and strain measured at a strain rate of 0.01 s^{-1} up to ε_0 = 5%.

5.7 Viscoelasticity models for stress relaxation

The experimentally determined stress relaxation curve of the Twaron CT709® fabric/natural rubber composite is shown in Fig 5.3. The initial stress, σ_0, corresponding to the initial strain, ε_0 (= 5%), is 73.8 MPa. The stress relaxation test reveals that σ_0 starts to decay exponentially up to 885 s and continues to decrease linearly with time until the end of the test at 3600 s, as shown in Fig. 5.3. The initial exponential stress decay amounts to 10.7 MPa (about 14.5% of σ_0). The stress relaxation response observed here and the rate at which it occurs are characteristic of the type of material

being studied. A description of two main stress relaxation characteristics of polymeric materials is provided next.

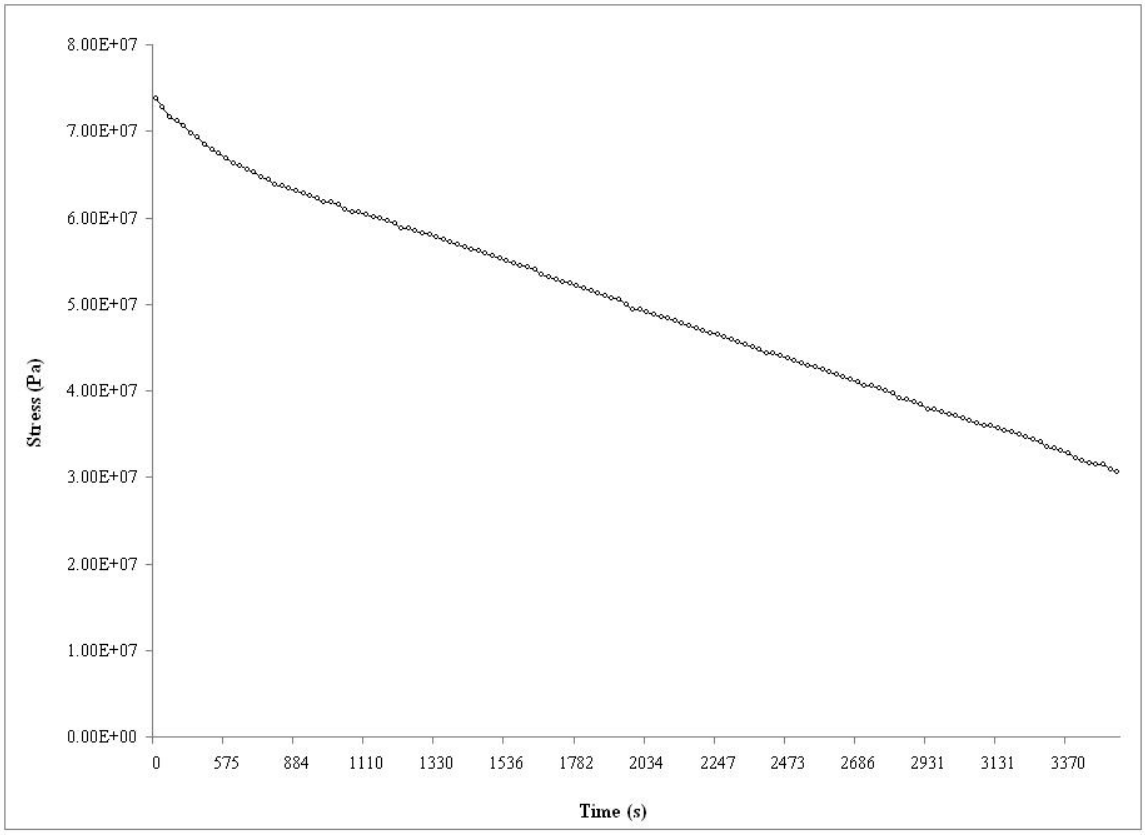

Fig. 5.3 Stress as a function time under the initial constant strain of 5%.

The stress relaxation characteristics of polymers and polymer composites are usually described by the stress relaxation time and the stress relaxation modulus (e.g., Slonimskii and Rogovina, 1964; Spontak et al., 2000). The stress relaxation time, τ, is a characteristic measure of time-dependent stress decay, $\sigma(t)$, from a deformed state (i.e., σ_0) under a constant 'initial' strain, ε_0. At the molecular scale, the relaxation time of a

polymer indicates the order of magnitude of time required for a certain proportion of the polymer chains in the polymer to relax via the processes mentioned in Sections 5.2 and 5.3 (Sperling, 2006). More specifically, τ is the time required for the stress to decrease 1/e (36.8%) of its initial value (Alger, 1997). This is equivalent to the time taken for a stress decay of 27.2 MPa from σ_0 = 73.8 MPa in the present study. The stress relaxation modulus, $E_r(t)$, is the time-dependent modulus observed during stress relaxation. The general relationship among the stress decay (in Pa), the stress relaxation modulus (in Pa) and the 'initial' strain is given by (Alger, 1997).

$$E_r(t) = \frac{\sigma(t)}{\varepsilon_0}. \tag{5.1}$$

Different viscoelasticity models can be employed to study the stress relaxation characteristics mentioned above and to predict the longer time response of the composite. In the present work, three viscoelasticity models are initially considered for modeling the stress relaxation response of the Twaron®/NR composite. These include a one-term generalized Maxwell model (comprising one Maxwell element with an additional spring in parallel; designated as $GM^{n=1}$), a two-term generalized Maxwell model (consisting of the $GM^{n=1}$ model with an additional Maxwell element in parallel; denoted as $GM^{n=2}$) and a four-parameter Burgers model. The $GM^{n=1}$ model is used here as a control model to study the effect of including an additional Maxwell element on the predictability of the resulting $GM^{n=2}$ model.

The schematic of all the three models and their stress relaxation functions are given in Table 5.1. The stiffness of a spring element (in Pa) and the viscosity constant of

a dashpot element (in Pa·s) in these models are denoted by K and η, respectively. The numeric subscripts in this denotation correspond to the element number in the models (see Table 5.1). The relaxation modulus of each model is the expression inside the parentheses of each stress relaxation function provided in Table 5.1. These expressions are consistent with the general relationship given in Eq. (5.1). The relaxation time (in seconds) just described above is, in general, defined by

$$\tau = \frac{\eta}{K}. \tag{5.2}$$

The method used to determine the values of the parameters in the models is as follows. The time at which the stress relaxation response started to be measured is set to be zero, i.e., $t = 0 = t_0$. The values of K_1 and K_2 in the GM$^{n=1}$ model are obtained by fitting its stress relaxation function to the instantaneous modulus, $E_i = \sigma_0 / \varepsilon_0$ = 1.476 GPa at t_0 with ε_0 = 5%. The relaxation times, τ_1 and τ_2, are then optimized in order to obtain a best fit to the experimental data. The 'fminunc' routine in the Matlab® Optimization Toolbox™ 4.3 as illustrated in Appendix C is used for the optimization. The values of the parameters of the other two models are obtained by first fixing the relaxation times, τ_1 and τ_2 and then optimizing the values of K_1, K_2, and K_3 for the GM$^{n=2}$ model, and K_1, K_2, η_1, and η_2 for the Burgers model. These values are tabulated in Table 5.2.

Table 5.1
The three viscoelasticity models considered for stress relaxation.

Model	Stress relaxation function
One-term generalized Maxwell ($GM^{n=1}$) model	
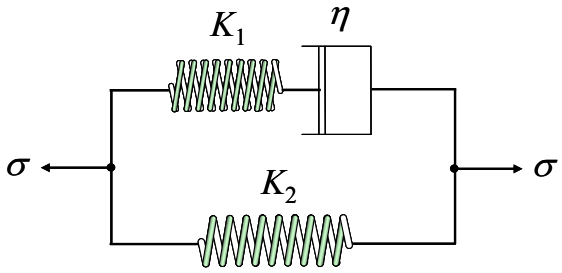	$\sigma(t) = \left(K_1 e^{-\frac{t}{\tau_1}} + K_2 \right) \varepsilon_o$ where the relaxation time is defined by, $\tau_1 = \frac{\eta}{K_1}$. (see *Appendix A.2* for derivations)
Two-term generalized Maxwell ($GM^{n=2}$) model	
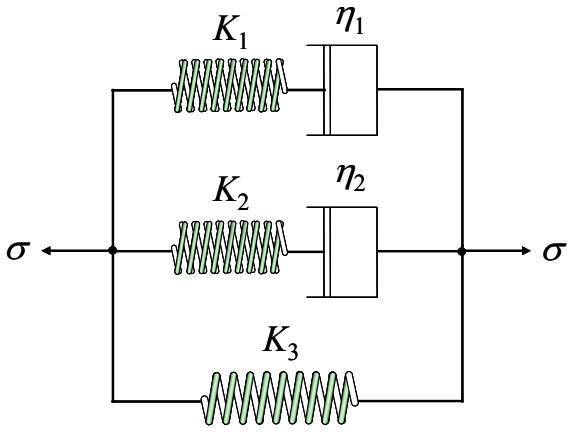	$\sigma(t) = \left(K_1 e^{-\frac{t}{\tau_1}} + K_2 e^{-\frac{t}{\tau_2}} + K_3 \right) \varepsilon_o$ where the relaxation times are defined by, $\tau_1 = \frac{\eta_1}{K_1}$ and $\tau_2 = \frac{\eta_2}{K_2}$. (see *Appendix F.2* for derivations)

Table 5.1 (*continued*)

Model	Stress relaxation function
Four-parameter Burgers model 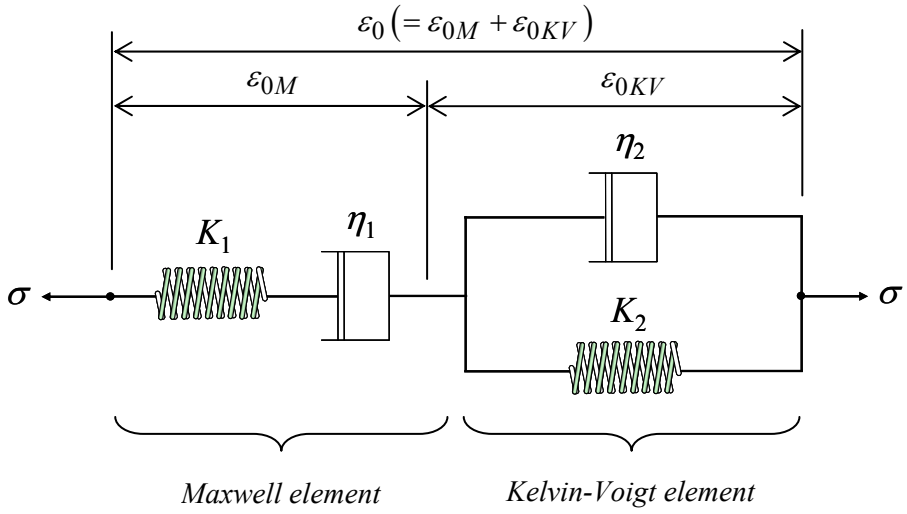 	$$\sigma(t) = \left(\bar{K}_1 e^{-\frac{t}{\tau_1}} + \bar{K}_2 e^{-\frac{t}{\tau_2}} \right) \sigma_0$$ where $$\bar{K}_{1,2} = \frac{\mp\frac{\eta_2}{K_2} \pm \left(\frac{\left(\frac{\eta_1}{K_1} + \frac{\eta_1}{K_2} + \frac{\eta_2}{K_2}\right) \pm \sqrt{\left(\frac{\eta_1}{K_1} + \frac{\eta_1}{K_2} + \frac{\eta_2}{K_2}\right)^2 - 4\frac{\eta_1\eta_2}{K_1K_2}}}{2} \right)}{\sqrt{\left(\frac{\eta_1}{K_1} + \frac{\eta_1}{K_2} + \frac{\eta_2}{K_2}\right)^2 - 4\frac{\eta_1\eta_2}{K_1K_2}}},$$ $$\tau_{1,2} = \frac{2\frac{\eta_1\eta_2}{K_1K_2}}{\left(\frac{\eta_1}{K_1} + \frac{\eta_1}{K_2} + \frac{\eta_2}{K_2}\right) \mp \sqrt{\left(\frac{\eta_1}{K_1} + \frac{\eta_1}{K_2} + \frac{\eta_2}{K_2}\right)^2 - 4\frac{\eta_1\eta_2}{K_1K_2}}}.$$ (see *Appendix E.2* for derivations)

Table 5.2
Values of the model parameters shown in Table 5.1.

Model	K_1 (Pa)	K_2 (Pa)	K_3 (Pa)	η_1 (or η) (Pa·s)	η_2 (Pa·s)	τ_1 (s)	τ_2 (s)
GM$^{n=1}$	4.8E+08	4.5E+09	–	6.8E+11	–	1420	–
GM$^{n=2}$	4.2E+07	8.3E+08	6.0E+08	6.0E+10	2.8E+12	1429	3374
Burgers	7.3E+07	1.3E+07	–	3.7E+11	2.3E+10	5070	1770

The stress relaxation curves obtained from the four models in Table 5.1 using the values of the corresponding parameters given in Table 5.2 are shown in Fig. 5.4.

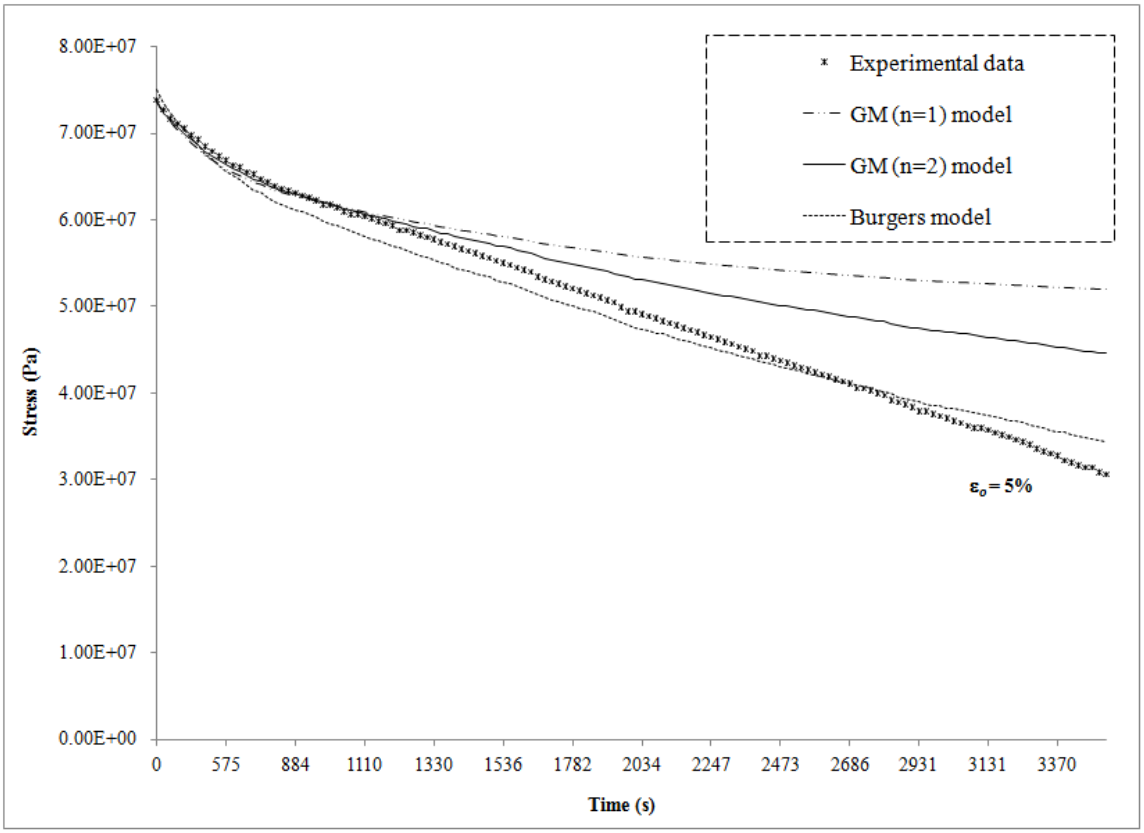

Fig. 5.4 Stress relaxation curves predicted by the three models compared with the experimental data.

As can be seen from Fig. 5.4, all the models considered here provide a reasonably good prediction of the stress decay up to $t \approx 575$ s (with an average stress reduction of 9.6% from σ_0). After this time, it is found that the $GM^{n=1}$ and $GM^{n=2}$ models give a better estimate of the stresses than the Burgers models until $t \approx 1110$ s. The $GM^{n=1}$ and $GM^{n=2}$ models subsequently overestimate the stresses compared to the experimental data. The stresses predicted by the $GM^{n=1}$ and $GM^{n=2}$ models match rather closely with each other until $t \approx 1330$ s, beyond which the $GM^{n=2}$ model gives a better approximation than the $GM^{n=1}$ model.

The observations made above indicate that the residual springs in the $GM^{n=1}$ and $GM^{n=2}$ models (i.e., K_2 and K_3, respectively, with $K_2^{GM^{n=1}} > K_3^{GM^{n=2}}$ (see Table 5.2)) and the number of Maxwell elements (n) influence the predictions of the stress decay by the two models as time progresses. The residual springs cause retention of some amount of the stress as equilibrium is reached under the constant applied strain. This is mathematically evident from the relaxation functions of the $GM^{n=1}$ and $GM^{n=2}$ models (see Table 5.1), which show that the stress tends to equilibrate to $K_2 \cdot \varepsilon_0$ and $K_3 \cdot \varepsilon_0$, respectively, as time advances. The stress values predicted by the one-term and two-term generalized Maxwell models are therefore generally larger than those determined experimentally. In this study, the divergence begins at 1330 s as can be seen in Fig. 5.4. Hence, for the $GM^{n=1}$ and $GM^{n=2}$ models, the residual springs exert the solid-like response.

The better approximation of the $GM^{n=2}$ model than that of the $GM^{n=1}$ model after $t \approx 1330$ s can be related to the two stress relaxation times, τ_1 and τ_2 (see Table 5.1), corresponding to the two Maxwell elements in the former. The $GM^{n=1}$ model has a single Maxwell element and thus only one relaxation time (i.e., τ (see Table 5.1)). As mentioned at the beginning of this section, the composite responds with different time scales to the constant applied strain. Consequently, a combination of more than one pair of K_i and η_i (or, equivalently, τ_i) is required to fit the predicted results to the experimental data (e.g., Gerdeen et al., 2006). This is elucidated next.

Stress relaxation of an entangled polymer chain network tends to be a complicated time-dependent behavior (see Sections 5.1–5.3). The complication is caused by, for example, different segments of chain lengths with different side groups that affect the localized stress reduction through chain motion and side group rotation (Brinson and Brinson, 2008). There are, therefore, more than one stress relieve mechanism involved in an entangled polymer chain network. These mechanisms can transpire individually or in concert at different times and rates during the relaxation process. The characteristic relaxation time corresponding to these mechanisms therefore also needs to be more than one. Assembling more than one Maxwell element in parallel improves the representation of stress relaxation response by providing more than one relaxation time, as evident in the case of the $GM^{n=2}$ model.

The Burgers model (a Maxwell element and a Kelvin-Voigt (KV) element in series as shown in Table 5.1) provides a reasonably good prediction on the $0 < t < 575$ s interval. This model continues to underestimate the stress decay up to $t \approx 2685$ s before

over-predicting the stress until the end of the test period. This can be attributed to the stress response of the KV element. For a constant strain of ε_{0KV}, the constitutive relation of this element is given by $\sigma = K_2\varepsilon_{0KV}$ (e.g., Arridge, 1975). The stress in the KV element, therefore, remains virtually constant at all times under the constant strain. On the other hand, the stress in the Maxwell element reduces exponentially according to $\sigma(t) = K_1 e^{-t/\tau}\varepsilon_{0M}$ after the strain is applied (see Table 5.1). This is substantiated by the smaller value of τ_2 (= 1770 s) as opposed τ_1 (= 5070 s) in Table 5.2, which means that the stress equilibrium is reached sooner in the KV element than in the Maxwell element.

Furthermore, both elements sustain smaller of stress during the initial decay because ε_{0M} and ε_{0KV} are small compared to ε_0. The stress decay is then controlled simply by the Maxwell element at longer times, i.e., t > 575 s, during which the stress values predicted are found to be distanced from the experimental data.

It is observed from Fig. 5.4 and is clear from the preceding discussions that the three models considered here are capable of predicting the initial, short-duration exponential decay of stress (t < 575 s) with varying degree of accuracy. The predictions by the models after this duration, however, are found to be imprecise. As shown in Fig. 5.4, all the models continue to either under-predict or over-predict the stress between 575 s and 3600 s. These observations indicate that the three models do not effectively represent the stress relaxation response of the Twaron®/NR composite. This motivates the use of the newly developed para-rheological model that: (i) embodies the mechanical analogue of the para-aramid Twaron® fibers from which the fabric is made (see Section

3.3), and (ii) takes into account the entropic elasticity of the NR constituent through the molecular theory of rubber elasticity (see Section 4.4). The stress relaxation function of the para-rheological model and the analysis of the relaxation behavior predicted by the model are presented next.

5.8 Para-rheological model for stress relaxation

The three viscoelasticity models applied in Section 5.7 are fully rheological in the sense that they contain only springs and dashpots, which are the two basic types of rheological elements. The para-rheological model developed Section 4.8, which includes the stress network element in addition to springs and dashpots, is used here to characterize the stress relaxation behavior of the Twaron®/NR composite.

It can be shown that the stress relaxation function provided by the para-rheological model illustrated in Fig. 4.6 has the following form (see *Appendix H.2* for derivations):

$$\sigma(t) = \left[K_1 e^{-\frac{t}{\tau}} + \left(K_2 + 3E_{NR} \right) \right] \varepsilon_0 , \tag{5.3}$$

where ε_0 is the initial strain (= 5%), and $\tau = \eta / K_1$ is the relaxation time. From Eq. (5.3), the instantaneous modulus, E_i ($\equiv E_r(0) = K_1 + K_2 + 3E_{NR}$) = 1.476 GPa and the equilibrium stress (as $t \to \infty$) = $K_2 + 3E_{NR}$.

The values of the parameters in the para-rheological model are taken to be: K_1 = 4.3×10^8 Pa, K_2 = 1.0×10^9 Pa, E_{NR} = 1.0×10^6 Pa and η = 2.1×10^{12} Pa·s. In the

mechanical analogue of the para-aramid Twaron® fibers (see Section 3.3), K_2 and K_1 refer to the strong intramolecular covalent bonds (primary bond) and the weak intermolecular van der Waals forces and hydrogen bonds (secondary bond), respectively (David et al., 2009a). This differentiation of the bond type is reflective in the values of the parameters given above where the stiffness of the K_2 spring is greater than that of the K_1 spring. The value of E_{NR} assigned here is in the range of experimentally determined values of the elastic modulus of NR (e.g., Treloar, 1944; Hamza et al., 2008; Ramorino et al., 2009).

The stress relaxation curves obtained from the para-rheological model using the values of the parameters specified above are shown in Fig. 5.5. It can be recalled that the three models used in Section 5.5 provide only a fair prediction of the stress reduction up to $t \approx 575$ s (with an average initial decay of 9.6%). In contrast, it is found that the para-rheological model provides a good estimation of the stress relaxation up to $t \approx 1536$ s with an initial decay of 15.1% compared with that of 14.5% displayed by the experimental data. A similar performance is seen for the relaxation modulus (see the figure on page 119).

However, the para-rheological model with a constant single value of $\tau \ \left(= \eta / K_1 = 2200 \text{ s}\right)$ over-predicts the stress beyond 1550 s. By optimizing the values of K_1 and η, it was found that τ satisfies the following characteristic time function for the best fit (see Fig. I1 in Appendix I):

$$\tau(t) = 5.3 \times 10^3 - 0.4t \ . \tag{5.4}$$

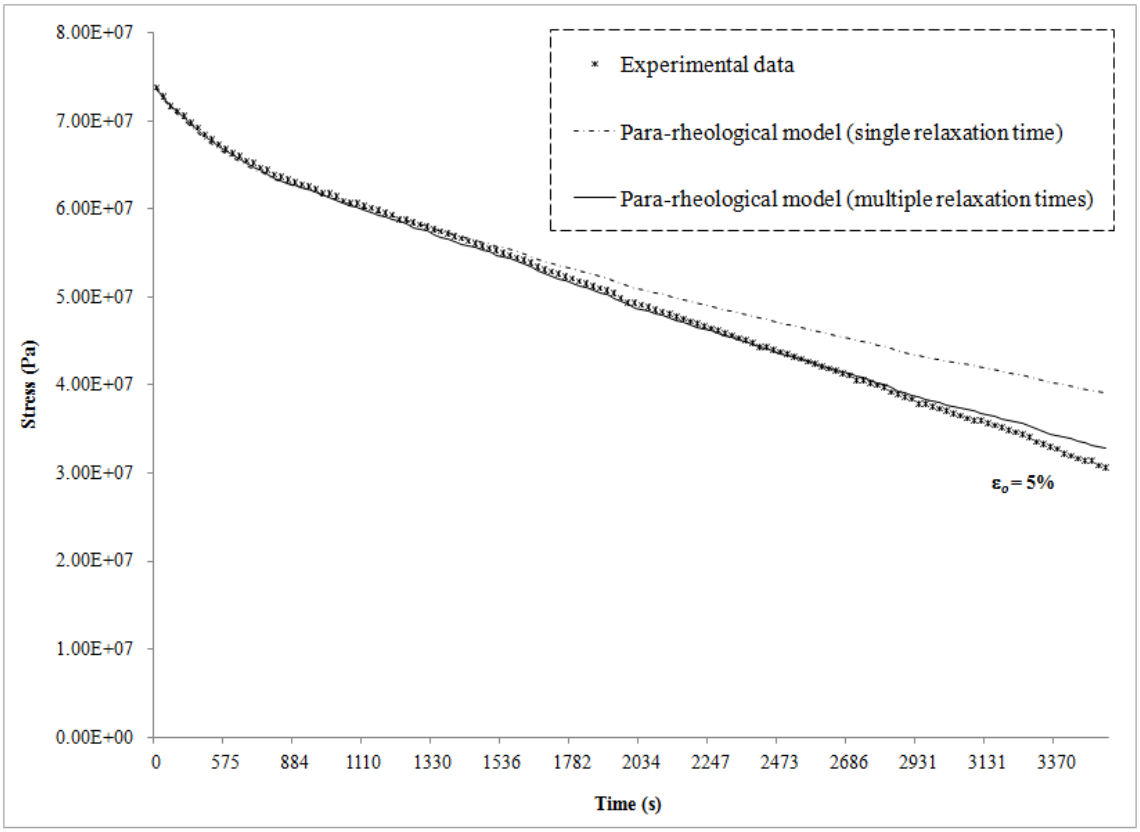

Fig. 5.5 Stress relaxation curves predicted by the para-rheological model compared with the experimental data.

The stresses predicted by using Eq. (5.4) (multiple characteristic relaxation times) in Eq. (5.3) are in excellent agreement with the experimental data, as can be seen from Fig. 5.5. This indicates that K_1 and η are actually phenomenological coefficients that become functions of time when stress relaxation is considered. It has been observed in Chapter III that when the duration of deformation is long, like in this case of a constant applied strain for 1 hour, the weaker secondary bonds are overcome first (see Section 3.7.1.2). This implies that the scission of the secondary bonds connecting adjacent chains (K_1) that connect adjacent chains and thereby the viscous motion of the

chains in the entangled network (η) are processes through which the stress in the polymer chains is relieved (see Section 5.2). These two time-dependent processes affect the evolving proportionate values of K_1 and η in accordance to Eq. (5.4). A similar observation was made in Joseph (2005), where K_1 and η were found to evolve with the strain and strain rate. In the present study, the evolution of these two parameters and their effect on τ can also be linked to the morphology of the Twaron® fibers as follows.

Twaron® fibers are semi-crystalline polymers consisting of both crystalline and amorphous phases (e.g. Maity et al., 2008). The K_1 and η parameters of the GM element, which represents the Twaron® constituent in the para-rheological model, are associated with the continuous short-term viscous motion (flow) of polymer chains in the amorphous phase of the fiber under a constant strain (Wang and Zhao, 2008). The rate at which the viscous motion process, which is one possible relaxation mechanism in polymers (see Section 5.2), contributes toward relaxing σ_0 will influence the overall rate of decay as measured by the τ (see Section 5.5).

The stress relaxation response of the Twaron®/NR composite due to the NR constituent is fairly limited. This may be attributed to the failure strain of NR that can reach about 450% at the room temperature of 25 °C (Findik et al., 2004). In this regard, the 5% strain imposed on the composite and thus on the NR constituent (by virtue of the iso-strain state of the para-rheological model) is significantly small. The application of a small strain permits the macromolecule chains in the NR, which is mainly comprised of an amorphous phase at the room temperature, to elongate without breaking via uncoiling. This reduces the entropy of the NR and increases its free energy.

Consequently, the chains start to recoil to a new conformation of higher entropy when the strain is held constant for a period of time (3600 s in this case). As mentioned in Section 5.3, the recoiling process of the chains reduces the free energy, which is time independent. Also, for a given constant temperature, the molecular entanglement, the molecular weight between entanglements and the cross-link density of the network in the NR remain the same. In fact, from the thermodynamics point of view, this shows that the value of E_{NR} does not change with time under a constant strain. It can then be said that the relaxation response of the NR constituent is due to the entropic effect mentioned above and this effect is accounted for by the stress network element σ_λ.

The foregoing discussion shows that the relaxation time of the para-rheological model relies on the relaxation mechanisms in the Twaron® constituent. The single relaxation time of the para-rheological model, determined from K_1 and η (see Eq. (5.3)), depicts the confluence of different relaxation mechanisms (modes) arising from the viscous motion, chain scission, and molecular entanglements of the polymer chains in the Twaron® fibers. The results obtained from this model suggest that the grand effect of the said confluence on the overall relaxation response be time-dependent.

5.9 Stress relaxation modulus and Prony series representation

Fig. 5.6 on page 119 shows the variation of the stress relaxation modulus obtained using all of the models and its comparison with that determined from the experiment. The relaxation modulus defined by Eq. (5.1) and shown inside the

parentheses for each viscoelasticity model listed in Table 5.1 can be expressed by a series expansion known as the Prony series. The general form of the Prony series is:

$$E_r(t) = E_\infty + \sum_{i=1}^{n} K_i e^{-\frac{t}{\tau_i}} \tag{5.5}$$

where $E_\infty = \lim_{t\to\infty} E_r(t)$ is the equilibrium modulus, and K_i and τ_i are the spring stiffness and the relaxation time, respectively.

The Prony series specified in Eq. (5.5) can be normalized against the instantaneous modulus, E_i. By using the normalized instantaneous ($\hat{E}_i$) and equilibrium ($\hat{E}_\infty$) moduli at the time limits $t = 0^-$ and $t \to \infty$, respectively, the normalized Prony series are given by (see *Appendix F.3* for an example of derivation)

$$\hat{E}_r(t) = 1 - \sum_{i=1}^{n} \hat{K}_i \left(1 - e^{-\frac{t}{\tau_i}}\right), \tag{5.6}$$

where $\hat{K}_i$ and τ_i are called the normalized Prony coefficients. The fitted parameters (see Table 5.2) for each model are normalized against E_i to obtain the normalized Prony coefficients. The normalized Prony series, $\hat{E}_r(t)$, for each of the model presented in Sections 5.5 and 5.6 together with the corresponding normalized Prony coefficients are shown in Table 5.3. The normalized stress relaxation moduli of all the models analyzed here are shown the Fig. 5.7.

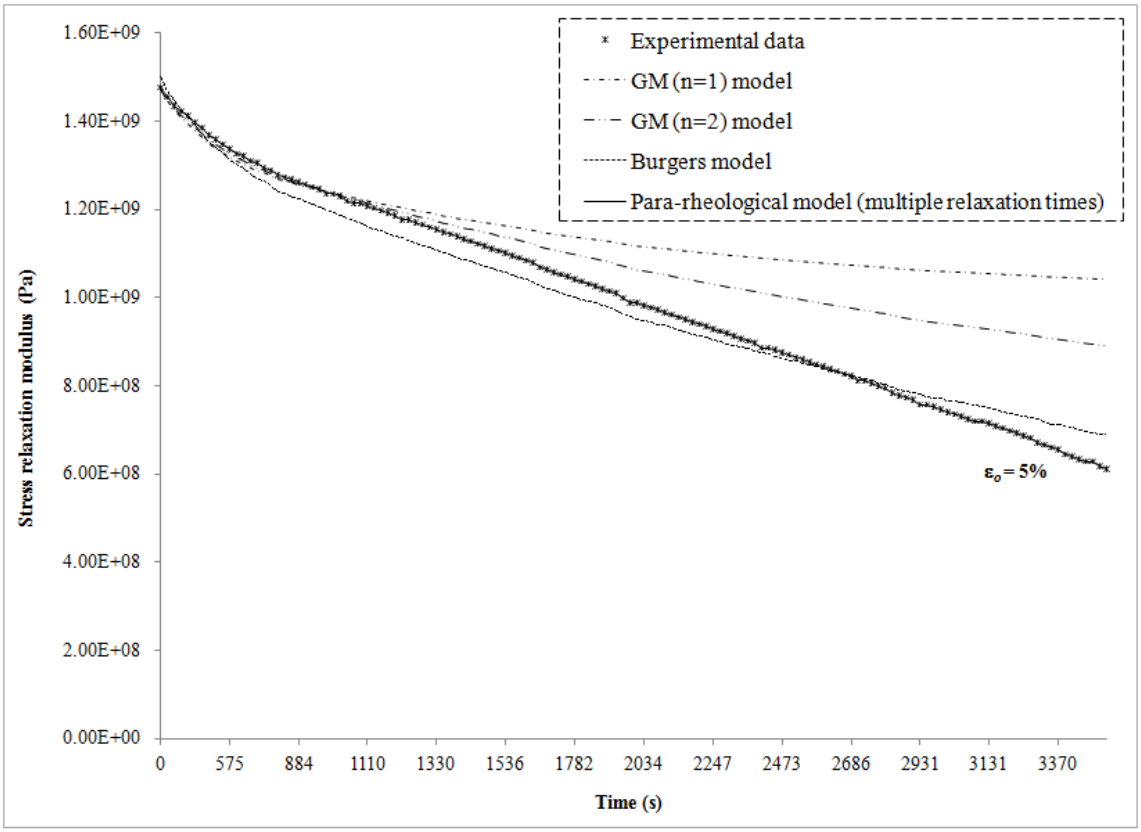

Fig. 5.6 Stress relaxation modulus predicted by the four models compared with the experimental data.

Table 5.3
Normalized Prony series and coefficients.

Model	Normalized Prony series, $\hat{E}_r(t)$	Normalized equilibrium modulus, $\hat{E}_\infty$	Normalized Prony coefficients
GM$^{n=1}$	$1-\hat{K}_1\left(1-e^{-\frac{t}{\tau}}\right)$	$1-\frac{K_1}{K_1+K_2}=0.676$	$\hat{K}_1=\frac{K_1}{K_1+K_2}=0.324$
GM$^{n=2}$	$1-\sum_{i=1}^{2}\hat{K}_i\left(1-e^{-\frac{t}{\tau_i}}\right)$	$1-\frac{K_1+K_2}{K_1+K_2+K_3}=0.408$	$\hat{K}_1=\frac{K_1}{K_1+K_2+K_3}=0.0285$ $\hat{K}_2=\frac{K_2}{K_1+K_2+K_3}=0.564$
Burgers	$\sum_{i=1}^{2}\hat{C}_i e^{-\frac{t}{\tau_i}}$	0	$\hat{C}_1=\frac{C_1}{C_1+C_2}=0.9$ $\hat{C}_2=\frac{C_2}{C_1+C_2}=0.1$
Para-rheological	$\left(1-\hat{K}_2-3\hat{E}_{NR}\right)e^{-\frac{t}{\tau}}+\left(\hat{K}_2+3\hat{E}_{NR}\right)$	$\hat{K}_2+3\hat{E}_{NR}=0.08$	$\hat{K}_2=\frac{K_2}{E_i}=0.078$ $\hat{E}_{NR}=\frac{E_{NR}}{E_i}=0.000184$ $\left(E_i=K_1+K_2+3E_{NR}\right)$

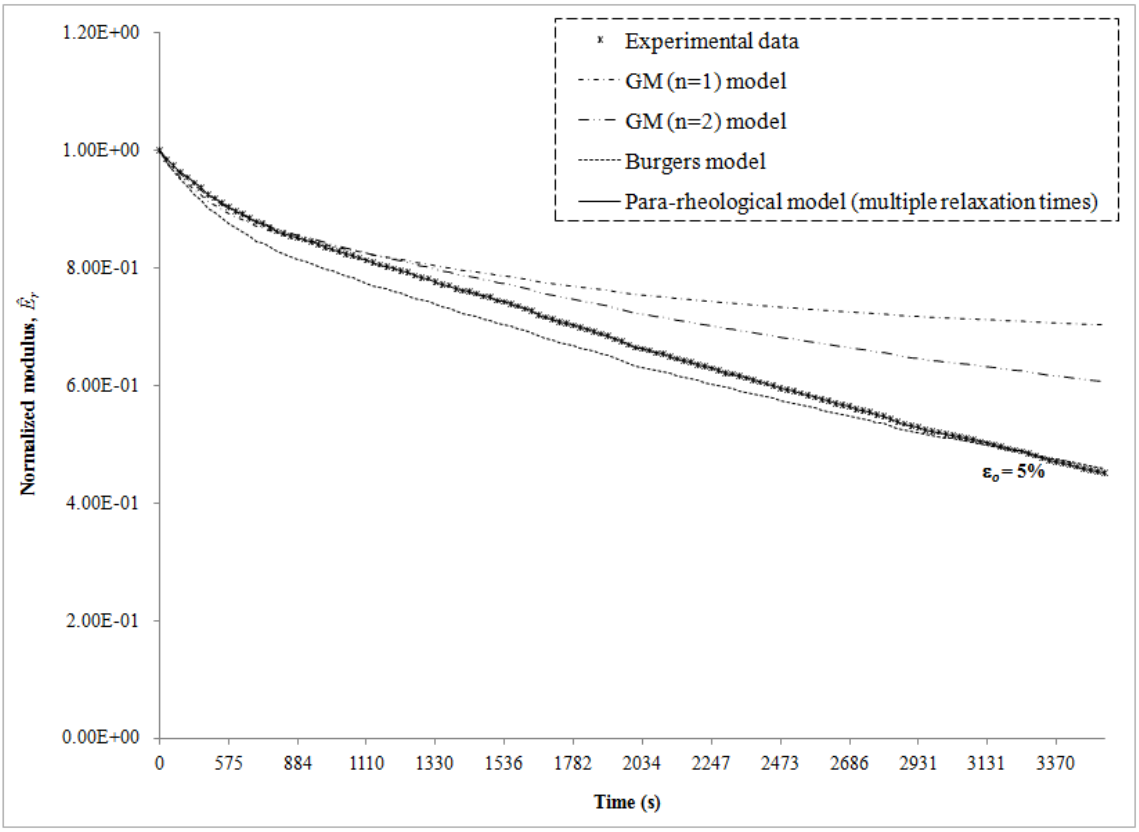

Fig. 5.7 Normalized stress relaxation modulus predicted by the four models compared with the experimental data.

5.10 Accuracy of the viscoelasticity and para-rheological models

As mentioned in Section 4.7.3, the coefficient of determination (*COD*) represents the percentage of the experimental data that is closest to the model curves. This measure is used here to quantitatively compare the predictability of the para-rheological model developed in the present study with that of the other viscoelasticity models. The coefficient of determination (*COD*), as defined in Eq. (4.17), is given here again as

$$COD = 1 - \frac{1}{n}\left[\frac{\sum\left(\sigma_{exp} - \sigma_{mod\,el}\right)^2}{\sum\left(\sigma_{exp} - \bar{\sigma}\right)^2}\right] \times 100\% \ , \tag{5.7}$$

where n is the total number of stress values each measured at time instants during the experiment (= 138 here), $\bar{\sigma}$ is the mean stress computed from $\left(\sum_{i=1}^{n}\sigma_i\right)/n$ (= 4.99×10^7), and σ_{exp} and σ_{model} denote, respectively, the stresses measured during the experiment and predicted by the model at every time instant. Table 5.4 lists the values of *COD* for all of the models presented here. The *COD* is calculated for the duration corresponding to the theoretical characteristic relaxation time described in Section 5.7. This time interval corresponds to the initial stress decrease of 27.2 MPa, which is a stress decay of 36.8% of its initial value.

Table 5.4
Coefficient of determination (*COD*) of all models.

Model	*COD*
$GM^{n=1}$	0.656
$GM^{n=2}$	0.877
Burgers	0.909
Para-rheological	0.995

It can be seen from Table 5.4 that the para-rheological model provides the best fit to the experimental data among all the four models during the initial decay. The Burgers model also exhibit a good fit to the experimental data, even though this model predicts that the equilibrium modulus goes to zero at $t \to \infty$ (see Table 5.4), which is typical of a

fluid. The Twaron®/NR composite is a viscoelastic solid that retains a minimum amount of stress at long times. In the present study, *COD* also provides a measure of certainty in forecasting the future values of the stress using the models and the associated values of parameters.

5.11 Prediction of longer time response

The normalized relaxation modulus, $\hat{E}_r(t)$, given by Eq. (5.6) can be used to extrapolate the longer time response of the composite under the constant applied strain. Normalization of the stress relaxation modulus to unity at t = 0 isolates the time dependence of the stress from the strain dependence and thereby permits the prediction of the longer time relaxation response of the composite (e.g., Hummel et al., 2001). The para-rheological model developed here is also utilized to forecast $\hat{E}_r(t)$ after the test duration, i.e., when t > 3600 s. Fig. 5.8 shows the prediction of the normalized modulus at longer times by all of the four models studied in this chapter. In consistent with Eq. (5.3), the moduli forecasted by the para-rheological model closely match the experimental data until t = 3600 s and continue to reduce to an equilibrium level of about 0.08 at around 7500 s. $\hat{E}_r(t)$ of the Burgers model diminishes to zero at around 25,000 s. The $GM^{n=1}$ and $GM^{n=2}$ models predict a much higher $\hat{E}_\infty$ compared to that by the para-rheological model.

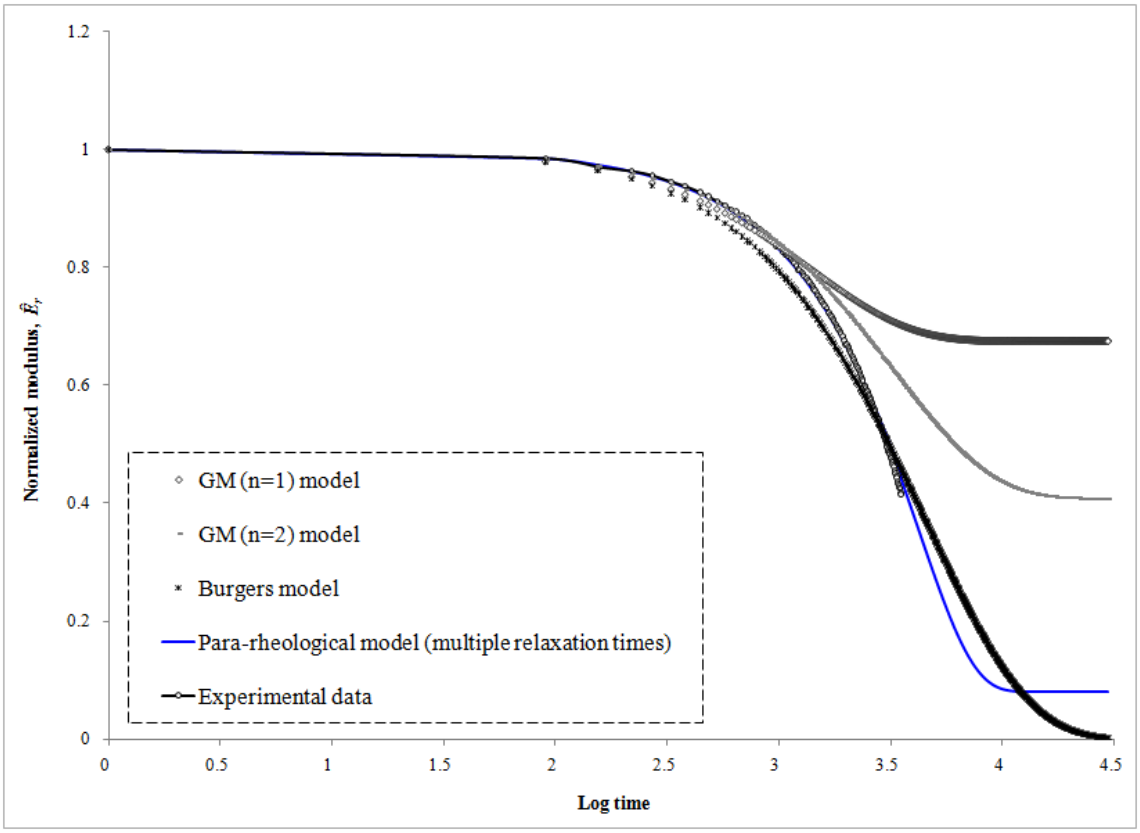

Fig. 5.8 The longer time stress relaxation response predicted by the viscoelasticity and the para-rheological models.

5.12 Summary

The experimentally determined stress relaxation behavior of a Twaron CT709® fabric/natural rubber composite under a uniaxial constant applied strain is studied using two GM^n models (n, number of Maxwell elements = 1, 2), the Burgers model and a newly developed para-rheological model. The new model utilizes a three-parameter element to represent the Twaron® fabric and the affine network based molecular theory of rubber elasticity to account for the deformation mechanisms of the NR constituent. The parameter values needed in each model to determine the stress relaxation modulus

and the characteristic relaxation time are extracted from the experimental data via curve fitting.

The experimental results show that the stress reduces exponentially with a decay of 14.5% during the first 885 s of the test duration (= 3600 s) and then continues to decrease linearly with time. It is found that the initial relaxation response of the composite is predicted fairly well by all of the four models, while the stress relaxation is more accurately represented by the para-rheological model until $t \approx 1536$ s. The addition of one more Maxwell element to the $GM^{n=1}$ model improves the predictability of the resulting $GM^{n=2}$ model by providing the second relaxation time.

The complexity of having more Maxwell elements (in order to obtain a spectrum of relaxation times) is traded with a simple characteristic time function in the para-rheological model, which is found to have greatly improve predictability for the values stress and relaxation modulus at all times. The characteristic time function represents the evolution of the K_1 and η parameters with time. The adjustment of these two parameters and their effect on the relaxation time is linked to the molecular stress relaxation mechanisms of the Twaron® fibers under the applied constant strain.

The para-rheological model also predicts a longer time response that is closely associated with the trend displayed by the experimental data. Based on this prediction, the stress in the composite should relax to a small but non-zero equilibrium level at $t \rightarrow \infty$.

CHAPTER VI

CREEP BEHAVIOR OF A TWARON®/NATURAL RUBBER COMPOSITE

6.1 Introduction

Viscoelastic responses of ballistic fabrics made from fibers such as the Kevlar® and Twaron® fibers have been studied extensively (e.g., Black and Preston, 1973; Ericksen, 1985; Allen and Roche, 1989; Baltussen and Northolt, 2003; Pramanik and Chakraborty, 2004; Sebastian et al., 2008). Creep tests are often used to describe the time-dependent behavior of such fabric materials.

Discussions on the constant strain rate behavior and stress relaxation (under a constant applied strain) response of a viscoelastic ballistic fabric composite, namely the Twaron CT709® fabric/natural rubber (Twaron®/NR) composite were given in Chapter IV and Chapter V, respectively. In order to further the understanding of the viscoelastic characteristics of this composite, its response to a constant applied stress is studied in this chapter. The deformation of a material under an invariable stress is called creep.

Creep test under uniaxial tensile load measures the change in the axial length of a specimen caused by a constant uniaxial tensile force (or stress). Creep is also considered to be a measure of the dimensional stability of a material under a prolonged applied load or stress.

In this chapter, the creep behavior of the Twaron®/NR composite under a uniaxial constant stress is studied using three viscoelasticity models and the newly developed para-rheological model. The three viscoelasticity models employed are the

one-term generalized Maxwell ($GM^{n=1}$) model, the two-term generalized Maxwell ($GM^{n=2}$) model and the four-parameter Burgers model. These three models, each with a different level of complexity and efficiency, have been developed and used in Chapter III and Chapter IV.

The creep behavior of the Twaron®/NR composite under a uniaxial constant applied stress of 30 MPa is first experimentally determined. The three viscoelasticity models mentioned above and the newly developed para-rheological model are then used to characterize the creep behavior and to predict the longer time response of the composite. The values of rheological parameters involved in each model to determine the creep compliance and the characteristic retardation time(s) are extracted from the experimental data via curve-fitting and optimized through a minimization algorithm. Consequently, the microstructural changes and molecular features that are linked to the macroscopic creep response of the composite are incorporated in each of the viscoelasticity model in a phenomenological manner. Finally, the accuracy of each model in simulating the creep response of the composite are compared quantitatively.

6.2 Descriptors of creep phenomenon

The two important descriptors of the tensile creep phenomenon in polymers (and most of other engineering materials) are the time-dependent uniaxial creep compliance (denoted as $J_c(t)$ in this study) and the retardation time (usually denoted as τ_c).

Creep compliance is a measure of the softness of a material (Rogozinsky and Bazhenov, 1992). This measure is the opposite of the relaxation modulus (determined

from a stress relaxation test), which is a direct measure of the stiffness of the material under a constant applied strain. Creep compliance is thus regarded as a time-dependent reciprocal modulus. In the case of small deformations, the compliance is a function of time, t, and temperature, T, i.e., $J_c(t,T)$ (Yang et al., 2006). This relation reduces to $J_c(t)$ if the creep test is conducted at a constant temperature.

The creep response of a material is expected to resemble an inverted image of the stress relaxation response. If the deformations and stresses are small and the time dependence is not strong, then the stress-relaxation and creep tests are inverse to each other. The inversion of the tensile relaxation modulus, $E_r(t)$, to $J_c(t)$ can be made using the convolution integral method (Bradshaw and Brinson, 1997; Schapery and Park, 1999).

Retardation time is, by definition, the time required for the test specimen to deform to 63.21% ($\equiv [1 - e^{-1}]$ %) of the total deformation. Polymeric viscoelastic materials have a large number of characteristic retardation times distributed over many decades (e.g., Brinson and Brinson, 2008). In order to accurately represent the creep responses of these materials, models would have to allow for a discrete set of or a continuous spectrum of retardation times. The multiple characteristic retardation times displayed by these materials signify different creep mechanisms occurring at different times and rates.

The molecular bases for creep in polymers are quite similar to those for stress relaxation, as discussed in Section 5.2. These include chain slippage (e.g., Sperling, 2006), molecular entanglement and cross-linking (e.g., Doi and Takimoto, 2003),

molecular re-configuration and re-orientation (e.g., Tashiro et al., 1977; Ortiz et al., 1998b), and viscous flow (e.g., Yang et al., 2006). Two or more of these causes can act simultaneously to produce an increase in strain as a function of time during a creep test. Some important aspects of the molecular bases for creep in polymers is discussed in the following section.

6.3 Creep phenomenon of polymeric materials

The application of a step stress in a creep test leads to the perturbation of macromolecular chains in the polymer from their equilibrium position. This perturbation and the subsequent material response are temperature dependent.

At temperatures below its glass transition temperature (T_g), the creep response of a polymer is attributed to the rotational motion of short chain segments comprising one to two monomer units. The chain segments initially respond with a elastic restoring force, which arises from the potential barrier to a rotational motion of molecules around the backbone chain. These segments then begin to diffuse in a Brownian motion toward a new equilibrium position. This motion, however, is impeded by the local viscosity of the surrounding chains, thereby resulting in the time dependent creep response. Above the T_g, the crystallinity of the polymer reduces the creep compliance and the creep rate (i.e., the rate of change of strain). This effect arises from the apparent cross-linking (that leads to the polymer crystallinity) as a result of the ends of chain segments being immobilized in different crystallites (Nielsen and Landel , 1994). Crystallinity thus slows down the creep process and enhances the dimensional stability of the polymer. A

discussion on the major phases of creep response, i.e., creep strain (ε) and creep rate ($\dot{\varepsilon}$), of a polymer is presented next.

For a constant applied load, the creep response may be described by three general stages (e.g., Findley et al., 1976; Yang et al., 2006). As shown in Fig. 6.1, the first stage (indicated by *P*) is called the primary creep that starts at a relatively high creep rate but continues at a decreasing rate. The secondary stage (specified by *S*) proceeds almost at a constant creep rate. Accordingly, this regime is also referred to as the steady state creep. However, $\dot{\varepsilon}$ at the secondary stage also depends on the physical features of the polymer such as entanglements and motion of the macromolecular chains and crystallinity of the polymer, which will be discussed further below. The third stage is known as the tertiary stage (labeled as *T*), which occurs at an increasing $\dot{\varepsilon}$ and ends when the material breaks. This three-stage representation is valid for linear viscoelastic materials where the stress is proportional to strain and the linear superposition principle holds (e.g., Povolo and Hermida, 1990). The strain ε shown in Fig. 6.1 is the sum of the instantaneous elastic strain (ε_0) and the creep strain. The absolute value of the creep strain can be obtained by shifting the strain axis up to ε_0.

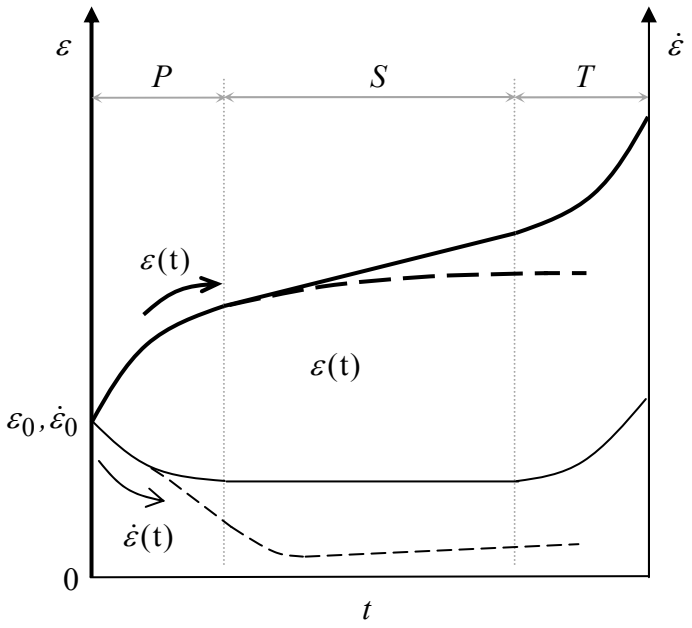

Fig. 6.1 Three idealized stages of creep phenomenon in most polymers: (**—**) total strain; (—) creep rate; dashed lines show typical responses of a crosslinked or a highly crystalline polymer.

In general, the time-dependent creep compliance and the creep rate of a viscoelastic polymer are influenced by the entanglement and chemical cross-linking of the macromolecular polymer chains. The orientation of the chains with respect to the direction of the applied force also affects the creep properties of the polymer. These factors are briefly discussed below.

Entanglements of macromolecular polymer chains are regarded as physical crosslinks, i.e., looping of chains around each other. Long chains tend to have high number of entanglements that provide resistance to moving past each other. Entanglements act as temporary crosslinks and assist in recovering the shape of the

polymer if the applied force is removed before the creep stage *T* is reached (e.g., Nielsen and Landel , 1994).

A thermosetting or crosslinked polymer such as the natural rubber is typically regarded as a viscoelastic solid that has a finite equilibrium creep compliance (J_c^{∞}) and a very small creep rate ($\dot{\varepsilon}$). Un-crosslinked polymers, e.g., the thermoplastic polyethylene, are composed of threadlike molecules that are not permanently attached to each other. That is, these polymers contain no or negligible amount of chemical crosslinks. Un-crosslinked polymers have a finite $\dot{\varepsilon}$ with no perceptible J_c^{∞} and behave like a viscoelastic liquid at longer times. Other types of polymers such as the semi-crystalline para-aramid fibers exhibit a viscoelastic behavior that lies in between the solid and liquid dichotomy mentioned above (e.g., Yang, 2000). In order to characterize how fluidic a viscoelastic material is, or how different viscoelastic models perceive the actual material to respond, a dimensionless number called the Deborah number, *D*, can be used. This number, defined by

$$D = \frac{\tau_c}{T_S} \tag{6.1}$$

is an indicator of how fluidic or solid the behavior of a viscoelastic polymer is relative to the time scale of the experiment or observation, T_S. In Eq. (6.1), τ_c is the retardation time. A greater value of *D* suggests a solid-like viscoelastic response (Reiner, 1964). The effects of physical entanglements and chemical crosslinks on the creep response, particularly on the creep compliance, of a crosslinked polymer are discussed next.

Fig. 6.2 shows the evolution of creep compliance ratio, i.e., $J_c(t)$, divided by the initial compliance at $t = 0$ (denoted as J_0), on a logarithmic time scale that is generally exhibited by solid polymers (e.g., Baltussen and Northolt, 2001; Urbelis et al., 2005; Yang et al., 2006). Chemical and physical cross-linking has three important effects on the creep compliance function of a polymer (Ferry, 1980): (1) The time when the initial perceptible increase of the compliance ratio occurs (see point ❶ in Fig. 6.2) is shifted right at a longer time; (2) The transition region (shown by point ❷ in Fig. 6.2) is broadened with the compliance ratio increasing at a lower rate; (3) The equilibrium compliance ratio (J_c^{∞} / J_0), known as the 'elastic ceiling', flattens at a lower value, i.e., height of ❸ reduces. Also, the dashed line in Fig. 6.2 represents the creep response in the case of significant viscous flow. This response is typical of a liquid or liquid-like behavior of a viscoelastic solid (e.g., Irgens, 2008). A similar response can also be seen in Fig. 6.1 at the tertiary creep stage for polymers that exhibit significant viscous flow under a sustained load at long times.

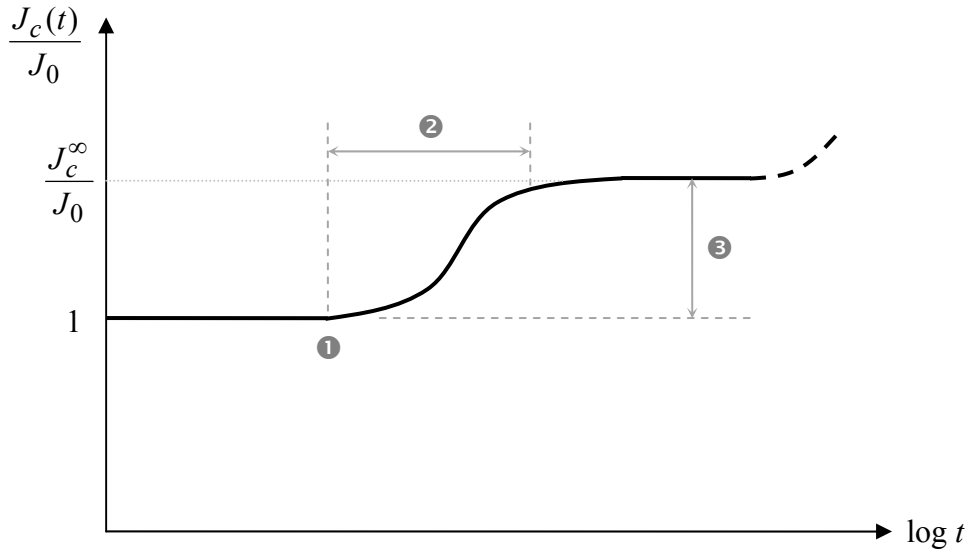

Fig. 6.2 Compliance changing with time in a creep test. Solid dashed line shows the fluidic response (viscous flow) of a viscoelastic solid.

Creep response is also affected by the orientation of the polymer chains. The chain orientation in a specific direction can be achieved via a suitable manufacturing process. For example, for the para-aramid fibers, the polymer chains get spontaneously oriented in the particular direction at which the fibers are spun (Machalaba et al., 2000). Creep is smaller in the direction parallel to the uniaxial orientation of the polymer chains than that in the perpendicular direction. This is attributed to the increased modulus in the direction parallel to the oriented chains in the para-aramid fibers. The increase in the modulus parallel to the direction of the orientation arises because the applied load mainly acts on the strong covalent bonds. At the right angles, the load mainly acts on the van der Waals forces between the molecules in the perpendicular orientation. The creep compliance is therefore small if the stretching is parallel to the direction of the uniaxially oriented chains.

6.4 Modeling of creep of polymers

Creep in polymers is a slow, continuous deformation under a constant uniaxial tensile load. The increment of the uniaxial strain during creep can be related to the constant uniaxial stress, σ_0, by

$$\varepsilon(t) = J_c(t) \cdot \sigma_0 \tag{6.2}$$

where $J_c(t)$ is the creep compliance to be determined from experiments. Eq. (6.2) is applicable for linear viscoelastic materials. There are several approaches to modeling the creep response of viscoelastic polymers, which include purely empirical methods, linear differential or integral operator methods and rheological modeling techniques.

Empirical equations for creep such as the power law relation of the forms (Lai and Findley, 1973)

$$\varepsilon(\sigma, t) = k\sigma^p t^m , \tag{6.3}$$

and

$$\varepsilon(t) = \left(A + Bt^n \right) \cdot \sigma_0 \tag{6.4}$$

have been satisfactorily used to represent both the primary and secondary creep ranges schematically shown in Fig. 6.1. k, p, and m in Eq. (6.3) and A, B and n in Eq. (6.4) are constants. Creep behavior in which the creep rate approaches zero at longer times (see the dashed line in Fig. 6.1) may be represented by

$$\varepsilon = \varepsilon_0 + A \log t \tag{6.5}$$

where ε_0 and A are functions of stress, temperature and material (Findley et al., 1976).

Similar empirical relations can be found in Vleeshouwers et al. (1989), Huang and Gibson (1991), Kromm et al. (2003), Kolarik and Pegoretti (2006) and Fallatah et al. (2007). These empirical expressions were developed to fit experimental data obtained under constant applied load (or stress).

In these empirical equations, the current strain value seemingly depends on the current time only. The actual creep behavior of a viscoelastic polymer is affected by the magnitude and chronology (temporal sequence) of stresses and strains in the time history of the material (e.g., Grzywinski and Woodford, 1995; Baltussen and Northolt, 2001; Urbelis et al., 2004). The creep function thus depends on all of the values of the applied constant stresses and the strains in the past, and not just the instantaneous values of these variables. In regard of this time-dependency of the creep response, the integral operator representation and the linear differential operator method are considered more appropriate. The creep function during a creep experiment with any number of step-like increments in load can be represented by a hereditary integral (Findley et al., 1976):

$$\varepsilon(t) = \int_0^t J_i(t-\xi_i)\frac{\partial\sigma}{\partial\xi_i}\mathrm{d}\xi_i \tag{6.6}$$

where ξ_i corresponds to an arbitrary time between 0 and t when the i-th step-load is applied. In this representation, the creep function is approximately the sum of a series of step functions that correspond to a series of step-loads. The kernel function of the integral, $J_i(t-\xi_i)$ is a memory function that evokes the stress history dependence of strain, which needs to be determined from experimental data.

This integral operator approach can be mathematically intricate (e.g., Schapery, 1965). Another widely used approach to modeling linear viscoelastic polymers is the linear differential operator method as described in Chapter I (see Eqs. (1.1) and (1.2)). These equations are repeated here to facilitate the forthcoming discussion. As mentioned in Chapter I, the linear differential operator method is summarized as

$$P\sigma = Q\varepsilon \quad . \tag{6.7}$$

Eq. (6.7) could be used to express the stress-strain relation of a linear viscoelastic polymer under a constant applied stress as in the case of creep. In Eq. (6.7), P and Q represent a series of linear time-derivative operators and are defined as follows:

$$P = \sum_{m=0}^{M} p_m \frac{d^m}{dt^m} \quad , \quad Q = \sum_{n=0}^{N} q_n \frac{d^n}{dt^n} \quad . \tag{6.8a,b}$$

Representation of the creep function of a specific viscoelastic material can be modeled by a proper selection of the number of terms of the series given by Eqs. (6.8a,b). The resulting differential equation can otherwise be derived from rheological models. Specifically, the form of the time-dependence of $J_c(t)$ can be replicated explicitly by rheological model with a sufficient number of elastic and viscous elements (Park, 2001). In this case, the coefficients p_m and q_n given in Eqs. (6.8a,b) will comprise the stiffness constants of the springs and viscosity constants of the dashpots. The use of rheological models also has the advantage of correlating the rheological parameters to the micro-mechanisms associated with different molecular processes that govern the

time-dependent viscoelastic response (Ferry, 1980). However, this correlation has to be made judiciously based on established theories and experimental evidences.

The mechanical response of a linearly behaving viscoelastic polymer to a constant applied force can be categorized as elastic, delayed elastic, or viscous flow. The elastic response is time-independent and reversible, while the viscous flow is time-dependent and irreversible. The former can be represented by a spring, whereas the latter can be characterized by a dashpot. On the other hand, the delayed elastic response is time-dependent and reversible, which can be described by combining a spring and a dashpot that are either in series or in parallel.

Accordingly, creep of polymers can also be represented by using rheological (viscoelasticity) models consisting of Hookean springs and Newtonian dashpots. For example, the four-element Burgers model (see Fig. 4.9 or Table 5.1) has been employed for the study of creep responses of different polymers (Ferry 1980; Chen at al., 1995; Yang et al., 2006). The three-element GKV model, which is also known as the Zener model, was utilized to study the creep behavior of a thin elastomeric membrane in (Ju and Liu, 2002). It is to be noted that the Zener model is equivalent to the $GM^{n=1}$ model or the Wiechert model (see Section 3.7.3). A generalized Kelvin-Voigt model with n Kelvin-Voigt (KV) elements and a free spring positioned in series to the KV elements was used to model the creep and creep recovery behavior of textile fabrics in (Urbelis et al., 2005).

The fitting of a rheological model to the time-domain experimental data involves identification and optimization of values of the model parameters, including stiffness

constants of the springs, K_i, and viscosity constants of the dashpots, η_i. As mentioned earlier, these parameters often directly contribute to the material function (e.g., $J_c(t)$) via the coefficients p_m and q_n given in Eqs. (6.8a,b). The retardation times, τ_i, which is defines in Section 6.2, are also related to K_i and η_i in a rheological model by

$$\tau_i = \frac{\eta_i}{K_i} . \tag{6.9}$$

Procedures to determine the values of the parameters are principally based on the least squared method (e.g., Schapery, 1961).

6.5 Experimental results

The specimens used here are made from a natural rubber (NR) coated Twaron CT709® plain-weave fabric. The uniaxial creep tests were performed at the room temperature and humidity (i.e., 25 °C and 50%, respectively) based on the ASTM D4964 – 96 (2008-e1) standard. The tests were conducted using a servo-hydraulic MTS 810™ tensile testing machine (see Fig. 6.3). This system was digitally controlled by the TestWorks®4 software. An extensometer (MTS 632.12B-50) was used to measure the displacement of each specimen during loading. A tare pre-load of 1 ~ 2 N was applied to straighten the coated fabric specimen.

Fig. 6.3 Experimental set-up for the creep test.

The ultimate tensile stress (UTS) of the composite is determined to be 127.60 MPa at a strain rate of 0.01 s^{-1} (see Table 4.5). A constant applied stress of 30 MPa, which is 23.5% of the UTS, is adopted in the present study to ensure that the applied stress is well below the tensile strength of the composite as per the ASTM standard requirement. The cross-sectional area of the composite specimen is 25 mm^2. The *force* corresponding to the 30-MPa *stress* is about 750 N. In terms of *mass* (for a constant *load*), this *force* can be approximately produced by a 76.5 kg deadweight. From Fig. 4.7, the strain corresponding to 30 MPa is roughly 4 %. Based on the gage length of 50 mm, the elongation would then be 2 mm. Under a constant weight of about 76.5 kg for one hour (3600 s), a strain greater than 4 % would be possible. In order to account for this, an upper limit of strain of was taken to be 8 %, which doubles the expected strain under the weight of 76.5 kg. The elongation at 8 % is 4 mm.

Two specimens designated as TC7 and TC8 were tested, and the average values were used in the analysis. The specimens were loaded at a constant loading rate of 50 N/s up to 750 N, which corresponds to a 30MPa 'initial' stress σ_0, assuming no changes in the cross-sectional dimensions. This stress is then held constant for 1 hour while the strain is measured as a function time (see Figs. 6.4(a) and 6.5(a)).

Results of the TC7 specimen

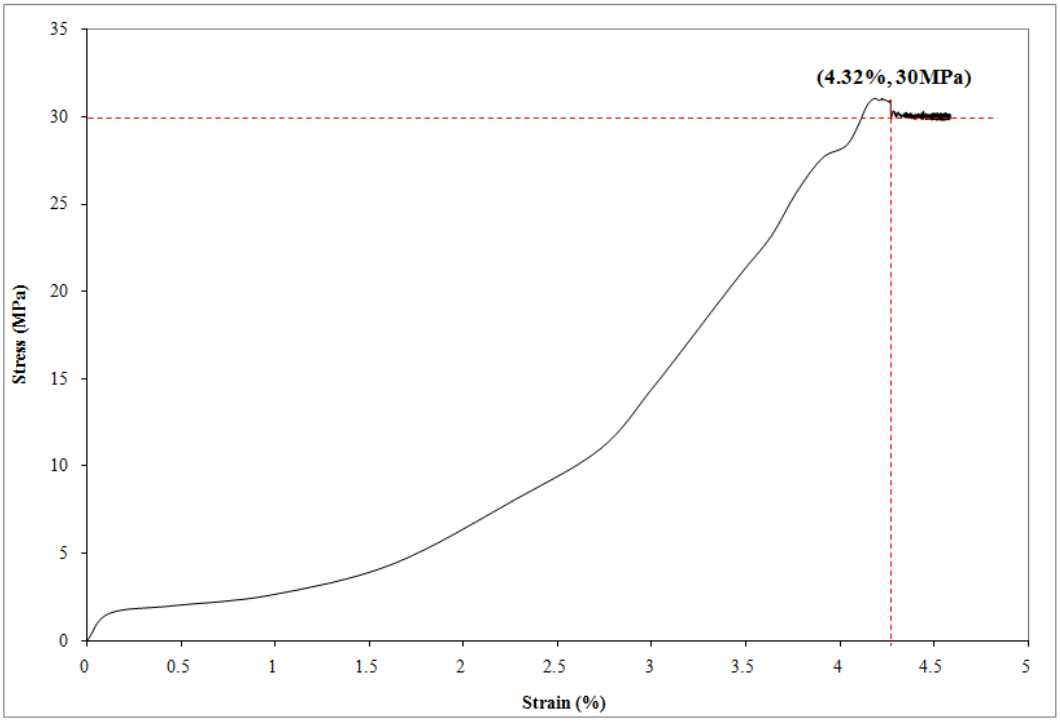

Fig. 6.4(a) Stress-strain plot of specimen TC7 at a loading rate of 50 N/s.

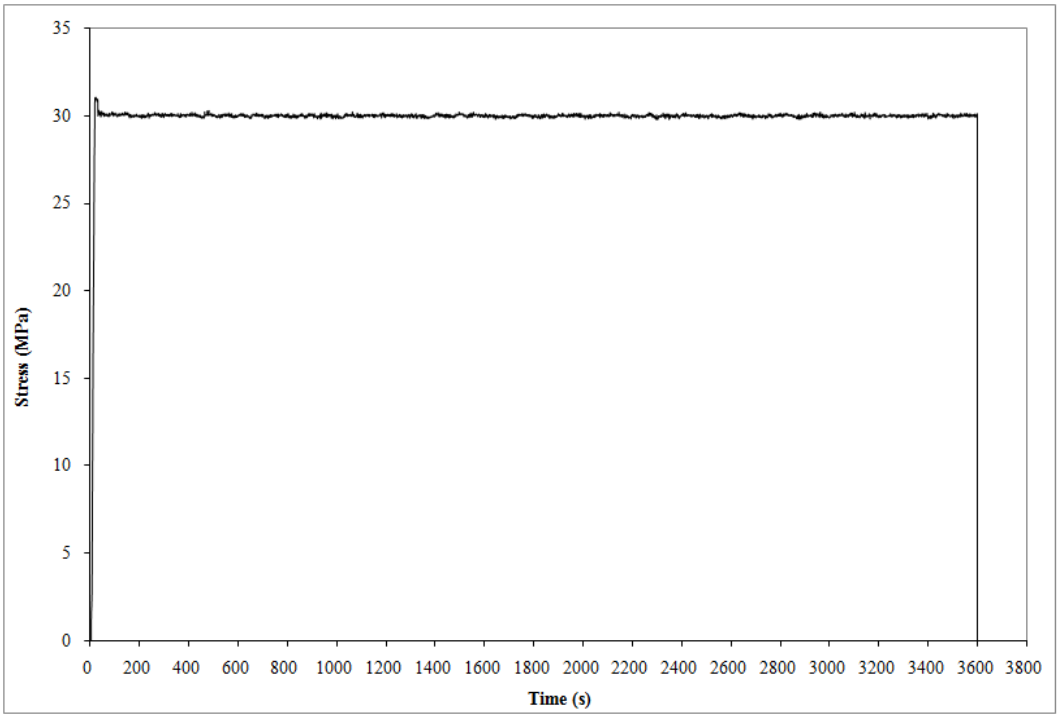

Fig. 6.4(b) Step-stress applied to the TC7 specimen.

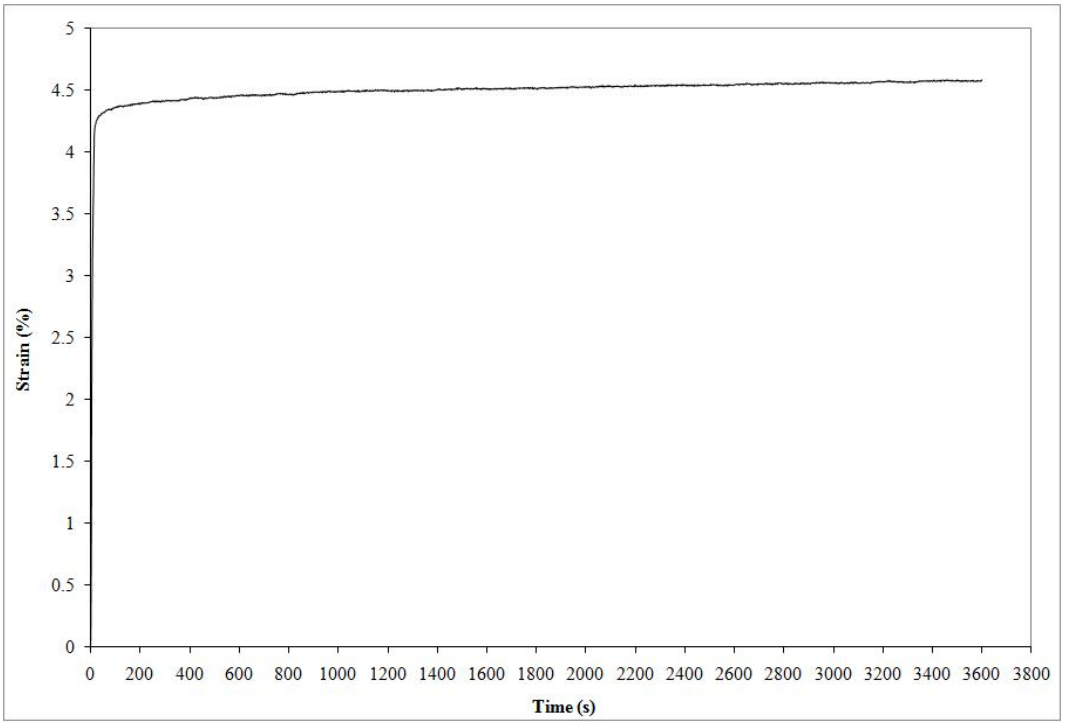

Fig. 6.4(c) Complete strain history of specimen TC7.

Results of the TC8 specimen

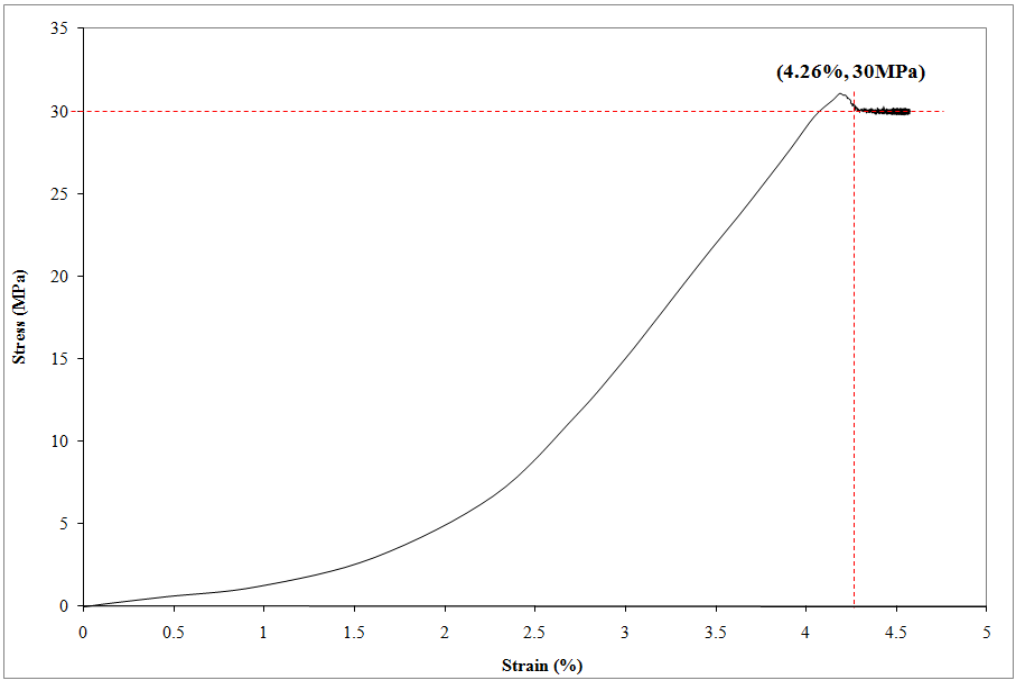

Fig. 6.5(a) Stress-strain plot of specimen TC8 at a loading rate of 50 N/s.

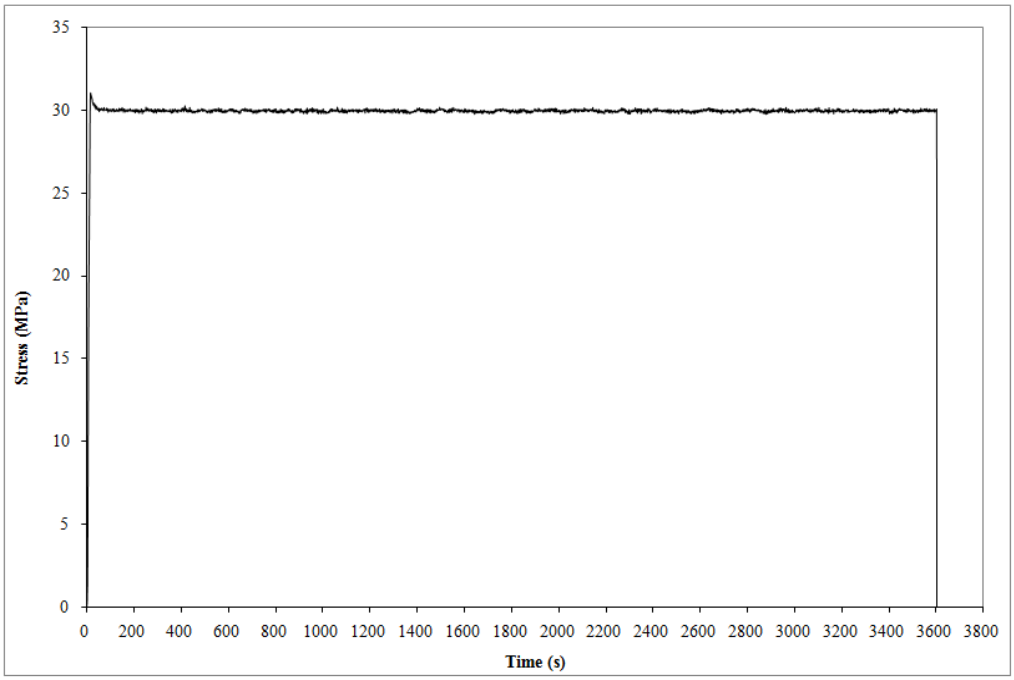

Fig. 6.5(b) Step-stress applied to the TC8 specimen.

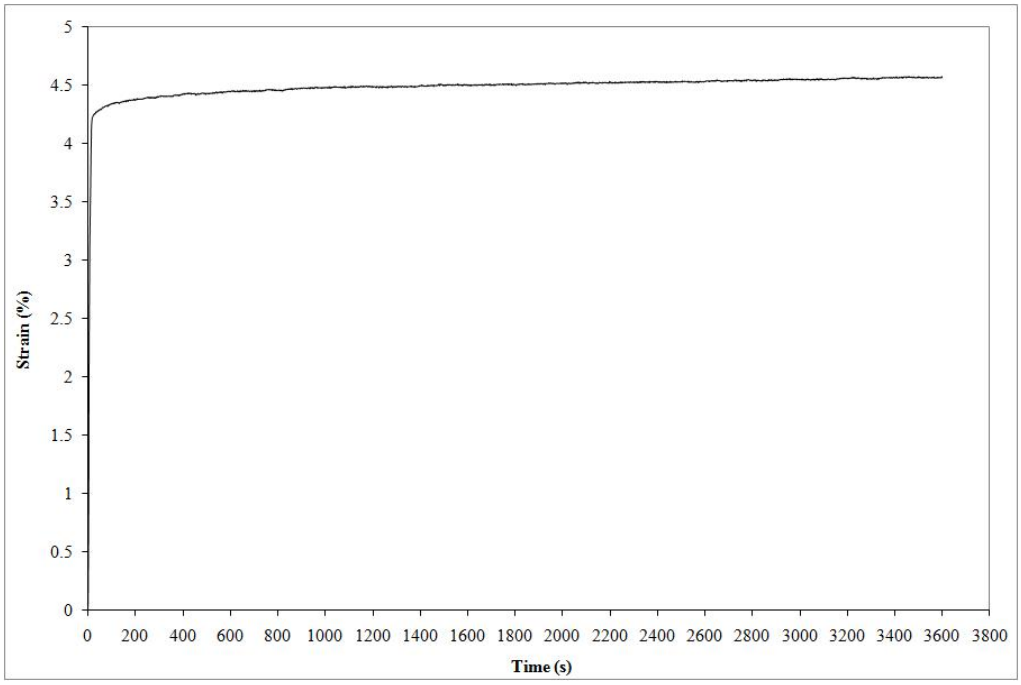

Fig. 6.5(c) Complete strain history of specimen TC8.

Table 6.1 shows the experimental results from both the specimens. The 'initial strain' in Table 6.1 refers to the value of strain at the beginning of the creep, i.e., just after the intended constant stress is reached. Final strain is the value of strain at the end of the test duration, i.e., at 3600 s. A 6.01% and 7.04% increase in strain during the test was computed for specimens TC7 and TC8, respectively. The average of the absolute difference in strain for both the specimens is 0.0028. The experimentally determined creep response curve of the Twaron®/NR composite is shown in Fig 6.6.

Table 6.1
Experimental data from the specimens tested.

Specimen ID	Constant applied stress, σ_0 (MPa)	Initial strain, ε_0 (%)	Final strain, ε_f (%)	Absolute difference in strain (%)	Percentage increase in strain (%)
TC7	30	4.32	4.57	0.26	6.01
TC8		4.26	4.55	0.30	7.04

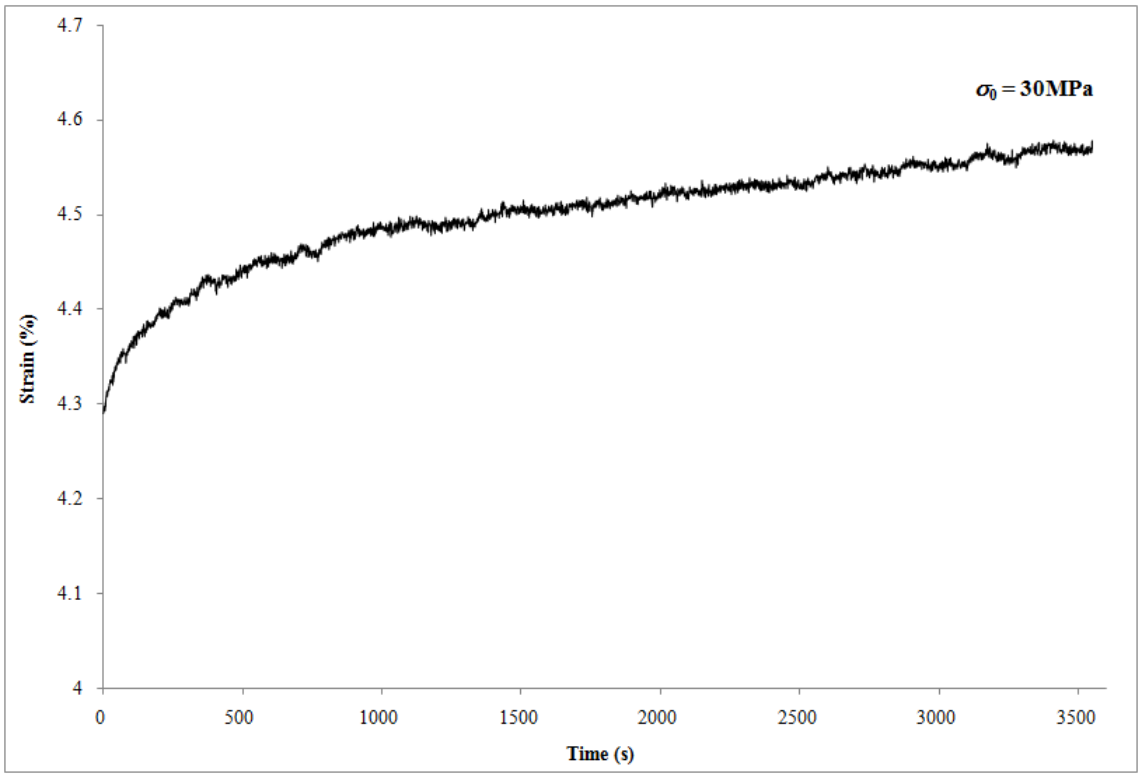

Fig. 6.6 Strain as a function time, under $\sigma_0 = 30$ MPa.

The values of strain and other creep properties used here and in the following sections are the averages of those measured from the TC7 and TC8 specimens. The initial strain, ε_o, corresponding to the constant applied stress, σ_0 (≡ 30 MPa), is 4.29%. The creep test reveals that the strain started to grow exponentially from ε_0 to 4.48% in

about 1000 s and continued to increase approximately linearly with time up to the end of the test duration. The initial exponential growth signifies the primary creep stage discussed in Section 6.3 (see Fig. 6.1). The average strain rate ($\dot{\varepsilon}$) during this stage is 0.00019 % s^{-1}. The linear increment of the strain after 1000 s that occurred more slowly at an average $\dot{\varepsilon}$ of 0.00003 % s^{-1} is characteristic of the secondary creep stage. Thus, the primary creep proceeded at a rate that is one order of magnitude greater than that for the secondary creep. The final strain (i.e., ε_f) recorded at 3600 s is 4.56%. Based on the definition of τ_c provided in Section 6.2, the time required for the specimen to deform to 63.21% of ε_f ($\equiv$ 4.46%) is $\tau_{c,exp}$ = 673.9 s. No apparent tertiary stage was observed during the test duration.

The creep response of the Twaron®/NR composite observed here is, to an extent, comparable with the creep behavior of a crosslinked or a crystalline polymer discussed in Section 6.3. The experimentally-determined creep response and the rate at which it occurs can be attributed to the microstructural features of the composite. At this juncture, it will be helpful to call upon the molecular and microstructural descriptions of the constituents of the composite based on which the results presented in Fig. 6.6 will be further discussed.

The Twaron®/NR composite is composed of the Twaron® fabric and the vulcanized natural rubber (NR). The Twaron® fiber, which makes up the fabric, is a semi-crystalline aramid fiber with para-oriented phenylene segments (see Fig. 3.1). T_g of the para-aramid fiber is circa 573 K (Machalaba, 1999). At the room temperature (~ 300 K), the Twaron® fiber will be in the glassy state with a certain degree of crystallinity. At

this state, the reaction of the fiber to a sudden applied force is primarily elastic and is attributed to the rotational motion of short chain segments (see Section 6.3). Under the sustained applied force, the chain segments begin to diffuse in a Brownian motion toward a new equilibrium position. These reactions are time-dependent and have a contribution to the primary creep stage seen in Fig. 6.6. There are other factors pertinent to the Twaron® fiber that influence the magnitude and rate of the deformation at the primary and steady-state stages of the creep process.

On the molecular level, the para-aramid fiber is made of rigid molecular chains (with the stronger covalent bonds between monomers) that aggregate under the weaker van der Waals forces into ordered domains (Yang, 2000). A degree of crystallinity in the Twaron® fiber thus impedes the motion of the domains and contributes to the retardation of the creep process. Deformability of the fibers is also reduced by strong inter-chain interactions in the domains (e.g., Tarakanov et al., 1999; David et al., 2009a).

At the micro-scale, the para-aramid fibers in the two dimensional plain-weave Twaron® fabric are highly oriented in both the vertical and horizontal directions, i.e., parallel to the yarn directions (David et al., 2009b). The uniaxially applied force therefore should act in a direction parallel as well as perpendicular to the orientation of the fibers. As was mentioned in Section 6.3, resistance to deformation due to the applied force is greater along the direction of the fibers than that along the perpendicular orientation (see also Perepelkin et al., 2001). The small total creep strain of 0.27% (of the composite) measured during the 3600 s duration is, to a large extent, attributable to the restricted elongation of the fabric constituent along the direction of the applied force.

The molecular and microstructural features of the NR constituent and their influence on the creep process of the composite observed during the experiment are discussed next.

The NR constituent is an elastomeric material composed of long macromolecular polymer chains of randomly oriented molecules, which are connected by covalent bonds (see Fig. 4.1). The long chains are subject to entanglement and chemical cross-linking, which are the two features that pose restrictions on the mobility and related to the entropic (conformational) changes of the macromolecular chains (David et al., 2009b). These aspects affect the creep behavior of NR, especially its steady-state creep rate and that of the composite.

The number average molecular weight, M, of a typical para-aramid fiber is on the order of 10^5 (Kiya-Oglu et al., 1999) and that for the NR is in the range of 10^3 to 10^5 (Treloar, 2005). This comparison of M qualitatively indicates that the degree of chemical cross-linking in the NR constituent is higher than that in the Twaron® fibers. The vague secondary creep stage with a sluggish increment of $\dot{\varepsilon}$ shown in Fig. 6.6 may therefore by attributed largely to the local constraint to the molecular motion by the crosslinks and to the motion of the crosslinks themselves in the NR constituent. The small increase of ε at the steady-state creep that corresponds to the plateau region indicated by the thick dashed line in Fig. 6.1 is related to the motion of the local constraints (i.e., crosslinks) that inhibit chain mobility (e.g., Farlie, 1970). The slight levitation of the slope suggests that this motion increases slowly as a function of time. The crosslinks in the NR tend to make the creep response to stabilize to an almost constant strain at long times. The restoring force at long times can be attributed to the entropic effect, for which a

discussion can be found in Section 5.5 and in *Appendix D.1*. A brief discussion on the influence of the temperature of the NR constituent during experiment in relation to its T_g on the long time creep response of the Twaron®/NR composite is provided next.

The T_g of NR is 200.5 ± 0.5 K (Loadman, 1985). At the room temperature (~ 300 K), that is above T_g of NR the chemical crosslinks in the NR reduce the importance of viscous flow and enhance the elastic limits of the NR. The creep strain of a highly crosslinked elastomer therefore tends to reach a limiting value at a long time (e.g., Nielsen and Landel, 1994). The creep strain in the Twaron® constituent continues to increase over time due to its smaller degree of cross-linking. A higher degree of cross-linking in the NR constituent curbs the increment of ε and thereby reduces the $\dot{\varepsilon}$. The interplay of these slightly opposing effects would reduce the creep rate significantly but would not cause it to fall to zero completely, as is evident in Fig. 6.6.

6.6 Analysis of creep characteristics using viscoelasticity models

As pointed out in Section 6.4, different modeling techniques can be used to characterize the creep response of a viscoelastic material. In the present study, the linear differential operator method based on the spring-dashpot rheological models will be employed to represent the creep behavior discussed in the preceding section and to predict the longer time response of the Twaron®/NR composite. The creep response of the composite is initially simulated using three viscoelasticity models, which include the $GM^{n=1}$, $GM^{n=2}$ and four-parameter Burgers models developed in Chapter IV. The schematic of all the three models and their creep functions are given in Table 6.2. The

stiffness of a spring element (in Pa) and the viscosity constant of a dashpot element (in Pa·s) in these models are denoted by K and η, respectively. The numeric subscript in $GM^{n=1}$ or $GM^{n=2}$ denotes the element number in each model (see Table 6.2). The creep compliance of each model is the expression inside the parentheses of the creep functions provided in Table 6.2. These expressions are consistent with the general relationship given in Eq. (6.2).

Table 6.2
Three viscoelasticity models considered for creep response.

One-term generalized Maxwell ($GM^{n=1}$) model

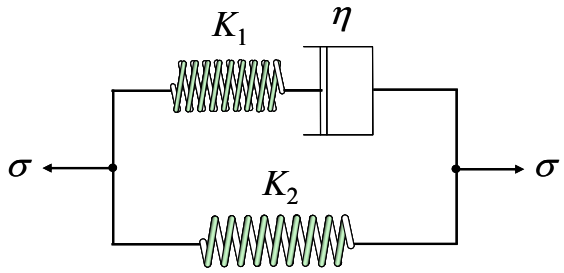

Creep function, $\varepsilon(t) = \left[\frac{1}{K_2} - \frac{K_1}{K_2(K_1 + K_2)} e^{-\frac{t}{\tau_{c1}}} \right] \sigma_0$

where retardation time, $\tau_{c1} = \frac{\eta(K_1 + K_2)}{K_1 K_2}$.

(see *Appendix A.3* for derivations)

Table 6.2 (*continued*)

Two-term generalized Maxwell ($GM^{n=2}$) model

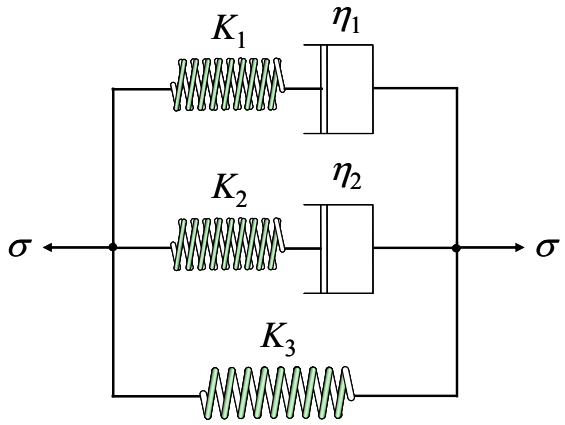

Creep function, $\varepsilon(t) = \left(\bar{K}_1 e^{-\psi_1 t} + \bar{K}_2 e^{-\psi_2 t} + \bar{K}_3 \right) \sigma_0$

where

$$\bar{K}_{1,2} = \frac{1}{\psi_1 - \psi_2} \left[\left[\pm \frac{1}{K_{eff}} \left(\frac{K_1}{\tau_{c21}} + \frac{K_2}{\tau_{c22}} \right) \mp \psi_{2,1} \right] J_0 \pm \bar{K}_3 \cdot \psi_{2,1} \right],$$

$$\bar{K}_3 = \frac{1}{K_3}, \quad K_{eff} = K_1 + K_2 + K_3,$$

$$\tau_{c21} = \frac{\eta_1}{K_1}, \quad \tau_{c22} = \frac{\eta_2}{K_2}$$

$$\psi_{1,2} = \frac{1}{2\eta_1\eta_2 \left(K_1 + K_2 + K_3 \right)} \left(\begin{array}{l} \left(K_1K_2\eta_1 + K_1K_2\eta_2 + K_1K_3\eta_2 + K_2K_3\eta_1 \right) \\ \mp \sqrt{\begin{array}{l} \left(K_1K_2\eta_1 \right)^2 + \left(K_1K_2 \right)^2 \eta_2 \left(2\eta_1 + \eta_2 \right) - 2K_1K_2K_3\eta_1\eta_2 \left(K_1 + K_2 + K_3 \right) \\ +2\left(K_1\eta_2 \right)^2 K_2K_3 + \left(K_1K_3\eta_2 \right)^2 + 2\left(K_2\eta_1 \right)^2 K_1K_3 + \left(K_2K_3\eta_1 \right)^2 \end{array}} \end{array} \right)$$

J_0 = initial creep compliance = ε_0/σ_0

(see *Appendix F.4* for derivations)

Table 6.2 (*continued*)

Burgers model

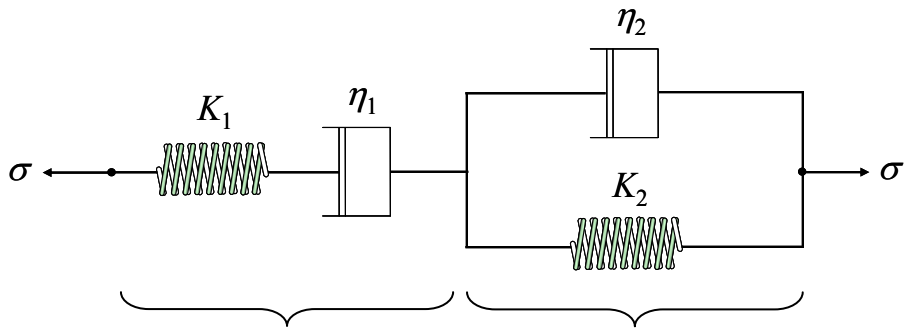

Creep function, $\varepsilon(t) = \left[\frac{1}{K_1} + \frac{1}{K_2}\left(1 - e^{-\frac{t}{\tau_B}}\right) + \frac{t}{\eta_1} \right] \sigma_0$

where retardation time, $\tau_B = \frac{\eta_2}{K_2}$.

(see *Appendix E.3* for derivations)

A technique similar to the collocation method of Schapery (1961) can be used to determine the values of the parameters. The following demonstration is intended for the GM$^{n=1}$ model. The time from when the creep response is measured is set to be zero, i.e., $t = 0 = t_0$. The retardation time τ is taken to be 1000 s. This value corresponds to the initial exponential growth of the creep strain, as observed during the experiment. The GM$^{n=1}$ model is a standard linear solid model (e.g., Arridge, 1975). Taking τ to be 1000 s and not as 673.9 s ($\equiv \tau_{c,exp}$) gives a greater Deborah number (see Eq. (1)) in qualitative

agreement with the experimental observation. That is, the composite behavior reflects more of a solid than a liquid under the constant applied stress for 3600 s. The value of the K_2 parameter in the GM$^{n=1}$ model is obtained by fitting its creep function to the equilibrium compliance, $J^{\infty} \equiv (K_2)^{-1} = \varepsilon^{\infty} / \sigma_0 = 1.52$ GPa^{-1} at $t \to \infty$. The equilibrium strain, ε^{∞}, at long times is taken to be 0.0456 ($\equiv \varepsilon_f$). The rationale behind taking $\varepsilon^{\infty} = \varepsilon_f$ is that the coefficient of the exponential term in the creep function of the GM$^{n=1}$ model involves the values of K_1 and K_2. The magnitude of the value of K_2 is on the order of 10^8. This resulting coefficient when multiplied by the exponential value at $t = 3600$ s with $\tau = 1000$ s makes the second term in the creep function negligibly small. The value of K_1 is then optimized using the 'fminunc' optimization routine in Matlab® Optimization Toolbox™ 4.3 (see Appendix C) to obtain a best fit to the experimental data.

The procedure of parameter identification for the GM$^{n=2}$ model and the Burgers model is automated using the 'fminunc' optimization algorithm. Predictions of the creep strain at every instant t_i using the creep functions of the models given in Table 6.2 are compared to the experimental data at that time, and the values of the model parameters are optimized by minimizing the least squares error of an objective function (see Appendix C). The optimized values of the parameters of the models presented in Table 6.2 are listed in Table 6.3.

Table 6.3
Values of the parameters for the three models compared in Table 6.2.

Model	K_1 **(Pa)**	K_2 **(Pa)**	K_3 **(Pa)**	η_1 **(or** η**) (Pa·s)**	η_2 **(Pa·s)**	τ_{c1} **(or** τ_{c21}**) (s)**	τ_{c22} **(or** τ_B**) (s)**
GM$^{n=1}$	4.12E+07	6.57E+08	–	3.90E+10	–	1005.9	–
GM$^{n=2}$	1.50E+09	4.60E+11	6.56E+08	8.65E+11	8.00E+12	578.0	17.4
Burgers	7.00E+08	1.11E+10	–	3.30E+14	3.70E+12	–	333.3

The creep response curves obtained from the three models given in Table 6.2 using the parameter values listed in Table 6.3 are shown in Fig. 6.7. As can be seen from Fig. 6.7, all the three models provide a comparable trend of creep strain increasing as a function of time. The initial exponential increase of the strain as predicted by all the models corresponds to the primary creep stage that spans about 1000 s (see Figs. 6.1 and 6.7).

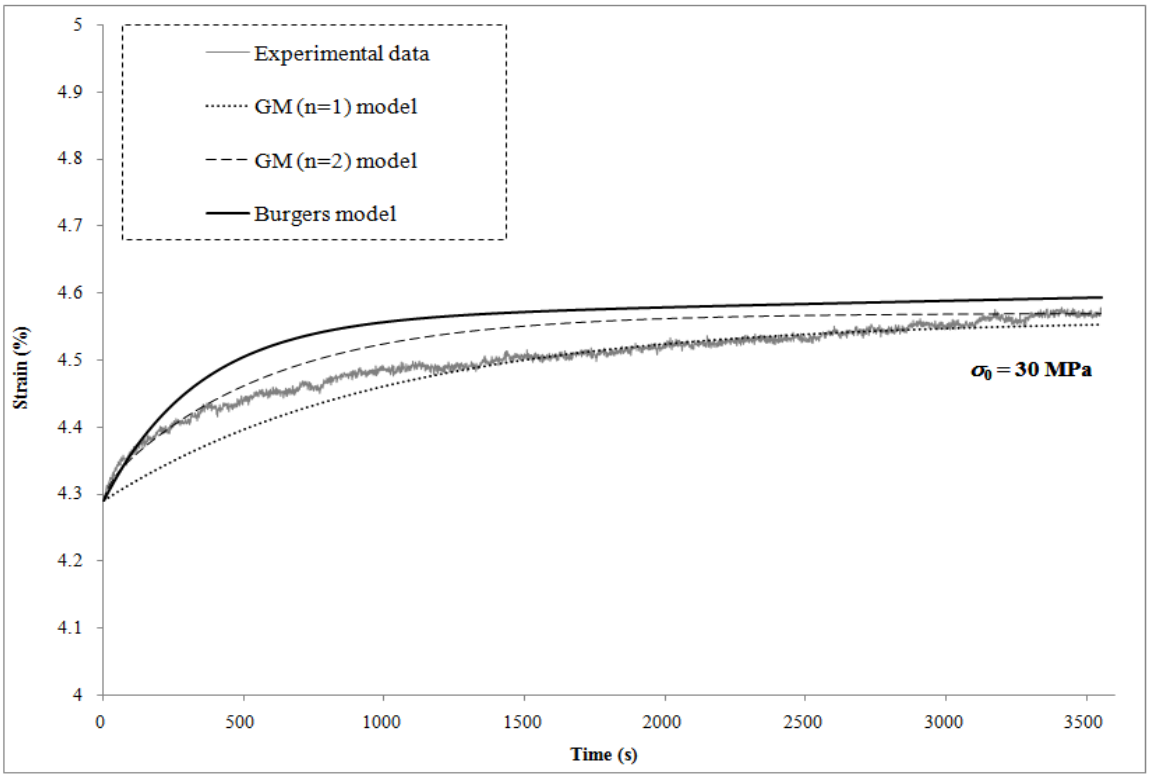

Fig. 6.7 Creep response curves obtained from the three different models and their comparison with the experimental data.

The overall trends predicted by the GM$^{n=1}$ and GM$^{n=2}$ models is the same, i.e., an initial exponential increase that is followed by an asymptotic increment of the strain to an equilibrium level as time progresses, albeit at different creep rates. The viscoelastic responses seen here imply a solid-like behavior of the composite under a constant stress (e.g., Ward and Sweeney, 2004).

It is evident from Fig. 6.7 that the predictions of strain values by the GM$^{n=1}$ model throughout the primary creep time span are poor compared to those by the GM$^{n=2}$ model. However, the GM$^{n=1}$ model provides good predictions at the secondary creep stage from $t \approx 1250$ s. The equilibrium strain predicted by the GM$^{n=1}$ model is 4.56%

(attained at t = 2800 s) and that by the $GM^{n=2}$ model is 4.57% (attained at t = 1500 s). Also, Fig. 6.7 shows that the strain–time curve of the $GM^{n=1}$ model bends at a slower rate to an equilibrium level than that of the $GM^{n=2}$ model. These observations can be related to the collective response of the rheological elements, and the quantity and value(s) of the characteristic retardation time(s) of the two rheological models, as will be discussed next.

The application of a constant stress at t_0 causes the springs in the $GM^{n=1}$ and $GM^{n=2}$ models to elongate instantaneously. The linear elastic responses of the springs are followed by delayed elasticity due to the time-dependent deformations of the springs together with the dashpot(s) in the models as time increases. As mentioned in Section 6.4, the combination of the elastic (spring) and viscous (dashpot) entities in the Maxwell element(s) describes the viscoelastic response. The contributions of the viscoelastic components of the $GM^{n=1}$ and $GM^{n=2}$ models, given respectively by the second and first two exponential terms of the corresponding creep compliance functions, to the strain increment under a constant applied stress reduce with the passage of time. At long times, the exponential terms become insignificant and the remaining significant term in each model is the total elastic contribution by the free springs, i.e., K_2 and K_3 in the $GM^{n=1}$ and $GM^{n=2}$ models, respectively. These collective effects of the model parameters lead to the overall initial exponential increase of the creep strain and the subsequent elastic plateau predicted by both the models. The discrepancies in the accuracy of estimation by these two models are explained next.

The better predictability of the GM$^{n=2}$ model than the GM$^{n=1}$ model at the primary creep stage can be ascribed to the fact that the former involves two discrete τ_c while the latter has just one (see Table 6.2). It was mentioned in Section 6.2 that the micro-mechanisms that govern different molecular processes associated with the creep response of a viscoelastic polymer can be characterized by retardation times. This correlation of distinct mechanisms to discrete retardation times is even more indispensable during the initial stage of the creep when more than one molecular process start to act together (e.g., Ericksen, 1985; Yang et al., 2006). The GM$^{n=2}$ model with two discrete τ_c is therefore able to represent more micro-mechanisms associated with the experimentally observed creep than the GM$^{n=1}$ model with a single retardation time. The optimized value of τ_{c1} for the GM$^{n=1}$ model is 1005.9 s (see Table 6.3), which indicates that it takes longer to reach ε_f = 63.21% and hence the creep rate is smaller.

The Burgers model also gives a trend similar to that by the GM$^{n=1}$ and GM$^{n=2}$ models. However, the asymptotic stabilization of strain due to the retarded elasticity term (i.e., second term) of the creep compliance function is accompanied by a minimal but steady increase of strain with time. This can be attributed to the third term (i.e., t/η_1) of the creep compliance function of the Burgers model that expresses the viscous effect (see Table 6.2 and *Appendix E.3*). This term (and thereby the effect) is due to the free dashpot in the Maxwell element in the Burgers model and gives rise to a component of the creep function that depends linearly on time.

The experimentally determined initial creep rate, $\dot{\varepsilon}_0$, is 0.001% s^{-1}. The value of $\dot{\varepsilon}_0$ predicted by the GM$^{n=1}$ is 0.0002% s^{-1} and that by both the GM$^{n=2}$ and the Burgers

models is 0.00098% s^{-1}. Thus, the value of $\dot{\varepsilon}_0$ computed using the $GM^{n=2}$ and the Burgers models is closer to the measured value than to that calculated using the $GM^{n=1}$ model. Furthermore, the strains estimated by the $GM^{n=2}$ model are closer to the experimental data up to 336 s than that forecasted by the Burgers model, which is accurate until only 112 s.

It is observed from Fig. 6.7 and is clear from the preceding discussions that the $GM^{n=2}$ and the Burgers models are capable of predicting the initial, short-duration exponential increase of strain at $t < 336$ s. The predictions of the models after this duration, however, are found to be inaccurate, with both models overestimating the strain values. In contrast, the $GM^{n=1}$ model provides a poor approximation to the strains during the primary creep but a good estimation at the secondary creep stage. These observations indicate that the three models do not consistently represent the creep response of the Twaron® fabric/NR composite throughout the different creep stages. It also has to be noted that applications involving relatively short loading times necessitate the consideration of the primary creep range (Findley, 1976). This motivates the use of the new para-rheological model that: (i) embodies the mechanical analogue of the para-aramid Twaron® fibers from which the fabric is made (see Section 3.3), and (ii) takes into account the elasticity of the NR constituent through the molecular theory of rubber elasticity (see Section 4.4), as in the case for the stress relaxation analysis presented in Chapter V. The para-rheological model for the case of creep analysis of the Twaron®/NR composite is presented next.

6.7 Para-rheological model for creep response

The GM$^{n=1}$, GM$^{n=2}$, and Burgers models are entirely rheological in the sense that they contain only springs and dashpots, which are the two basic types of rheological elements. The para-rheological model developed Section 4.8, which includes a stress network element in addition to springs and dashpots, is used here to characterize the creep behavior of the Twaron®/NR composite.

For a constant applied stress, with $\sigma = \sigma_0$ and $\dot{\sigma} = 0$, the para-rheological model gives a non-linear ordinary differential equation as follows (see *Appendix H.3* for derivations):

$$\frac{K_1}{\eta}\sigma_0 = \left(K_1 + K_2 + 3E_{NR}\right)\dot{\varepsilon} - 6E_{NR}\varepsilon\dot{\varepsilon} + \left(\frac{K_1}{\eta}\left(K_2 + 3E_{NR}\right)\right)\varepsilon \,. \tag{6.10}$$

In order to abridge the problem to a linear analysis, only the first term of the linearized $\dot{\hat{e}}$ in Eq. (H.7) (see Appendix H), i.e., $\dot{\hat{e}} \cong 3\dot{\varepsilon}$, need to be considered. This is an approximation to the time derivative of the strain measure $\hat{e}$ involved in the σ_λ-network element (see Fig. 4.8) and leads to the following linearized differential equation:

$$\frac{K_1}{\eta}\sigma_0 = \left(K_1 + K_2 + 3E_{NR}\right)\dot{\varepsilon} + \frac{K_1}{\eta}\left(K_2 + 3E_{NR}\right)\varepsilon \,. \tag{6.11}$$

Solutions of both Eq. (6.10) (non-linear) and Eq. (6.11) (linearized) are presented next.

6.7.1 Analytical solution of the non-linear differential equation

It can be shown that the analytical solution of Eq. (6.10), i.e., the creep function of the para-rheological model illustrated in Fig. 4.8, is (see *Appendix H.3*):

$$\tau_p \cdot \left[\Phi \ln\left(\frac{C_o - \varepsilon_0}{C_o - \varepsilon} \right) + \Psi \left(\varepsilon_0 - \varepsilon \right) \right] = t \,, \tag{6.12}$$

where

$$\tau_p = \frac{K_1}{\eta} \,, \quad C_o = \frac{\sigma_0}{K_2 + 3E_{NR}} \,, \tag{6.13a,b}$$

$$\Psi = \frac{6E_{NR}}{K_2 + 3E_{NR}} \,, \quad \Phi = 1 + \frac{K_1}{K_2 + 3E_{NR}} - \frac{\Psi}{K_2 + 3E_{NR}} \sigma_0 \,. \tag{6.13c,d}$$

In Eq. (6.13a-d), σ_o is the constant applied stress (= 30 MPa), τ_p is the retardation time, and C_o, Φ and Ψ are dimensionless constants whose values depend on the parameters K_1, K_2, E_{NR}, and σ_0. The creep function given by Eq. (6.12) is in an implicit form. That is, the desired solution of the strain ε as a function of time could not be directly obtained from Eq. (6.12). However, due to the unique relation between the strain and time during the creep process, Eq. (6.12) can be used to compute time t for each strain value The optimized values for the parameters of the para-rheological model are: K_1 = 4.5E+08 Pa, K_2 = 6.5E+08 Pa, E_{NR} = 1.0E+06 Pa, and η = 2.9E+11 Pa·s. Using these values in Eqs. (6.13a-d) yields τ_p = 632.6 s, C_o = 0.0457, Ψ = 0.009146, and Φ = 1.6835.

If the τ_p parameter is allowed to vary with time, i.e., $\tau_p(t)$, Eq. (6.12) can be rewritten as

$$\tau_p(t)\cdot\left[\Phi\ln\left(\frac{C_o-\varepsilon_0}{C_o-\varepsilon}\right)+\Psi\left(\varepsilon_0-\varepsilon\right)\right]=t\,, \tag{6.14}$$

where C_o = 0.0457, Φ = 1.6835 and Ψ = 0.009146, which are independent of time and have just been determined. The functional form of the variation of τ_p with time can be obtained by optimizing $\tau(t)$ in Eq.(6.14). Optimizing here refers to obtaining a range of values of τ_p corresponding to different time steps within the time domain of the creep test, (i.e., 0 < t < 3600 s), in order to attain the best fit of the model curve to the experimental data. A regularly spaced time steps of 250 s were used for first 1000 s during which the strain increases exponentially. The entire data to be fit is thus divided into segments corresponding to different time-dependent phases of the creep process.

6.7.2 Analytical solution of the linearized differential equation

It can be shown that the analytical solution of Eq. (6.11) is (see *Appendix H.4*):

$$\varepsilon(t)=\left(J_0\cdot e^{-\frac{t}{\tau_{pl}}}+J\cdot\left(1-e^{-\frac{t}{\tau_{pl}}}\right)\right)\sigma_0\,, \tag{6.15}$$

where

$$J_0=\frac{\varepsilon_0}{\sigma_0},\quad J=\frac{1}{K_2+3E_{NR}},\quad \tau_{pl}=\frac{\eta\left(K_1+K_2+3E_{NR}\right)}{K_1\left(K_2+3E_{NR}\right)}. \tag{6.16a-c}$$

Relations (6.16a) and (6.16c) represent the initial creep compliance and the characteristic retardation time obtained from the present solution, respectively. From Eq. (6.15), the creep compliance of the model based on this simplified analysis is given by

$$J_c(t) = J_0 \cdot e^{-\frac{t}{\tau_{pl}}} + J\left(1 - e^{-\frac{t}{\tau_{pl}}}\right). \tag{6.17}$$

Using the initial conditions ($\varepsilon_0 = 0.0429$ and $\sigma_0 = 30\text{MPa}$) and the parameter values identified earlier in Eqs. (6.16a-c) yields the creep function parameters as follows: $J_0 = 1.43\times10^{-9}$ Pa^{-1}, $J = 1.53\times10^{-9}$ Pa^{-1}, and $\tau_{pl} = 1069.9$ s.

6.7.3 Numerical results and discussion

Fig. 6.8 shows some numerical results obtained using the solutions of the non-linear and linearized differential equations derived in Section 6.7.2. The solution for Eq. (6.10) given by Eqs. (6.12) and (6.13a-d) are indicated as 'non-linear: single retardation time' and 'non-linear: multiple retardation times', respectively. Similarly, the numerical results of the solution in Eq. (6.15) for Eq. (6.11) is indicated as 'linearized differential equation' in Fig. 6.8.

The results reveals that the creep curve given by the solution of the linearized differential equation is close to that simulated by the GM$^{n=2}$ model. Also, the creep curve based on the solution of the non-linear differential equation with a single retardation time is close to that by the GM$^{n=1}$ model.

As shown in Fig. 6.8, the predictions of both the solutions for the non-linear (with a single τ_p) and the linearized differential equations are still inadequate. By optimizing $\tau_p(t)$ in Eq.(6.14) in order to improve the curve fit in the test duration, it was found that τ_p assumes the following form for the best fit (see Fig. I.2 in Appendix I):

$$\tau_p(t) = 3.1\times10^2 + 0.1t \ . \tag{6.18}$$

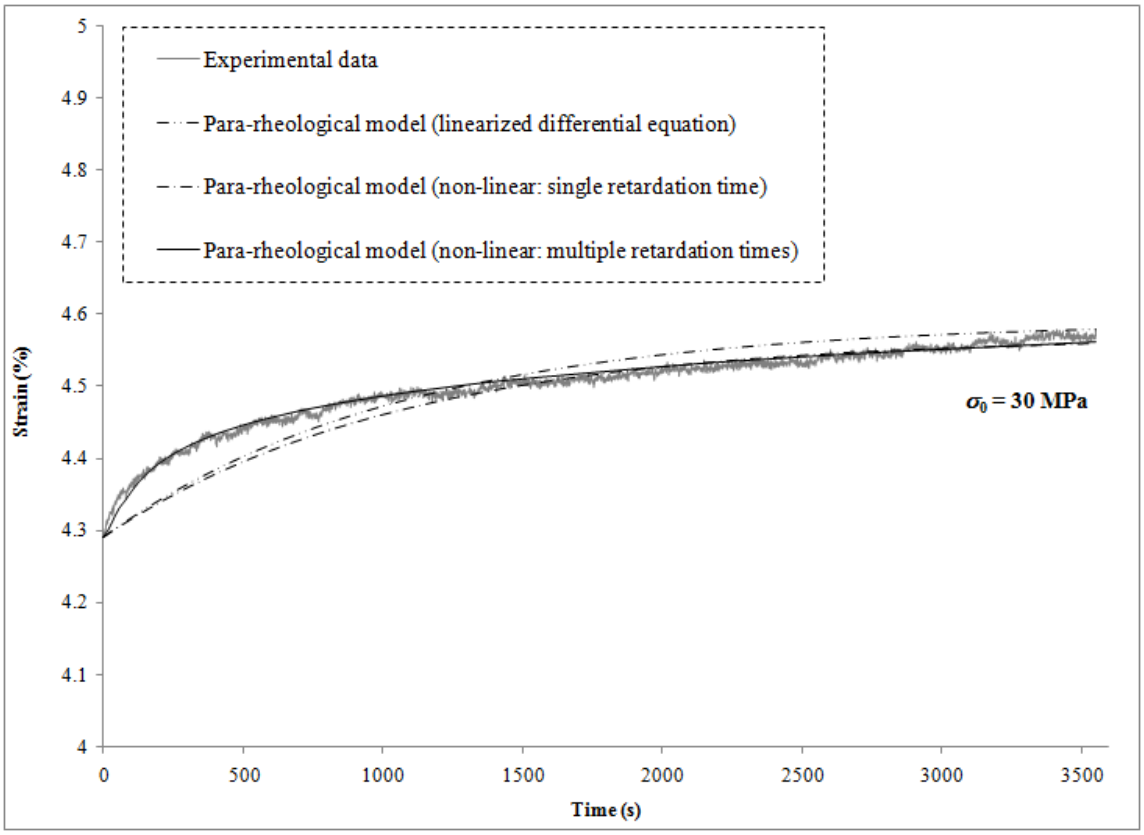

Fig. 6.8 Creep response curves using the para-rheological model compared with the experimental data.

The retardation spectrum (i.e., multiple τ_p) given by Eq. (6.18) in tandem with Eq. (6.14) provides excellent predictions as can be seen in Fig. 6.8. This finding indicates that the time-dependent response of the constituents requires the use of a suitable retardation spectrum with multiple numbers of τ_p. Thus, by allowing the characteristic retardation time to take the form of a spectrum (instead of one or two discrete values), the rates of micro-mechanisms associated with the creep response of the composite can be accounted for. This is in agreement with that observed in Section 6.6 using the other viscoelasticity models and also that found by Smith Jr. (2002).

Fig. 6.9 shows the viscosities of the composite predicted at different times during the creep process. The evolution of the viscosity of the composite is determined from the following relation (e.g., Menard, 2008):

$$\eta(t) = \frac{\sigma_0}{\dot{\varepsilon}(t)} \tag{6.19}$$

where the creep rate, $\dot{\varepsilon}(t)$, at different times are calculated from the non-linear analytical solution of the para-rheological model (see Eq. (H3.3) in *Appendix H.3*). Eq. (6.19) conjures the visualization of the composite as a single Newtonian dashpot whose viscosity changes with time. The typical value of viscosity of a viscoelastic solid is 10^{12} Pa·s (Lakes, 2009).

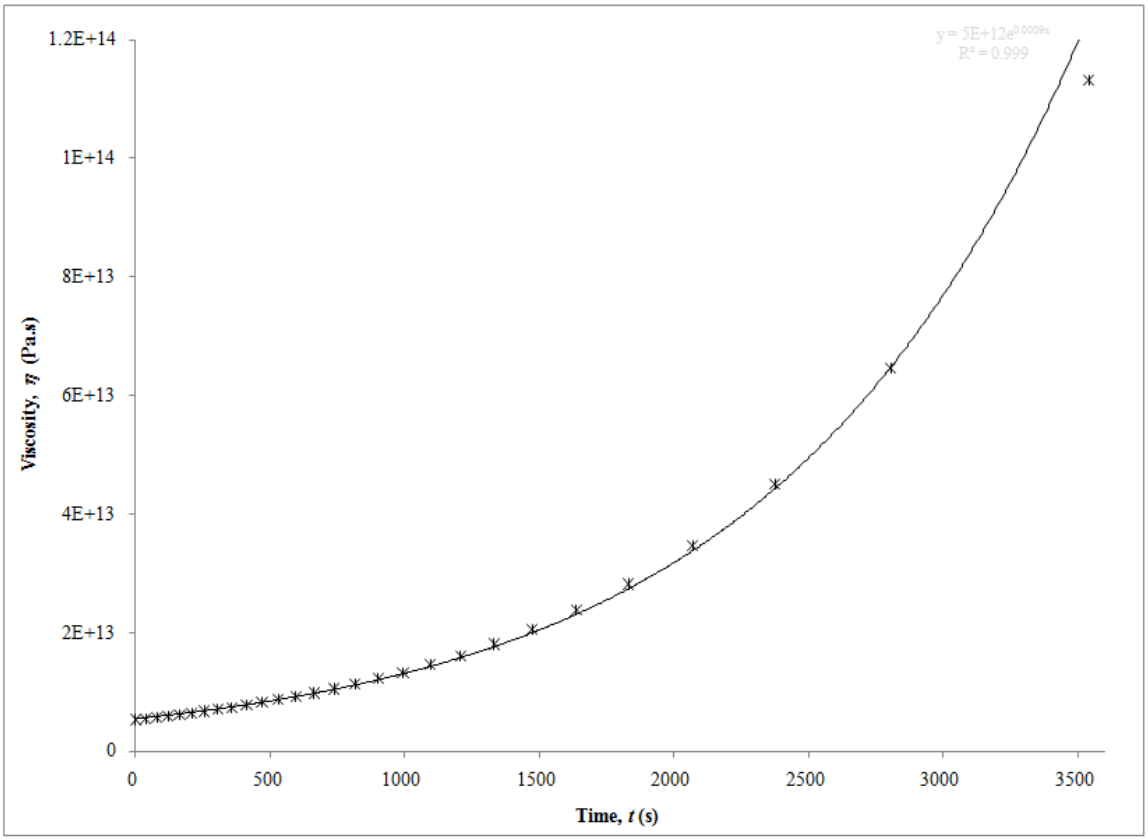

Fig. 6.9 Evolution of the viscosity of the Twaron®/NR composite predicted by the non-linear solution of the para-rheological model.

The exponential increase of the viscosity as time advances indicates the reduction of the number of crosslink points as more physical entanglements (temporary crosslinks) get disentangled under the constant applied force at long times. This observation is also consistent with the general observation made by Ferry (1980). That is, the molecular network structure of the constituents of the composite tends to undergo segmental rearrangements under a constant applied force as time advances. The increase of the viscosity also indicates the greater resistance of the composite to deformation at long

times, which is signified by the predictions of the para-rheological model (the non-linear solution with multiple τ_p).

6.8 Prediction of longer time response

The creep compliance functions and the corresponding coefficients of the three viscoelasticity and para-rheological models are tabulated in Table 6.4. The creep compliance functions are computed using the values of the coefficients given in Table 6.4. The experimentally determined compliance is simply the ratio of the creep strain to the constant applied stress, σ_0. Division of the creep compliance function with the initial compliance at $t = 0$ gives a dimensionless measure of the time-dependent compliance function that is independent of σ_0. The creep compliance ratio, denoted here as $\hat{J}_c(t)$ ($\equiv J_c(t)/J_0$), is therefore a time-dependent material function. This allows the extrapolation of the predicted creep compliance to times longer than the duration of experiment.

Table 6.4
Creep compliance function and related coefficients.

Model	**Creep compliance function,** $J_c(t)$	**Coefficients of** $J_c(t)$
GM$^{n=1}$	$\bar{K}_2\left(1-\bar{K}_1\right)e^{-\frac{t}{\tau_{c1}}}$	$\bar{K}_1=\dfrac{K_1}{K_1+K_2}=5.90\times10^{-2}$ $\bar{K}_2=1/K_2=1.52\ \times\ 10^{-9}\ \text{Pa}^{-1}$ $\tau_{c1}=\dfrac{\eta\left(K_1+K_2\right)}{K_1K_2}=1005.9\ \text{s}$
*GM$^{n=2}$	$\left[\bar{K}_1\ \ \bar{K}_2\right]\left[e^{-\psi_1 t}\ \ e^{-\psi_2 t}\right]^{\mathrm{T}}+\bar{K}_3$	$\bar{K}_1=-4.74\times10^{-2}\ \text{Pa}^{-1}$ $\bar{K}_2=-2.61\times10^{-3}\ \text{Pa}^{-1}$ $\bar{K}_3=1.52\times10^{-9}\ \text{Pa}^{-1}$ $\psi_1=7.36\times10^{-5}\ \text{s}^{-1}$ $\psi_2=1.92\times10^{-3}\ \text{s}^{-1}$
Burgers	$\bar{K}_1+\bar{K}_2\left(1-e^{-\frac{t}{\tau_B}}\right)+\bar{\eta}_1\cdot t$	$\bar{K}_1=1/K_1=1.43\times10^{-9}\ \text{Pa}^{-1}$ $\bar{K}_2=1/K_2=9.01\times10^{-11}\ \text{Pa}^{-1}$ $\bar{\eta}_1=1/\eta_1=3.03\times10^{-15}\ \left(\text{Pa}\cdot\text{s}\right)^{-1}$ $\tau_B=333\ \text{s}$
†Para-rheological (linearized differential equation)	$J_0e^{-\frac{t}{\tau}}+J\left(1-e^{-\frac{t}{\tau_{pl}}}\right)$	$J_0=1.43\times10^{-9}\ \text{Pa}^{-1}$ $J=1.53\times10^{-9}\ \text{Pa}^{-1}$ $\tau_{pl}=1069.9\ \text{s}$

*Refer to Table 6.2 for full expressions of the related coefficients. Standard matrix operation applies between the two matrices.
†See relations (6.16a-c) and subsequent definitions of the coefficients of the creep compliance.

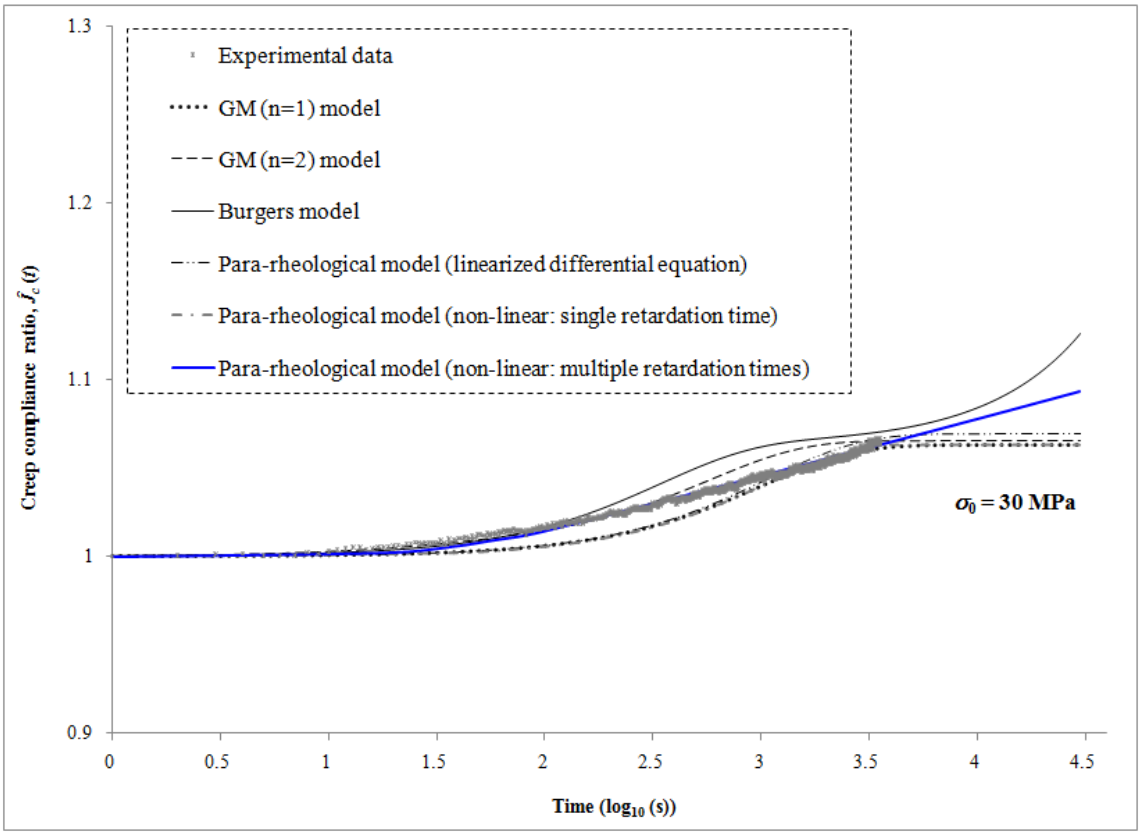

Fig. 6.10 The longer time creep response obtained from the viscoelasticity models and the different solutions of the para-rheological model. The curve for the GM$^{n=1}$ model overlies the curve for the para-rheological model (NLS).

Fig. 6.10 shows the experimental and predicted creep compliance ratio as a function of time. The three viscoelasticity models and the para-rheological model developed here are utilized to forecast $\hat{J}_c(t)$ in the period of 3600 s < t < 29,750 s after the test duration. The $\hat{J}_c(t)$ predicted by the Burgers model increases without limit around 25,000 s, which is indicative of a fluidic behavior (or viscous flow) of a polymeric solid at long times, as mentioned in Section 6.3 and discussed in Section 6.6. The trends predicted by the other three models are discussed next.

The noticeable initial increase of $\hat{J}_c(t)$ from unity occurs at 17 s according to the GM$^{n=1}$ model, which has single retardation time of 1005.9 s. A similar observation is made pertaining to the para-rheological model including the non-linear solution with a single τ_p (NLS) and the solution for the linearized differential equation (SLDE). The GM$^{n=2}$ model with τ_{c21} = 17 s and τ_{c22} = 578 s predicts an earlier discernible increase of $\hat{J}_c(t)$ at 7 s. The GM$^{n=1}$ model and the para-rheological model (NLS) both predict an equilibrium creep compliance ratio, $\hat{J}_\infty(t)$, of 1.063. The GM$^{n=2}$ model provides a slightly higher $\hat{J}_\infty(t)$ of 1.065, while the corresponding estimation of the para-rheological model (SLDE) is 1.069. The transition region between the unity and equilibrium plateau is somewhat broader for the GM$^{n=1}$ model and the para-rheological model (NLS) than that for the GM$^{n=2}$ model, with the rate of increment of $\hat{J}_c(t)$ being greater for the latter than for the former two. The transition of $\hat{J}_c(t)$ from unity to the equilibrium plateau for the para-rheological model (SLDE) occurs over the widest time span compared to the three models discussed above. However, the increment rate of $\hat{J}_c(t)$ for the para-rheological model (SLDE) is greater than that for the GM$^{n=1}$ model and for the para-rheological (NLS) model but smaller than that for the GM$^{n=2}$ model.

The observed responses by the GM$^{n=1}$ model and the para-rheological model (NLS) are consistent with the general creep behavior of a highly crosslinked polymer, i.e., the NR constituent in this study (see discussion related to Fig. 6.2 in Section 6.3).

On a similar note, the $GM^{n=2}$ model and the para-rheological model (SLDE) predict a trend that starts to deviate from the ideal response of a crosslinked polymer.

The predictions of $\hat{J}_c(t)$ by the $GM^{n=2}$ model are closer to those determined from the experimental data for most of the initial part of the transition region. This, together with the smaller breadth and taller height of the transition region of $\hat{J}_c(t)$ estimated using the $GM^{n=2}$ model than those predicted using the $GM^{n=1}$ model, provides a qualitative understanding of the benefit of an added Maxwell element in the $GM^{n=2}$ model. The added Maxwell element improves the predictability of the $GM^{n=2}$ model by providing the second retardation time to represent additional creep mechanism(s) of the constituents of the composite other than those related to the cross-linking in NR. This inference is parallel to that made in Section 5. The predictions of the para-rheological model (NLS) are discussed next.

$\hat{J}_c(t)$ estimated by the para-rheological model (non-linear solution along with a retardation spectrum) closely matches the experimentally determined values until t = 3600 s and continues to increase linearly with time. Also, the longer time trend predicted by the para-rheological model (non-linear solution: multiple τ_p) lies in between the typical creep response of a crosslinked polymer and a thermoplastic (e.g., Brinson and Brinson, 2008). This is an acceptable forecast grounded in the fact that the constituents of the current composite are of the thermosetting (NR) and thermoplastic (Twaron®) polymer types.

It is found here again that the use of a retardation spectrum, $\tau_p(t)$, instead of one or two discrete retardation times enhances the accountability of this solution for various time-dependent micro-mechanisms of the constituents during the creep process. Correspondingly, $\tau_p(t)$ indicates the evolution of the K_1 and η parameters with time (see Eq.(6.13a)). It was mentioned above that the GM$^{n=2}$ model could account for additional creep micro-mechanism(s) owing to an extra Maxwell element in that model compared with the GM$^{n=1}$ model. However, adding more Maxwell elements will render the mathematical analysis complex (e.g., Sebastian et al., 2008; Lakes, 2009). The experimentally identified retardation spectrum circumvents the long and cumbersome mathematical derivations that would transpire if more Maxwell elements were to be added.

6.9 Accuracy of the viscoelasticity and para-rheological models

The coefficient of determination (*COD*) represents the percentage of the experimental data that is closest to the model curves (see Section 4.7.3). The *COD* indicates the numerical accuracy of the results predicted by a model (relative to the measured data) without allusion to any explainable cause(s) for the model behavior. This measure is used here just for a quantitative comparison of the predictability of the para-rheological model developed in this chapter with that of the other viscoelasticity models. The *COD*, defined in Eq. (4.17), is given here again as

$$COD = 1 - \frac{1}{n}\left[\frac{\sum\left(\varepsilon_{exp} - \varepsilon_{mod\,el}\right)^2}{\sum\left(\varepsilon_{exp} - \bar{\varepsilon}\right)^2}\right] \times 100\% \ . \tag{6.20}$$

In Eq. (6.20), n is the total number of strain values each measured at every time instant during the experiment, $\bar{\varepsilon}$ is the mean strain computed from $\left(\sum_{i=1}^{n}\varepsilon_i\right)/n$, and ε_{exp} and ε_{model} denote the strain values measured during the experiment and predicted by a model at every time instant, respectively. The *COD* is calculated for the entire test duration of 3600 s, and for the $0 < t < 674$ s interval that corresponds to the experimentally determined characteristic retardation time ($\equiv \tau_{c,exp}$) during which most of the strain increment occurred (see Section 6.5). The n and $\bar{\varepsilon}$ corresponding to this time interval are 675 and 4.41%, respectively. Table 6.5 lists the values of the *COD* for all of the models and related solutions.

Table 6.5
Coefficient of determination (*COD*) of all models for the characteristic time domain and for the entire test duration.

Model		*COD*	
		$0 < t < 674$ s (Characteristic time)	$0 < t < 3600$s (Entire test duration)
$GM^{n=1}$		0.782	0.994
$GM^{n=2}$		0.975	0.989
Burgers		0.784	0.971
Para-rheological	Linearized differential equation	0.810	0.993
	Non-linear solution: single retardation time	0.783	0.994
	Non-linear solution: multiple retardation times	0.995	0.999

Fig. 6.11 shows the creep responses predicted by all the models and related solutions. The overall performance of the GM$^{n=1}$ model with a *COD* of 0.994 seems to be better than the GM$^{n=2}$ model but it fares poorly in the characteristic $\tau_{c,exp}$ domain where the latter outperformed the former (*COD* = 0.782). The Burgers model provides a trend comparable to the experimentally observed one but lacks the overall quantitative accuracy. Clearly, the predictions of the para-rheological model (non-linear solution: multiple τ_p) is more accurate than any of the other models and solutions at both in the $\tau_{c,exp}$ domain and for the entire test duration.

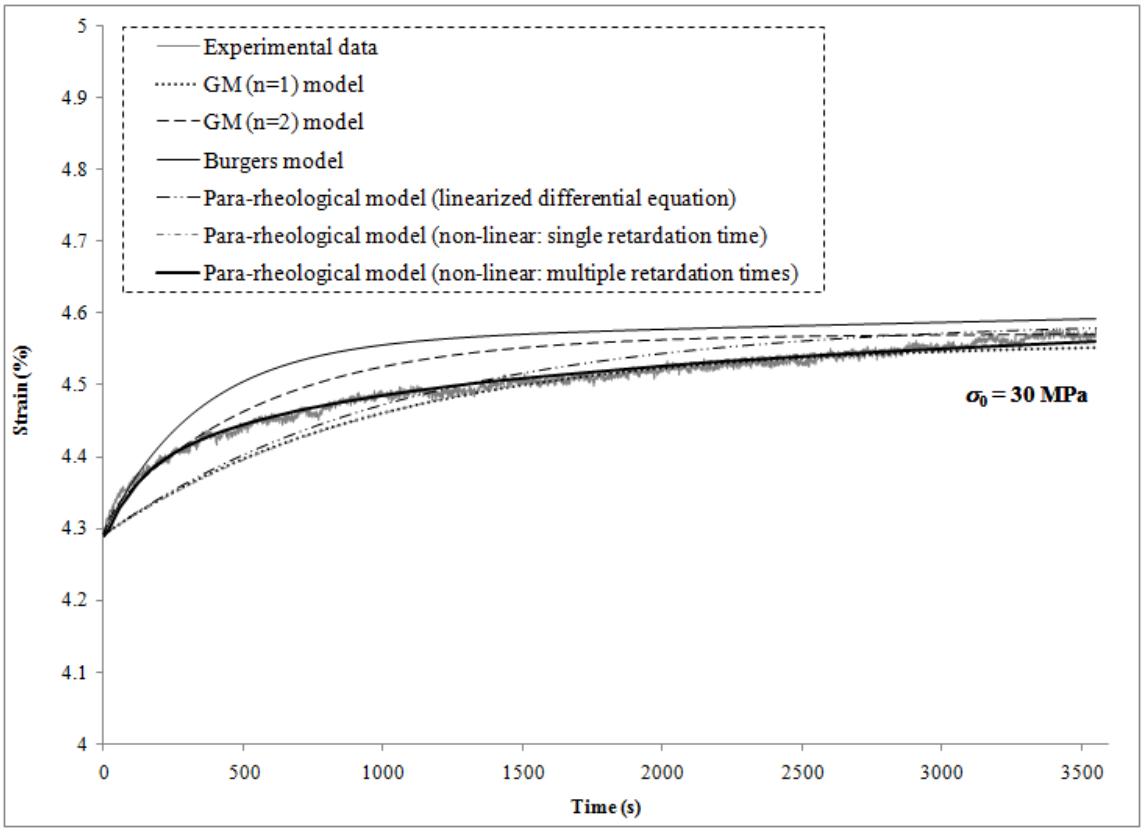

Fig. 6.11 Comparison of the creep response curves predicted by all the models (and solution types) considered in the present study with the experimental data.

6.10 Summary

The experimentally determined creep behavior of a Twaron CT709® fabric/natural rubber (NR) composite under a uniaxial constant stress is studied using two GM^n models (n, the number of Maxwell elements = 1, 2), the Burgers model and a newly developed para-rheological model. The new model utilizes a three-parameter element to represent the Twaron® fabric and the affine network based molecular theory of rubber elasticity to account for the deformation mechanisms of the NR constituent. The parameter values needed in each model to determine the creep compliance function and the characteristic retardation time (τ_c) are extracted from the experimental data via a curve fitting optimization procedure.

The experimental results show an initial exponential increase of strain (of 4.43%) in about 1000 s. Thereafter, the strain continues to increase approximately linearly with time until the end of the test at 3600 s. For a constant applied stress, the para-rheological model gives a non-linear ordinary differential equation (ODE) for which an implicit solution with a single characteristic retardation time, τ_p, is obtained. This solution is then modified by using a spectrum of retardation times, $\tau_p(t)$. The $\tau_p(t)$ spectrum is found to be useful in representing the causal micro-mechanisms, which are each characterized by a specific τ_c, responsible for the observed creep behavior of the constituents. A solution to the linearized ODE of the para-rheological model is also used to predict the creep response of the composite.

The numerical results show that the initial creep response of the composite is predicted well by the GM$^{n=2}$ model (with two τ_c), while the strain values at the

secondary creep stage are estimated more accurately by the $GM^{n=1}$ model (with one τ_c). The Burgers model predicts a trend comparable to the experimentally observed one but lacks the overall quantitative accuracy.

The results obtained from the implicit solution with a single τ_p and the linearized ODE solution (of the para-rheological model), both indicate a creep response between that of the $GM^{n=1}$ and $GM^{n=2}$ models. The implicit solution together with the $\tau_p(t)$ obtained from the para-rheological model is found to predict the creep behavior of the composite more accurately than any of the other models at both the primary and secondary creep stages. The qualitative usefulness of the para-rheological model in exploring the effect of different micro-mechanisms and molecular features on the creep response of the composite is demonstrated.

The newly developed para-rheological model predicts a longer time response that is closely associated with the trend showed by the experimental data. Based on this prediction, the creep deformation of the composite should continue to increase slowly with time in a linear fashion as time progresses.

CHAPTER VII

CONCLUSIONS

7.1 Summary of major findings

The constitutive behavior of a Twaron CT709® fabric/natural rubber (Twaron®/NR) composite at two constant strain rates of 0.00001 s^{-1} and 0.01 s^{-1} has been experimentally studied and theoretically predicted using different viscoelasticity models. An initial exploratory study indicated that a one-term generalized Maxwell ($GM^{n=1}$) model having three parameters is a simple and efficient model that is capable of simulating the viscoelastic behavior of the Twaron® fabric. Three viscoelasticity models (i.e., the four-parameter Burgers model, an iso-stress five-parameter model, and a two-term generalized Maxwell model ($GM^{n=2}$)) are then used to predict the constitutive behavior of the composite. The parameters involved in these models are extracted from experimental data.

It is found that these three fully rheological models have limited capabilities of predicting the viscoelastic behavior of the composite. The Burgers model and the five-parameter model are seen to underestimate the stress for large strain values at both the strain rates. A comparison of the results predicted using the $GM^{n=2}$ and five-parameter models with the experimental data indicate that the representation of the NR constituent by a Maxwell element is inadequate and that an iso-strain assumption enables the simulation of the actual loading condition.

In order to improve the accuracy of the predictions, a new para-rheological model is developed in the present study. This model utilizes the $GM^{n=1}$ model (as a unit) to represent the Twaron® fabric and the affine network based molecular theory of rubber elasticity to account for the deformation mechanisms of the NR constituent. The numerical results reveal that the stress values predicted by the newly developed para-rheological model agree very well with the experimental data. The new model also predicts the elastic moduli and the ultimate stress well at both the strain rates. Besides the constitutive behavior under constant strain rate loading, two other viscoelastic responses of the Twaron®/NR composite studied in this work are the stress relaxation and creep.

The stress relaxation of the Twaron®/NR composite under a uniaxial constant strain of 5% for 1 hour is experimentally studied. The experimental results show that the stress reduces with an initial exponential decay, which is continued by a linear reduction with time. The four models employed to study the stress relaxation response of the composite are the $GM^{n=1}$ model, the $GM^{n=2}$ model, the Burgers model, and the newly developed para-rheological model. The $GM^{n=1}$ model is used as a control model to study the effect of having an additional Maxwell element on the predictability of the resulting $GM^{n=2}$ model. It is found that the initial relaxation response of the composite is predicted fairly well by all the models. The addition of one more Maxwell element to the $GM^{n=1}$ model, which has a single characteristic relaxation time (τ) improves the predictability of the resulting $GM^{n=2}$ model by providing two distinct values of τ. The complexity of having more Maxwell elements (in order to obtain a spectrum of τ) is bartered with a

simple characteristic time function in the para-rheological model, which is found to greatly improve the predictions of the stress and the relaxation modulus of this model at all times. The characteristic time function represents the evolution of the K_1 and η parameters with time. The adjustment of these two parameters and their effects on τ is linked to the molecular stress relaxation mechanisms of the Twaron® fibers under the applied constant strain. The para-rheological model also predicts a long time response that is closely associated with the trend showed by the experimental data.

The creep behavior of the Twaron®/NR composite under a uniaxial constant applied stress of 30 MPa for 1 hour is experimentally studied. The three viscoelasticity models mentioned above and the para-rheological model are then used to characterize the stress relaxation behavior and predict the long time response of the composite. The experimental results show an initial exponential increase of strain with time, which is followed by a linear increment toward a plateau (i.e., without a pronounced secondary stage) in the time duration of the test. The numerical results show that the initial creep response of the composite is predicted relatively well by the $GM^{n=2}$ model (with two different values of characteristic retardation time, τ_c) while the strain values at the secondary creep stage is estimated more accurately by the $GM^{n=1}$ model (with one τ_c). The Burgers model predicts a trend comparable with the experimentally observed one but lacks the overall quantitative accuracy. For a constant applied stress, the para-rheological model gives a non-linear ordinary differential equation (ODE) for which an implicit solution with a single characteristic retardation time (τ_p) was obtained. This solution is then modified by using a spectrum of retardation times, $\tau_p(t)$. The $\tau_p(t)$

spectrum is found to be useful in representing the causal micro-mechanisms, each of which is characterized by a specific τ_c responsible for the observed creep behavior of the composite. A solution to the linearized ODE of the para-rheological model (with a single τ_c) predicts a creep response slightly better than that by the $GM^{n=1}$ model. The long time trend predicted by the para-rheological model (non-linear ODE solution with $\tau_p(t)$) lies between the typical creep response of a crosslinked polymer and a thermoplastic. The adequacy of this forecast is grounded on the fact that the constituents of the composite are of the thermosetting (NR) and thermoplastic (Twaron®) polymers.

The ability of the newly developed para-rheological model in simulating the viscoelastic behavior of the Twaron®/NR composite and the fidelity of this model in accounting for the deformation mechanisms of the constituents of the composite is demonstrated in this study. The fundamental viscoelastic behaviors of the novel Twaron®/NR composite has been investigated and characterized. It is anticipated that the findings reported here would facilitate the development of the composite for ballistic body armor or other anti-ballistic applications in the future.

7.2 Recommendations for future work

The strain rates used in the present study is quasi-static. It is observed in this study that when the strain rate is increased from 0.00001 s^{-1} to 0.01 s^{-1}, the mechanical properties of the composite increases. The failure type of the Twaron® fabric as reported in other studies also indicates a transition from ductile to brittle when the strain rate is increased by several orders of magnitude (e.g., Shim et al., 2001). The micro-

mechanisms that are responsible for the observed viscoelastic behavior and their characteristic time constant also change with the strain rate in polymeric materials (e.g., Kokoshvili, 1968; Wang and Arruda, 2006). Furthermore, the viscoelastic responses, namely, creep and stress relaxation of the Twaron®/NR composite that are experimentally studied this work cover a relatively long time scale with a lower limit of less than 10 s. The study of the viscoelastic responses of the composite in cases where the loading time is even shorter, e.g., $10^{-2} – 10^{-5}$ s as in the event of ballistic impact, is of practical importance. In order to predict the stress under high strain rates, the mechanical behavior of the composite under short duration loading or at high loading rates (i.e., dynamic loading) have to be determined.

It is therefore crucial that the newly developed para-rheological model be validated for high strain rates. A high strain rate test facility such as the Split Hopkinson Pressure Bar (SHPB) or the Dynamic Mechanical Analysis (DMA) instrument can be used to determine the mechanical and viscoelastic properties of the composite at high strain rates (about 10^{-5} s) that correspond to the ballistic impact velocities. It has to be noted, however, that characterization using the DMA approach involves sinusoidally varying load (or deformation). Care must be taken to avoid or minimize the variation of specimen temperature through heat generation during the oscillatory motion of the specimen. Modern state-of-the-art SHPB techniques make it possible to conduct tensile impact tests of ballistic fibers at high strain rates (e.g., Zhou and Xia, 1998; Sun et al., 2005; Tan et al., 2008; Ruan et al., 2009)

The newly developed para-rheological model is versatile in that it is capable of incorporating the temperature-dependent elastic modulus of the NR constituent. A thermo-para-rheological model can be possibly built from the current model, which is designed for constant temperature analysis. In this case, the model parameters (i.e., K_1, K_2, and η) will be functions of both time and temperature. For example, the Weibull statistical approach can be used to represent the temperature dependence of the secondary bonding (described by K_1) and related chain motions that are associated with both the glassy and rubbery phases of polymers.

There are several conditions that must be satisfied in order to verify the linearity of a viscoelastic material. These definitely include the stress-strain proportionality condition at a given time (i.e., a linear iso-chronal plot) and the compliance to the linear superposition principle. Non-linearity entails the strain dependence of the stress besides its usual time dependence. The assumption made regarding the linearity of the composite and hence the applicability of the linear viscoelasticity analysis approach used in this study are therefore bound to a limiting range of the stress, strain, time and temperature. A series of creep experiments at different stress levels could be conducted to find out if the measured (time-dependent) creep function is independent of the stress or if there is a restrictive stress level beyond which the shape of the creep curve changes, which is indicative of stress-dependency (quasi-linear behavior). It can also be determined if the composite is thermorheologically simple by conducting a series of stress relaxation experiments at different temperatures. These are some additional features of the composite that can be possibly investigated.

REFERENCES

Abadi, M.T., 2009. Micromechanical analysis of stress relaxation response of fiber-reinforced polymers. Composite Science and Technology 69, 1286–1292.

Ahmad, M.R., Wan Yunus, W.A., Salleh, J., Samsuri, A., 2007. Performance of natural rubber coated fabrics under ballistic impact. Malaysian Polymer Journal 24, 39–51.

Akyildiz, F., Jones R.S., Walters, K., 1990. On the spring-dashpot representation of linear viscoelastic behaviour. Rheologica Acta 29, 482–484.

Alger, M., 1997. Polymer Science Dictionary. Chapman and Hall, London, United Kingdom.

Allen, S.R., Roche, E.J., 1989. Deformation behaviour of Kevlar® aramid fibres. Polymer 30, 996–1003.

Andrews, R.D., Tobolsky, A.V., Hanson, E.E., 1946. The theory of permanent set at elevated temperatures in natural and synthetic rubber vulcanizates. Journal of Applied Physics 17, 352–361.

Arridge, R.G.C., 1975. Mechanics of Polymers. Oxford University Press, London, United Kingdom.

ASTM Standard D5035 – 95, 2003. Standard test method for breaking force and elongation of textile fabrics (strip method).

ASTM Standard D4964 – 96, 2008-e1. Standard test method for tension and elongation of elastic fabrics (constant-rate-of-extension type tensile testing machine).

ASTM Standard E328 – 02, 2008. Standard test methods for stress relaxation tests for materials and structures.

Averyanov, A.A., Botchenko, O.K., Fil'bert, D.F., 1980. Rheological properties of polycaproamide in uniaxial extension with necking. Fibre Chemistry 12, 137–139.

Baltussen, J.J.M., Northolt, M.G., 2001. The viscoelastic extension of polymer fibres: Creep behaviour. Polymer 42, 3835–3846.

Baltussen, J.J.M, Northolt, M.G., 2003. The viscoelastic extension of polymer fibers: Complex loadings. Polymer 44, 1957–1966.

Barauskas, R., 2005. Combining mezzo- and macro-mechanical approaches in a computational model of a ballistic impact upon textile targets. In: Proceedings of the 5th WSEAS International Conference on Simulation, Modeling and Optimization, Corfu, Greece, pp. 427–432.

Barauskas, R., Abraitiene, A., 2007. Computational analysis of impact of a bullet against the multilayer fabrics in LS-DYNA. International Journal of Impact Engineering 34, 1286–1305.

Barbero, E.J., Damiani, T.M., Trovillion, J., 2005. Micromechanics of fabric reinforced composites with periodic microstructure. International Journal of Solids and Structures 42, 2489–2504.

Bartenev, G.M., Kucherskii, A.M., Radayeva, G.I., 1981. Relaxation processes in elastomers at low strains from the data of relaxation spectrometry, stress-strain and thermomechanical curves. Polymer Science U.S.S.R. 23, 313–322.

Bender, J., Wagner, N. J., 1996. Reversible shear thickening in monodisperse and bidisperse colloidal dispersions. Journal of Rheology 40, 899–916.

Bernard, C., Delaizir, G., Sangleboeuf, J.-C., Keryvin, V., Lucas, P., Bureau, B., Zhang, X.-H., Rouxel, T., 2007. Room temperature viscosity and delayed elasticity in infrared glass fiber. Journal of the European Ceramic Society 27, 3253–3259.

Bhowmick, A.K., Stephens, H.L., 2001. Handbook of Elastomers. Marcel Dekker, New York.

Biot, M.A., 1954. Theory of stress-strain relations in anisotropic viscoelastic and relaxation phenomena. Journal of Applied Physics 25, 1385–1391.

Bjork, F., Stenberg, B., 1990. Stress relaxation of a nitrile rubber surrounded by an oil that increases the network density. Polymer 31, 1649–1657.

Black, W.B., Preston, J., 1973. High Modulus Wholly Aromatic Fibers. Marcel Dekker, New York.

Boubaker, B.B., Haussy, B., Ganghoffer, J.-F., 2007. Consideration of the yarn–yarn interactions in meso/macro discrete model of fabric Part II: Woven fabric under uniaxial and biaxial extension. Mechanics Research Communications 34, 371 –378.

Boyce, M.C., Socrate, S., Llana, P.G., 2000. Constitutive model for the finite deformation stress–strain behavior of poly(ethylene terephthalate) above the glass transition. Polymer 41, 2183–2201.

Bradshaw, R.D., Brinson, L.C., 1997. A sign control method for fitting and interconverting material functions for linearly viscoelastic solids. Mechanics of Time-Dependent Materials 1, 85–108.

Brinson, H.F., Brinson, L.C., 2008. Polymer Engineering Science and Viscoelasticity: An Introduction. Springer, New York.

Briscoe, B.J., Motamedi, F., 1992. The ballistic impact characteristics of aramid fabrics: The influence of interface friction. Wear 158, 229–247.

Cervenka, A.J., Young, R.J., Kueseng, K., 2005. Micromechanical phenomena during hygrothermal ageing of model composites investigated by Raman spectroscopy. Part II: Comparison of the behaviour of PBO and M5 fibres compared with Twaron. Composites Part A: Applied Science and Manufacturing 36, 1020–1026.

Cheeseman, B.A., Bogetti, T.A., 2003. Ballistic impact into fabric and compliant composite laminates. Composites Structures 61, 161–173.

Chen, C.-H., Chang, Y.H., Cheng, C.-H., 1995. Micromechanics and creep behavior of fiber-reinforced polyehter-ether-ketone composites. Journal of Composite Materials 29, 359–370.

Chenal, J.-M., Chazeau, L., Guy, L., Bomal, Y., Gauthier, C., 2007. Molecular weight between physical entanglements in natural rubber: A critical parameter during strain-induced crystallization. Polymer 48, 1042–1046.

Cheng, M., Chen. W., 2006. Modeling transverse behavior of Kevlar® KM2 single fibers with deformation-induced damage. International Journal of Damage Mechanics 15, 121–132.

Christensen, R.M., 2003. Theory of Viscoelasticity. Dover Publications, New York.

Colakoglu, M., Soykasap, O., Özek, T., 2007. Experimental and numerical investigations on the ballistic performance of polymer matrix composites used in armor design. Applied Composite Materials 14, 47–58.

Corr, D.T., Starr, M.J., Vanderby Jr., R., Best, T.M., 2001. A nonlinear generalized Maxwell model for viscoelastic materials. Journal of Applied Mechanics 68, 787–790.

Cunniff, P.M., 1999. Decoupled response of textile body armor. In: Proceedings of the 18th International Symposium of Ballistics, San Antonio, Texas, pp. 814–821.

Curro, J.G., Pincus, P., 1983. A theoretical basis for viscoelastic relaxation of elastomers in long-time limit. Macromolecules 16, 559–562.

D'Amore, A., Caputo, F., Grassia, L., Zarrelli, M., 2006. Numerical evaluation of structural relaxation-induced stresses in amorphous polymers. Composites Part A: Applied Science and Manufacturing 37, 556–564.

David, N.V., Gao, X.-L., Zheng, J.Q., 2009a. Modeling of viscoelastic behavior of ballistic fabrics at low and high strain rates. International Journal for Multiscale Computational Engineering 7, 295–308.

David, N.V., Gao, X.-L., Zheng, J.Q., 2009b. Constitutive behavior of a Twaron®/natural rubber composite. Mechanics of Advance Materials and Structures (in press).

Dietrich, L., Lekszycki, T., Turski, K., 1998. Problems of identification of mechanical characteristics of viscoelastic composites. Acta Mechanica 126, 153–167.

Doi, M., Takimoto, J., 2003. Molecular modelling of entanglement. The Philosophical Transactions of the Royal Society A 361, 641–652.

Duan, Y., Keefe, M., Bogetti, T.A., Cheeseman, B.A., 2005. Modeling the role of friction during ballistic impact of a high-strength plain-weave fabric. Composite Structures 68, 331–337.

Duan, Y., Keefe, M., Bogetti, T.A., Cheeseman, B.A., Powers, B., 2006. A numerical investigation of the influence of friction on energy absorption by a high-strength fabric subjected to ballistic impact. International Journal of Impact Engineering 32, 1299–1312.

Ebewele, R. O., 2000. Polymer Science and Technology. CRC Press, Boca Raton, Florida.

Egres Jr., R.G., Decker, M.J., Halbach, C.J., Lee, Y.S., Kirkwood, J.E., Kirkwood, K.M., Wagner, N.J., Wetzel, E.D., 2004. Stab resistance of shear thickening fluid (STF)–Kevlar composites for body armor applications. In: Proceedings of the 24th Army Science Conference, Orlando, Florida, pp. 264–271.

Ellyin, F., Vaziri, R., Bigot, L., 2007. Predictions of two nonlinear viscoelastic constitutive relations for polymers under multiaxial loadings. Polymer Engineering and Science 47, 593–607.

Ericksen, R.H., 1985. Creep of aromatic polyamide fibres. Polymer 26, 733–746.

Erman, B., Mark, J.E., 1989. Rubber-like elasticity. Annual Review of Physical Chemistry 40, 351–374.

Fallatah, G.M., Dodds, N., Gibson, A.G., 2007. Long term creep and stress rupture of aramid fibre. Plastics, Rubber and Composites 36, 403–412.

Farlie, E.D., 1970. Creep and stress relaxation of natural rubber vulcanizates. Part I. Effect of crosslink density on the rate of creep in different vulcanizing systems. Journal of Applied Polymer Science 14, 1127–1141.

Faur-Csukat, G., 2006. A study on the ballistic performance of composites. Macromolecular Symposia 239, 217–226.

Ferry, J.D., 1980. Viscoelastic Properties of Polymers. John Wiley and Sons Incorporated, Hoboken, New Jersey.

Findik, F., Yilmaz, R., Koksal, T., 2004. Investigation of mechanical and physical properties of several industrial rubbers. Material and Design 25, 269–276.

Findley, W.N., Lai, J.S., Onaran, K., 1976. Creep and Relaxation of Nonlinear Viscoelastic Materials. North-Holland Publishing Company, Amsterdam.

Fisher, D.G., 1948. The molecular structure and arrangement in stretched natural rubber. Proceedings of the Physical Society 60, 99–114.

Flory, P.J., 1961. Thermodynamic relations for high elastic materials. Transactions of the Faraday Society 57, 829–838.

Flory, P.J., 1985. Molecular theory of rubber elasticity. Polymer Journal 17, 1–12.

Fritsch, J., Hiermaier, S., Strobl, G., 2009. Characterizing and modeling the non-linear viscoelastic tensile deformation of a glass fiber reinforced polypropylene. Composite Science and Technology 69, 2460–2466.

Fuller, K.N.G., Fulton, W.S., 1990. The influence of molecular weight distribution and branching on the relaxation behaviour of uncrosslinked natural rubber. Polymer 31, 609–615.

Gao, X.-L., Mall, S., 2000. A two-dimensional rule-of-mixtures micromechanics model for woven fabric composites. Journal of Composites Technology and Research 22, 60–70.

Gauthier, C., Pelletier, J.M., David, L., Vigier, G., Perez, J., 2000. Relaxation of non-crystalline solids under mechanical stress. Journal of Non-Crystalline Solids 274, 181–187.

Gehring, Jr. G.G., 2000. U.S. Patent 6,103,641: Blunt trauma reduction fabric for body armor.

Gerdeen, J.C., Lord, H.W., Rorrer R.A.L., 2006. Engineering Design with Polymers and Composites. Taylor and Francis Group, Boca Raton, Florida.

Ginic-Markovic, M., Dutta, N.K., Dimopoulos, M., Roy Choudhury, N., Matisons, J.G., 2000. Viscoelastic behaviour of filled and unfilled EPDM elastomer. Thermochimica Acta 357-358, 211–216.

Grassia, P., Hinch, E.J., 1996. Computer simulations of polymer chain relaxation via Brownian motion. Journal of Fluid Mechanics 308, 255–288.

Grogan, J., Tekalur, S.A., Shukla, A., Bogdanovich, A., Coffelt, R.A., 2007. Ballistic resistance of 2D and 3D woven sandwich composites. Journal of Sandwich Structures and Materials 9, 283–302.

Grzywinski, G.G., Woodford, D.A., 1995. Creep analysis of thermoplastics using stress relaxation data. Polymer Engineering and Science 35, 1931–1937.

Hamza, S. S., El-sabbagh, S., Shokr, F. 2008. Elastic behavior of NR/IIR rubber blend loaded with different compatibilizers. International Journal of Polymeric Materials 57, 203–215.

Hiemenz, P.C., 1984. Polymer Chemistry: The Basic Concepts. Marcel Dekker, New York.

Hogg, P. J., 2006. Composites in armor. Science 314, 1100–1101.

Huang, J.S., Gibson, L.J., 1991. Creep of polymer foams. Materials Science 26, 637–647.

Hummel, S.R., Hossain, K., Hayes, G.T., 2001. Biaxial stress relaxation of high impact polystyrene (HIPS) above the glass transition temperature. Polymer Engineering and Science 41, 566–574.

Illers, K.H., Kilian, H.G., Kosfeld, R., 1961. Physical properties of high polymers. Annual Review of Physical Chemistry 12, 49–82.

Irgens, F., 2008. Continuum Mechanics. Springer-Verlag, Berlin, Germany.

Ito, M., 1982. On the separation of physical and chemical component of stress relaxation. Polymer 23, 1515–1518.

IUPAC Compendium of Chemical Terminology (the 'Gold Book'), 1997. 2nd edition compiled by McNaught, A.D. and Wilkinson, A. Blackwell Science, Oxford, United Kingdom. Online version: http://old.iupac.org/publications/compendium/index.html.

Joseph, S.H., 2005. A method for modelling the nonlinear viscoelastic response of polymers. Mechanics of Time-Dependent Materials 9, 35–69.

Ju, B.F., Liu, K.K., 2002. Characterising viscoelastic properties of thin elastomeric membrane. Mechanics of Materials 34, 485–491.

Kalantar, J., Drzal, L.T., 1990. The bonding mechanism of aramid fibres to epoxy matrices: Part 1 A review of the literature. Journal of Materials Science 25, 4186–4193.

Karim, M.R., Hoo Fatt, M.S., 2006. Rate-dependent constitutive equations for carbon fiber-reinforced epoxy. Polymer Composites 27, 513–528.

Katangur, P., Patra, P.K., Warner, S.B., 2006. Nanostructured ultraviolet resistant polymer coatings. Polymer Degradation and Stability 91, 2437–2442.

Khan, A., Zhang, H., 2001. Finite deformation of a polymer: Experiments and modeling. International Journal of Plasticity 17, 1167–1188.

Kiya-Oglu, V.N., Volokhina, A.V., Banduryan, S.I., 1999. Effect of the molecular weight of poly-para-aramids and structural changes in heat treatment on the mechanical indexes of the fibres. Fibre Chemistry 31, 208–214.

Koh, C.P., Shim, V.P.W., Tan, V.B.C., Tan, B.L., 2008. Response of a high-strength flexible laminate to dynamic tension. International Journal of Impact Engineering 35, 559–568.

Kokoshvili, S.M., 1968. Mechanical properties of polyethylene and Teflon over a broad range of strain rates. Mechanics of Composite Materials 4, 30–34.

Kolarik, J., Pegoretti, A., 2006. Non-linear tensile creep of polypropylene: Time-strain superposition and creep prediction. Polymer 47, 346–356.

Konyali, H., Menceloglu, Y., Erman, B., 2008. Long time stress relaxation of amorphous networks under uniaxial tension: The dynamic constrained junction model. Polymer 49, 1056–1065.

Kromm, F.X., Quenisset, J.M., Lorriot, T., Harry, R., 2003. Design and behaviour numerical simulation of multi-materials for an energetic matter container. Materials and Design 24, 235–246.

Lai, J.S., Findley, W.N., 1973. Creep of polyurethane under varying temperature for nonlinear uniaxial stress. Transactions of the Society of Rheology 17, 63–87.

Lakes, R., 2009. Viscoelastic Materials. Cambridge University Press, New York.

Lane, R.A., 2005. High performance fibers for personnel and vehicle armor systems: Putting a stop to current and future threats. AMPTIAC Quarterly 9, 3–9.

Le, H.H., Ilisch, S., Radusch, H.-J., 2009. Characterization of the effect of the filler dispersion on the stress relaxation behavior of carbon black filled rubber composites. Polymer 50, 2294–2303.

Lee, B.L., Walsh, T.F., Won, S.T., Patts, H.M., Song, J.W., Mayer, A.H., 2001. Penetration failure mechanisms of armor-grade fiber composites under impact. Journal of Composite Materials 35, 1605–1633.

Lee, Y.S., Wetzel, E.D., Wagner N.J., 2003. The ballistic impact characteristics of Kevlar woven fabrics impregnated with colloidal shear thickening fluid. Journal of Materials Science 38, 2825–2833.

Lim, C.T., Shim, V.P.W., Ng, Y.H., 2003. Finite-element modeling of the ballistic impact of fabric armor. International Journal of Impact Engineering 28, 13–31.

Loadman, M.J.R., 1985. The glass transition temperature of natural rubber. Journal of Thermal Analysis and Calorimetry 30, 929–941.

Machalaba, N.N., 1999. Modern para-aramid fibres. The role of Tver'khimvolokno joint-stock company in the creation of an armos fibre plant. Fibre Chemistry 31, 171–179.

Machalaba, N.N., Kuryleva, N.N., Okhlobystina, L.V., Matytsin, P.A., Andriyuk, I.A., 2000. Tver' fibres of the armos type: Manufacture and properties. Fibre Chemistry 32, 319–324.

Machiraju, C., Phan, A.-V., Pearsall, A.W., Madanagopal, S., 2006. Viscoelastic studies of human subscapularis tendon: Relaxation test and a Wiechert model. Computer Methods and Programs in Biomedicine 83, 29–33.

Magat, E.E., 1980. Fibres from extended chain aromatic polyamides. Philosophical Transactions of the Royal Society A 294, 463 – 472.

Maity, J., Jacob, C., Das, C.K., Alam, S., Singh, R.P., 2008. Direct fluorination of Twaron fiber and the mechanical, thermal and crystallization behaviour of short Twaron fiber reinforced polypropylene composites. Composites Part A: Applied Science and Manufacturing 39, 825–833.

Mark, J.E., 1981. Rubber elasticity. Journal of Chemical Education 58 (11), 898–903.

Mark, J.E., 1992. Molecular aspects of rubberlike elasticity. Angewandte Makromolekulare Chemie 202, 1–30.

Matveev, V.S., Budnitskii, G.A., 1996. Materials for protection from ballistic injury. Fibre Chemistry 27, 147–149.

McConnell, V.P., 2006. Ballistic protection materials: A moving target. Reinforced Plastics, December 2006, 20–25.

Meera, A.P., Said, S., Grohens, Y., Luyt, A.S., Thomas S., 2009. Tensile stress relaxation studies of TiO_2 and nanosilica filled natural rubber composites. Industrial and Engineering Chemistry Research 48, 5123–5123.

Menard, K.P., 2008. Dynamic Mechanical Analysis: A Practical Introduction. Taylor and Francis Group, Boca Raton, Florida.

MIL-STD-662F Standard, 1997. V50 ballistic test for armor. Department of Defense Test Method Standard.

Mil-Tech Editorial Review, 2006. Body armour – Technological issues. Mil. Tech. 4, 72–79.

Miravete, A., 1999. 3-D Textile Reinforcements in Composites Materials. CRC Press, Boca Raton, Florida.

Morye, S.S., Hine, P.J., Duckett, R.A., Carr, D.J., Ward, I.M., 2000. Modelling of the energy absorption by polymer composites upon ballistic impact. Composite Science and Technology 60, 2631–2642.

Munch, E., Pelletier, J.M., Sixou, B., Vigier, G., 2006. Molecular mobility of crosslinked elastomers stretched above T_g. Polymer 47, 3477–3485.

Nadler, B., Steigmann, D.J., 2003. A model for frictional slip in woven fabrics. Comptes Rendus Mecanique 331, 794–804.

Nadler, B., Papadopoulos, P., Steigmann, D. J., 2006. Multi-scale constitutive modeling and numerical simulation of fabric material. International Journal of Solids and Structures 43, 206–221.

Naik, N.K., Shrirao, P., 2004. Composite structures under ballistic impact. Composites Structures 66, 579–590.

Naik, N.K., Shrirao, P., Reddy, B.C.K., 2006. Ballistic impact behaviour of woven fabric composites: Formulation. International Journal of Impact Engineering 32, 1521–1552.

Ngai, K.L., 1998. Relation between some secondary relaxations and the α-relaxations in glass-forming materials according to the coupling model. The Journal of Chemical Physics 109, 6982–6994.

Ngai, K.L., Plazek, D.J., 2005. The Viscoelastic Behavior of Rubber. In: Mark, J.E., Erman B., and Eirich, F.R., Science and Technology of Rubber, 3rd edition. Academic Press, Burlington, Massachusetts.

Nielsen, L.E., Landel, R.F., 1994. Mechanical Properties of Polymers and Composites. Marcel Dekker, New York.

NIJ Guide 100–01, 2001. Selection and application guide to personal body armor. National Institute of Justice (US Department of Justice). Retrieved March 05, 2008, http://www.ncjrs.gov/pdffiles1/nij/189633.pdf.

NIJ Standard–0101.06, 2008. Ballistic resistance of personal body armor. National Institute of Justice (US Department of Justice). Retrieved March 05, 2008, http://www.ncjrs.gov/pdffiles1/nij/223054.pdf.

Ortiz, C., Kim, R., Rodighiero, E., Ober, C.K., Kramer, E.J., 1998a. Deformation of a polydomain, liquid crystalline epoxy-based thermoset. Macromolecules 31, 4074–4088.

Ortiz, C., Ober, C.K., Kramer E.J., 1998b. Stress relaxation of a main-chain, smectic, polydomain liquid crystalline elastomer. Polymer 39, 3713–3718.

Park, S.W., 2001. Analytical modelling of viscoelastic dampers for structural and vibration control. International Journal of Solids and Structures 38, 8065–8092.

Patel, M., Morrell, P.R., Murphy, J.J., 2005. Continuous and intermittent stress relaxation studies on foamed polysiloxane rubber. Polymer Degradation and Stability 87, 201–206.

Perepelkin, K.E., Machalaba, N.N., Kvarachelia, V.A., 2001. Para-aramid yarns: Armos properties at under conditions of use. Comparison with other para-aramids. Chemical Fibers 2, 22–29.

Povolo, F., Hermida, E.B., 1990. Superposition properties of relaxation or retardation spectra. Journal of Materials Science 25, 4036–4041.

Pramanik, P., Chakraborty, R., 2004. The unique story of a high-tech polymer. Resonance 9, 39–50.

Pritz, T., 1996. Analysis of four-parameter fractional derivative model of real solid materials. Journal of Sound and Vibration 195, 103–115.

Ramirez, J., Sukumaran, S.K., Likhtman, A.E., 2007. Significance of cross correlations in the stress relaxation of polymer melts. The Journal of Chemical Physics 126, 244904, DOI:10.1063/1.2746867

Ramorino, G., Bignotti, F., Pandini, S., Ricco, T., 2009. Mechanical reinforcement in natural rubber/organoclay nanocomposites. Composite Science and Technology 69, 1206–1211.

Rao, M.P., Duan, Y., Keefe, M., Powers, B.M., Bogetti, T.A., 2009. Modeling the effects of yarn material properties and friction on the ballistic impact of a plain-weave fabric. Composite Structures 89, 556–566.

Reddy, J.N., 2008. An Introduction to Continuum Mechanics with Applications. Cambridge University Press, New York.

Reiner, M., 1964. The Deborah number. Physics Today 17, 62–64.

Rogozinsky, A.K., Bazhenov, S.L., 1992. Effect of creep on the Young's modulus of aramid fibres. Polymer 33, 1391–1398.

Rouse, Jr., P.E., 1953. A theory of the linear viscoelastic properties of dilute solutions of coiling polymers. The Journal of Chemical Physics 21, 1272–1280.

Roy, A.K., Sihn, S., 2001. Development of a three-dimensional mixed variational model for woven composites. I. Mathematical formulation. International Journal of Solids and Structures 38, 5935–5947.

Roylance, D., 1977. Ballistics of transversely impacted fibers. Textile Research Journal 47, 679–684.

Roylance, D., Hammas, P., Ting, J., Chi, H., Scott, B., 1995. Numerical modeling of fabric impact. In: Proceedings of the National Meeting of the American Society of Mechanical Engineers, San Francisco, California, pp. 155–160.

Ruan, D., Leung, M.Y., Lu, G., Yu, T., Cao, J., Blicblau, A.S., 2009. Impact tests on Lincoln wool fibers using a mini split Hopkinson tensile bar. Textile Research Journal 79, 444–452.

Sabet, A.R., Beheshty, M.H., Rahimi, H., 2008. High velocity impact behavior of GRP panels containing coarse-sized sand filler. Polymer Composites 29, 932–938.

Said, M.A., Dingwall, B., Gupta, A., Seyam, A.M., Mock, G., Theyson, T., 2006. Investigation of ultra violet (UV) resistance for high strength fibers. Advances in Space Research 37, 2052–2058.

Salem, N.S., Watts, D.C., Combe, E.C., 1987. Stress relaxation of elastomers. Dental Materials 3, 37–39.

Scales, R.H., 2006. Clausewitz and world war IV. Armed Forces Journal July 2006. Retrieved February 11, 2008, http://www.armedforcesjournal.com/2006/07/1866019.

Schallamach, A., Sellen, D.B., Greensmith, H.W., 1965. Dynamic behaviour of rubber during moderate extensions. British Journal of Applied Physics 16, 241–251.

Schapery, R.A., 1961. A simple collocation method for fitting viscoelastic models to experimental data. Report GALCIT SM 61-23A, California Institute of Technology, Pasadena, CA.

Schapery, R.A., 1965. A method of viscoelastic stress analysis using elastic solutions. The Journal of the Franklin Institute 279, 268–289.

Schapery, R.A., Park, S.W., 1999. Methods of interconversion between linear viscoelastic material functions. Part II – An approximate analytical method. International Journal of Solids and Structures 36, 1677–1699.

Schiessel, H., Metzler, R., Blumen, A., Nonnenmacher, T.F., 1995. Generalized viscoelastic models: Their fractional equations with solutions. Journal of Physics A: Mathematical and Theoretical 28, 6567–6584.

Sebastian, M.S., Unnikrishnan, K.C., Narayanan, S., 2008. Viscoelastic properties of Kevlar-29 fabric tape strength member. Mechanics of Materials 40, 949–960.

Shim, V.P.W., Lim, C.T., Tay, T.E., 1995. Modelling deformation and damage characteristics of woven fabric under small projectile impact. International Journal of Impact Engineering 16, 585–605.

Shim, V.P.W., Lim, C.T., Foo, K.J., 2001. Dynamic mechanical properties of fabric armor. International Journal of Impact Engineering 25, 1–15.

Silva, M.A.G., Cismaşiu, C., Chiorean, C.G., 2003. Low velocity impact on laminates reinforced with polyethylene and aramidic fibres. In: Proceedings of the 9th International Conference on Enhancement and Promotion of Computational Methods in Engineering and Science, Macao, China, pp. 843–851.

Slonimskii, G.L., Rogovina, L.Z., 1964. Determination of the mechanical characteristics of a polymeric material by stress relaxation at constant deformation. Polymer Science U.S.S.R. 6, 684–688.

Smith, J.C., Blandford, J.M., Towne, K.M., 1962. Stress-strain relationship in yarns subjected to rapid impact loading: Part VIII shock waves, limiting breaking velocities and critical velocities. Textile Research Journal 32, 67–76.

Smith Jr., K.J., 2002. A random distribution (spectrum) of mechanical relaxation/retardation rate constants and its influence on tensile strength of imperfect (real, visco-elastic) polymer fibers in constant strain-rate extension. Polymer 43, 583–590.

Sperling, L.H., 2006. Introduction to Physical Polymer Science. John Wiley and Sons Incorporated, New Jersey.

Spontak, R.J., Roberge, R.L., Vratsanos, M.S., Starner, W.E., 2000. Model acrylate-terminated urethane blends in toughened epoxies: A morphology and stress relaxation study. Polymer 41, 6341–6349.

SSC-Natick Press Release, 2003. New fibers could lighten body armor. U.S. Army Soldier Systems Center-Natick – December 1, 2003 (No. 03-41). Retrieved February 14, 2008, from http://www.m5fiber.com/magellan/about_m5.htm

Starley, D., 1999. Determining the technological origins of iron and steel. Journal of Archaeological Science 26, 1127–1133.

Sun, B., Liu, F., Gu, B., 2005. Influence of the strain rate on the uniaxial tensile behavior of 4-step 3D braided composites. Composites Part A: Applied Science and Manufacturing 36, 1477–1485.

Tabiei, A., Nilakantan, G., 2008. Ballistic impact of dry woven fabric composites: A review. Applied Mechanics Review 61, 010801–13.

Tan, P., Tong, L., Steven, G.P., 1999. Micromechanics models for the elastic constants and failure strengths of plain weave composites. Composite Structures 47, 797–804.

Tan, V.B.C., Shim, V.P.W., Zeng, X., 2005a. Modelling crimp in woven fabrics subjected to ballistic impact. International Journal of Impact Engineering 32, 561–574.

Tan, V.B.C., Tay, T.E., Teo, W.K., 2005b. Strengthening fabric armour with silica colloidal suspensions. International Journal of Solids and Structures 42, 1561–1576.

Tan, V.B.C., Ching, T.W., 2006. Computational simulation of fabric armour subjected to ballistic impacts. International Journal of Impact Engineering 32, 1737–1751.

Tan, V.B.C., Zeng, X.S., Shim, V.P.W., 2008. Characterization and constitutive modeling of aramid fibers at high strain rates. International Journal of Impact Engineering 35, 1303–1313.

Tarakanov, B.M., Burkert, B.I., Gromova, E.S., Sokolov, Yu, I., Starodubov, D.M., 1999. Effect of molecular mobility on the deformation characteristics of polycaproamide fibres. Fibre Chemistry 31, 449–451.

Tashiro, K., Kobayashi, M. and Tadokoro, H., 1977. Elastic moduli and molecular structures of several crystalline polymers, including aromatic polyamides. Macromolecules 10, 413–420.

Termonia, Y., Smith, P., 1986. Theoretical study of the ultimate mechanical properties of poly(p-phenyleneterephthalamide) fibres. Polymer 27, 1845–1849.

Thaumaturgo, C., Da Costa Jr., A.M., 1997. Shock-waves on polymer composites. Journal of Materials Science Letters 16, 1480–1482.

Tobolsky, A.V., 1960. Properties and Structure of Polymers. John Wiley and Sons Incorporated, Hoboken, New Jersey.

Tobolsky, A.V., Aklonis, J.J., 1964. A molecular theory for viscoelastic behavior of amorphous polymers. Journal of Physical Chemistry 68, 1970–1973.

Tomita, Y., Uchida, M., 2005. Computational characterization of micro- to macroscopic deformation behavior of amorphous, crystalline and semi-crystalline polyethylene. International Journal for Multiscale Computational Engineering 3, 149–160.

Torvik, P.J., Bagley, R.L., 1984. On the appearance of the fractional derivative in the behavior of real materials. Journal of Applied Mechanics 51, 294–298.

Treloar, L.R.G., 1944. Stress-strain data for vulcanised rubber under various types of deformation. Transactions of the Faraday Society 40, 59–70.

Treloar, L.R.G., 1976. The mechanics of rubber elasticity. Proceedings of the Royal Society A 351, 301–330.

Treloar, L.R.G., 2005. The Physics of Rubber Elasticity. Oxford University Press, New York.

Ulven, C., Vaidya, U.K., Hosur, M.V., 2003. Effect of projectile shape during ballistic perforation of vartm carbon/epoxy composite panels. Composite Structures 61, 143–150.

Urayama, K., Kawamura, T., Kohjiya, S., 2009. Structure–mechanical property correlations of model siloxane elastomers with controlled network topology. Polymer 50, 347–356.

Urbelis, V., Petrauskas, A., Vitkauskas, A., 2004. Time-dependent mechanical behavior of heterogeneous textile fabric systems. Fibres and Textiles in Eastern Europe 12, 37–42.

Urbelis, V., Petrauskas, A., Vitkauskas, A., 2005. Creep and creep recovery behavior of textile fabrics and their fused systems. Materials Science 11, 162–168.

Vleeshouwers, S. Jamieson A.M., Simha, R., 1989. Effect of physical aging on tensile stress relaxation and tensile creep of cured EPON 828/epoxy adhesives in the linear viscoelastic region. Polymer Engineering and Science 29, 662–670.

Walker, J.D., 2001. Ballistic limit of fabrics with resin. In: Proceedings of the 19th International Symposium on Ballistics, Interlaken, Switzerland, pp. 1409–1414.

Wang, X., Hu, B., Feng, Y., Liang, F., Mo, J., Xiong, J., Qiu, Y., 2008. Low velocity impact properties of 3D woven basalt/aramid hybrid composites. Composite Science and Technology 68, 444–450.

Wang, Y., Arruda, E.M., 2006. Constitutive modeling of a thermoplastic olefin over a broad range of strain rates. Journal of Engineering Materials and Technology 128, 551–558.

Wang, Z.D., Zhao, X.X., 2008. Modeling and characterization of viscoelasticity of PI/SiO_2 nanocomposite films under constant and fatigue loading. Materials Science and Engineering A 486, 517–527.

Ward, I.M., Sweeney, J., 2004. An Introduction to the Mechanical Properties of Solid Polymers. John Wiley and Sons Incorporated, New Jersey.

Xue, P., Cao, J., Chen, J., 2005. Integrated micro/macro-mechanical model of woven fabric composites under large deformation. Composite Structures 70, 69–80.

Yang, H.H., 2000. Aramid Fibers, in Comprehensive Composite Materials, ed. Anthony Kelly and Carl Zweben. Pergamon, Oxford, United Kingdom.

Yang, J.-L., Zhang, Z., Schlarb, A.K., Friedrich, K., 2006. On the characterization of tensile creep resistance of polyamide 66 nanocomposites. Part I. experimental results and general discussions. Polymer 47, 2791–2801.

Yeh, W.Y., Young R.J., 1999. Molecular deformation processes in aromatic high modulus polymer fibres. Polymer 40, 857–870.

Zeng, X.S., Shim, V.P.W., Tan, V.B.C., 2005. Influence of boundary conditions on the ballistic performance of high-strength fabric targets. International Journal of Impact Engineering 32, 631–642.

Zeng, X.S., Tan, V.B.C., Shim, V.P.W., 2006. Modeling inter-yarn friction in woven fabric armour. International Journal for Numerical Methods in Engineering 66, 1309–1330.

Zhou, Y., Xia, Y., 1998. The effect of strain rate and prestress on the mechanical behavior of ALL. Composites Part A: Applied Science and Manufacturing 29A, 517–524.

APPENDIX A

A one-term generalized Maxwell model ($GM^{n=1}$) is shown in Fig. A.

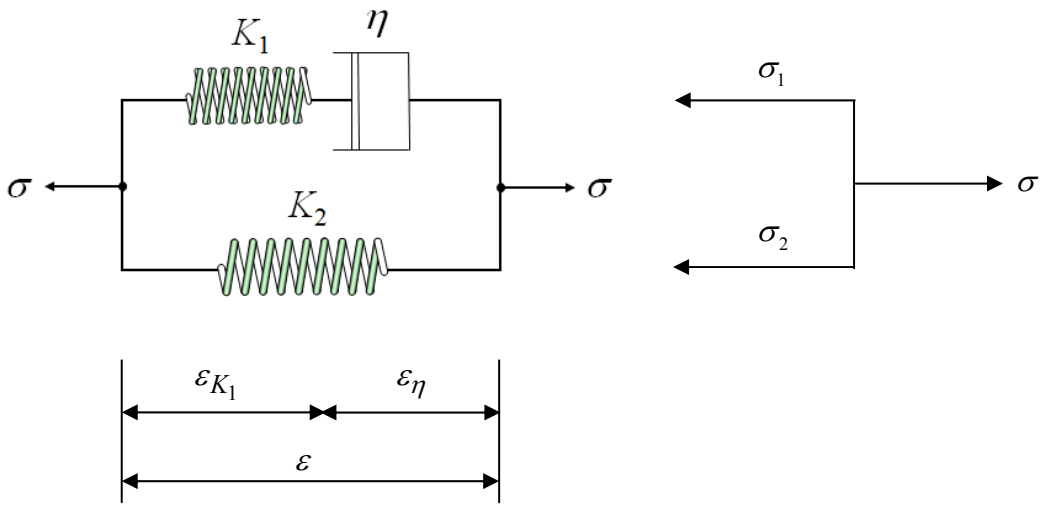

Fig. A $GM^{n=1}$ model.

From Fig. A it is clear that

$$\sigma = \sigma_1 + \sigma_2 , \tag{A1}$$

and

$$\varepsilon = \varepsilon_{K_1} + \varepsilon_\eta , \tag{A2}$$

where ε_{K_1} is the strain in the spring K_1, and ε_η is the strain in the dashpot.

Note that the constitutive relations for the three rheological elements in Fig. A are

$$\sigma_1 = K_1 \varepsilon_{K_1} , \ \sigma_2 = K_2 \varepsilon , \ \sigma_1 = \eta \dot{\varepsilon}_\eta , \tag{A3a-c}$$

where η is the dashpot viscous constant, and $\dot{\varepsilon}_\eta$ is the strain rate in the dashpot.

Substituting Eqs. (A3a,b) and (A2) into Eq. (A1) gives

$$\sigma = K_1(\varepsilon - \varepsilon_\eta) + K_2 \varepsilon. \tag{A4}$$

Taking the time derivative on both sides of Eq. (A4) yields, with $\dot{K}_1 = \dot{K}_2 = 0$,

$$\dot{\sigma} = (K_1 + K_2)\dot{\varepsilon} - K_1\dot{\varepsilon}_\eta. \tag{A5}$$

From Eqs. (A3a,c) and (A1),

$$\dot{\varepsilon}_\eta = \frac{\sigma - K_2\varepsilon}{\eta}. \tag{A6}$$

Using Eq. (A6) in Eq. (A5) leads to

$$\dot{\sigma}(t) + \frac{K_1}{\eta}\sigma(t) = \left(K_1 + K_2\right)\dot{\varepsilon}(t) + \frac{K_1K_2}{\eta}\varepsilon(t), \tag{A7}$$

which is a first-order, non-homogenous, linear ordinary differential equation (ODE) that represents the stress-strain behavior of the $GM^{n=1}$ model. The independent variable is time, *t*, and the unknown function is the stress, $\sigma(t)$, which also depends on the strain $\varepsilon(t)$.

Appendix A.1

Derivation of the constitutive equation of the $GM^{n=1}$ model for constant strain rate

A general solution of Eq. (A7) in Appendix A can be obtained using the method of integrating factors,

$$\sigma(t) = e^{-\int p_0 dt}\left[\int e^{\int p_0 dt}(q_0\varepsilon + c)dt + \mathrm{c}_1\right] \tag{A1.1}$$

where, from Eq. (A9), $p_0 = \frac{K_1}{\eta}, q_0 = \frac{K_1K_2}{\eta}$, and $c = q_1 \cdot \dot{\varepsilon}$.

The integrating factor method is illustrated below for a general case with *a*, *b*, and *c* as the constant coefficients:

$$\sigma(t) = e^{-\int a dt}\left[\int e^{\int a dt}(b\varepsilon + c)dt + \mathrm{c}_1\right]$$

where the integrating factor, $h(t)$, is $\int a dt$ and constant c_1 is to be determined from the initial conditions. The integrating factor in this case is

$$h(t) = at + c_2.$$

The integrating constant, c_2, in the result above need not be determined because only a general solution is needed here. The integrating factor can be reduced to

$$h(t) = at.$$

Substituting this factor into Eq. (A1.1) and performing the integrations yields

$$\sigma(t) = \frac{b}{a}\varepsilon - \frac{b}{a^2}\dot{\varepsilon} + \frac{c}{a} + c_1 e^{-at} \tag{A1.2}$$

By taking $a = p_0$ and $b = q_0$ in Eq. (A1.2), the general solution of Eq. (A1.1) can be readily obtained as

$$\sigma(t) = K_2\varepsilon(t) + \eta\dot{\varepsilon} + c_1 e^{-\frac{K_1}{\eta}t} \tag{A1.3}$$

where c_1 is an integration constant to be determined from the initial conditions (see Eqs. (3.2) and (3.3). Eq. (A1.3) is the constitutive relation based on the $GM^{n=1}$ model shown in Fig. A, which has been given in Eq. (3.1) and used in the simulations.

Appendix A.2

Derivation of the stress relaxation function of the $GM^{n=1}$ model

For a constant applied strain with $\varepsilon = \varepsilon_0$ and $\dot{\varepsilon} = 0$, Eq. (A7) in Appendix A becomes

$$\dot{\sigma}(t) + \frac{K_1}{\eta}\sigma(t) = \frac{K_1 K_2}{\eta}\varepsilon(t) \tag{A2.1}$$

The general solution of Eq. (A2.1), which is again a first-order ODE, can be readily obtained as

$$\sigma(t) = ce^{-\frac{t}{\tau}} + K_2\varepsilon_0 \tag{A2.2}$$

where $\tau = \dfrac{\eta}{K_1}$, and c is a constant to be determined from an initial condition. Using the initial condition for the stress, i.e., $\sigma(0) = \sigma_0$, in Eq. (A2.2) gives

$$c = \sigma_0 - K_2\varepsilon_0 . \tag{A2.3}$$

The general relationship between the stress decay ($\sigma(t)$), the stress relaxation modulus ($E_r(t)$), and the initial strain, ε_0, is given by

$$E_r(t) = \frac{\sigma(t)}{\varepsilon_0} \tag{A2.4}$$

which, at time $t = 0$, can be written as

$$\sigma_0 = E_i \cdot \varepsilon_0 \tag{A2.5}$$

If the instantaneous modulus of the composite just before the beginning of the relaxation test, i.e., elastic modulus at time $t = 0^-$, is taken to be

$$E_i = K_1 + K_2 , \tag{A2.6}$$

then using Eqs. (A2.5) and (A2.6) in the expression for the constant gives

$$c = K_1\varepsilon_0 . \tag{A2.7}$$

Substituting Eq. (A2.7) into Eq. (A2.2) yields the relaxation function as follows:

$$\sigma(t) = \left(K_1 e^{-\frac{t}{\tau}} + K_2 \right) \varepsilon_o , \tag{A2.8}$$

It then follows from Eq. (A2.4) and (A2.8) that the stress relaxation modulus, $E_r(t)$ is given by

$$E_r(t) = K_1 e^{-\frac{t}{\tau}} + K_2 . \tag{A2.9}$$

Eq. (A2.8) is the stress relaxation function of the $GM^{n=1}$ model, which is listed in Table 5.1 and has been used to obtain the relevant numerical results presented in Fig. 5.4.

Appendix A.3

Derivation of the creep function of the $GM^{n=1}$ model

For a constant applied stress with $\sigma = \sigma_0$ and $\dot{\sigma} = 0$, $p_1 = 0$ and Eq. (A7) in Appendix A becomes

$$\frac{K_1}{\eta}\sigma_0 = \frac{K_1 K_2}{\eta}\varepsilon + \left(K_1 + K_2\right)\dot{\varepsilon} \tag{A3.1}$$

The general solution of Eq. (A3.1), which is again a first-order ODE, can be readily obtained as

$$\varepsilon(t) = ce^{-\frac{t}{\tau_{c1}}} + \frac{\sigma_0}{K_2} \tag{A3.2}$$

where τ_{c1} is the retardation time defined by, $\tau_{c1} = \dfrac{\eta\left(K_1 + K_2\right)}{K_1 K_2}$, and c is a constant to be determined from an initial condition.

Using the initial condition for the strain, i.e., $\varepsilon(0) = \dfrac{\sigma_0}{K_1 + K_2}$, in Eq. (A3.2) gives

$$c = \sigma_0 \left(\frac{K_1}{K_2\left(K_1 + K_2\right)} \right). \tag{A3.3}$$

Substituting Eq. (A3.3) into Eq. (A3.2) yields the creep function as

$$\varepsilon(t) = \left[\frac{1}{K_2} - \frac{K_1}{K_2(K_1 + K_2)} e^{-\frac{t}{\tau_{c1}}} \right] \sigma_o \equiv J(t)\sigma_o , \tag{A3.4}$$

where the creep compliance, $J(t)$ is given by (see Table 6.2)

$$J(t) = \frac{1}{K_2} - \frac{K_1}{K_2(K_1 + K_2)} \mathrm{e}^{-\frac{t}{\tau_{c1}}} . \tag{A3.5}$$

APPENDIX B

Derivation of the constitutive equation of the GKV model for constant strain rate

A generalized Kelvin-Voigt model (GKV) is shown in Fig. B.

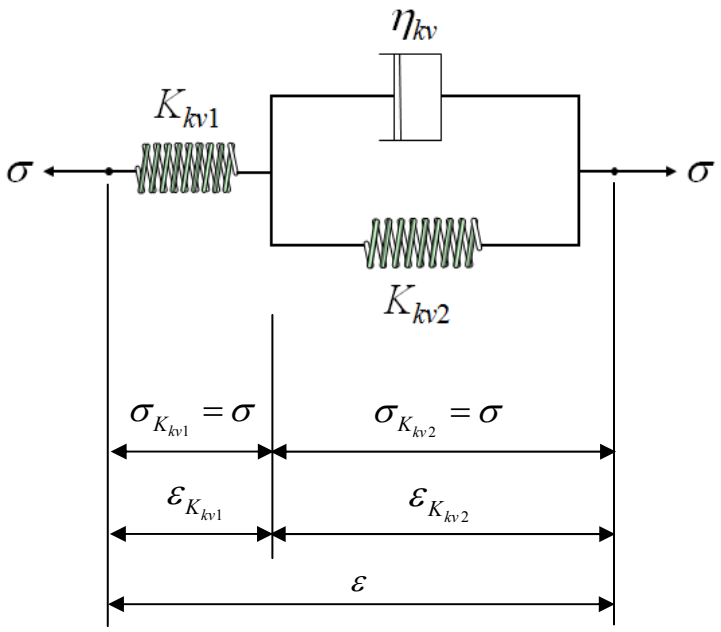

Fig. B GKV model.

Clearly, it is seen from Fig. B that

$$\sigma_{K_{kv1}} = K_{kv1}\varepsilon_{K_{kv1}} = \sigma, \tag{B.1}$$

$$\sigma_{K_{kv2}} = K_{kv2}\varepsilon_{K_{kv2}} + \eta\dot{\varepsilon}_{K_{kv2}} \tag{B.2}$$

and

$$\varepsilon = \varepsilon_{K_{kv1}} + \varepsilon_{K_{kv2}}\,. \tag{B.3}$$

From Eqs. (B.1)–(B.3) it follows that

$$\varepsilon = \frac{\sigma}{K_{kv1}} + \frac{\sigma}{K_{kv2}} - \frac{\eta}{K_{kv2}}\dot{\varepsilon} + \frac{\eta}{K_{kv2}}\frac{\dot{\sigma}}{K_{kv1}}, \tag{B.4}$$

which can be rewritten as

$$\frac{\eta}{K_{kv1}}\dot{\sigma} + \left(1 + \frac{K_{kv2}}{K_{kv1}}\right)\sigma = K_{kv2}\varepsilon + \eta\dot{\varepsilon} \tag{B.5}$$

The general solution of Eq. (B.5), a first-order ordinary differential equation, can be readily found to be

$$\sigma(t) = \frac{K_{kv1}K_{kv2}}{K_{kv1} + K_{kv2}}\varepsilon(t) + \frac{{K_{kv1}}^2\eta_{kv}}{(K_{kv1} + K_{kv2})^2}\dot{\varepsilon} + c_2 e^{-\frac{K_{kv1}+K_{kv2}}{\eta_{kv}}t} \tag{B.6}$$

where c_2 is an integration constant to be determined from an initial condition.

Consider the initial conditions:

$$\sigma(0) = 0,\ \varepsilon(0) = 0, \tag{B.7}$$

which are the same as those used for the $GM^{n=1}$ model. Using Eq. (B.6) in Eq. (B.7) gives

$$c_2 = -\frac{{K_{kv1}}^2\eta_{kv}}{(K_{kv1} + K_{kv2})^2}\dot{\varepsilon} \tag{B.8}$$

Inserting Eq. (B.8) into Eq. (B.6) then leads to, with $\varepsilon = \dot{\varepsilon}t$ (from $\frac{d\varepsilon}{dt} = \dot{\varepsilon}$ = constant and $\varepsilon(0) = 0$),

$$\sigma(t) = \frac{K_{kv1}K_{kv2}}{K_{kv1} + K_{kv2}}\varepsilon(t) - \frac{{K_{kv1}}^2\eta_{kv}}{(K_{kv1} + K_{kv2})^2}\left(e^{-\frac{K_{kv1}+K_{kv2}}{\eta_{kv}}\frac{\varepsilon}{\dot{\varepsilon}}} - 1\right)\dot{\varepsilon} \tag{B.9}$$

as the constitutive relation based on the GKV model, which has been given in Eq. (3.5) and utilized in the simulations.

APPENDIX C

Illustration of a curve fitting procedure using the 'fminunc' optimization algorithm in the Matlab® Optimization Toolbox

The 'fminunc' optimization algorithm can be found in the Matlab® Optimization Toolbox™ 4.3 and is based on the least squares method. The 'fminunc' algorithm has an inbuilt convergence procedure and will exit when the convergence criterion, i.e., minimization of the least squares error, is met. In this illustration, the predictions of the creep strain at every instant t_i from the creep functions of the models given in Table 6.2, $\varepsilon_i^{mod\,el}(t_i)$, are compared to the experimental data corresponding to that time instant ($\varepsilon_i^{exp}(t_i)$), and the values of the model parameters are determined by minimizing the least square error of an objective function, *g*. For instance, the objective function (also known as the cost function) for the GM$^{n=1}$ model is

$$\min_{A,B,c} g = \sum_{t_i=0}^{3600} \left[\varepsilon_i^{model}(t_i) - \varepsilon_i^{exp}(t_i) \right]^2 . \tag{C1}$$

where, from *Appendix A.3*,

$$\varepsilon_i^{model}(t_i) = \left(A - Be^{-\frac{t}{c}} \right) D$$

with

$$A = \frac{1}{K_2}, \quad B = \frac{K_1}{K_2(K_1 + K_2)}, \quad c = \tau, \quad D = 30 \times 10^6 . \tag{C2a-e}$$

Here, $\varepsilon_i^{mod\,el}(t_i)$ is a scalar-valued function of three coefficients, namely, *A*, *B*, and *c*. For this example, the 'fminunc' optimization procedure will return the optimized values of *A*, *B* and *c* that give the (global) minimum value of the objective function, i.e., the minimum error between $\varepsilon_i^{mod\,el}(t_i)$ and $\varepsilon_i^{exp}(t_i)$ values. The 'fminunc' optimization algorithm is an unconstrained minimization solver.

A step-by-step procedure of the 'fminunc' optimization algorithm that was used to determine the optimal values of the model parameters (*A*, *B*, *c*) of the GM$^{n=1}$ model for the case of creep (see Chapter VI) in the Matlab® environment is provided next.

Step 1: The following associations are made for the optimization procedure:

x(1) = K_1
x(2) = K_2
x(3) = η

Step 2: An M-file is written for the objective function. i.e., the Matlab® function that will evaluate the objective function given by Eq. (C1).

```
function g = gmn1fitun(x)

t0 = 0

sigc = 3.0E+09

tstrn = [0  1   2   3   4   5   6   7   8   9   10  50  100 150 200 250
300 350 400 450 500 550 600 650 700 750 800 850 900 950 1000     1100
1200    1300    1400    1500    1600    1700    1800    1900    2000
2100    2200    2300    2400    2500    2600    2700    2800    2900
3000    3100    3200    3300    3400    3500    3550];

strn = [4.2904  4.2905  4.2929  4.2964  4.2978  4.2931  4.2948  4.2933
4.3018  4.2974  4.3039  4.3445  4.3604  4.3746  4.3974  4.4037  4.4091
4.4219  4.4307  4.4294  4.4381  4.4476  4.4495  4.4581  4.4618  4.4537
4.4709  4.4749  4.4797  4.4793  4.4855  4.4909  4.4834  4.4898  4.5033
4.5016  4.5060  4.5085  4.5075  4.5199  4.5232  4.5190  4.5261  4.5315
4.5267  4.5273  4.5431  4.5452  4.5467  4.5563  4.5506  4.5458  4.5661
4.5706  4.5703  4.5677  4.5687];

g1 = 0.

for i = 1:57

g1 = g1+((((1/x(2))-((x(1)/(x(2)*(x(1)+x(2))))*(exp(-tstrn(i)/x(3)))))*
sigc)-strn(i))^2

end

g = g1

end
```

(*Note*: The value of `sigc` is equal to the constant applied stress (30 MPa) multiplied by 100. The multiplication is done to offset the values of the `strn` data, which should be divided by 100).

Step 3: In this step, the 'fminunc' (unconstrained) optimization routine is invoked.

```
x0 = [1E+07, 1E+08, 1E+10];   % initial guessed values of the variables
options = optimset('LargeScale','off');        % to set the Hessian off
[x,fval,exitflag,output] = fminunc(@gmn1fitun,x0,options)
```

This routine produced the following output:

```
x =
    1.0e+010 *
    0.0041    0.0657    3.9000

fval =

4.0489e-005

exitflag =

1

output =
       iterations: 12
        funcCount: 92
         stepsize: 1
    firstorderopt: 9.8982e-007
        algorithm: 'medium-scale: Quasi-Newton line search'
          message: [1x85 char]
                   Optimization terminated: relative infinity-norm of
                   gradient less than options.TolFun.
```

The `fval` is the value of the objective function. The `firstorderopt` is a measure of optimality, which in this unconstrained case is the infinity norm of the gradient. The `exitflag` is an integer that identifies the reason why the algorithm exited. The `exitflag` value of 1 shows that the magnitude of the gradient is smaller than the `TolFun` tolerance (an built-in value by default) and that the algorithm converged to a solution with the following coefficients:

x(1) = K_1 = 4.1E+07,

x(2) = K_2 = 6.5E+08,

x(3) = η = 3.9E+10.

The above procedure is also used to determine the optimal parameter values of all of the other models under different loading and deformation conditions studied in this work.

APPENDIX D

(Proofs are available for some equations in this appendix. They are marked with ♣ and can be obtained from the author.)

D.1 The entropic effect in rubber elasticity

Natural rubber (NR) is an incompressible elastomeric material composed of long polymer chains of randomly oriented molecules. The molecular theory of rubber elasticity is based on the entropic effect of macromolecular chains. At the molecular scale, the entropic effect is influenced by (i) the chain length, (ii) the crosslink network, and (iii) the temperature of NR.

Long chains are necessary for generating a wide range of molecular conformations of the macromolecular polymer chains[*]. In NR, the usual conformation of the polymer chains has a disordered-coil shape (see Fig. D1). The large length of the chains is essential but not sufficient to afford a high entropic state of NR at the room/ambient temperature. The macromolecular chain segments should have adequate conformational mobility, which increases as temperature is raised above the glass transition temperature, T_g, of NR. Sufficient mobility is required to enable the long polymer chains to rearrange to a new conformation of increased entropy after applied loading is removed. Since the ambient temperature (of 25°C) is well above the T_g (of –73°C) of NR[†], NR is always at a high entropic state at the ambient/room temperature.

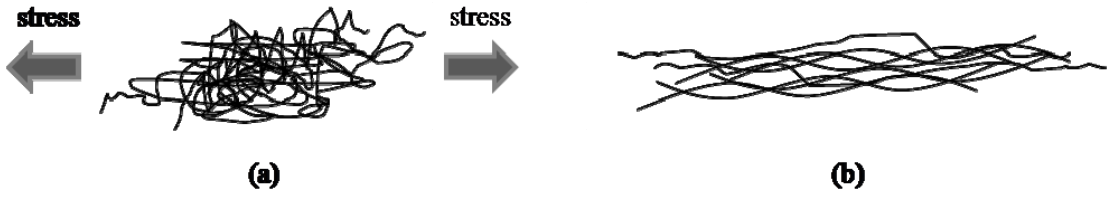

Fig. D1 Typical NR molecular chain conformation: (a) the 'squirmed' – disordered and coiled conformation at equilibrium (high entropy), and (b) straightened conformation under loading.

The high entropic state denotes the thermo-kinetic equilibrium of the chemical bonds in the chains. When NR is stretched, the equilibrium is perturbed, resulting in a conformation with reduced entropy. The macromolecule chains would then shrivel to a higher entropic state to regain their thermo-kinetic equilibrium. This may be explained

[*] The length of a linear chain is about 10,000Å. (Fisher, D.G., 1948, "The molecular structure and arrangement in stretched natural rubber," *Proc. Phys. Soc.* **60**, 99 – 114.)

[†] Loadman, M.J.R., 1985, "The glass transition temperature of natural rubber," *J. Therm. Analy. Calorimetry* **30** (4), 929 - 941.

as follows. In a crosslink network, individual polymer molecules are linked by secondary bonds (e.g., the hydrogen bond). In contrary to the saturated *cis*-$(C_5H_8)_n$ structure (see Fig. D1 in the main text), the hydrocarbon molecules in the unvulcanized rubber have points of unsaturation[‡], which enables two molecular chains to crosslink when raw rubber is vulcanized[§]. The NR coating involved in this study is a vulcanized rubber material. When NR is stressed, the chains begin to uncoil and elongate. At sufficiently higher stresses, the chains are unable to elongate further and will slip-pass each other. Unlike in an un-crosslinked structure, the slippage in NR is limited by the crosslinked network structure. All polymer chains are held together in a crosslink network (see Fig. D2(a)). The chains retract to an equilibrium conformational state when the applied stress is removed. The crosslinked network thus provides the memory effect of NR.

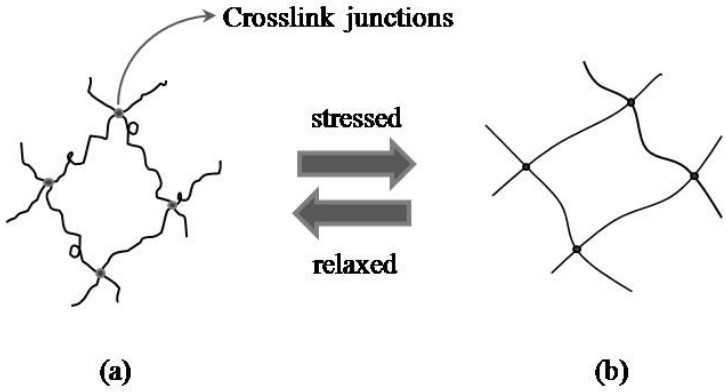

Fig. D2 Deformation of the crosslinked network: (a) original, and (b) stretched conformations.

The entropic effect that forms the basis of rubber elasticity is partly entailed by the minimization of internal energy. The internal energy, U, of a material is determined by the atomic positions at equilibrium. The positions are optimized by the electrostatic bonding forces, which are either attractive or repulsive. The optimization always tends to minimize the internal energy of the material. At a constant absolute temperature, T (in Kelvin) and a constant volume, V (in m^3), the dynamic exchange of U (in Joules) and the entropy of the material, S (in Joules/ Kelvin), can be described by the Helmholtz free energy, F (in Joules), through

$$F = U - TS. \tag{D1}$$

[‡] A chemical structure is saturated if each available carbon bond holds a hydrogen atom. Points of unsaturation refer to points in the chemical structure where the hydrogen atoms are missing, which make it possible for adjacent macromolecular chains to crosslink.

[§] The definition of the *cis*- descriptor is given in IUPAC (1997).

The Helmholtz free energy is a thermodynamic potential representing the amount of energy that can be stored or taken from a closed thermodynamic system (i.e., the NR material in this case). When a load is applied, the NR material will attempt to minimize its Helmholtz energy either by reducing its internal energy or increasing its entropy in accordance with the second law of thermodynamics. The latter indicates that under the applied loading the original conformation of the macromolecular chains will be reconfigured to a new equilibrium state of higher entropy. As can be seen from Eq. (D1), the entropic contribution (i.e., the second term) increases with temperature, which is consistent with the conformational mobility discussed above.

Mechanical work is done to the NR material when it is stretched through a displacement, dl, by the applied force, f. The work done, dW, to the material by f is given by

$$\mathrm{d}W = f\,\mathrm{d}l. \tag{D2a}$$

For constant temperature and volume with dT = dV = 0, it follows from Eq. (D1) and the first law of thermodynamics that

$$\mathrm{d}F = \mathrm{d}U - T\mathrm{d}S = \mathrm{d}W. \tag{D2b}$$

Combining Eqs. (D2a) and (D2b) then yields

$$f = \frac{\mathrm{d}W}{\mathrm{d}l} = \left(\frac{\partial U}{\partial l}\right)_{T,V} - T\left(\frac{\partial S}{\partial l}\right)_{T,V}. \tag{D3}$$

Clearly, Eq. (D3) indicates that the application of f results in the change of entropy. Since the change of internal energy in NR due to bond distortions is usually negligible, i.e., $\partial U/\partial l = 0$, Eq. (D3) becomes

$$f = -T\left(\frac{\partial S}{\partial l}\right)_{T,V}, \tag{D4}$$

which relates f directly to the temperature and entropic change. Eq. (D4) shows that a tensile force (i.e., $f > 0$) applied at a constant temperature and a constant volume will reduce the entropy rate (i.e., the change of entropy per unit length). Conversely, a positive entropy rate will give a compressive force, thereby leading to the retraction of the chains. These observations will be further discussed using statistical mechanics and thermodynamics in tandem with a random-walk model.

D.2 Molecular-extension based on a random-walk model and thermodynamics

The analysis presumes that each bonded segment between two crosslink junctions of a molecular chain is made up of a series of n pinned rigid links. The basis for this idealization is that the chain stiffness arising from the rotation of carbon atoms about each carbon-carbon (C-C) bond is insignificant compared to that due to the extension or bending of the bond[**]. The latter needs to overcome the strong covalent bonds. The C-C bond in the bonded segment is assumed to have a length of h. Hence, there are n C-C bonds in a segment of the crosslink chain, each of which has a bond length of h. The parameter of interest is thus the segment length, which is different from the total length of the entire molecular chain. The relative position of each link is independent of its neighboring links. The probable segment length is then determined not only by n and h but also by how each link positions itself to acquire the resulting length of the segment.

A one-dimensional random-walk approach is employed to derive the change of entropy per unit length. Suppose that a uni-axial tensile force is applied to elongate the NR material to a length of l. It is assumed that a particular polymer chain segment inside the NR material is also extended to a length of l. The extension is now imagined as the total distance traveled by a person through n steps consisting of, say, p steps forward and q steps backward with a step length h. That is,

$$n = p + q, \tag{D5}$$

$$l = (p - q)h. \tag{D6}$$

From Eqs. (D5) and (D6) it follows that

$$p = \frac{1}{2}\left(n + \frac{l}{h}\right), \tag{D7}$$

$$q = \frac{1}{2}\left(n - \frac{l}{h}\right). \tag{D8}$$

The probability, N, of attaining the total extension of the chain by taking p steps forward and q steps backward (with $p + q = n$) is given by

---

[**] Rotation is easier due to the non-collinear single valence bonds in the chemical structure of NR. See, for example, [1] Hertz, Jr., D.L., 1984. Theory and practice of vulcanization. Elastomerics, November 1984, (ISSN 0146-0706). Retrieved October 24, 2008, http://www.sealseastern.com/PDF/Vulcanization.pdf, and [2] Bower, D.I., 2002. An Introduction to Polymer Physics. Cambridge University Press, England, p. 9 (ISBN 052163721X).

$$N = \frac{n!}{p!q!}. \tag{D9}$$

This probability corresponds to the possible number of microstates (i.e., the configurational probability) of the macromolecular chains that generate any macroscopic thermodynamic descriptor, e.g., energy. In statistical thermodynamics, entropy is related to the number of microstates ($\equiv N$) by

$$S = k \ln N, \tag{D10}$$

where $k = 1.38 \times 10^{-23}$ J/K is the Boltzmann constant. Two more assumptions need to be made to facilitate the ensuing derivation: (i) p and q are integers (so that n is even), and (ii) $nh >> l$. The latter has a physical correspondence to the NR molecules. That is, the fully stretched length, l, of a chain segment is much greater than the separating length of the two ends of the segment. The Stirling approximation can be utilized to expand Eq. (D9) and to obtain the natural logarithm of the same.[††] According to this approximation,

$$n! \cong \sqrt{2\,\pi\, n}\,.\left(\frac{n}{e}\right)^{n}, \tag{D11a}$$

which, for a large n, can be simplified to

$$\ln n! \cong n \ln n - n. \tag{D11b}^{\clubsuit}$$

From Eqs. (D9) and (D11a,b), it follows that, upon using the two assumptions and the Taylor expansion,

$$\ln N = n \ln 2 - \frac{l^2}{2nh^2}. \tag{D12}^{\clubsuit}$$

Substituting Eq. (D12) into Eq. (D10) yields

$$\mathrm{S} = nk \ln 2 - \frac{kl^2}{2nh^2}. \tag{D13}$$

Using Eq. (D13) in Eq. (D4) then leads to

[††] Marsaglia, G. and Marsaglia, J.C.W., 1990. A new derivation of Stirling's approximation to n!. The American Mathematical Monthly 97, 826–829.

$$f = \left(-\frac{kT}{nh^2} \right) l \,. \tag{D14}$$

Clearly, the force-extension relation given in Eq. (D14) resembles the elastic response of a Hookean spring, with the term in the parenthesis acting as the spring constant.

D.3 Determination of the configurational probability of chain conformation

When a NR specimen is stretched, the molecular chains inside the specimen are forced to elongate. Both ends of a chain may be involved in the extension. The simplest way to visualize this is the elongation of a segment of a one-dimension (1D) chain. It is assumed that one end of the segment is fixed at the origin and the other end is stretched horizontally to the right (denoted as the positive x-direction in a conventional Cartesian coordinate system). The probability, $\Omega(l_x)$, of finding the other end of the segment at a particular coordinate l_x along the 1D path (i.e., the x-direction) is directly proportional to the probability N, i.e.,

$$\Omega(l_x) = DN,$$

where D is a proportionality constant.

From Eq. (D12),

$$N = \mathrm{C}\, e^{-\left(\psi_l l^2\right)} \tag{D15}$$

where $C = 2^n$, and $\psi_l = \dfrac{1}{2nh^2}$ is a length scale parameter relating the bond length, h and the number of bonds, n. Thus,

$$\Omega(l_x) \; = E\, e^{-\left(\psi_l l_x^2\right)}, \tag{D16}$$

where $E \equiv CD$ is a normalizing constant which can be readily determined from the probability condition given by the normalization integral:

$$\int_{-\infty}^{+\infty} \left|\Omega(l_x)\right|^2 \, dl_x \; = \; 1, \tag{D17}$$

which says that the probability density of locating the free end at any of the possible locations from $l_x = -nh$ to $l_x = +nh$ is unity. Here, the step lengths are very small such

that the discrete steps can be taken to be continuous over the total length traveled in the x direction.

Using Eq. (D16) in Eq. (D17) gives

$$E = \sqrt{\frac{1}{\pi}\frac{1}{2nh^2}}\,.$$

Eq. (D16) can then be written as

$$\Omega(l_x) = \sqrt{\frac{1}{\pi}\left(\frac{1}{2nh^2}\right)}\,\mathrm{e}^{-\left(\psi_l l_x^2\right)}. \qquad \text{(D18)}^{\clubsuit}$$

The 1D analysis (i.e., the random walk model) performed above can be generalized to a three-dimensional (3D) space. The model resulting from the 3D analysis is called the random flight model. Fig. D3 shows the geometrical configuration of a crosslink segment in a 3D Cartesian coordinate system.

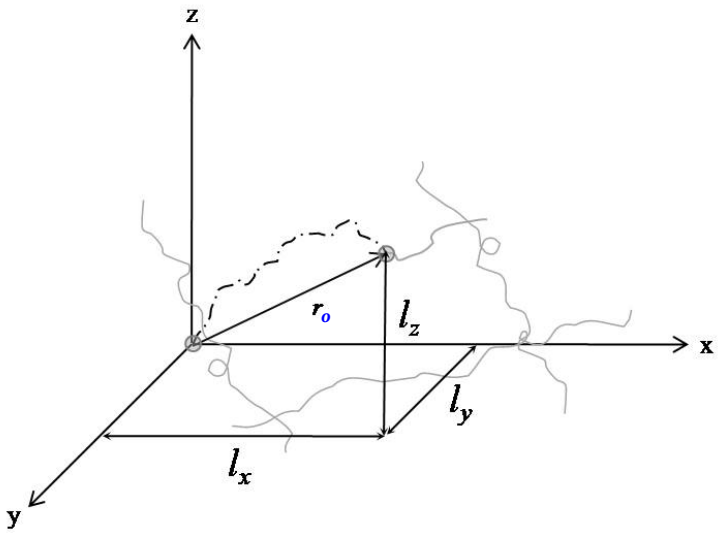

Fig. D3 Geometrical configuration of a crosslink segment.

The origin is fixed at one end of the crosslink chain. The series of links mentioned earlier is represented by the small line fragments (of the line-dot curve in Fig. D3), which are randomly oriented relative to each other. The other (free) end of the segment is at the position $\boldsymbol{r}$, whose magnitude is

$$r = \sqrt{{l_x}^2 + {l_y}^2 + {l_z}^2}\ , \tag{D19}$$

where l_x, l_y and l_z are, respectively, the x-, y- and z- components of $\boldsymbol{r}$.

The probability of locating the free end of the segment in the 3D space is given by (Tabor (1991)[‡‡]

$$\Omega(r) = \frac{\beta^3}{\sqrt{\pi}} e^{\left(-\beta^2 r^2\right)} = \frac{\beta^3}{\sqrt{\pi}} e^{-\left[\beta^2\left({l_x}^2 + {l_y}^2 + {l_z}^2\right)\right]}, \tag{D20}$$

where $\beta = \sqrt{\frac{3}{2}\frac{1}{nb^2}} = \sqrt{3\psi_l}$, b is the 3D step length (equivalent to the length of the bond that connects two segments in the 3D space). In the case of a 1D extension, $l_y = l_z = 0$, and Eq. (D20) reduces to Eq. (D18).

D.4 Determination of the constitutive relation of NR

Fig. D4 shows the geometrical change in an idealized 3D crosslinked isotropic network under a uni-axial tensile stress, σ. In this networked structure, each point-to-point link represents a chain segment. Extensions in the x-, y-, and z-directions are denoted as λ_x, λ_y, and λ_z, respectively. These are the ratios of the extended (final) length to the original (initial) length in each dimension. For simplicity[§§], it is assumed that the length of each segment increases (or decreases) by these same ratios. The initial ($\boldsymbol{r_o}$) and final ($\boldsymbol{r}$) 3D position vectors are given by $\left(l_x, l_y, l_z\right)$ and $\left(\lambda_x l_x, \lambda_y l_y, \lambda_z l_z\right)$, respectively.

Then it follows that

$$\left|\boldsymbol{r_o}\right|^2 = l_x^2 + l_y^2 + l_z^2\ , \tag{D21a}$$

$$\left|\boldsymbol{r}\right|^2 = \lambda_x^2 l_x^2 + \lambda_y^2 l_y^2 + \lambda_z^2 l_z^2\ . \tag{D21b}$$

[‡‡] Tabor, D., 1991. Gases, liquids, and solids: and other states of matter. 3rd edition, Cambridge University Press, New York, p. 197 (ISBN 0521406676).

[§§] Treloar, L.R.G., 2005. The Physics of Rubber Elasticity. 3rd edition, Oxford University Press, England, p. 61 (ISBN 978-0-19-857027-1). "The effect of the deformation is to change the components of displacement length of each chain in the same ratio as the corresponding dimensions of the bulk rubber. This assumption is arbitrary and obviously the simplest and most natural if some assumption about the transformation of chain displacement lengths on deformation has to be introduced."

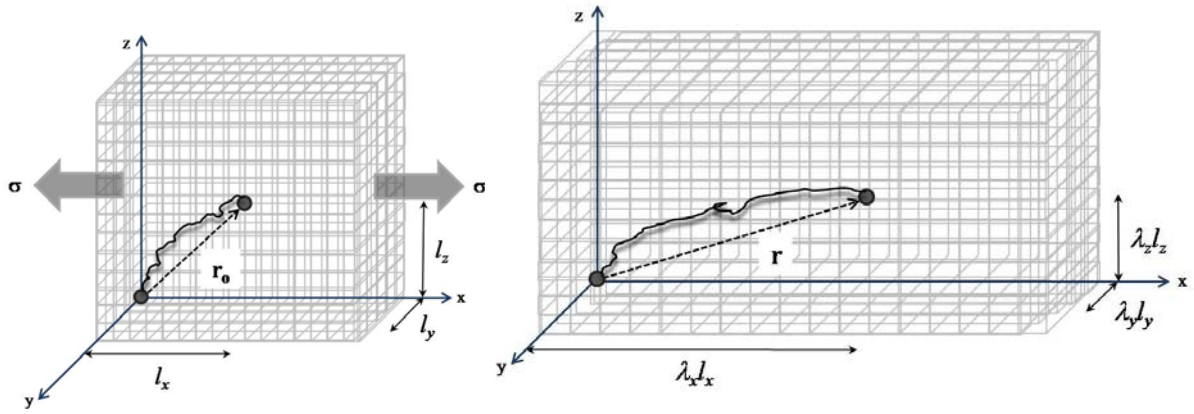

(a) (b)

Fig. D4 (a) Original and (b) deformed configurations of an idealized crosslinked network.

The 1D entropy relation given in Eq. (D13) can be generalized to the 3D case as

$$\mathrm{S} = 3\left(nk \ln 2 - \frac{k|r|^2}{2nb^2} \right). \tag{D22}$$

The initial entropy of the NR material before the deformation can be obtained from Eqs. (D21a) and (D22) as

$$S_0 = 3\left[nk \ln 2 - \frac{k\left(l_x^2 + l_y^2 + l_z^2\right)}{2nb^2} \right]. \tag{D23a}$$

Similarly, using Eq. (D21b) in Eq. (D22) gives the entropy of the NR material after the deformation as

$$S = 3\left[nk \ln 2 - \frac{k\left(\lambda_x^2 l_x^2 + \lambda_y^2 l_y^2 + \lambda_z^2 l_z^2\right)}{2nb^2} \right]. \tag{D23b}$$

In view of the elastic isotropy of the initial network (i.e., undeformed configuration),[***] it is assumed that $l_x^2 = l_y^2 = l_z^2$ .Then, it follows from Eq. (D21a) that

$$l_x^2 = l_y^2 = l_z^2 = \frac{1}{3}|\mathbf{r}_o|^2 = \frac{1}{3}nb^2 . \tag{D24}$$

Furthermore, since NR is an incompressible material, the volume incompressibility requires, for the uniaxial stress in the x-direction with $\lambda_x = \lambda$ and $\lambda_y = \lambda_z$, that $\lambda_x\lambda_y\lambda_z = 1$, which gives $\lambda_y = \lambda_z = 1/\sqrt{\lambda}$. Using this result and Eq. (D24) in Eq. (D23b) then yields the entropy of a single unit (bond) due to the uniaxial deformation as

$$S_{unit} = 3\left[nk\ln 2 - \frac{k}{6}\left(\lambda^2 + \frac{2}{\lambda} \right) \right]. \tag{D25}$$

Since it is presumed that there are n units in a segment, the total entropy for the entire segment is given by

$$S = nS_{unit} = 3n\left[nk\ln 2 - \frac{k}{6}\left(\lambda^2 + \frac{2}{\lambda} \right) \right]. \tag{D26}$$

Using Eq. (D25) in Eq. (D4) then results in, with the help of chain rule,

$$f = \frac{nkT}{l_o}\left(\lambda - \frac{1}{\lambda^2} \right), \tag{D27}$$

where l_0 is the original length of the NR material parallel to the applied force.

The stress-strain relation can then be obtained from Eq. (D27) as

$$\sigma_\lambda = \frac{f}{A_0} = \frac{nkT}{V_0}\left(\lambda - \frac{1}{\lambda^2} \right), \tag{D28}$$

where A_0 is the original (undeformed) area, and V_0 (= $A_0 l_0$) is the riginal volume of the NR specimen containing the segmental units. Eq. (D28) can be rewritten as

[***] Lodge, A. S., 1960. The isotropy of Gaussian molecular networks and the stress-birefringence relations for rubberlike materials cross-linked in stressed states. Colloids and Polymer Science 171, 46–51. “In the undeformed state, the network exhibits elastic isotropy. The relation between the stress and strain tensors is evidently isotropic in the sense that no anisotropic constant tensors are involved.”

$$\sigma_\lambda = \left(NkT\right)\hat{e} = E_{NR}\hat{e}\,, \tag{D29}$$

where N (= n/V_0) is the number of elastically effective segmental units per unit original volume, E_{NR} (= NkT = $3\underline{N}RT$, see Eq. (4.2)) is the elastic modulus of the NR, and $\hat{e}\,(=\lambda-\frac{1}{\lambda^2})$ is the true strain, with λ being the extension ratio (parallel to the applied force) of the elastically effective macromolecular chains, which is identical to the extension ratio of the NR specimen in the context of affine deformation.

APPENDIX E

The four-parameter Burgers model is formed by a Maxwell element and a Kelvin-Voigt (KV) element in series, as illustrated in Fig. E1.

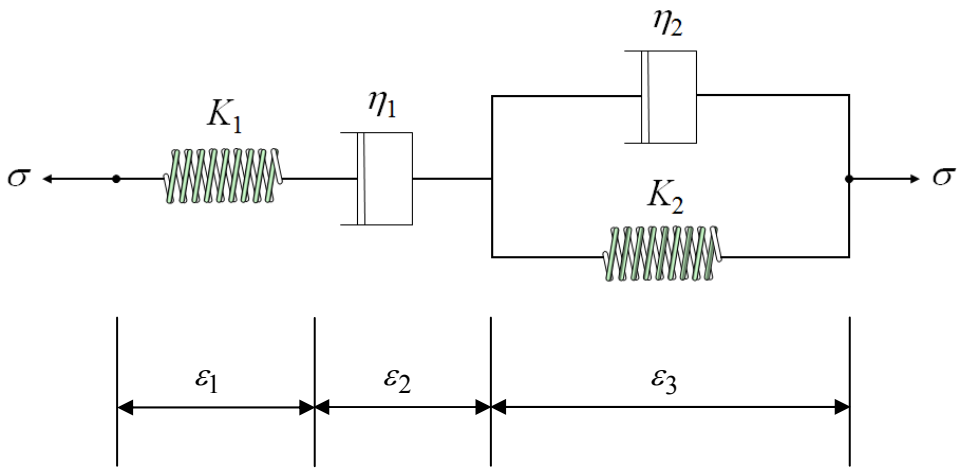

Fig. E1 Burgers model.

It is clear from Fig. E1 that

$$\sigma = K_1\varepsilon_1, \quad \sigma = \eta_1\dot{\varepsilon}_2, \quad \sigma = K_2\varepsilon_3 + \eta_2\dot{\varepsilon}_3, \tag{E1a-c}$$

where σ is the applied stress, and ε_1, ε_2 and ε_3 are, respectively, the strains in the K_1 spring, the η_1 dashpot and the K_2 spring. Also, Fig. E1 shows that the total strain induced by σ is

$$\varepsilon = \varepsilon_1 + \varepsilon_2 + \varepsilon_3. \tag{E2}$$

From (E2) it follows that

$$\dot{\varepsilon}_1 = \dot{\varepsilon} - \dot{\varepsilon}_2 - \dot{\varepsilon}_3, \tag{E3}$$

where the dot "·" denotes the first derivative with respect to time.

Using Eqs. (E1a-c) in Eq. (E3) gives

$$\frac{\dot{\sigma}}{K_1} = \dot{\varepsilon} - \left(\frac{1}{\eta_1} + \frac{1}{\eta_2} \right) \sigma + \frac{K_2 \varepsilon_3}{\eta_2} . \tag{E4}$$

The substitution of Eqs. (E1a) and (E2) into Eq. (E4) leads to

$$\frac{\dot{\sigma}}{K_1} = \dot{\varepsilon} - \left(\frac{1}{\eta_1} + \frac{1}{\eta_2} \right) \sigma + \frac{K_2}{\eta_2} \left(\varepsilon - \frac{\sigma}{K_1} - \varepsilon_2 \right) . \tag{E5}$$

Differentiating Eq. (E5) with respect to time yields, together with Eq. (E1b),

$$\frac{\ddot{\sigma}}{K_1} = \ddot{\varepsilon} - \left(\frac{1}{\eta_1} + \frac{1}{\eta_2} \right) \dot{\sigma} + \frac{K_2}{\eta_2} \dot{\varepsilon} - \frac{K_2}{\eta_2 K_1} \dot{\sigma} - \frac{K_2}{\eta_2} \frac{\sigma}{\eta_1} , \tag{E6}$$

where the double dot "··" stands for the second derivative with respect to time.

Eq. (E6) can be rewritten as

$$\frac{\eta_1 \eta_2}{K_1 K_2} \ddot{\sigma} + \left[\frac{\eta_2}{K_2} + \eta_1 \left(\frac{1}{K_1} + \frac{1}{K_2} \right) \right] \dot{\sigma} + \sigma = \eta_1 \dot{\varepsilon} + \frac{\eta_1 \eta_2}{K_2} \ddot{\varepsilon} . \tag{E7}$$

Eq. (E7) is a second-order inhomogeneous ordinary differential equation (ODE). The independent variable is time, t, and the unknown function is the stress, $\sigma(t)$, which also depends on the strain $\varepsilon(t)$.

Appendix E.1

Derivation of the constitutive equation of the Burgers model for constant strain rate

The following initial conditions, which can represent the actual test conditions, are invoked:

$$\sigma(0) = 0, \quad \varepsilon(0) = 0, \quad \ddot{\varepsilon}(0) = 0 . \tag{E1.1a,b,c}$$

For constant strain rate deformations with $\dot{\varepsilon}(t) = \text{constant}$ and $\ddot{\varepsilon}(t) = 0$, which represent the actual tests performed in the current and many existing studies, Eq. (E1.1c) is satisfied and Eq. (E7) in Appendix E becomes

$$p_2\ddot{\sigma} + p_1\dot{\sigma} + p_0\sigma = \dot{\varepsilon}\,, \tag{E1.2}$$

where, from Eqs. (1.1) and (1.2) in Chapter I together with Eq. (E7),

$$p_2 \equiv \frac{\eta_2}{K_1K_2}, \quad p_1 \equiv \frac{1}{K_1} + \frac{1}{K_2}\left(1 + \frac{\eta_2}{\eta_1}\right), \quad p_0 \equiv \frac{1}{\eta_1}. \tag{E1.3}$$

The general solution of the second-order ODE given in Eq. (E1.2) can be readily obtained to be

$$\sigma = c_1 e^{\lambda_1 t} + c_2 e^{\lambda_2 t} + \frac{\dot{\varepsilon}}{p_0}, \tag{E1.4}$$

where c_1 and c_2 are integration constants to be determined from the initial conditions, and λ_1 and λ_2 are the roots of the characteristic equation of the homogeneous part of Eq. (E1.2) given by

$$\lambda_1 = -\frac{1}{2\eta_1\eta_2}\left[\eta_1\left(K_1 + K_2\right) + \eta_2 K_1 - \sqrt{(\eta_1+\eta_2)^2K_1^2 + \eta_1^2K_2^2 + 2\eta_1^2K_1K_2 - 2\eta_1\eta_2K_1K_2}\right], \tag{E1.5a}$$

$$\lambda_2 = -\frac{1}{2\eta_1\eta_2}\left[\eta_1\left(K_1 + K_2\right) + \eta_2 K_1 + \sqrt{(\eta_1+\eta_2)^2K_1^2 + \eta_1^2K_2^2 + 2\eta_1^2K_1K_2 - 2\eta_1\eta_2K_1K_2}\right]. \tag{E1.5b}$$

Eq. (E1.1a) provides one relation for determining c_1 and c_2. A second relation can be obtained as follows.

From Eqs. (E1c) and (E4) it follows that

$$\dot{\varepsilon} = \frac{\dot{\sigma}(0)}{K_1} + \frac{\sigma(0)}{\eta_1} + \frac{\dot{\sigma}(0)}{K_2} - \frac{\eta_2\ddot{\varepsilon}_3(0)}{K_2}, \tag{E1.6}$$

where use has been made of the fact that $\dot{\varepsilon} = \text{constant}$ at any time $t \geq 0$. With $\sigma(0) = 0$ (see Eq. (E1.1a)) and $\ddot{\varepsilon}_3 = 0$, Eq. (E1.6) gives

$$\dot{\sigma}(0) = \frac{K_1 K_2}{K_1 + K_2}\,\dot{\varepsilon} \tag{E1.7}$$

as the second relation needed.

Using Eq. (E1.4) in Eqs. (E1.1a) and (E1.7) then results in

$$c_1 = -\left[\eta_1 + \frac{1}{\lambda_2 - \lambda_1}\left(K_{eff} + \eta_1\lambda_1\right)\right]\dot{\varepsilon}, \quad c_2 = \frac{1}{\lambda_2 - \lambda_1}\left(K_{eff} + \eta_1\lambda_1\right)\dot{\varepsilon}, \tag{E1.8}$$

where

$$K_{eff} = \frac{K_1 K_2}{K_1 + K_2}\,. \tag{E1.9}$$

Substituting Eq. (E1.8) into Eq. (E1.4) then leads to

$$\sigma(t) = \left[\left(1 + \frac{\lambda_1 \mathrm{e}^{\lambda_2 t} - \lambda_2 \mathrm{e}^{\lambda_1 t}}{\lambda_2 - \lambda_1}\right)\eta_1 + \frac{\mathrm{e}^{\lambda_2 t} - \mathrm{e}^{\lambda_1 t}}{\lambda_2 - \lambda_1} K_{eff}\right]\dot{\varepsilon}\ . \tag{E1.10}$$

Note that $\frac{d\varepsilon}{dt} = \dot{\varepsilon}$ = constant, together with Eq. (A8b), gives $\varepsilon = \dot{\varepsilon} t$ or $t = \frac{\varepsilon}{\dot{\varepsilon}}$. Using this in Eq. (E1.10) finally yields

$$\sigma = \left[\left(1 + \frac{\lambda_1 e^{\lambda_2 \frac{\varepsilon}{\dot{\varepsilon}}} - \lambda_2 e^{\lambda_1 \frac{\varepsilon}{\dot{\varepsilon}}}}{\lambda_2 - \lambda_1}\right)\eta_1 + \frac{e^{\lambda_2 \frac{\varepsilon}{\dot{\varepsilon}}} - e^{\lambda_1 \frac{\varepsilon}{\dot{\varepsilon}}}}{\lambda_2 - \lambda_1} K_{eff}\right]\dot{\varepsilon} \tag{E1.11}$$

as the stress-strain relation provided by the four-parameter Burgers model (see Fig. E1), which is listed as Eq. (4.3) and has been used to generate the relevant numerical results presented in Section 4.7.

Appendix E.2

Derivation of the stress relaxation function of the Burgers model

For a constant applied strain with $\varepsilon = \varepsilon_0$ and $\dot{\varepsilon} = \ddot{\varepsilon} = 0$, Eq. (E7) in Appendix E becomes

$$\frac{\eta_1\eta_2}{K_1K_2}\ddot{\sigma}+\left[\frac{\eta_2}{K_2}+\eta_1\left(\frac{1}{K_1}+\frac{1}{K_2}\right)\right]\dot{\sigma}+\sigma=0\,. \tag{E2.1}$$

The general solution of Eq. (E2.1), which is a homogenous, second order ODE, is

$$\sigma(t)=c_1e^{\lambda_1 t}+c_2e^{\lambda_2 t} \tag{E2.2}$$

where c_1 and c_2 are integration constants to be determined from the initial conditions, and λ_1 and λ_2 are the roots of the characteristic equation of Eq. (E2.1) given by

$$\lambda_1=-\frac{K_1K_2}{2\eta_1\eta_2}\left[\left(\frac{\eta_1}{K_1}+\frac{\eta_1}{K_2}+\frac{\eta_2}{K_2}\right)-\sqrt{\left(\frac{\eta_1}{K_1}+\frac{\eta_1}{K_2}+\frac{\eta_2}{K_2}\right)^2-4\frac{\eta_1\eta_2}{K_1K_2}}\right], \tag{E2.3a}$$

$$\lambda_2=-\frac{K_1K_2}{2\eta_1\eta_2}\left[\left(\frac{\eta_1}{K_1}+\frac{\eta_1}{K_2}+\frac{\eta_2}{K_2}\right)+\sqrt{\left(\frac{\eta_1}{K_1}+\frac{\eta_1}{K_2}+\frac{\eta_2}{K_2}\right)^2-4\frac{\eta_1\eta_2}{K_1K_2}}\right]. \tag{E2.3b}$$

Substituting the first initial condition, $\sigma(0)=\sigma_0$, into Eq. (E2.2) gives

$$\sigma(0)=c_1+c_2=\sigma_0 \tag{E2.4}$$

A second initial condition is obtained as follows. Differentiating Eq. (E1a) with respect to time gives

$$\dot{\sigma}=K_1\dot{\varepsilon}_1\,. \tag{E2.5}$$

Using Eqs. (E1b), (E3), (E2.2) and (E2.5) with $\dot{\varepsilon}(0)=\dot{\varepsilon}_3(0)=0$ yields

$$\dot{\sigma}(0)=c_1\lambda_1+c_2\lambda_2=-\frac{K_1}{\eta_1}\sigma_0 \tag{E2.6}$$

as the second relation needed.

Using Eq. (E2.2) in Eqs. (E2.4) and (E2.5) then results in

$$\frac{c_1}{\sigma_0} \equiv \bar{K}_1 = \frac{-\frac{\eta_2}{K_2} + \left(\frac{\left(\frac{\eta_1}{K_1} + \frac{\eta_1}{K_2} + \frac{\eta_2}{K_2} \right) + \sqrt{\left(\frac{\eta_1}{K_1} + \frac{\eta_1}{K_2} + \frac{\eta_2}{K_2} \right)^2 - 4\frac{\eta_1\eta_2}{K_1K_2}}}{2} \right)}{\sqrt{\left(\frac{\eta_1}{K_1} + \frac{\eta_1}{K_2} + \frac{\eta_2}{K_2} \right)^2 - 4\frac{\eta_1\eta_2}{K_1K_2}}}, \qquad \text{(E2.7a)}$$

$$\frac{c_2}{\sigma_0} \equiv \bar{K}_2 = \frac{\frac{\eta_2}{K_2} - \left(\frac{\left(\frac{\eta_1}{K_1} + \frac{\eta_1}{K_2} + \frac{\eta_2}{K_2} \right) - \sqrt{\left(\frac{\eta_1}{K_1} + \frac{\eta_1}{K_2} + \frac{\eta_2}{K_2} \right)^2 - 4\frac{\eta_1\eta_2}{K_1K_2}}}{2} \right)}{\sqrt{\left(\frac{\eta_1}{K_1} + \frac{\eta_1}{K_2} + \frac{\eta_2}{K_2} \right)^2 - 4\frac{\eta_1\eta_2}{K_1K_2}}}. \qquad \text{(E2.7b)}$$

Eq. (E2.2) can finally be written as (see Table 5.1):

$$\sigma(t) = \left(\bar{K}_1 e^{-\frac{t}{\tau_1}} + \bar{K}_2 e^{-\frac{t}{\tau_2}} \right) \sigma_0 \qquad \text{(E2.8)}$$

where $\bar{K}_1$ and $\bar{K}_2$ are defined in Eqs. (E2.7a,b), and τ_1 and τ_2 are the reciprocals of λ_1 and λ_2 (see Eqs. (E2.3a) and (E2.3b)) given by

$$\tau_1 = \frac{2\frac{\eta_1\eta_2}{K_1K_2}}{\left(\frac{\eta_1}{K_1} + \frac{\eta_1}{K_2} + \frac{\eta_2}{K_2} \right) - \sqrt{\left(\frac{\eta_1}{K_1} + \frac{\eta_1}{K_2} + \frac{\eta_2}{K_2} \right)^2 - 4\frac{\eta_1\eta_2}{K_1K_2}}}, \qquad \text{(E2.9a)}$$

$$\tau_2 = \frac{2\frac{\eta_1\eta_2}{K_1K_2}}{\left(\frac{\eta_1}{K_1} + \frac{\eta_1}{K_2} + \frac{\eta_2}{K_2} \right) + \sqrt{\left(\frac{\eta_1}{K_1} + \frac{\eta_1}{K_2} + \frac{\eta_2}{K_2} \right)^2 - 4\frac{\eta_1\eta_2}{K_1K_2}}}. \qquad \text{(E2.9b)}$$

Appendix E.3

Derivation of the creep function of the Burgers model

The strain conditions of the Maxwell and Kelvin-Voigt elements in the four-parameter Burgers model for creep analysis are shown in Fig. E2.

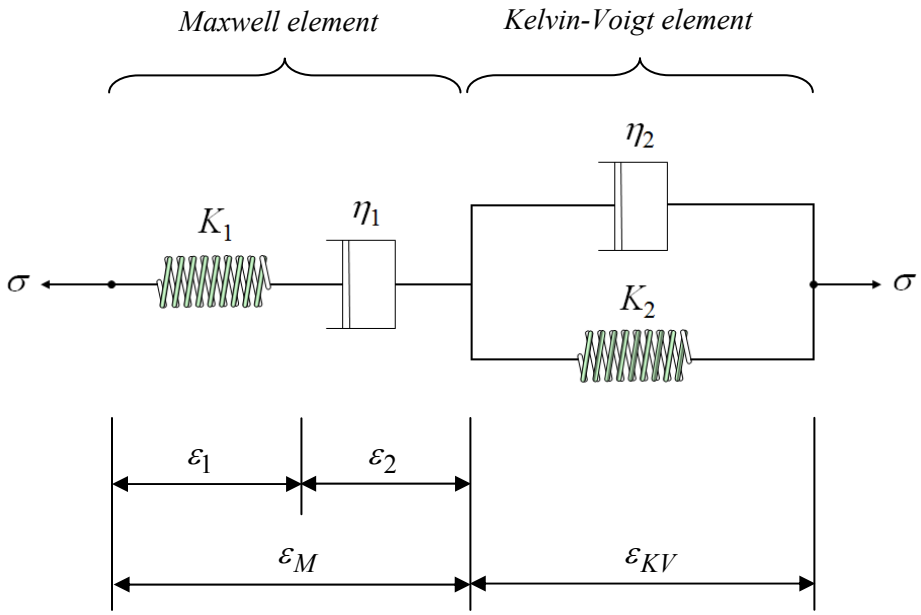

Fig. E2 Strain conditions in the Burgers model for creep analysis.

It is clear from Fig. E2 that

$$\varepsilon(t) = \varepsilon_M(t) + \varepsilon_{KV}(t), \tag{E3.1}$$

where ε_M and ε_{KV} are the strains in the Maxwell and Kelvin-Voigt elements, respectively. The following analysis is thus separated into two parts, i.e., one part for the Maxwell element, and the other for the Kelvin-Voigt element, in order to determine ε_M and ε_{KV} individually.

Maxwell element

In Fig. E2, σ is the applied stress, and ε_1 and ε_2 are, respectively, the strains in the K_1 spring and the η_1 dashpot. The stresses in the K_1 spring and the η_1 dashpot is

$$\sigma = K_1 \varepsilon_1, \ \sigma = \eta_1 \dot{\varepsilon}_2 \tag{E3.2a,b}$$

Also, Fig. E2 shows that

$$\varepsilon_M = \varepsilon_1 + \varepsilon_2 . \tag{E3.3}$$

From Eq. (E3.3) it follows that

$$\dot{\varepsilon}_M = \dot{\varepsilon}_1 + \dot{\varepsilon}_2 , \tag{E3.4}$$

where the dot "·" denotes the first derivative with respect to time.

Subtituting Eqs. (E3.2a,b) into Eq. (E3.4) gives

$$\dot{\varepsilon}_M = \frac{\dot{\sigma}}{K_1} + \frac{\sigma}{\eta_1} . \tag{E3.5}$$

Integrating Eq. (E3.5) leads to

$$\varepsilon_M (t) = \frac{\sigma}{K_1} + \frac{\sigma}{\eta_1} t . \tag{E3.6}$$

where use has been made of the initial conditions[ce] $\varepsilon_M \big|_{t=0} = 0 = \sigma \big|_{t=0}$.

Kelvin-Voigt element

The strain in the KV element is denoted by ε_{KV} (see Fig. E2). From Fig. E2, it is evident that

$$\varepsilon_{KV} = \varepsilon_{K_2} = \varepsilon_{\eta_2} , \tag{E3.7a,b}$$

where ε_{K_2} and ε_{η_2} are, respectively, the strain in the K_2 spring and the η_2 dashpot.

[ce] This time ($t = 0$) refers to the time at the onset of loading. The applied stress is increased from zero ($\sigma(t = 0) = 0$) up to the desired constant applied stress, σ_0. The time at which this particular stress level is achieved is denoted as t_0 ($\sigma(t = t_0) = \sigma_0$). In order to simplify the numerical calculations involved in the creep analysis, t_0 is taken as the zero time.

Also, it can be seen from Fig. E2 that

$$\sigma = \sigma_{K_2} + \sigma_{\eta_2}, \tag{E3.8}$$

where

$$\sigma_{K_2} = K_2 \varepsilon_{KV}, \ \sigma_{\eta_2} = \eta_2 \dot{\varepsilon}_{KV}. \tag{E3.9a,b}$$

Subtituting Eqs. (E3.9a,b) in Eq. (E3.8) gives

$$\frac{\sigma_M}{\eta_2} = \dot{\varepsilon}_{KV} + \frac{K_2}{\eta_2} \varepsilon_{\mathrm{KV}}. \tag{E3.10}$$

For σ = constant, the general solution of Eq. (E3.10), which is a first-order ordinary differential equation, can be readily obtained as

$$\varepsilon_{KV} = ce^{-\frac{t}{\tau_B}} + \frac{\sigma}{K_2}, \tag{E3.11}$$

where $\tau_B = \dfrac{\eta_2}{K_2}$, and c is a constant to be determined from an initial condition.

Using the initial condition for the strain: i.e., $\varepsilon_{KV} = 0$ at $t = 0$, in Eq. (E3.11) gives

$$c = -\frac{\sigma}{K_2}. \tag{E3.12}$$

Inserting Eq. (E3.12) into Eq. (E3.11) yields

$$\varepsilon_{KV}(t) = \frac{\sigma_{KV}}{K_2}\left(1 - e^{-\frac{t}{\tau_B}}\right) \tag{E3.13}$$

Substituting Eqs. (E3.6) and (E3.13) into Eq. (E3.1) finally yields the creep function as

$$\varepsilon(t)=\left[\frac{1}{K_1}+\frac{t}{\eta_1}+\frac{1}{K_2}\left(1-e^{-\frac{t}{\tau_B}}\right)\right]\sigma_0, \quad t\geq t_0 \tag{E3.14}$$

where $\sigma_0 = \sigma\ (t \geq t_0)$ is a constant applied stress, and $\tau_B=\frac{\eta_2}{K_2}$ is a retardation time, pertinent to the KV element. Eq. (E3.14) is the creep function of the Burgers model, which is listed in Table 6.2 and has been used to obtain the relevant numerical results presented in Fig. 6.7.

From Eq. (E3.14), the creep compliance of the Burgers model is given by

$$J(t)=\frac{\varepsilon(t)}{\sigma_0}=\frac{1}{K_1}+\frac{1}{K_2}\left(1-e^{-\frac{t}{\tau_B}}\right)+\frac{t}{\eta_1} \tag{E3.15}$$

where the first term represents an elastic term, the second term describes the viscoelastic response, and the third term stands for the viscous effect.

APPENDIX F

A two-term generalized Maxwell ($GM^{n=2}$) model is shown in Fig. F.

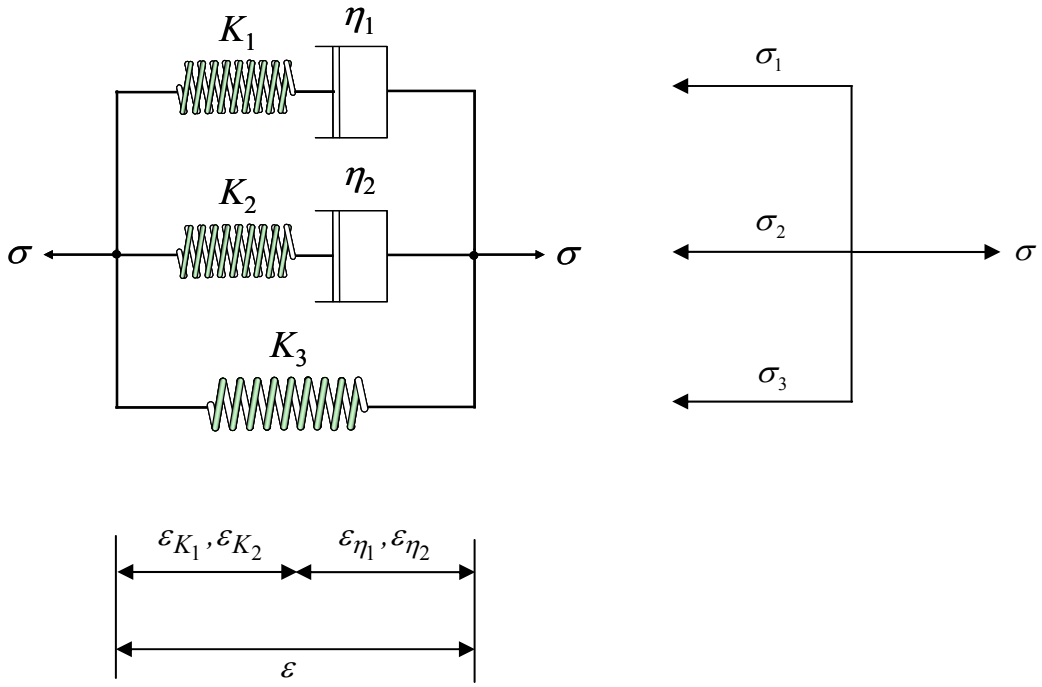

Fig. F $GM^{n=2}$ model.

From Fig. F, it can be readily seen that

$$\sigma_1 = K_1\varepsilon_{K_1} = \eta_1\dot{\varepsilon}_{\eta_1},\ \sigma_2 = K_2\varepsilon_{K_2} = \eta_2\dot{\varepsilon}_{\eta_2},\ \sigma_3 = K_3\varepsilon, \qquad \text{(F1a–c)}$$

where σ is the applied stress, and σ_1, σ_2 and σ_3 are the branch stresses, with

$$\sigma = \sigma_1 + \sigma_2 + \sigma_3 \qquad \text{(F2)}$$

Fig. F also shows that

$$\varepsilon = \varepsilon_{K_1} + \varepsilon_{\eta_1} \qquad \text{(F3a)}$$

$$\varepsilon = \varepsilon_{K_2} + \varepsilon_{\eta_2} \qquad \text{(F3b)}$$

It can be shown that the governing differential equation of the $GM^{n=2}$ model is (e.g., Findley et al., 1976)

$$\frac{\eta_1\eta_2}{K_1K_2}\ddot{\sigma}+\left(\frac{\eta_1}{K_1}+\frac{\eta_2}{K_2}\right)\dot{\sigma}+\sigma = \frac{\eta_1\eta_2}{K_1K_2}\left(K_1+K_2+K_3\right)\ddot{\varepsilon}+\left[\frac{\eta_1}{K_1}\left(K_1+K_3\right)+\frac{\eta_2}{K_2}\left(K_2+K_3\right)\right]\dot{\varepsilon}+K_3\varepsilon \tag{F4}$$

Eq. (F4) is a second order non-homogenous ordinary linear (i.e., first degree) differential equation that represents the stress-strain behavior of the four-parameter model. The independent variable is time, t, and the unknown function is the strain, $\varepsilon(t)$ and the stress, depends upon the strain, i.e., $\sigma(\varepsilon(t))$. Eq. (4) can be written as

$$p_2\ddot{\sigma}+p_1\dot{\sigma}+p_0\sigma = q_2\ddot{\varepsilon}+q_1\dot{\varepsilon}+q_0\varepsilon \tag{F5}$$

where p_i and q_i (i = 0, 1, 2) are constant coefficients whose values are dependent on the parameters of the $GM^{n=2}$ model as follows:

$$p_2=\frac{\eta_1\eta_2}{K_1K_2},\ p_1=\frac{\eta_1}{K_1}+\frac{\eta_2}{K_2},\ p_0=1,$$
$$q_2=\frac{\eta_1\eta_2}{K_1K_2}\left(K_1+K_2+K_3\right),\ q_1=\frac{\eta_1}{K_1}\left(K_1+K_3\right)+\frac{\eta_2}{K_2}\left(K_2+K_3\right),\ \text{and}\ q_0=K_3. \tag{F6}$$

Appendix F.1

Derivation of the constitutive equation of the $GM^{n=2}$ model for constant strain rate

For a constant strain rate experiment, $\dot{\varepsilon}$ = constant and $\ddot{\varepsilon}$ = 0, and therefore Eq. (F4) in Appendix F reduces to

$$\frac{\eta_1\eta_2}{K_1K_2}\ddot{\sigma}+\left(\frac{\eta_1}{K_1}+\frac{\eta_2}{K_2}\right)\dot{\sigma}+\sigma=\left[\frac{\eta_1}{K_1}\left(K_1+K_3\right)+\frac{\eta_2}{K_2}\left(K_2+K_3\right)\right]\dot{\varepsilon}+K_3\varepsilon \tag{F1.1}$$

Eq. (F1.1) can be written in terms of the constant coefficients given in relations (F6) with $q_2 = 0$ as follows:

$$p_2\ddot{\sigma} + p_1\dot{\sigma} + p_0\sigma = q_1\dot{\varepsilon} + q_0\varepsilon \tag{F1.2}$$

The complete solution of the Eq. (F1.2), $\sigma(t)$, will comprise the homogenous solution, $\sigma_H(t)$ and particular solution, $\sigma_p(t)$,

$$\sigma = \sigma_H + \sigma_p \tag{F1.3}$$

The homogenous part of Eq. (F1.2) with regard to relations (F9) can be written as:

$$p_2\ddot{\sigma}_H + p_1\dot{\sigma}_H + p_0\sigma_H = 0 \tag{F1.4}$$

for which a general solution is,

$$\sigma_H = c_1 e^{\lambda_1 t} + c_2 e^{\lambda_2 t} \tag{F1.5}$$

where c_1 and c_2 are constants that can be determined from the initial conditions, and λ_1 and λ_2 are the roots of the characteristic equation of Eq. (F1.4), i.e.,

$$p_2\lambda^2 + p_1\lambda + p_0 = 0\,.$$

The roots thus are,

$$\lambda_{1,2} = -\frac{1}{2p_2}\left(p_1 \mp \sqrt{p_1^2 - 4p_2p_0}\right)$$

Using the constant coefficients as defined in relations (F6), the explicit form of the roots are

$$\lambda_1 = -\frac{K_1}{\eta_1} \tag{F1.6a}$$

$$\lambda_2 = -\frac{K_2}{\eta_2} \tag{F1.6b}$$

Substituting a trial solution, i.e., $\sigma_p = A\varepsilon + B$, and its respective derivatives into Eq. (F1.2) gives

$$A = K_3 \text{ and } B = \left(\eta_1 + \eta_2\right)\dot{\varepsilon} \;\Rightarrow\; \sigma_p = K_3\varepsilon + \left(\eta_1 + \eta_2\right)\dot{\varepsilon}\ . \tag{F1.7}$$

The complete solution thus can be written by using Eq. (F1.5) and (F1.7) in Eq. (F1.3) as

$$\sigma(t) = K_3\varepsilon(t) + c_1 e^{\lambda_1 t} + c_2 e^{\lambda_2 t} + \left(\eta_1 + \eta_2\right)\dot{\varepsilon} \tag{F1.8}$$

where λ_1 and λ_2 are given by relations (F1.6a) and (F1.6b), respectively. The c_1 and c_2 constants are determined to be $c_1 = -\eta_1\dot{\varepsilon}$ and $c_2 = -\eta_2\dot{\varepsilon}$ using the initial conditions $\varepsilon(0) = 0$ and $\sigma(0) = 0$ in Eq. (F1.8) together with $\dot{\sigma} = K_3\dot{\varepsilon}$ (from Eq. (F1c)) in the first time derivative of Eq. (F1.8).

Back substituting these relations together with relations (F1.6a) and (F1.6b) into Eq. (F1.8) yields the final solution of Eq. (F1.1) as follows:

$$\sigma(t) \;=\; \eta_1\left(1 - e^{-\frac{t}{\tau_1}}\right)\dot{\varepsilon} + \eta_2\left(1 - e^{-\frac{t}{\tau_2}}\right)\dot{\varepsilon} + K_3\varepsilon \tag{F1.9}$$

where $\tau_1 = \dfrac{K_1}{\eta_1}$ and $\tau_2 = \dfrac{K_2}{\eta_2}$. This constitutive equation is given as Eq. (4.7) and has been used to obtain the relevant numerical results presented in Section 4.7. From Eq. (F1.9), the elastic (Young's) modulus of the model shown in Fig. F1 can be analytically determined as

$$E = \lim_{\varepsilon \to 0} \frac{d\sigma}{d\varepsilon} = K_1 + K_2 + K_3\,. \tag{F1.10}$$

Appendix F.2

Derivation of the stress relaxation function of the GM$^{n=2}$ model

For a constant applied strain with $\varepsilon = \varepsilon_0$ and $\dot{\varepsilon} = \ddot{\varepsilon} = 0$, Eq. (F4) in Appendix F becomes

$$\ddot{\sigma} + \left(\frac{K_1}{\eta_1} + \frac{K_2}{\eta_2} \right) \dot{\sigma} + \frac{K_1 K_2}{\eta_1 \eta_2} \sigma = \frac{K_1 K_2 K_3}{\eta_1 \eta_2} \varepsilon_0 \tag{F2.1}$$

The general solution of Eq. (F2.1), which is again a second-order ODE, can be readily obtained as

$$\sigma(t) = c_1 e^{-\frac{t}{\tau_1}} + c_2 e^{-\frac{t}{\tau_2}} + K_3 \varepsilon_0 \tag{F2.2}$$

where $\tau_1 = \frac{\eta_1}{K_1}$ and $\tau_2 = \frac{\eta_2}{K_2}$, and c_1 and c_2 are constants to be determined from two initial conditions. The first initial condition is $\sigma(0) = \sigma_0$. A second initial condition on $\dot{\sigma}(0)$ is determined by differentiating Eq. (F2) in tandem with Eq. (F1a-c) with respect to time and evaluating it at $t = 0$.

$$\dot{\sigma}(0) = K_1 \dot{\varepsilon}_{K_1}(0) + K_2 \dot{\varepsilon}_{K_2}(0) + K_3 \dot{\varepsilon}(0) \tag{F2.3}$$

At time $t = 0$, the springs are displaced with an initial strain $\varepsilon(0) = \varepsilon_0$ but the dashpots are not (instantaneously) deformed. Thus, from Eqs. (F3a) and (F3b),

$$\varepsilon(0) = \varepsilon_{K_1}(0) = \varepsilon_0 \tag{F2.4a}$$

$$\varepsilon(0) = \varepsilon_{K_2}(0) = \varepsilon_0 \tag{F2.4b}$$

Differentiating Eqs. (F3a) and (F3b) with respect to time and setting $\dot{\varepsilon}(0) = 0$ gives

$$\dot{\varepsilon}_{K_1}(0) = -\dot{\varepsilon}_{\eta_1}(0) \tag{F2.5a}$$

$$\dot{\varepsilon}_{K_2}(0) = -\dot{\varepsilon}_{\eta_2}(0) \tag{F2.5b}$$

From Eqs. (F1a), (F1c), (F2.4a) and (F2.4b),

$$\dot{\varepsilon}_{\eta_1} = \frac{K_1}{\eta_1} \varepsilon_{K_1}(0) = \frac{\varepsilon_0}{\tau_1} \tag{F2.6a}$$

$$\dot{\varepsilon}_{\eta_2} = \frac{K_2}{\eta_2} \varepsilon_{K_2}(0) = \frac{\varepsilon_0}{\tau_2} \tag{F2.6b}$$

Substituting Eqs. (F2.6a) and (F2.6b) into Eqs. (F2.5a) and (F2.5b) gives

$$\dot{\varepsilon}_{K_1}(0) = \frac{\varepsilon_0}{\tau_1} \tag{F2.7a}$$

$$\dot{\varepsilon}_{K_2}(0) = \frac{\varepsilon_0}{\tau_2} \tag{F2.7b}$$

Substituting Eqs. (F2.7a) and (F2.7b) together with $\dot{\varepsilon}(0) = 0$ into Eq. (F2.3) gives the second initial condition necessary to determine the c_1 and c_2 constants as

$$\dot{\sigma}(0) = -K_1 \frac{\varepsilon_0}{\tau_1} - K_2 \frac{\varepsilon_0}{\tau_2} \tag{F2.8}$$

Using these two initial conditions, the c_1 and c_2 constants are evaluated as follows:

$$c_1 = \left(\frac{\tau_1}{\tau_1 - \tau_2} \right) \sigma_0 - \left(\frac{K_1\tau_2 + K_3\tau_1 + K_2\tau_1}{\tau_1 - \tau_2} \right) \varepsilon_0 ,$$

$$c_2 = \left(\frac{\tau_2}{\tau_2 - \tau_1} \right) \sigma_0 + \left(\frac{K_1\tau_2 + K_3\tau_2 + K_2\tau_1}{\tau_1 - \tau_2} \right) \varepsilon_0 .$$

The general relationship between the stress decay ($\sigma(t)$), the stress relaxation modulus ($E_r(t)$), and the initial strain, ε_0, is given by

$$E_r(t) = \frac{\sigma(t)}{\varepsilon_0} \tag{F2.9}$$

Using the first initial condition, i.e., $\sigma(0) = \sigma_0$, the relation shown in Eq. (F2.9) can be written as

$$\sigma_0 = E_i \cdot \varepsilon_0 \tag{F2.10}$$

If the instantaneous modulus of the composite just before the beginning of the relaxation test, i.e., tensile modulus at time $t = 0^-$, is taken to be

$$E_i = K_1 + K_2 + K_3 . \tag{F2.11}$$

then the expressions for the constants, using Eqs. (F2.10) and (F2.11), are

$$c_1 = K_1\varepsilon_0\,,$$

$$c_2 = K_2\varepsilon_0\,.$$

Substituting these expressions into Eq. (F2.2) yields the relaxation function as follows:

$$\sigma(t) = \left(K_1 e^{-\frac{t}{\tau_1}} + K_2 e^{-\frac{t}{\tau_2}} + K_3 \right)\varepsilon_o\,, \tag{F2.12}$$

where the stress relaxation modulus, $E_r(t)$ is given by

$$E_r(t) = K_1 e^{-\frac{t}{\tau_1}} + K_2 e^{-\frac{t}{\tau_2}} + K_3\,. \tag{F2.13}$$

Eq. (F2.12) is the stress relaxation function of the GM$^{n=2}$ model, which is listed in Table 5.1 and has been used to obtain the relevant numerical results presented in Fig. 5.4.

Appendix F.3

Derivation of the normalized Prony series for the GM$^{n=2}$ model

The stress relaxation modulus given by Eq. (F2.13) can be expressed by a series expansion known as the Prony series. Eq. (F2.13) can be represented by a two-term Prony series as follows,

$$E_r(t) = \sum_{i=1}^{2} K_i e^{-\frac{t}{\tau_i}} + K_3\,. \tag{F3.1}$$

From Eq. (F2.13), the relaxation modulus at the time limits $t = 0$ (i.e., the instantaneous modulus) and $t = \infty$ (i.e., the equilibrium modulus) are:

$$E_r(0) \equiv E_0 = K_1 + K_2 + K_3 \tag{F3.2a}$$

$$\lim_{t\to\infty} E_r(t) \equiv E_\infty = K_3 \tag{F3.2b}$$

The relaxation modulus at $t = 0$ (see Eq. (F2.13)), normalized with respect to E_0 given by Eq. (F3.2a), is

$$\frac{E_r(0)}{E_0} = \hat{E}_0 = 1 \tag{F3.3}$$

The normalized relaxation modulus (with respect to E_0) at $t = \infty$, i.e., $\hat{E}_\infty$, can be computed from Eqs. (F3.2a) and (F3.2b) as follows:

$$\frac{E_\infty}{E_0} = \frac{K_3}{K_1 + K_2 + K_3} = 1 - \frac{K_1 + K_2}{K_1 + K_2 + K_3} = 1 - \sum_{i=1}^{2} \hat{K}_i \tag{F3.4}$$

where

$$\hat{K}_i = \frac{K_i}{K_1 + K_2 + K_3} = \frac{K_i}{E_0} \quad (i = 1,2) \tag{F3.5}$$

is the normalized stiffness (of springs 1 and 2).

From Eqs. (F3.2b) and (F3.4),

$$\frac{K_3}{E_0} = \hat{K}_3 = 1 - \sum_{i=1}^{2} \hat{K}_i \tag{F3.6}$$

The Prony series can then be written in terms of the normalized parameters by substituting Eq. (F3.6) into Eq. (F3.1) as follows:

$$\hat{E}_r(t) = 1 - \sum_{i=1}^{2} \hat{K}_i + \sum_{i=1}^{2} \hat{K}_i \cdot e^{-\frac{t}{\tau_i}}$$

$$\hat{E}_r(t) = 1 - \sum_{i=1}^{2} \hat{K}_i \left(1 - e^{-\frac{t}{\tau_i}} \right) \tag{F3.7}$$

where $\hat{K}_i$ is defined in Eq. (F3.5), $\tau_i = \frac{\eta_i}{K_i}$ and $i = 1, 2$.

Appendix F.4

Derivation of the creep function of the GM$^{n=2}$ model

For a constant applied stress with $\sigma = \sigma_0$ and $\dot{\sigma} = \ddot{\sigma} = 0$, Eq. (F4) in Appendix F becomes

$$\sigma_0 = \frac{\eta_1\eta_2}{K_1K_2}\left(K_1 + K_2 + K_3\right)\ddot{\varepsilon} + \left(\frac{\eta_1}{K_1}\left(K_1 + K_3\right) + \frac{\eta_2}{K_2}\left(K_2 + K_3\right)\right)\dot{\varepsilon} + K_3\varepsilon \qquad \text{(F4.1)}$$

The general solution of Eq. (F4.1), which is a second-order linear ODE, can be readily obtained as

$$\varepsilon(t) = c_1 e^{-\psi_1 t} + c_2 e^{-\psi_2 t} + \frac{\sigma_0}{K_3} \qquad \text{(F4.2)}$$

where c_1 and c_2 are constants to be determined from two initial conditions and ψ_1 and ψ_2 are the roots of the characteristic equation of Eq. (F4.1), i.e.,

$$q_2\psi^2 + q_1\psi + q_0 = 0\,.$$

The roots thus are,

$$\psi_{1,2} = \frac{1}{2q_2}\left(q_1 \mp \sqrt{q_1^2 - 4q_2q_0}\right)$$

Using the constant coefficients as defined in relations (F6), the explicit form of the roots are

$$\psi_1 = \frac{1}{2\eta_1\eta_2\left(K_1 + K_2 + K_3\right)}\left(\begin{array}{l}\left(K_1K_2\eta_1 + K_1K_2\eta_2 + K_1K_3\eta_2 + K_2K_3\eta_1\right) \\ -\sqrt{\begin{array}{l}\left(K_1K_2\eta_1\right)^2 + \left(K_1K_2\right)^2\eta_2\left(2\eta_1 + \eta_2\right) - 2K_1K_2K_3\eta_1\eta_2\left(K_1 + K_2 + K_3\right) \\ +2\left(K_1\eta_2\right)^2K_2K_3 + \left(K_1K_3\eta_2\right)^2 + 2\left(K_2\eta_1\right)^2K_1K_3 + \left(K_2K_3\eta_1\right)^2\end{array}}\end{array}\right)$$

(F4.3a)

$$\psi_2 = \frac{1}{2\eta_1\eta_2\left(K_1 + K_2 + K_3\right)}\left(\begin{array}{l}\left(K_1K_2\eta_1 + K_1K_2\eta_2 + K_1K_3\eta_2 + K_2K_3\eta_1\right) \\ +\sqrt{\begin{array}{l}\left(K_1K_2\eta_1\right)^2 + \left(K_1K_2\right)^2\eta_2\left(2\eta_1 + \eta_2\right) - 2K_1K_2K_3\eta_1\eta_2\left(K_1 + K_2 + K_3\right) \\ +2\left(K_1\eta_2\right)^2K_2K_3 + \left(K_1K_3\eta_2\right)^2 + 2\left(K_2\eta_1\right)^2K_1K_3 + \left(K_2K_3\eta_1\right)^2\end{array}}\end{array}\right)$$

(F4.3b)

The first initial condition is $\varepsilon(0) = \varepsilon_o$. A second initial condition on $\dot{\varepsilon}(0)$ is determined by differentiating Eq. (B6a) with respect to time and evaluating it at $t = 0$.

$$\dot{\sigma}(0) = K_1\dot{\varepsilon}_{K_1}(0) + K_2\dot{\varepsilon}_{K_2}(0) + K_3\dot{\varepsilon}(0) \tag{F4.4}$$

At time $t = 0$, the springs are displaced with an initial strain $\varepsilon(0) = \varepsilon_0$ but the dashpots are not (instantaneously) deformed. Thus, from Eqs. (F3a) and (F3b),

$$\varepsilon(0) = \varepsilon_{K_1}(0) = \varepsilon_0 \tag{F4.5a}$$

$$\varepsilon(0) = \varepsilon_{K_2}(0) = \varepsilon_0 \tag{F4.5b}$$

Differentiating Eqs. (F3a) and (F3b) with respect to time gives

$$\dot{\varepsilon}_{K_1}(0) = \dot{\varepsilon}(0) - \dot{\varepsilon}_{\eta_1}(0) \tag{F4.6a}$$

$$\dot{\varepsilon}_{K_2}(0) = \dot{\varepsilon}(0) - \dot{\varepsilon}_{\eta_2}(0) \tag{F4.6b}$$

From Eqs. (F1a), (F1b), (F4.5a) and (F4.5b),

$$\dot{\varepsilon}_{\eta_1} = \frac{K_1}{\eta_1}\varepsilon_{K_1}(0) = \frac{\varepsilon_0}{\tau_{c21}} \tag{F4.7a}$$

$$\dot{\varepsilon}_{\eta_2} = \frac{K_2}{\eta_2}\varepsilon_{K_2}(0) = \frac{\varepsilon_0}{\tau_{c22}} \tag{F4.7b}$$

where $\tau_{c21} = \frac{\eta_1}{K_1}$ and $\tau_{c22} = \frac{\eta_2}{K_2}$.

Substituting Eqs. (F4.7a) and (F4.7b) into Eqs. (F4.6a) and (F4.6b) gives

$$\dot{\varepsilon}_{K_1}(0) = \dot{\varepsilon}_0 - \frac{\varepsilon_0}{\tau_{c21}} \tag{F4.8a}$$

$$\dot{\varepsilon}_{K_2}(0) = \dot{\varepsilon}_0 - \frac{\varepsilon_0}{\tau_{c22}} \tag{F4.8b}$$

where $\dot{\varepsilon}(0) = \varepsilon_0$.

Substituting Eqs. (F4.8a) and (F4.8b) together with $\dot{\sigma}(0) = 0$ into Eq. (F4.4) gives the second initial condition necessary to determine the c_1 and c_2 constants.

$$\dot{\varepsilon}_0 = \frac{1}{K_1 + K_2 + K_3}\left(\frac{K_1}{\tau_{c21}} + \frac{K_2}{\tau_{c22}}\right)\varepsilon_0 \tag{F4.9}$$

Using these two initial conditions, the c_1 and c_2 constants are evaluated as follows:

$$c_1 \equiv \bar{K}_1 = \frac{1}{\psi_1 - \psi_2}\left[\left[\frac{1}{K_{eff}}\left(\frac{K_1}{\tau_{c21}} + \frac{K_2}{\tau_{c22}}\right) - \psi_2\right] J_0\sigma_0 + \frac{\sigma_0}{K_3}\psi_2\right]$$

$$c_2 \equiv \bar{K}_2 = \frac{1}{\psi_1 - \psi_2}\cdot\left[\left[\psi_1 - \frac{1}{K_{eff}}\left(\frac{K_1}{\tau_{c21}} + \frac{K_2}{\tau_{c22}}\right)\right] J_0\sigma_0 - \frac{\sigma_0}{K_3}\psi_1\right]$$

where $K_{eff} = K_1 + K_2 + K_3$ and use has been made of the relationship between the initial strain and the initial creep compliance, i.e., $\varepsilon_0 = J_0\sigma_0$.

Substituting the expressions for the c_1 and c_2 constants into Eq. (F4.2) yields the creep function as follows:

$$\varepsilon(t) = \bar{K}_1 e^{-\psi_1 t} + \bar{K}_2 e^{-\psi_2 t} + \bar{K}_3\sigma_o \tag{F4.10}$$

where $\bar{K}_3 = \frac{1}{K_3}$.

Eq. (F4.10) is the creep function of the GM$^{n=2}$ model, which is listed in Table 6.2 and has been used to obtain the relevant numerical results presented in Fig. 6.7.

APPENDIX G

Derivation of the constitutive equation of the five-parameter model for constant strain rate

The five-parameter model proposed in this study includes a Maxwell element and a GM element (unit) in series, as shown in Fig. G. The subscript '*f*' that was used in Section 4.6.3 to denote to the parameters of the five-parameter model is not used in the following derivations.

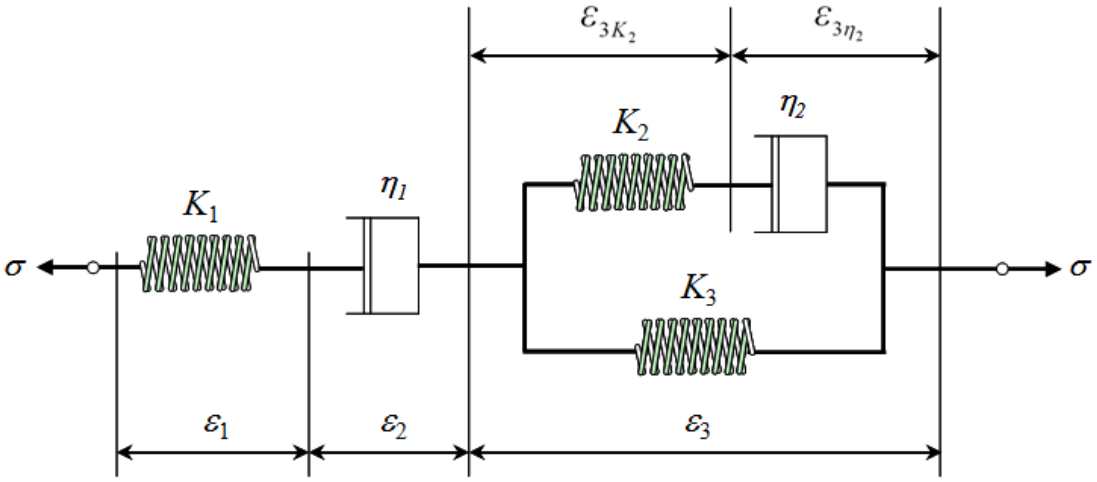

Fig. G Five-parameter model.

From Fig. G, it can be readily seen that

$$\sigma = K_1\varepsilon_1,\ \ \sigma = \eta_1\dot{\varepsilon}_2,\ \ \sigma_1 = K_3\varepsilon_3,\ \ \sigma_2 = K_2\varepsilon_{3K_2} = \eta_2\dot{\varepsilon}_{3\eta_2}, \tag{G1a–d}$$

where σ is the applied stress, and σ_1 and σ_2 are the branch stresses related to the GM element, with

$$\sigma = \sigma_1 + \sigma_2 = K_3\varepsilon_3 + K_2\varepsilon_{3K_2}. \tag{G2}$$

Fig. G also shows that

$$\varepsilon = \varepsilon_1 + \varepsilon_2 + \varepsilon_3, \tag{G3}$$

where ε is the total strain induced by the applied stress, and ε_1, ε_2, and ε_3 are, respectively, the strain in the K_1 spring, the η_1 dashpot, and the GM unit, with

$$\varepsilon_3 = \varepsilon_{3K_2} + \varepsilon_{3\eta_2} . \tag{G4}$$

Using Eq. (G4) in Eq. (G2) gives

$$\dot{\sigma} = \left(K_2 + K_3\right)\dot{\varepsilon}_3 - K_2\dot{\varepsilon}_{3\eta_2} . \tag{G5}$$

From Eqs. (G1c), (G1d) and (G2) it follows that

$$\dot{\varepsilon}_{3\eta_2} = \frac{1}{\eta_2}\left(\sigma - K_3\varepsilon_3\right). \tag{G6}$$

Substituting Eq. (G6) into Eq. (G5) leads to

$$\dot{\varepsilon}_3 = \frac{1}{K_2 + K_3}\left[\dot{\sigma} + \frac{K_2}{\eta_2}\left(\sigma - K_3\varepsilon_3\right)\right]. \tag{G7}$$

The use of Eqs. (G1a), (G1b), (G3) and (G7) then results in

$$\left[\frac{K_1 + K_2 + K_3}{K_1\left(K_2 + K_3\right)}\right]\dot{\sigma} + \left[\frac{1}{\eta_1} + \frac{K_2}{\eta_2\left(K_2 + K_3\right)}\left(1 + \frac{K_3}{K_1}\right)\right]\sigma = \dot{\varepsilon} + \left[\frac{K_2K_3}{\eta_2\left(K_2 + K_3\right)}\right]\varepsilon - \left[\frac{K_2K_3}{\eta_2\left(K_2 + K_3\right)}\right]\varepsilon_2 \tag{G8}$$

Differentiating Eq. (G8) with respect to time gives, with the help of Eq. (G1b),

$$\left[\frac{\eta_2\left(K_1 + K_2 + K_3\right)}{K_1K_2K_3}\right]\ddot{\sigma} + \left[\frac{\eta_2\left(K_2 + K_3\right)}{\eta_1\left(K_2K_3\right)} + \frac{1}{K_3}\left(1 + \frac{K_3}{K_1}\right)\right]\dot{\sigma} + \left(\frac{1}{\eta_1}\right)\sigma = \left[\frac{\eta_2\left(K_2 + K_3\right)}{K_2K_3}\right]\ddot{\varepsilon} + \dot{\varepsilon} \tag{G9}$$

Eq. (G9) is a second-order inhomogeneous ODE. The independent variable is time, t, and the unknown function is the stress, $\sigma(t)$, which also depends on the strain, $\varepsilon(t)$.

The initial conditions to be invoked in solving Eq. (G9) are the following:

$$\sigma(0) = 0, \quad \varepsilon(0) = 0, \quad \ddot{\varepsilon}(0) = 0\,. \tag{G10a,b,c}$$

For constant strain rate deformations with $\dot{\varepsilon}(t) = \text{constant}$ and $\ddot{\varepsilon}(t) = 0$, Eq. (G10c) is satisfied and Eq. (G9) reduces to

$$p_2\ddot{\sigma} + p_1\dot{\sigma} + p_0\sigma = \dot{\varepsilon}\,, \tag{G11}$$

where

$$p_2 = \frac{\eta_2\left(K_1 + K_2 + K_3\right)}{K_1K_2K_3}, \quad p_1 = \frac{\eta_2\left(K_2 + K_3\right)}{\eta_1\left(K_2K_3\right)} + \frac{1}{K_3}\left(1 + \frac{K_3}{K_1}\right), \quad p_0 = \frac{1}{\eta_1}. \tag{G12}$$

The general solution of the second-order ODE given in Eq. (G11) is

$$\sigma = d_1e^{\omega_1 t} + d_2e^{\omega_2 t} + \frac{\dot{\varepsilon}}{p_0}\,, \tag{G13}$$

where ω_1 and ω_2 are the roots of the characteristic equation of the homogeneous part of Eq. (G11) given by

$$\omega_1 = -\frac{1}{2\eta_1\eta_2\left(K_1 + K_2 + K_3\right)}\left[\begin{array}{l}\eta_1\left(K_1K_2 + K_2K_3\right) + \eta_2\left(K_1K_2 + K_1K_3\right) - \\ \sqrt{\eta_1^2\left(K_1^2K_2^2 + K_2^2K_3^2 + 2K_1K_2^2K_3\right) + \eta_2^2\left(K_1^2K_2^2 + K_1^2K_3^2 + 2K_1^2K_2K_3\right)} \\ -\eta_1\eta_2\left(2K_1^2K_2K_3 + 2K_1K_2^2K_3 + 2K_1K_2K_3^2 - 2K_1^2K_2^2\right)\end{array}\right], \tag{G14a}$$

$$\omega_2 = -\frac{1}{2\eta_1\eta_2\left(K_1 + K_2 + K_3\right)}\left[\begin{array}{l}\eta_1\left(K_1K_2 + K_2K_3\right) + \eta_2\left(K_1K_2 + K_1K_3\right) + \\ \sqrt{\eta_1^2\left(K_1^2K_2^2 + K_2^2K_3^2 + 2K_1K_2^2K_3\right) + \eta_2^2\left(K_1^2K_2^2 + K_1^2K_3^2 + 2K_1^2K_2K_3\right)} \\ -\eta_1\eta_2\left(2K_1^2K_2K_3 + 2K_1K_2^2K_3 + 2K_1K_2K_3^2 - 2K_1^2K_2^2\right)\end{array}\right], \tag{G14b}$$

and d_1 and d_2 are integration constants that can be determined from the initial conditions as follows.

From Eqs. (G1a,b), (G3) and (G7) it follows that

$$\left[\frac{1}{K_1}+\frac{1}{K_2+K_3}\right]\dot{\sigma}(0)+\left[\frac{1}{\eta_1}+\frac{K_2}{\eta_2\left(K_2+K_3\right)}\right]\sigma(0)=\dot{\varepsilon}+\frac{K_2K_3}{\eta_2\left(K_2+K_3\right)}\varepsilon_3(0)\,, \qquad \text{(G15)}$$

where use has been made of the fact that $\dot{\varepsilon}$ = constant at any time $t \geq 0$. With $\sigma(0) = 0$ (see Eq. (G10a)) and $\varepsilon_3(0) = 0$, Eq. (G15) reduces to

$$\dot{\sigma}(0)=\frac{K_1\left(K_2+K_3\right)}{K_1+K_2+K_3}\dot{\varepsilon}. \qquad \text{(G16)}$$

Using Eq. (G13) in Eqs. (G10a) and (G16) then leads to

$$d_1=-\left(\eta_1+\frac{K_{eff}+\eta_1\omega_1}{\omega_2-\omega_1}\right)\dot{\varepsilon}, \qquad d_2=\frac{K_{eff}+\eta_1\omega_1}{\omega_2-\omega_1}\dot{\varepsilon}, \qquad \text{(G17)}$$

where

$$K_{eff}=\frac{K_1\left(K_2+K_3\right)}{K_1+K_2+K_3}. \qquad \text{(G18)}$$

Substituting Eq. (G17) into Eq. (G13) then leads to

$$\sigma(t)=\left[\left(1+\frac{\omega_1e^{\lambda_2t}-\omega_2e^{\lambda_1t}}{\omega_2-\omega_1}\right)\eta_1+\frac{e^{\omega_2t}-e^{\omega_1t}}{\omega_2-\omega_1}K_{eff}\right]\dot{\varepsilon}\ . \qquad \text{(G19)}$$

Note that $\frac{d\varepsilon}{dt}=\dot{\varepsilon}$ = constant, together with Eq. (B10b), gives $\varepsilon=\dot{\varepsilon}t$ or $t=\frac{\varepsilon}{\dot{\varepsilon}}$. Using this in Eq. (G19) finally gives

$$\sigma=\left[\left(1+\frac{\omega_1e^{\omega_2\frac{\varepsilon}{\dot{\varepsilon}}}-\omega_2e^{\omega_1\frac{\varepsilon}{\dot{\varepsilon}}}}{\omega_2-\omega_1}\right)\eta_1+\frac{e^{\omega_2\frac{\varepsilon}{\dot{\varepsilon}}}-e^{\omega_1\frac{\varepsilon}{\dot{\varepsilon}}}}{\omega_2-\omega_1}K_{eff}\right]\dot{\varepsilon} \qquad \text{(G20)}$$

as the stress-strain relation provided by the five-parameter model proposed in the current study. This constitutive equation is given as Eq. (4.11) and has been used to obtain the relevant numerical results presented in Section 4.7.

It should be mentioned that Eq. (G20) obtained for the five-parameter model here is the same in form as that derived in Eq. (E1.11) for the Burgers model (see *Appendix E1*), but the four parameters involved in Eq. (G20) and Eq. (E1.11) are different, as seen from Eqs. (E1.5a,b), (E1.9) and (G14a,b), (G18).

APPENDIX H

The para-rheological model, which consists of consists of a GM element and a stress network element in parallel, is shown in Fig. H.

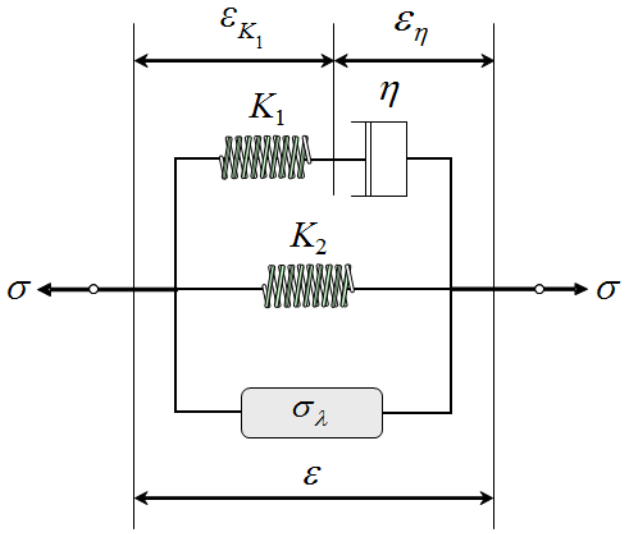

Fig. H Para-rheological model.

The stress-strain relations for the elements and network involved in Fig. H are given by

$$\sigma_1 = K_1\varepsilon_{K_1} = \eta\dot{\varepsilon}_\eta,\ \sigma_2 = K_2\varepsilon,\ \text{and}\ \sigma_\lambda = E_{NR}\hat{e}\,, \tag{H1a,b,c}$$

where Eq. (H1c) is first given in Eq. (4.2) (see also Eq. (D29)), with the strain measure $\hat{e}$ defined in terms of the extension ratio λ as

$$\hat{e} = \lambda - \frac{1}{\lambda^2}\ . \tag{H2}$$

Note that λ is related to the engineering strain ε by

$$\varepsilon = \lambda - 1\,. \tag{H3}$$

Using Eq. (H3) in Eq. (H2) then gives, with the help of Taylor's expansion,

$$\hat{e} = 1 + \varepsilon - \frac{1}{(1+\varepsilon)^2} = 3\varepsilon - \left(3\varepsilon^2 - 4\varepsilon^3 + 5\varepsilon^4 - \cdots\right). \tag{H4}$$

For small deformations, $\varepsilon << 1$ and the higher-order terms in Eq. (H4) can be ignored to obtain the following linearized relation:

$$\hat{e} \cong 3\varepsilon. \tag{H5}$$

Next, differentiating Eq. (H4) with respect to time gives

$$\dot{\hat{e}} = \frac{3 + 3\varepsilon + 3\varepsilon^2 + \varepsilon^3}{(1+\varepsilon)^3}\dot{\varepsilon}. \tag{H6}$$

By using Taylor's expansion and ignoring the higher-order terms for small deformations with $\varepsilon << 1$, Eq. (H6) can be linearized as

$$\dot{\hat{e}} \cong 3(1 - 2\varepsilon)\dot{\varepsilon}. \tag{H7}$$

From Fig. H it follows that

$$\varepsilon = \varepsilon_{K_2} + \varepsilon_{\eta_1} \tag{H8}$$

where ε is the total strain induced by the applied stress. Also,

$$\sigma = \sigma_1 + \sigma_2 + \sigma_\lambda\,. \tag{H9}$$

Using Eqs. (H1a-c) and (H8) in Eq. (H9) yields

$$\dot{\sigma} = K_1\dot{\varepsilon} - K_1\dot{\varepsilon}_\eta + K_2\dot{\varepsilon} + E_{NR}\dot{\hat{e}}. \tag{H10}$$

From Eqs. (H1a,b) and (H9),

$$\dot{\varepsilon}_\eta = \frac{1}{\eta}(\sigma - \sigma_\lambda - K_2\varepsilon). \tag{H11}$$

Substituting Eqs. (H1c), (H5), (H7) and (H11) into Eq. (H10) then leads to

$$\dot{\sigma}(t) + \frac{K_1}{\eta}\sigma(t) = (K_1 + K_2 + 3E_{NR})\dot{\varepsilon}(t) + \left[\frac{K_1K_2}{\eta} + 3E_{NR}\left(\frac{K_1}{\eta} - 2\dot{\varepsilon}\right)\right]\varepsilon(t). \tag{H12}$$

Appendix H.1

Derivation of the constitutive equation of the para-rheological model for constant strain rate

For constant strain rate deformations with $\dot{\varepsilon}$ = constant, Eq. (H12), a first-order linear ODE (see Appendix H), can be readily solved to obtain its general solution as

$$\sigma(t) = \left[K_2 + 3E_{NR}\left(1 - \frac{2\eta}{K_1}\dot{\varepsilon}\right)\right]\varepsilon + \eta\left(1 + \frac{6E_{NR}\eta}{K_1^2}\dot{\varepsilon}\right)\dot{\varepsilon} + ce^{-at}. \tag{H1.1}$$

where c is an integration constant. From Eq. (H1.1) and the initial conditions:

$$\sigma(0) = 0, \quad \varepsilon(0) = 0, \tag{H1.2a,b}$$

it follows that

$$c = -\eta_1\left(1 + \frac{6E_{NR}\eta}{K_1^2}\dot{\varepsilon}\right)\dot{\varepsilon}. \tag{H1.3}$$

Note that $\frac{d\varepsilon}{dt} = \dot{\varepsilon}$ = constant, together with Eq. (C14b), gives $t = \frac{\varepsilon}{\dot{\varepsilon}}$. Substituting this relation and Eq. (H1.3) into Eq. (H1.1) finally yields

$$\sigma = K_{eff}\varepsilon + K_{ve}\left[1 - e^{-\left(\frac{1}{\tau}\right)\frac{\varepsilon}{\dot{\varepsilon}}}\right]\dot{\varepsilon}, \tag{H1.4}$$

where K_{eff}, K_{ve}, and τ are, respectively, the effective stiffness, the viscous stiffness, and the retardation time defined by

$$K_{eff} = K_2 + 3E_{NR}\left(1 - \frac{2\eta}{K_1}\dot{\varepsilon}\right), \tag{H1.5a}$$

$$K_{ve} = \eta\left(1 + \frac{6E_{NR}\eta}{K_1^2}\dot{\varepsilon}\right) = \tau\left(\frac{K_1^2 + 6E_{NR}\eta\dot{\varepsilon}}{K_1}\right), \tag{H1.5b}$$

$$\tau = \frac{\eta}{K_1}. \tag{H1.5c}$$

Eq. (H1.4) is the constitutive relation given by the newly developed para-rheological model, which is listed as Eq. (4.14) and has been used to obtain the relevant numerical results presented in Section 4.7.

Appendix H.2

Derivation of the stress relaxation function of the para-rheological model

For a constant applied strain with $\varepsilon = \varepsilon_o$ and $\dot{\varepsilon} = 0$, Eq. (H12), a first-order linear ODE (see Appendix H), can be readily solved to obtain its general solution as

$$\sigma(t) = e^{-\frac{t}{\tau}}\left(\left(K_2 + 3E_{NR}\right)\varepsilon_o e^{\frac{t}{\tau}} + c \right), \tag{H2.1}$$

where $\tau = \dfrac{\eta}{K_1}$ and c is an integration constant. From Eq. (H2.1) and the initial conditions:

$$\sigma(0) = \sigma_o, \tag{H2.2}$$

it follows that

$$c = \sigma_o - \left(K_2 + 3E_{NR}\right)\varepsilon_o . \tag{H2.3}$$

Substituting Eq. (H2.3) into Eq. (H2.1) gives

$$\sigma(t) = \sigma_o e^{-\frac{t}{\tau}} + \left(1 - e^{-\frac{t}{\tau}}\right)\left(K_2 + 3E_{NR}\right)\varepsilon_o . \tag{H2.4}$$

If the instantaneous modulus of the composite just before the beginning of the relaxation test, i.e., tensile modulus at time $t = 0^-$, is taken to be

$$E_i = K_1 + K_2 + 3E_{NR} . \tag{H2.5}$$

Eq. (H2.2) can then be written in terms of the instantaneous modulus and the initial strain as

$$\sigma_o = E_i \varepsilon_o \,. \tag{H2.6}$$

Substituting Eqs. (H2.6) and Eq. (H2.5) into Eq. (H2.4) finally yields

$$\sigma(t) = \left[K_1 e^{-\frac{t}{\tau}} + \left(K_2 + 3E_{NR} \right) \right] \varepsilon_o \,. \tag{H2.7}$$

Eq. (H2.7) is the stress relaxation function given by the newly developed para-rheological model, which is listed as Eq. (5.4) and has been used to obtain the relevant numerical results presented in Fig. 5.5. From Eq. (H2.7), the stress relaxation modulus, $E_r(t)$, is defined as

$$E_r(t) = K_1 e^{-\frac{t}{\tau}} + \left(K_2 + 3E_{NR} \right). \tag{H2.8}$$

Appendix H.3

Derivation of the creep function from a non-linear differential equation of the para-rheological model

For a constant applied stress with $\sigma = \sigma_o$ and $\dot{\sigma} = 0$, Eq. (H12), which is a non-linear ordinary differential equation for $\varepsilon(t)$, becomes

$$A\dot{\varepsilon} + B\dot{\varepsilon}\varepsilon + C\varepsilon = D \,, \tag{H3.1}$$

where

$$A = K_1 + K_2 + 3E_{NR} \,, \quad B = -6E_{NR} \,, \quad C = \frac{K_1}{\eta}\left(K_2 + 3E_{NR} \right), \quad D = \frac{K_1}{\eta}\sigma_0 . \tag{H3.2a-d}$$

Eq. (H3.1) can be rewritten as

$$\dot{\varepsilon} = \frac{D - C\varepsilon}{A + B\varepsilon} \tag{H3.3}$$

Eq. (H3.3) can be readily solved by integration to obtain

$$-A_o \ln\left(D - C\varepsilon\right) + B_o^{'}\left(D - C\varepsilon\right) + k = t\,, \tag{H3.4}$$

where constants A_o and $B_o^{'}$ are given by

$$A_o = \frac{1}{C}\left(A + \frac{BD}{C}\right), \quad B_o^{'} = \frac{B}{C^2} \tag{H3.5a,b}$$

and k is a constant to be determined from the initial condition.

Using the initial condition for the strain, i.e., $\varepsilon(0) = \varepsilon_0$ in Eq. (H3.4) gives constant k as follows:

$$k = A_o \ln\left(D - C\varepsilon_0\right) - B_o^{'}\left(D - C\varepsilon_0\right) \tag{H3.6}$$

Substituting Eq. (H3.6) into Eq. (H3.4) gives the final solution as follows:

$$A_o \ln\left(\frac{C_o - \varepsilon_0}{C_o - \varepsilon}\right) + B_o\left(\varepsilon - \varepsilon_0\right) = t\ , \tag{H3.7}$$

where constants B_o and C_o are given by, with the help Eqs. (H3.2c,d) and Eq. (H3.5b),

$$B_o = -\frac{B}{C}, \quad C_o = \frac{D}{C} = \frac{\sigma_0}{K_2 + 3E_{NR}}\,. \tag{H3.8a,b}$$

Using Eqs.(H3.2b,c) in Eq. (H3.8a) gives

$$B_o = \Psi\,\tau_p \tag{H3.9}$$

where

$$\tau_p = \frac{\eta}{K_1}, \quad \Psi = \frac{6E_{NR}}{K_2 + 3E_{NR}}\,. \tag{H3.10a,b}$$

From Eqs.(H3.2a,b,c,d) and (H3.5a),

$$A_o = \left(Y - X\sigma_0\right)\cdot\tau_p \tag{H3.11}$$

where

$$Y = 1 + \frac{K_1}{K_2 + 3E_{NR}}, \quad X = \frac{\Psi}{K_2 + 3E_{NR}}, \tag{H3.12a,b}$$

in which τ_p and Ψ are defined in Eqs. (H3.10a,b).

Substituting Eqs. (H3.9) and (H3.11) into Eq. (H3.7) finally yields the solution of Eq. (H3.1) in the following form:

$$\tau_p\left[\Phi\ln\left(\frac{C_o - \varepsilon_0}{C_o - \varepsilon}\right) + \Psi\left(\varepsilon_0 - \varepsilon\right)\right] = t\ , \tag{H3.13}$$

where

$$\Phi = Y - X\sigma_0. \tag{H3.14}$$

It is to be noted that C_o, Φ and Ψ are dimensionless. Eq. (H3.13) is the creep function derived from the non-linear differential equation of the newly developed para-rheological model, which is listed as Eq. (6.12) in Section 6.7.1 and has been used to obtain the relevant numerical results presented in Fig. 6.8.

Appendix H.4

Derivation of the creep function from a linearized differential equation of the para-rheological model

In order to simplify the problem further, only the first term of the linearized $\dot{\hat{e}}$ in Eq. (H7), i.e., $\dot{\hat{e}} \cong 3\dot{\varepsilon}$, need to be considered. The differential equation given by Eq. (H12) for a constant stress, $\sigma = \sigma_o$, then becomes

$$A\dot{\varepsilon} + B\varepsilon = C\,, \tag{H4.1}$$

where

$$A = K_1 + K_2 + 3E_{NR}, \quad B = \frac{K_1}{\eta}\left(K_2 + 3E_{NR}\right), \quad C = \frac{K_1}{\eta}\sigma_0. \tag{H4.2a-c}$$

Eq. (H4.1) is a first-order linear ODE that can be readily solved to obtain its general solution as

$$\varepsilon(t) = \frac{C}{B} + ke^{-\frac{B}{A}t}. \tag{H4.3}$$

where k is an integration constant. From Eq. (H4.1) and the initial condition

$$\varepsilon(0) = \varepsilon_0, \tag{H4.4}$$

it follows that

$$k = \varepsilon_0 - \frac{C}{B}. \tag{H4.5}$$

Substituting Eq. (H4.5) and Eqs. (H4.2a,b,c) into Eq. (H4.3) finally yields the creep function as

$$\varepsilon(t) = \left[J_0 \cdot e^{-\frac{t}{\tau_{pl}}} + J \cdot \left(1 - e^{-\frac{t}{\tau_{pl}}} \right) \right] \sigma_0, \tag{H4.6}$$

where

$$J_0 = \frac{\varepsilon_0}{\sigma_0}, \quad J = \frac{1}{K_2 + 3E_{NR}}, \quad \tau_{pl} = \frac{\eta\left(K_1 + K_2 + 3E_{NR}\right)}{K_1\left(K_2 + 3E_{NR}\right)}. \tag{H4.7a-c}$$

Eqs. (H4.7a) and (H4.7c) are the initial creep compliance (at $t = 0$) and the retardation time, respectively. From Eq. (H4.6), the creep compliance based on this simplified analysis is given by

$$J(t) = J_0 \cdot e^{-\frac{t}{\tau_{pl}}} + J \cdot \left(1 - e^{-\frac{t}{\tau_{pl}}} \right). \tag{H4.8}$$

Eq. (H4.6) is the creep function derived from the linearized differential equation of the newly developed para-rheological model, which is listed as Eq. (6.15) and has been used to obtain the relevant numerical results presented in Fig. 6.8.

APPENDIX I

Approximations of continuous relaxation and retardation times

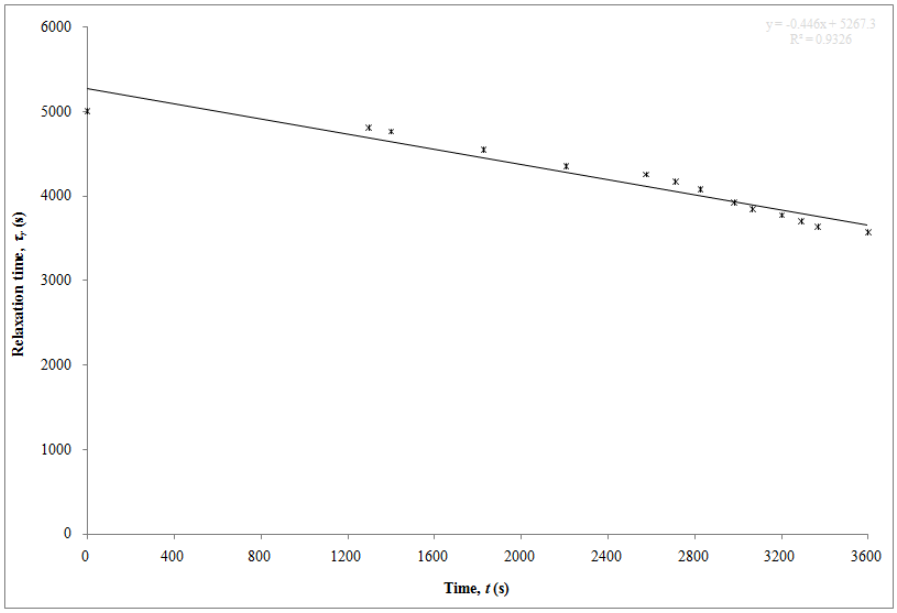

Fig. I1 Time history of the relaxation time obtained from the para-rheological model.

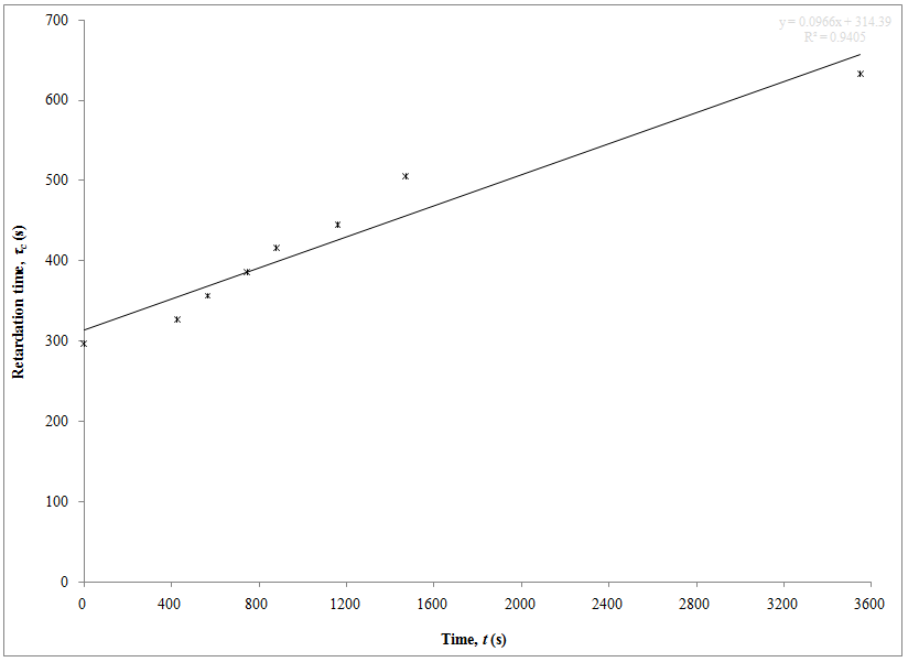

Fig. I2 Time history of the retardation time obtained from the solution of the non-linear differential equation of the para-rheological model.

VITA

Valliyappan David Natarajan earned a Bachelor of Engineering (Honors) degree in mechanical engineering (1999) and a Master of Science degree in mechanical and materials engineering (2001) from Universiti Kebangsaan Malaysia (National University of Malaysia). He has been a lecturer in the Department of Mechanical Engineering, MARA University of Technology (UiTM) in Shah Alam, Malaysia since 2002. He has consulted various private establishments related to polymer manufacturing, automotive, and oil and gas industries. David has conducted research in the areas of composites engineering and structural health monitoring and is an author/co-author of 9 published/in-press journal papers, 35 conference proceedings papers and 5 book chapters as of October 2009. His research interests are in composite materials, viscoelasticity, acoustics, and condition-based monitoring.

David obtained his doctoral degree in mechanical engineering (major: Materials Science and Engineering) in December 2009 under the auspices of UiTM and the Fulbright Fellowship at Texas A&M University. He may be reached at nv_david@yahoo.com or Department of Mechanical Engineering (Attn. to: Associate Professor Dr. Xin-Lin Gao), Texas A&M University, 3123 TAMU, College Station, Texas 77843-3123, United States of America.